UNIVERSITY OF EXETER

DOCTORAL THESIS

Making the Grade: Generating & Controlling Spin Waves with a Graded Refractive Index

---

Author:
Natalie WHITEHEAD

Supervisors:
Prof. Volodymyr V. KRUGLYAK
Dr. Thomas G. PHILBIN
Dr. Simon A. R. HORSLEY

A thesis submitted for the degree of Doctor of Philosophy in Physics

in the

EPSRC Centre for Doctoral Training in Metamaterials
College of Engineering, Mathematics and Physical Sciences

September 2019

Making the Grade: Generating & Controlling Spin Waves with a Graded Refractive Index

Declaration of Authorship

Submitted by Natalie Whitehead, to the University of Exeter as a thesis for the degree of Doctor of Philosophy in Physics, September 2019.

I certify that all material in this thesis which is not my own work has been identified and that any material that has previously been submitted and approved for the award of a degree by this or any other University has been acknowledged.

I acknowledge financial support from the Engineering and Physical Sciences Research Council (EPSRC) of the United Kingdom, via the EPSRC Centre for Doctoral Training in Metamaterials (Grant No. EP/L015331/1).

All data created during this research are available from the University of Exeter's institutional repository ORE at https://doi.org/10.24378/exe.2203.

Signed:

_____

Abstract

In this thesis, the magnetic parameters of a ferromagnetic film are varied to create refractive index profiles for spin waves. The properties of this "magnonic" refractive index are studied for different frequency regimes. Analytical theory and numerical modelling are used throughout.

The research in this work is along two main themes. The first involves the generation of spin waves from a graded (or stepped) refractive index region. The energy is driven into the system via a harmonic yet spatially-uniform external magnetic field, and it is shown that the graded index feature may then act as a spin wave source. Exchange (short wavelength) spin waves are studied in this case, since their dynamics are described by the Landau-Lifshitz equation that can be linearised to form a Schrödinger-like equation. This exchange regime is therefore ideal for exploring how the features of well-known exactly-solvable models manifest themselves for spin waves.

The exactly-solvable models in this case are a square potential barrier and a Pöschl-Teller potential well. The latter naturally occurs as a magnetic domain wall in a ferromagnet, with a fixed potential 'height'. Spin waves can be generated by both features, but spin wave emission is not guaranteed. The excitation frequency must primarily be above a threshold value, akin to the 'work function' energy in quantum mechanics. Furthermore, certain heights of the potential (or frequencies of excitation) can lead to confinement within the potential region.

The second theme studied in this work involves using a graded refractive index to focus or steer spin waves. The rotationally-symmetric graded index lenses, well known in optics, are realised here for spin waves in a perpendicularly-magnetised film, for magnetostatic (long wavelength) spin waves. In this regime, the magnetisation only needs to be changed by a tiny amount, of the order of 2%, to create a Luneburg lens. For the steering lenses, which require a singular refractive index in the centre, just a 10% increase in the magnetisation can create the steering lenses almost exactly. The general properties of the magnonic refractive index are also analysed, for the entire range of spin wave wavelengths, from millimetres to nanometres. The magnetostatic regime is found to be ideal for creating extreme changes in the refractive index, theoretically from 1 to over 100.

Acknowledgements

It is a pleasure to be finally writing these acknowledgements! I firstly need to thank my three supervisors, Volodymyr, Tom and Simon, for all their time, effort and patience over the past 4 years. I count myself very lucky to have worked with such intelligent, interesting people who have all given their time so generously.

I've been here at Exeter University for 8 years now, and there are a great number of people I need to give my thanks to, for making the whole experience so enjoyable. Thanks to Angus for not eating *all* of my chocolate supplies, and to both him and Tom for helping me to understand and appreciate so many aspects of magnetism (i.e. magic), physics, maths, programming, history, food, wine,... You've been great friends, and I've enjoyed the many gastronomic afternoons / evenings over the years (especially the 8 course extravaganza!).

Also to the lovely CDT people who I enjoyed many nice chats / cakes / tea-making sessions with, especially Lauren (and honorary member Adolfo), Erick, Ilya, Sathya, Chris, Yulia, Vicky, Liam, Kishan, Joseph, Jacob, Lizzie, David,... there are far too many to list! Thanks as well to everyone on the 3rd floor who have made me feel very welcome for the past year. Misha, thanks for dutifully helping me finish all the cakes, back when I had time to make them! Thanks also to all the people in the Theory Group for all the nice discussions, and for listening to all my spin wave woes for the past 4 years!

A hugely rewarding part of my time here (in the Undergrad and PhD) has been in doing physics outreach, and I have to thank Pete Vukusic for getting me involved back in 2012, and for giving me so many opportunities since then. You've been a constant source of inspiration and enthusiasm, and a wonderful unofficial mentor throughout. I'm also hugely grateful to Alice Mills for the many outreach opportunities and all the help over the years — thank you for keeping me going with all your infectious enthusiasm and positivity.

To all the people who keep the physics building functioning in various ways, who have patiently put up with me asking them for help / equipment... Derek, Dave, Nick, Peter, Paul and Richard, I really appreciate it! Theresa, thank you for being my Gardening Guru — I've enjoyed our chats about plants and everything else under the sun. Noris, muchas gracias for all the smiles and Spanish lessons!

To Callum, for being 24/7 Tech (and everything else) Support, and my family, for all the endless help and encouragement — I'm so grateful for everything you do for me.

Contents

List of Figures

Chapter 1

Introduction

The study of spin waves in ferromagnets, or their quasiparticles "magnons", is a growing research area, primarily due to the promising applications in wave-based computing. This is due to the reduced losses involved in chargeless spin transport [1–3], their easy integration with spintronics (spin-polarized electron transport) systems [4], and the many possible spin wave regimes for different geometries and frequencies [5]. Although the main theoretical foundations were laid just less than a century ago [6, 7] , the experimental analysis of more interesting spin wave behaviour has only been possible in the past couple of decades. As experimental and modelling techniques become more advanced, we can naturally take inspiration from other areas of wave physics to find interesting phenomena to realise for spin waves. In this thesis, the inspiration comes from the most well-established area of wave physics: optics.

The particular area of interest in optics involves the concept of a graded refractive index. In contrast to a step change, a graded index allows for a smooth change of the wavelength with minimal reflections due to the infinitesimal interfaces [8, 9]. Graded index optics has found many practical applications in graded index fibres and, more importantly for this work, graded index lenses. The method of gradually changing the refractive index has also been realised in many other areas of wave physics, including (and certainly not limited to) plasmonics [10], phononics and acoustics [11], and, quite recently, magnonics [12].

The theme of "graded index magnonics" has been gaining a great deal of interest recently as the parameter space of magnetic materials is further exploited to confine [13, 14], direct [15–17], generate [18, 19] or focus [20] spin waves. The work in this thesis can be separated into to two sub-topics — firstly, using a stepped or graded index region as a source of spin waves. This work aims to show an alternative to antennas for generating nanometre-wavelength spin waves (or spin waves of any other wavelength; the mechanism should still be

valid). Secondly, creating graded index lenses to focus or direct propagating spin waves. The rotationally-symmetric profiles studied here are made for spin waves with a surprisingly small change in the material parameters, and may be useful in spin wave circuitry, in focusing/steering spin waves from any angle.

The outline of this thesis is as follows. In Chapter 2, the relevant background theory of magnetism is highlighted, with particular emphasis on magnetism dynamics — spin waves. For this work, it is important to understand the spin wave behaviour in different regimes, determined by the dispersion relation, so this forms an important focus of this Chapter.

In Chapter 3, the analytical method for working with short-wavelength (exchange) spin waves is described. We look at the simplest case of a square potential, represented as a step in the anisotropy, and show that this region may act as a source of spin waves, when simply excited by a uniform, harmonic magnetic field. In Chapter 4, a similar methodology to Chapter 3 is used to explore spin wave emission from a Bloch domain wall, which naturally occurs in magnetic films of certain geometries.

In Chapter 5, spin wave focusing lenses are investigated. The work is primarily based on the Luneburg lens, but the behaviour of a parabolic lens, fitted to the Luneburg profile, is also studied in comparison. This work is mainly concerned with the purely magnetostatic regime, where the spin waves are dominated by the long-range dipole-dipole interaction. In Chapter 6, the methodology of Chapter 5 is extended to consider steering lenses for spin waves, which require an extreme change in the refractive index.

Finally, in Chapter 7, the properties of the magnonic refractive index are explored in more detail for different spin wave frequency regimes. The results and prospects are summarised in Chapter 8.

Chapter 2

Background Theory

2.1 Introduction

This chapter presents the background theory relevant to this thesis, and a much more exhaustive study can be found in any good textbook on magnetism or magnonics, such as [5, 21, 22]. The discussion is separated in to two main topics: the static properties of ferromagnets, and then the dynamic behaviour of these materials. We will only consider ferromagnets in this study (and will often refer to them simply as magnets), which contain permanent magnetic moments that spontaneously align parallel to each other in the absence of an external magnetic field. Other substances with permanent magnetic moments fall into the categories of paramagnets (with no long-range order), and ferrimagnets and antiferromagnets, whose magnetic moments are aligned antiparallel to their nearest neighbours.

2.2 Quantum Mechanical Origin

We begin by considering the origin of ferromagnetism, which is accurately predicted and explained using quantum mechanics. The details discussed here are summarised from [5, 22].

The most common ferromagnetic elements - iron, nickel and cobalt - all share the same property: they have partially-filled $3d$ electron shells. The properties of the electrons in these shells, and in particular, the alignment of the magnetic dipole moments of these electrons, is the cause of ferromagnetism in these elements. We will first look at the properties of the electron that leads to this effect.

The two important properties of the electron that we are concerned with are: 1) its orbital motion around the nucleus[1], which has an associated angular momentum **L**, and 2) its intrinsic spin angular momentum **S**. The latter is a completely quantum mechanical property, with no analogue in classical mechanics. Importantly, these two angular momenta are quantised, which means they may only take certain discreet values. Both of these angular momenta have an associated magnetic (dipole) moment. For the orbital component, this can be compared to the magnetic moment of a classical current loop. The magnetic moment due to the electron spin cannot be analogised so easily, so we will just have to accept it as a fact. We write the total magnetic moment $\boldsymbol{\mu}$ in SI units, as a function of the total angular momentum **J** and the Bohr magneton μ_B, which is the natural unit of the magnetic moment:

$$\boldsymbol{\mu} = -\frac{e g_J \hbar}{2m_e}\mathbf{J} = g_J \mu_B \mathbf{J} = \gamma \mathbf{J}, \tag{2.2.1}$$

where $\mathbf{J} = \mathbf{L} + \mathbf{S}$, $-e$ is the electron charge, $\hbar$ is the reduced Planck constant, m_e is the electron mass, $\gamma = g_J \mu_B$ is the gyromagnetic ratio, and g_J is the Landé g-factor

$$g_J = \frac{3}{2} + \frac{S(S+1) - L(L+1)}{2J(J+1)}. \tag{2.2.2}$$

From (2.2.1), the overall magnetic dipole moment μ of an electron[2] is found to be around 10^{-23}JT^{-1}. We know from classical electrostatics that two magnetic dipoles exert a force on each other, called a dipole-dipole interaction. The potential energy of the dipole moments of two electrons, which is minimised when the dipoles are *antiparallel*, is of the order of $\mu_0 \boldsymbol{\mu}^2 / r^3 \approx 10^{-23}$ J $\equiv$ 1 K. So, we can see two clear reasons why the magnetic dipole-dipole interaction *cannot* be the significant contribution to ferromagnetism: firstly, the dipole moments in ferromagnets are aligned parallel to each other, and the dipole-dipole interaction resists this alignment. Secondly, at room temperature, the thermal energy is 300 times greater than this interaction energy, and thus any ordering due to this effect would be short-lived.

[1] Of course, from the point of view of quantum mechanics, an electron's 'orbit' is unlike a classical orbit of, say, a planet around a star. Rather, it has a probability distribution about the nucleus, and does not follow a fixed trajectory; this would violate the Heisenberg Uncertainty Principle. However, we use the term 'orbit' because, surprisingly, the behaviour of an electron *can* be accurately predicted by assuming a classical orbit [5].

[2] The *nuclear* magnetic moments are significantly smaller, at around 10^{-26} JT^{-1}, and are thus negligible [22].

Though the dipole-dipole interaction is important in the study of (longer wavelength) spin waves, there must be another, dominant interaction which leads to spontaneous ferromagnetic ordering. It is an effect called the exchange interaction, which, for fermions, is due to the Pauli Exclusion Principle. This principle requires that two fermions cannot occupy the same energy state, meaning that electrons with parallel spins must occupy separate energy levels (orbitals), and thus be further apart, or they may share the same orbital (and be closer together) but have antiparallel spins. In the latter case, these two oppositely charged electrons will have a greater Coulomb repulsion energy, and so the former state must be more energetically favourable. The exchange interaction is a short-range effect, and is usually confined to nearest-neighbour atoms, and we define the exchange energy between two neighbouring spin magnetic moments as

$$E_{\text{ex}} = -J_{\text{ex}}\,\mathbf{S}_1 \cdot \mathbf{S}_2, \tag{2.2.3}$$

where J_{ex} is the exchange integral. In a ferromagnet this energy is minimised when the spins are parallel, and so J_{ex} must be positive in this case.

2.3 Macroscopic Magnetism: Definitions

So far we have discussed the quantum mechanical origin of ferromagnetism, and it is remarkable that such an effect is detectable at the macroscopic scale. At this scale however, we only see the overall, averaged (or 'mean field') effect, and so we must introduce appropriate, measurable properties. Firstly, leading on from our discussion on the magnetic moment, we can introduce the magnetisation $\mathbf{M}$ as the average magnetic dipole moment per unit volume V, i.e.

$$\mathbf{M} = \frac{\sum_V \boldsymbol{\mu}}{V}. \tag{2.3.1}$$

In order to measure the magnetisation, we must introduce another macroscopic quantity, the magnetic field $\mathbf{H}$, which can be related to the magnetisation via the susceptibility tensor $\bar{\chi}$:

$$\mathbf{M} = \mathbf{M}_0 + \bar{\chi}\,\mathbf{H}, \tag{2.3.2}$$

where $\mathbf{M}_0$ is the spontaneous magnetisation occurring without an external field. In order for this relation to be valid for ferromagnets, we must assume that the

applied magnetic field, **H**, is small. When testing the magnetic properties of a sample in large magnetic fields, the magnetisation does not vary linearly with **H**, and the relationship can be traced out on a hysteresis loop (otherwise known as a magnetisation curve). We show some examples in relation to magnetic anisotropy in Section 2.4.2.

Importantly, a magnetic field will exert a torque τ on a magnetic dipole, given by

$$\tau = \boldsymbol{\mu} \times \mathbf{H}, \tag{2.3.3}$$

and we can see that $\boldsymbol{\mu}$ will be forced to align with **H**. We will work with this concept for now and not be concerned with the manner in which this alignment occurs — we will go into these details in due course, since this is more related to magneto-dynamics.

The discussion above is only relevant below a threshold temperature, called the Curie temperature T_C, above which the thermal energy destroys any long-range order. A ferromagnet will then become paramagnetic above T_C; its permanent magnetic moments are randomly oriented. The Curie temperature of most ferromagnets is over 500K, so although some thermal agitation will mean that the magnetisation is not fully saturated, the overall behaviour is still ferromagnetic at room temperature.

2.4 Energy of a Static Ferromagnet

We will now outline the main contributions to the energy of a static ferromagnet[3]. It is convenient to use Gaussian (otherwise known as CGS) units in analytical theory, since there is the great benefit of **H**, **M** & **B**, (along with **E**, **D** and **P** in electrostatics) all having the same *dimensions*. They are still, confusingly, given different *units*; for example, **B** and **M** are usually given in Gauss (G), where **H** is given in Oersted (Oe). Although working with Gaussian units is somewhat easier (we do not need to carry around a factor of μ_0 in each equation), translating this to the more experimentally useful (and dimensionally rational) SI units can be slightly cumbersome. In this thesis, we will work with Gaussian units for the

[3]These are the contributions encountered in this thesis - there are a number of other exotic energy contributions which we do not detail here.

analytical derivations[4], but list out the quantities in both Gaussian and SI units when appropriate.

Energy of an Applied Magnetic Field

When a magnetic field is applied to a ferromagnet, the energy contribution is

$$E_H = -\mathbf{H} \cdot \mathbf{M}. \tag{2.4.1}$$

This is the Zeeman energy, and is minimised when the magnetisation is aligned with the external ("bias") magnetic field.

2.4.1 Magnetostatic (Demagnetising) Energy

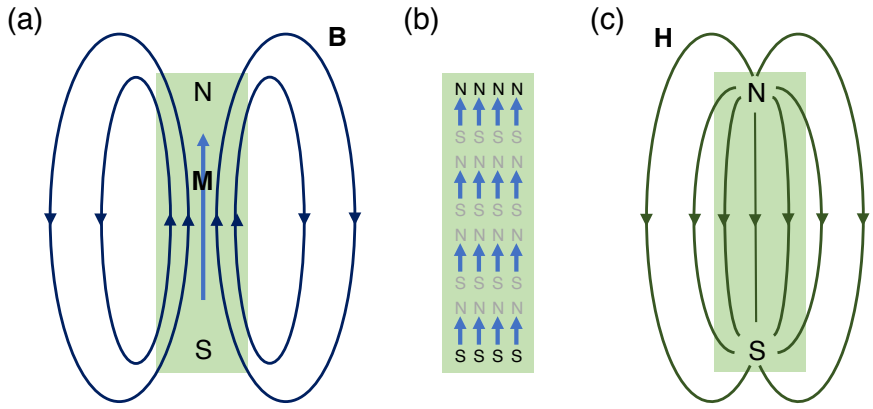

FIGURE 2.1: Uniaxial ferromagnet, showing (a) net magnetisation **M** and magnetic **B** field lines and resultant north (N) and south (S) poles, (b) magnetisation arrows of clusters of spins in each region, each with effective N and S poles, and (c) **H** field lines, which start at N and end at S poles. This is based on Ref. [22].

The magnetostatic energy E_{ms} is directly proportional to the demagnetising field $\mathbf{H}_{\text{d}}$,

$$E_{\text{ms}} = -\frac{1}{2}\mathbf{H}_{\text{d}} \cdot \mathbf{M}. \tag{2.4.2}$$

The demagnetising field arises from, and acts to reduce the effect of, the magnetisation in a finite magnet. The source is the north and south magnetic poles, such

[4]We will do so carefully, bearing in mind that the Gaussian unit of length is the cm. This unfortunate unit has the tendency to induce panic in PhD students who worry that the spin wave wavelength is 100 times larger than it should be...

as at each end of a saturated bar magnet (Fig. 2.1 (a)). The poles exist because the magnetic field (i.e. the north pole and south pole) of each spin is uncompensated at each end of the magnet, yet compensated in the bulk, since the spins are aligned head to tail (Fig. 2.1 (b)). These uncompensated poles at the two ends induce a field within the magnet which point from the north directly to the south pole, and this field is the demagnetising field. The term 'magnetic charges' is often used to describe the apparent sources of this field outside of the sample (akin to an electric charge with diverging field lines). Since the source of $\mathbf{H}_d$ is only the spins towards each end of the magnet, its magnitude is much less than the internal magnetic **B** field from the south to north pole (**B** fields form closed loops, as in panel (c)). The field $\mathbf{H}_d$ tends to vary nontrivially within the magnet, and so it is often difficult to determine. Luckily, depending on the shape of the sample, you may be able to approximate it as some form of ellipsoid, and thus write

$$\mathbf{H}_\mathrm{d} = -N_\mathrm{d}\mathbf{M}, \tag{2.4.3}$$

where N_d is a demagnetising factor, which, for a sphere, is equal to $4\pi/3$ (Gaussian units), and a flatter 'spheroid' (disc) shape may have $N_\mathrm{d} \approx 4\pi$. The equivalent SI units can be obtained by dividing N_d (Gaussian) by 4π. We can see that the demagnetising energy tends to increase with increasing M, and is always a positive quantity. Naturally then, the magnetic configuration will tend to minimise its demagnetising field, which is why bar magnets tend to be aligned along the long axis, or vortex structures tend to occur in discs or square elements; there are fewer uncompensated poles / magnetic 'charges'.

As a final note, when we consider short wavelength spin waves, we can usually neglect the demagnetising (dipole-dipole) field if the dimensions of the ferromagnet are much larger than the spin wave wavelength, i.e. the sample is effectively infinite. Since dipole-dipole interactions can be neglected, there are instances where we do not need to apply an external magnetic field; the self-induced alignment of the spins, perhaps combined with strong anisotropy, is sufficient to ensure the energy state is stable. We will see an example of this in Chapter 4. For spin waves in an out-of-plane (perpendicularly) magnetised thin film, the demagnetising field becomes important, as we will see in later Chapters. We will always assume a demagnetising field of $H_0 - N_\mathrm{d}M_0$, with N_d equal to 4π in Gaussian units, or 1 in SI units, in this thesis.

2.4.2 Anisotropy Energy

The next component of the magnetic energy to consider is due to anisotropy, which (in the absence of an external field) completely determines the static configuration of a ferromagnet. Anisotropy means that the properties of a magnet are directionally-dependent, and we can quantify it in terms of its direction and its strength. We will use the terms easy/hard axis to describe the direction along which it is easy/hard to align the magnetisation. There are many different forms of anisotropy: crystal (magnetocrystalline) / shape / stress / exchange (due to interface between ferro- and antiferro- magnets), to name the most common forms.

The only intrinsic property listed above is the magnetocrystalline anisotropy, which depends upon the lattice structure of the material, and is thus difficult to manipulate. The more interesting form of anisotropy for this work, because it is easy to manipulate, is shape anisotropy. The demagnetising field along a short axis is larger than the field along a long axis, and so you must apply a larger magnetic field along the short axis, compared to the long axis, to achieve the same overall field inside the sample. This is the origin of shape anisotropy; it is easier to magnetise a sample along certain directions than others.

The strength of the anisotropy, along with many other material properties, can be established by plotting how the magnetisation varies with the applied magnetic field. This plot is called a magnetisation curve or hysteresis loop, and we show an example in Figure 2.2 where the different loops show the different behaviour as the angle α between $\mathbf{H}$ and the easy axis varies. The first thing to note is that these loops have a direction associated with them; the value of the magnetisation therefore depends on the previous magnetic state. The loop of $\alpha = 0^\circ$ is characteristic of an easy axis, and the loop of $\alpha = 90^\circ$ shows a hard axis. A narrow loop, or rather a small change in $\mathbf{H}$ required to change the magnetisation, corresponds to a 'soft' magnetic material, whereas a 'hard' material would have a wide loop.

The anisotropy energy is associated with the magnetisation's projection onto the anisotropy axes, and can be written as (in Gaussian units)

$$E_{\text{anis}} = \sum_i \pm \frac{1}{2} \beta_i (\mathbf{M} \cdot \hat{\mathbf{n}}_i)^2, \tag{2.4.4}$$

where the different contributions from the i anisotropy axes ($i = 1$ for a uniaxial ferromagnet) which point in the $\hat{\mathbf{n}}$ directions are summed, and we introduce the anisotropy constant β. The $\pm$ sign depends on the type of anisotropy axis; a

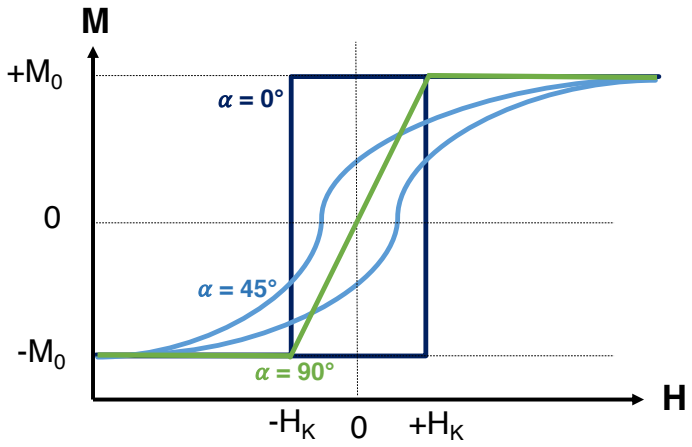

FIGURE 2.2: Hysteresis loop for a single-domain particle, where the stated angle α is between **H** and the single anisotropy axis. Image based on results in [22].

negative sign is used for an easy axis, so the energy is minimised when **M** is parallel or antiparallel to $\hat{\mathbf{n}}$, and a positive sign is used to denote a hard axis, so the energy is minimised when $\mathbf{M} \perp \hat{\mathbf{n}}$ - i.e. when it does not lie along the hard axis.

The anisotropy constant β is dimensionless, and is related to the commonly-used anisotropy constant K (units of energy density) or anisotropy field H_K (units of Oersted) by the following relation:

$$\frac{1}{2}\beta M_0^2 = K = \frac{1}{2}H_K M_0, \tag{2.4.5}$$

with M_0 being the magnitude of the saturation magnetisation. The anisotropy field H_K is the field required to saturate the magnet, so that $M = M_0$, and can be extracted from the hysteresis loop.

2.4.3 Exchange Energy

The exchange energy, as discussed earlier, is a short-range interaction, and describes how adjacent spins in a ferromagnet tend to align parallel to each other. We can write the exchange energy in Gaussian units as

$$E_{\text{ex}} = \frac{1}{2}\alpha(\nabla \mathbf{M})^2, \tag{2.4.6}$$

We introduce the exchange constant α, which has units of length squared (recall in Gaussian units, this is in cm^2). The constant α is related to the exchange length l_{ex} by $\alpha = l_{ex}^2$, and the commonly-used exchange constant A_{ex} (in erg/cm) by (see [23], p.5)

$$A_{ex} = \frac{1}{2}\alpha M_s^2. \tag{2.4.7}$$

2.5 Spin Waves

Now we consider the dynamics of a magnetic system, and we are more concerned with the study of spin waves, known as magnonics (where the magnon is the spin wave's quasiparticle). Technically, spin waves are typically described by a classical, mean-field approximation (most relevant to this research), and magnons are studied in terms of their Bose-Einstein statistics, which we do not cover here. As is customary, we will use the terms spin waves and magnonics interchangeably.

The other main branch of magneto-dynamics is the study of spintronics [24], which involves the movement of spin-polarised currents. Magnonics, in contrast, deals with the precessional excitation of localised spins - there is no mass / charge / spin transfer involved. Although there is some overlap in research interests in these two sub-fields, we will only discuss the relevant theory relating to magnonics. In this section we will discuss the origin, characteristics, and experimental observation of spin waves, and this theory is primarily summarised from References [5, 21] except where stated.

2.5.1 Larmor Precession

We previously introduced the concept of an external magnetic field exerting a torque on an electron's spin dipole moment, to rotate that moment to align with the field. Now, we specify the details of this motion using a semi-classical picture of a magnetic dipole. We will review the quantum mechanical interpretation at the end of this discussion. In the next section, we cover the equations which describe the precessional motion of the magnetisation (the collection of dipole moments).

Remember that the electron has angular momentum, so the torque does not simply rotate its magnetic moment to point in the direction of an external field. In fact, it causes the moment to undergo gyroscopic precession around the magnetic field, until it loses energy through damping to point in the new direction along

H. This motion is analogous to the precession of a (tilted) gyroscope in a gravitational field, but in the specific case of a magnetic moment precessing about a magnetic field, the behaviour is known as Larmor precession.

Magnetic dipoles will not only interact with an external magnetic field, but they will also interact with their nearest neighbours (via the exchange interaction), and other nearby dipoles (via the dipole-dipole interaction), as we have already mentioned. The most interesting effects of these interactions occur when a collection of spins are excited by a pulsed or continuous (but oscillatory) magnetic field[5]. If they are all excited instantaneously with a field at the same frequency, they will oscillate in phase. As in any oscillatory system, if they are excited at their resonant frequency they all oscillate (precess) in-phase with a large amplitude, and this is called ferromagnetic resonance. More interestingly, if we instead introduce some kind of inhomogeneity into the system — either in the field, or in the magnetisation configuration (more on this later) — then we could excite a spin wave, where neighbouring spins precess with a phase difference which travels through the array, as shown for a 1D chain of spins in Figure 2.3.

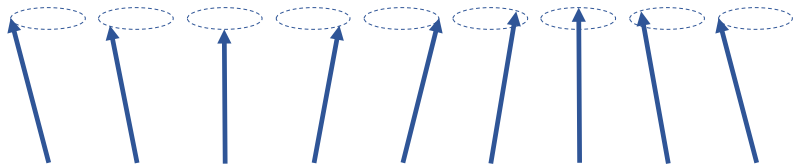

FIGURE 2.3: A spin wave travelling along a 1D chain of spins.

Since it is not possible to visualise the individual dipoles precessing in a magnetic material, the term 'spin wave' is more often used to describe the precessional excitation of the magnetisation, i.e. the oscillation of a larger cluster of spins interacting with nearby clusters of spins. It can be confusing to compare the macroscopic spin wave with the fundamental *spin* wave, and so in the following sections we will just examine the macroscopic picture. Before we do so, we need to consolidate this classical picture of precessing spins with the quantum mechanical interpretation of a *spin* wave. We know that we can never specify the exact position or momentum for a quantum object, and so we cannot suppose

[5]You could also excite spin waves using a (suitably powerful) electromagnetic field or via localised heating, or via a combination of the two in an ultrafast laser pulse [25]. We will focus on excitation via an external magnetic field in this discussion, and in this work.

that the dipole precesses with a precise phase, or with a well-defined phase relation compared to its neighbours. All we really know is that there is a probability distribution of the magnetic dipole moment's orientation, and a probability associated with it pointing along the direction of the magnetic field. In terms of the quantised states of the spin (not just the overall dipole moment) we would have to talk of a spin wave as a movement of a flipped spin through the array of spins, regardless of whether $\mathbf{H} \perp \mathbf{S}$ or not, because the spin can only occupy the 'up' or 'down' state, where one state will have higher energy than the other. This is where we could introduce the concept of a magnon - the quasiparticle of a magnetic excitation - because it completely avoids the description of what the excitation actually *is*, other than some packet of energy. Nevertheless, we will continue to work with the semi-classical description of the magnetisation, because although it is technically an approximation, at the macroscopic scale is does describe the behaviour of the magnetisation of an excited ferromagnet very well.

2.5.2 The Landau-Lifshitz Equation

We can now go into more detail about the precessional behaviour of the magnetisation about the external field. This motion is described by the Landau-Lifshitz equation,

$$\frac{\partial \mathbf{M}}{\partial t} = -\gamma[\mathbf{M} \times \mathbf{H}_{\text{eff}}], \tag{2.5.1}$$

where γ is the electron gyromagnetic ratio, introduced in equation (2.2.1) as the constant of proportionality between the magnetic moment and the angular momentum of an electron. $\mathbf{H}_{\text{eff}}$ is the effective magnetic field, which is the functional derivative of the free energy,

$$\mathbf{H}_{\text{eff}} = -\frac{\delta W}{\delta \mathbf{M}} = -\frac{\partial W}{\partial \mathbf{M}} + \frac{\partial}{\partial x_i} \frac{\partial W}{\partial \left(\frac{\partial \mathbf{M}}{\partial x_i}\right)}. \tag{2.5.2}$$

This shows us that the terms contributing to the free energy that we saw in the last section, i.e. magnetostatic, anisotropy or exchange, all create an *effective* magnetic field that the magnetisation experiences. So we may apply an external magnetic field, but the overall (effective) field may be increased or decreased by these additional contributions. It is this effective field that determines the precessional behaviour of the magnetisation.

Eq. (2.5.1) is akin to the torque equation we saw as Eq. (2.3.3), and is a formal expression of the Larmor precession discussed in Section 2.5.1. We can see that the magnetisation precesses around the (effective) magnetic field in time, and this vector is perpendicular to both $\mathbf{M}$ and $\mathbf{H}_{\text{eff}}$, directed to follow a circular precession. The Landau-Lifshitz equation was first postulated in Ref. [7], and is a phenomenological equation which can be derived from the method of Lagrange multipliers[6], amongst other methods.

Equation (2.5.1) is the simplest model which does not account for damping, nor the change in the magnitude (length) of the magnetisation[7]. Damping is included in the Landau-Lifshitz-Gilbert equation [27],

$$\frac{\partial \mathbf{M}}{\partial t} = -\gamma[\mathbf{M} \times \mathbf{H}_{\text{eff}}] + \frac{\alpha_{\text{G}}}{M_{\text{S}}}\left(\mathbf{M} \times \frac{\partial \mathbf{M}}{\partial t}\right), \tag{2.5.3}$$

and it typically originates from interactions between spin waves and the lattice (in quantum-mechanical terms: phonon-magnon scattering). Here, α_{G} is the Gilbert damping parameter. This precession is compared to the undamped precession from Eq. (2.5.1) in Fig. 2.4. Note that we do not account for damping in our analytical calculations in this thesis, since we are not concerned in that case with how the spin waves evolve in time. The results could include the effects of damping approximately by including an imaginary contribution to the frequency (see Ref. [21] p.17), but we avoid this complexity in the equations. Damping is included in the micromagnetic simulations for later Chapters, although we use the low-damping material yittrium-iron-garnet (YIG). YIG has a damping factor of around 1×10^{-4} [28], which is far less than the next best option of Permalloy with $\alpha_{\text{G}} \approx 6 \times 10^{-3}$ [29]. As a result, spin waves in YIG may propagate over distances of centimetres, compared to tens of micrometres in Permalloy [2].

2.5.3 Exchange Regime

In the next subsections, we will consider the main spin wave regimes. For ease of comparison with other works, and since this is the convention for Chapters 5-7, we use SI units when describing dispersion relations.

The simplest regime to work with is the exchange regime, applicable for small-wavelength spin waves (depending on the material, this is usually up to around

[6] which explains the origin of the functional derivative as $\mathbf{H}_{\text{eff}}$. See, for example [21] p.32.

[7] Changing the length of M via an excitation would be a highly nonlinear effect, and may be induced by intense laser heating, for example. A description of this, with relation to its implementation in micromagnetic modelling, is described in e.g. Ref. [26].

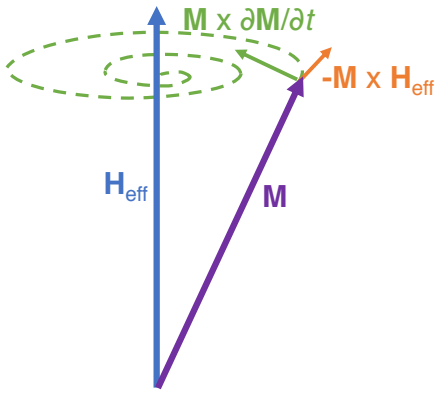

FIGURE 2.4: Sketch of the vectors H and M, showing the circular precession vector $\mathbf{M} \times \mathbf{H}$ and the damping vector $\mathbf{M} \times \partial\mathbf{M}/\partial t$, the combination of which leads to the magnetisation spiraling towards alignment with the effective field.

50nm), governed by the exchange interaction. Their dispersion relation, in the absence of anisotropy and dipolar interactions, is given by [30, 31]

$$\omega_{\text{ex}} = \omega_H + l_{\text{ex}}^2 \omega_M k^2, \tag{2.5.4}$$

where (for an infinite sample)

$$\omega_H = \gamma\mu_0 H_0, \quad \omega_M \ = \gamma\mu_0 M_0. \tag{2.5.5}$$

Here, ω_H is the ferromagnetic resonance frequency (H_0 is the static magnetic field), ω_M is the frequency associated with the static magnetisation strength M_0, and $k = 2\pi/\lambda$ is the wave number. Later, we will need to adapt this for a perpendicularly-magnetised thin film (which is finite in the direction of M, but infinite in the plane), so we modify ω_H to

$$\omega_H = \gamma\mu_0(H_0 - M_0), \tag{2.5.6}$$

where the quantity $(H_0 - M_0)$ is the internal field. This takes into account the demagnetising field of the sample (given by M_0). The exchange length l_{ex} can be

written in terms of A_{ex} in SI units[8] as [32]

$$l_{\text{ex}} = \sqrt{\frac{2A_{\text{ex}}}{\mu_0 M_0^2}}. \tag{2.5.7}$$

Since this is a simple parabolic dispersion relation we will not show it graphically here — see Chapter 7 for some examples for real material parameters.

There are a number of positive features of exchange spin waves. Firstly, the wavelength is on the nanometre length scale - a perfect size for nanoscale circuitry. In addition, the quadratic dispersion is beneficial for technological applications; smaller, exchange spin wave devices should have faster computing speeds, since the frequency scales quadratically with decreasing wavelength - and the frequency is a good measure of the device speed [4]. Finally, exchange-only spin waves are generally easier to work with analytically, at least in the linear regime, since their dynamics can be described by a Schrödinger-like equation. The main disadvantage is that they are difficult to generate, because a spin wave source (typically a point contact or waveguide) needs to be at most the same size as the wavelength of the generated spin waves [1], and this is difficult to achieve.

We will mention now the region of applicability for exchange spin waves. The usual supposition [33] is that exchange spin waves fulfill the condition $k \gg \alpha^{-1/2}$. In Chapters 3 and 4 we study exchange spin waves in a Permalloy-like material, with $\alpha \approx 3 \times 10^{-16}\ \text{m}^2$, so this would correspond to[9] $k \gg 58\ \text{rad}/\mu\text{m}$, i.e. $\lambda \ll 110$ nm. So, 126 rad/μm, corresponding to 50 nm, is a reasonable limit to omit the dipolar contribution and expect a k^2-dependence of the dispersion relation [34] as in Eq. (2.5.4). The smaller the wavelength (towards single or a few tens of nanometres), the more accurate this approximation will be.

2.5.4 Dipolar (Magnetostatic) Regime

We next outline the properties of longer wavelength spin waves, when the dipolar contributions are dominant. For forward volume spin waves, we also show

[8] We related A_{ex} to the exchange constant α in Gaussian units in Eq. (2.4.7). For completeness, we can relate l_{ex} to α in Gaussian units, by using [32] (Gaussian units:) $l_{\text{ex}} = \sqrt{A_{\text{ex}}/2\pi M_0^2}$, thus $l_{\text{ex}} = \sqrt{\alpha/4\pi}$.

[9] The authors in Ref. [33] state k in units of cm^{-1}, but we must assume that they actually mean rad·cm^{-1}, omitting the radian because it is not technically a unit. Otherwise, the wavelength would need to be much less than 17 nm, which is unreasonable considering the minimum possible spin wave wavelength (twice the lattice spacing) is 7×10^{-10} m. To avoid confusion, it will always be stated in the units here when radians are being used.

how the effects of the exchange interaction may be accounted for, as we use this in Chapter 6.

We will use the terms dipolar or magnetostatic interchangeably, and we will now see where the latter term originates from. The behaviour of these dipole-dominated spin waves is governed by the magnetostatic Maxwell equations, $\nabla \times \mathbf{H} = 0$ and $\nabla \cdot \mathbf{B} = 0$. These should rather be termed magneto*quasi*static, because the magnetisation still precesses at microwave frequencies, and is therefore rather dynamic! It instead makes an analogy with electrostatics, where charges do not move in time; in the magnetostatic approximation, there are (approximately) no moving currents, so Ampere's Law of $\nabla \times \mathbf{H} = \mathbf{J}$ equals zero. For a ferromagnet, the magnetostatic Maxwell equations are reformed into the more useful Walker equation, which is a function of the magnetic scalar potential ψ and the permeability tensor $\hat{\mu}$,

$$\nabla \cdot (\hat{\mu} \nabla \psi) = 0. \tag{2.5.8}$$

The Walker equation is solved with suitable boundary conditions for ψ, to establish the dispersion of magnetostatic spin waves within a ferromagnet. The details of this derivation are provided in Appendix A. An important feature of volume (i.e. not surface) magnetostatic spin waves is that they exist in a band of frequencies known as the spin wave manifold, given by

$$\omega_H \leq \omega \leq \sqrt{\omega_H(\omega_H + \omega_M)}. \tag{2.5.9}$$

This does not account for the exchange interaction however, which would have an effect on the dispersion relation towards the higher-k range of the manifold, as we will see at the end of this section. We will now consider the dispersion relations of the three main magnetostatic wave geometries, which are compared at the end of this discussion.

Forward Volume Spin Waves

In Chapters 5-7 we work in the forward volume geometry, where the magnetic field and magnetisation are perpendicular to the film plane. In this case, the group and phase velocity are in the same direction, and the wave propagation in this geometry can be isotropic, supposing that magnetocrystalline anisotropy is not present. The dipolar dispersion relation for the lowest order thickness

mode[10], neglecting any contributions from anisotropy or the exchange interaction, is given by ([5] p.155)

$$k = \frac{1}{s}\frac{2}{\sqrt{-(1+\kappa)}}\left[\arctan\left(\frac{1}{\sqrt{-(1+\kappa)}}\right)\right]. \tag{2.5.10}$$

where s is the film thickness, and

$$\kappa = \frac{\omega_H \omega_M}{\omega_H^2 - \omega^2}, \quad \text{with: } \omega_H = \gamma\mu_0(H_0 - M_0). \tag{2.5.11}$$

All other parameters are as before, except that the demagnetising field must now be included, hence the change to ω_H. The details of the derivation for (2.5.10) is provided in Appendix A. A very good approximation which is valid for smaller values of k (more on this later) was found in Ref. [30], which is somewhat easier to work with as ω is a function of k:

$$\omega = \sqrt{\omega_H\left[\omega_H + \omega_M\left(1 - \frac{1-\exp[-ks]}{ks}\right)\right]}. \tag{2.5.12}$$

Towards the end of this section, the dispersion relation Eq. (2.5.10) is plotted along with Eq. (2.5.12), and compared to the following magnetostatic dispersion relations.

Backward Volume Waves

If the field and magnetisation lie in the film plane, and the direction of propagation is parallel/antiparallel to **H** and **M** (which are still parallel to each other), then this is called the *backward volume wave* geometry. Strangely in this case, the group and phase velocity are antiparallel, i.e. the wavefronts appear to travel backwards, although the energy must move forwards, away from the source. This geometry also allows for multiple thickness modes, although we are only concerned with the lowest order mode as before. The dispersion relation, derived in a similar way to Eq. (2.5.10), can be written as [5] (p.159)

$$k = \frac{2}{s}\sqrt{-(1+\kappa)}\cdot\arctan\left(\sqrt{-(1+\kappa)}\right) \qquad \text{with: } \omega_H = \gamma\mu_0 H_0. \tag{2.5.13}$$

[10]The zeroth order mode is approximately uniform through the film thickness, and is the mode which is excited most efficiently [2], so for our purposes we can neglect the higher order modes.

Notice that the demagnetising field is neglected in ω_H since the sample is magnetised in the film plane, which we assume is effectively infinite in extent. There is also a convenient approximation to Eq. (2.5.13), derived by [33]:

$$\omega = \sqrt{\omega_H \left[\omega_H + \omega_M \left(\frac{1 - \exp[-ks]}{ks}\right)\right]}. \tag{2.5.14}$$

The group velocity is given by $v_g = \delta\omega/\delta k$, which, for the lowest order mode and where $k_z \ll 1$, is [5]

$$v_g \approx -\frac{\omega_M s}{4} \frac{\omega_H}{\sqrt{\omega_H(\omega_H + \omega_M)}}. \tag{2.5.15}$$

The group velocity is *negative*, and yet the phase velocity $v_p = \omega/k$ will always be positive, leading to the unusual wavefront behaviour mentioned earlier.

Surface Waves

Finally, if **H** and **M** still both lie in the film plane (and are still parallel to each other) there is the possibility of exciting a *surface wave* if the propagation direction is perpendicular to the field. The phase and group velocities are in the same direction (it is a forward mode), but only one mode exists, in contrast to the volume modes. A peculiar feature of these waves is that, when the direction of propagation is reversed, the wave propagates on the opposite face of the thin film — a property known as 'field displacement non-reciprocity'. As we would expect for surface waves, the amplitude of this mode decays exponentially from the film's surfaces. The dispersion for surface spin waves is [5] (p.163)

$$\omega = \sqrt{\omega_H(\omega_H + \omega_M) + \frac{\omega_M^2}{4}\left(1 - \exp(-2ks)\right)} \qquad \text{with: } \omega_H = \gamma\mu_0 H_0, \tag{2.5.16}$$

again assuming no demagnetising field. Note also that k may only take positive values in this equation. Since this is no longer a volume wave, the spin wave manifold Eq. (2.5.9) no longer applies. The surface spin wave mode does exist between two frequencies however, starting from the top of the manifold for

backward volume waves[11]):

$$\sqrt{\omega_H(\omega_H+\omega_M)} \leq \omega \leq (\omega_H - 0.5\omega_M). \tag{2.5.17}$$

Comparison: Magnetostatic Spin Wave Dispersion Relations

Now we can compare the magnetostatic spin wave dispersion relations listed previously. The results for each geometry, forward volume (FV), backward volume (BV) and surface (S) waves, are given in Fig. 2.5, using the parameters for a YIG-like film[12]. Note that the frequency units are in GHz, so the volume spin wave manifold goes from $f_1 = \omega_H/(2\pi)$ to $f_2 = \sqrt{\omega_H(\omega_H+\omega_M)}/(2\pi)$, with ω_H including the demagnetising field for the FV geometry only (hence the different frequency ranges). Recall that the surface wave manifold starts at f_2 for the BV geometry, and goes to $f_S = (\omega_H - (\omega_M/2))/(2\pi)$, and has a much narrower frequency range than for FV or BV waves.

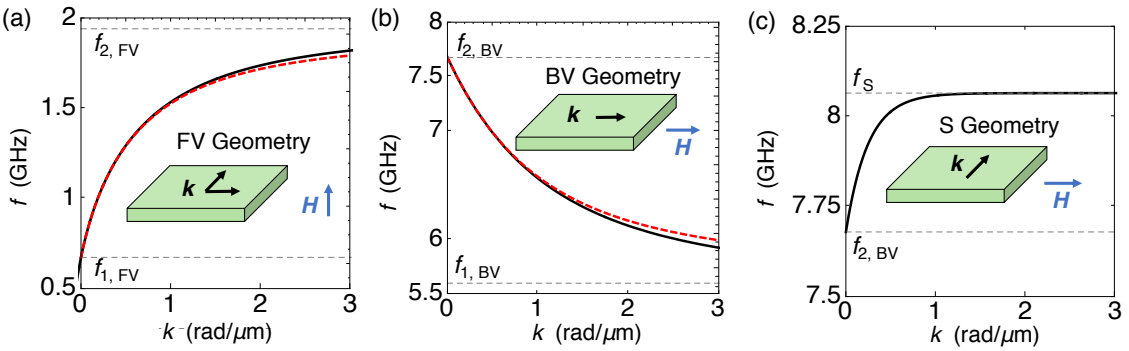

FIGURE 2.5: Magnetostatic dispersion relations, for (a) FV spin waves, using Eq. (2.5.10) (black) and Eq. (2.5.12) (red, dashed), (b) BV spin waves, using Eq. (2.5.13) (black) and (2.5.14) (red, dashed) and (c) S spin waves using Eq. (2.5.16). The spin wave manifolds described in the main text are shown in grey lines.

The exact and approximate forms of the FV and BV geometries are compared in Fig. 2.5 (a) and (b). For $k \leq 0.5$ rad/μm (corresponding to wavelength $\lambda = 12.5$ μm) for our choice of parameters, the approximate form matches the exact form very well, but they start to diverge with increasing k. This is quite acceptable; the exchange interaction would soon need to be accounted for, beyond around $\lambda = 12.5$ μm anyway. We look at the effect of including exchange next.

[11] For the same values of the external magnetic field and magnetisation, the manifold will necessarily be different for forward and backward volume waves, since ω_H is different in each case.

[12] using $s = 2$ μm, $H = 2$ kG ($\mu_0 H = 200$ mT) and $M = 140$ G (140 kA/m) comparable to the results in Chapter 5.

Approximate Dipole-Exchange Dispersions

Rigorously and accurately including the effect of the exchange interaction in the three magnetostatic dispersion relations is nontrivial [33]. Luckily, a good approximation ([5] (p.141)) can be obtained when the dipolar interaction still dominates[13]. The dipolar dispersions given by Eq's. (2.5.12), (2.5.14) and (2.5.16) are used, and exchange is included by replacing ω_H with ω_{ex}, which was defined in Eq. (2.5.4). Note that the demagnetising field is included in ω_H (contained in ω_{ex}) only for forward volume spin waves. A good explanation and analysis of these effects can be found in e.g. Ref. [31], and the dispersion relations are summarised here in the same manner for forward volume (FV), backward volume (BV) and surface (S) waves:

$$\text{FV:} \quad \omega = \sqrt{\omega_{\text{ex}}\left(\omega_{\text{ex}} + \omega_M\left(1 - \frac{1-\exp(-ks)}{ks}\right)\right)}, \tag{2.5.18}$$

$$\text{BV:} \quad \omega = \sqrt{\omega_{\text{ex}}\left(\omega_{\text{ex}} + \omega_M\frac{1-\exp(-ks)}{ks}\right)}, \tag{2.5.19}$$

$$\text{S:} \quad \omega = \sqrt{\omega_{\text{ex}}(\omega_{\text{ex}} + \omega_M) + \frac{\omega_M^2}{4}\left(1-\exp(-2ks)\right)}, \tag{2.5.20}$$

where

$$\omega_{\text{ex}} = \omega_H + l_{\text{ex}}^2\omega_M k^2, \qquad \omega_H = \begin{cases} \gamma\mu_0(H_0 - M_0) & \text{FV} \\ \gamma\mu_0 H_0 & \text{BV and S} \end{cases}. \tag{2.5.21}$$

We will make use of Eq. (2.5.18) in Chapters 6 and 7.

2.6 The Graded Refractive Index: Optics to Magnonics

As we have seen so far, the dispersion properties of spin waves in magnetic materials is highly dependent on the mutual orientations of the magnetisation, magnetic field, and wave vector. We have only looked at some simple geometries, and the situation becomes far more complicated if we introduce additional shape

[13] According to Ref. [33], the dipole-exchange dispersion relation should be a good approximation for forward volume spin waves in the range $0 < k < 100$ rad/μm, where the error "never exceeds several per cent".

/ crystal anisotropies. This complexity offers many opportunities for controlling the propagation of spin waves — and this is where we take inspiration from the well-established research area of graded index *optics*, which is concerned with the control of light using a designed refractive index profile.

2.6.1 Refractive Index Definition

Although a refractive index is really reserved for describing the interaction of light with matter, we will use the concept of a graded *magnonic* refractive index to describe a landscape in which the magnetic properties are varied, to control the direction / velocity of spin waves. In this section, we will summarise some important results from optics, which will form an important part of the graded index magnonics toolkit.

We start by defining the refractive index n, which may vary as a function of position $\mathbf{r}$. Generally,

$$n(\mathbf{r}) \equiv \frac{k(\mathbf{r})}{k_0}, \tag{2.6.1}$$

with $k(\mathbf{r})$ the wave number at position $\mathbf{r}$ (which depends on the material properties at that position) and k_0 is the reference wave number. This reference wave number could be defined anywhere[14], though for light it is always the wave number for light in a vacuum. Subsequently, the refractive index can also be written as $n(\mathbf{r}) = \frac{c}{v(\mathbf{r})}$, with c and $v(\mathbf{r})$ the phase velocity of light in a vacuum or at position $\mathbf{r}$ in the medium, respectively.

So the refractive index, most generally, just refers to the change in the wave number compared to a reference value. In later chapters, we go into more detail on how the index may be changed for spin waves for different frequencies.

2.6.2 Grading the Refractive Index

The understanding of how a graded refractive index can gradually 'bend' a beam of light has been known for centuries [35]. A relevant 'recent' application known as 'Maxwell's fish eye' lens was proposed theoretically by Maxwell in 1854. The spherically-symmetric refractive index distribution bends light rays from a source on one side of the lensing medium to produce a perfect image on the other side. Since the source and image are *inside* the lens, it has limited applications for light. However, it has served as the inspiration for much research on the subject [36]. In

[14] Later, we use k_0 as the wave number outside of the graded index lens region.

Chapters 5 and 6, we look at making similar rotationally-symmetric, graded index lenses for spin waves. More exotic profiles may make use of 'transformation optics' [37, 38], and the concepts have already been used for spin waves [39].

Graded refractive index profiles may be implemented via gradually changing a material parameter in space, either literally (via a smooth gradient in thickness, for example — we see similar examples in later Chapters) or via the metamaterial approach [40]; changing the material properties in finite steps, but on a length scale smaller than the wavelength. Metamaterials have applications in a broad range of wave physics, and primarily rely on controlling the properties of waves via the careful design of 'meta-atoms'. The composition, shape, and arrangement of these sub-wavelength features create an overall, effective medium for the wave that encounters it. These features can then be changed gradually, on a scale much *larger* than the wavelength (as we explain in the next section) to create an effective graded index [41]. There are various examples of metamaterials for spin waves [42], often involving the inclusion of holes or other non-magnetic materials into a magnetic film to manipulate the spin wave dispersion.

2.6.3 The Geometrical Optics Approximation

When we consider how to create a graded magnonic refractive index, we are relying on the important geometrical optics approximation, which allows us to consider propagating waves in terms of rays. This approximation does not account for diffraction effects or other complications, and treats the propagating wave locally as a plane wave / beam [43]. The rays are thus perpendicular to the local plane wavefronts. For our purposes, the important criterion is that [36, 44]

$$|\nabla\lambda| \ll 1 \quad \implies \lambda \ll a, \tag{2.6.2}$$

where a is a distance over which the wavelength (hence the index) changes noticeably, thus the characteristic size of a graded index feature [44]. For our purposes when creating graded index lenses later, we need to ensure that the radius R of the lens itself obeys

$$R \gg \lambda, \tag{2.6.3}$$

and if the index changes by a large amount in a region, that region ought to be as large as possible to fulfill Eq. (2.6.2), otherwise the wave will experience scattering. As we will see later, the geometrical optics approximation holds very well

even when the lenses are sized at around $R = 6\lambda$, as long as the index changes on a length scale much larger than the wavelength.

2.7 Micromagnetic Simulations: MuMax3 Software

For the work in Chapters 5 and 6, we test the operation of the graded index lenses by using MuMax3 software [45]. This is an open-source, finite-difference micromagnetic software, which solves the Landau-Lifshitz equation with damping accounted for by the Landau-Lifshitz damping term α_{LL}:

$$\frac{\partial \mathbf{m}}{\partial t} = \gamma \frac{1}{1+\alpha_{\mathrm{LL}}^2} \left(\mathbf{m} \times \mathbf{B}_{\mathrm{eff}} + \alpha_{\mathrm{LL}}(\mathbf{m} \times (\mathbf{m} \times \mathbf{B}_{\mathrm{eff}}))\right), \tag{2.7.1}$$

where $\mathbf{B}_{\mathrm{eff}}$ is the effective magnetic field (T) in this case. There are a few important considerations for using this software, the majority of which are explained in Ref. [45], and the relevant points for this work are listed and discussed below. Any additional modelling techniques are discussed where relevant in later Chapters.

2.7.1 Spatial Discretisation

Firstly, since MuMax3 is a finite-difference software, the model is discretised into equally-sized cubic cells, where the volumetric material parameters (such as $\mathbf{M}$ and $\mathbf{H}_{\mathrm{eff}}$) are defined in each cell. This means that if these parameters are changing in space, they will vary in steps at least as small as the cell size.

The size of each cell should be much smaller than the size of the smallest wavelength/feature of interest, and usually around $\lambda/10$ is sufficient [46]. In addition, if the exchange interaction is to be accounted for, the cell size should also be less than the exchange length given in Eq. (2.5.7) in general [47, 48]. If the exchange interaction can be completely neglected, as in the dipole-dominated regime, then the cell size just needs to be much smaller than the wavelength (see Ref. [17], for example).

It would seem sensible, then, to make the cell size as small as possible (i.e. the same as the atomic separation), and not worry about whether the discretisation is small enough. However, there is always a restriction on how large the model can be, since the computer only has a finite amount of memory. It is primarily the random access memory onboard the GPU that limits the number of calculations that can be carried out, but the computer's memory (CPU RAM) will also be a

limitation for the analysis of the data produced by the simulation. In addition, the storage of this data requires a large (gigabytes to terrabytes) amount of disk space, which is also important if a large number of data points are being recorded (in space, and time). For our system, we are limited to about 16 million cells in total. To make the calculations most efficient, the number of cells should ideally be a power of 2; we tend to use the maximum of $4096 \times 4096 \times 1$ cells in our calculations. Having one cell across the thickness also makes the analysis far more straightforward, and is usually appropriate if the thickness is smaller than the wavelength (and yet much larger than the exchange length, for dipolar spin waves).

To test if the cell size is appropriately representing the waves in the system, the numerical dispersion can be calculated and compared to the expected (analytical) dispersion relation, and the two should be equal in the region of interest. Note that this involves a Fourier transform, and the largest wave number k detectable corresponds to the wavelength equal to twice the cell size. The resolution in k-space is determined by the size of the model. So, the largest model size possible, with the smallest cell size, is desirable for the most accurate results.

Another important test that the cells are sized correctly is by checking the maximum angle attained between neighbouring spins in the results. Supposing that the amplitude of the excitation is suitably small (around 0.5% of the bias field for the systems studied in this thesis) then the amplitude of the magnetisation precession should also be small, and correctly-sized cells should thus make the magnetisation vary smoothly and slowly. If the cells are sized to be no more than $1/10$ of the smallest wavelength, then the spin angle should be at most $2\pi/10$ i.e. 0.6 radians. According to Ref. [45], the spin angle should ideally be no more than 20-30°, i.e. around 0.3-0.5 radians. A large spin angle, despite sizing the cells to be at least $\lambda/10$, may mean that unanticipated nonlinear effects are occurring, in which case the amplitude of the magnetisation and the maximum torque should also be scrutinised.

2.7.2 Sampling in Time

The temporal 'discretisation' is also important, because it determines how accurately we can observe the wave behaviour and determine the frequency response. The Nyquist-Shannon sampling theorem [49, 50] is important here, which requires that the sampling frequency is at least twice the largest frequency of interest in the system, so $f_0 > 2f_{\max}$. In order to simply observe the wave motion

in the time domain, it is not a crucial requirement to have many more sampling points (in time) than the Nyquist frequency $2f_{\max}$. Indeed, for a fixed simulation time, the smaller the time step between consecutive samples (i.e. the higher the sampling frequency), the more data that needs to be stored and processed. This can be a significant problem for large simulations.

The sampling rate for Fourier transforms should generally be as high as possible (the time step should be as small as possible), as this will primarily determine the range of detectable frequencies. Crucially, this also reduces the risk of aliasing [51], where the frequencies of two waveforms (which are not necessarily 'in time' with each other) appear indistinguishable because the sampling rate is too low. This could also be a problem if viewing the wave behaviour in the time domain. Next, the resolution in frequency space is determined by the total time of the simulation; we saw an equivalent requirement for k-space extent/resolution. Clearly, a balance needs to be struck between making the largest, most finely-discretised system which is sampled at a high frequency for a long time — and processing the results efficiently and quickly.

For the results in this work, the sampling rate was set at 4 times the excitation frequency for time-domain analyses, and 32 times the excitation frequency for the dispersion (Fourier transform) analyses, except where stated. The Nvidia GTX 1080 Ti graphics card is used in our simulations.

2.8 Experimental Considerations: Spin Wave Generation & Detection

Although the work in this project is theoretical, we have to ensure that this work considers the experiments which could test these predictions. Here, we consider some of the experimental methods commonly used to create and image spin waves.

Spin wave generation is, in theory, simple: you apply a time-varying magnetic field to a magnetic sample, oriented so it exerts a torque on the magnetisation. A spin wave can be generated if the local field induced by the external field is inhomogeneous, and this can be achieved via a local antenna, for example.

Antennas are not the only way to generate spin waves. Another, increasingly popular approach is the injection of a spin-polarised current into a ferromagnetic material, which exerts a torque on the magnetisation and leads to precession [52]. A considerably more chaotic method is to excite the system with an ultrafast laser

pulse [25]. This not only excites the magnetism dynamics, but the electron and phonon dynamics also - which leads to interesting effects (such as caustic spin wave beams), but the interactions of the different subsystems is complicated and poorly-understood.

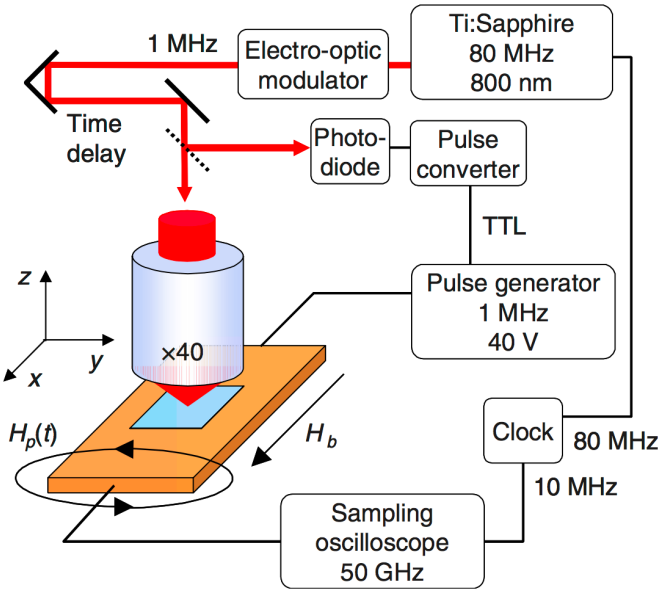

FIGURE 2.6: TRSKM setup, from [53]. The system is pumped using a time-varying magnetic field, and probed using a Kerr microscope with quadrant photodiode, to resolve the 3 magnetisation components.

Though ultrafast laser excitation is somewhat complicated, it does integrate smoothly with an optical imaging method known generally as the pump and probe technique [25]. In a typical pump and probe experiment, such as time-resolved scanning Kerr microscopy (TRSKM), a laser pulse can be used to pump the sample, and a carefully-timed, circularly-polarised probe laser beam detects the change in the magnetisation via the magneto-optical Kerr effect (MOKE) [54]. This can be repeated on femtosecond timescales, but, since the resolution is limited by the wavelength of the probing light, spatial resolution is typically hundreds of nanometres. TRSKM can also be used as a probe-only technique, with, say, a periodic external magnetic field to excite the spin waves, as shown in Figure 2.6.

An alternative optical probing method is Brillouin light scattering (BLS). This involves the scattering of light from magnons, and hence the energy, wave vector and position of the spin waves can be determined [55]. With suitable focusing optics (such as in micro-focus BLS), the spatial resolution may be equivalent to

or better than a typical TRSKM setup, even down to tens of nm [56], but the time resolution is still much slower at around 1ns.

Finally, we mention the other promising technique of time-resolved x-ray magnetic circular dichroism (TR XMCD), which uses a beam of X-rays generated at a synchrotron facility to image spin waves. This technique can offer high spatial resolution (tens of nm) and temporal resolution (tens of ps) [57]. In addition, it has the ability to detect very small amplitude spin waves, with a spin deflection angle potentially down to 0.05° [58]. As a note, the linear regime (which we are interested in) occupies spin angles of around 3° or less [59], and can be detectable with most measurement techniques discussed so far.

There is no perfect measurement technique, however, and the price of high spatial and temporal resolution (as in TR XMCD) is an extremely large, time-consuming and costly experimental setup. All of the above-mentioned techniques have a long way to go before they can be integrated into nanotechnologies (size and cost-wise), especially if we want to reliably image nanometre, exchange-dominated spin waves.

Chapter 3

Exchange Spin Wave Emission from an Anisotropy Defect

3.1 Introduction

As discussed in Chapter 2, spin waves dominated by the short-range exchange interaction are a promising candidate as information carriers on the nanoscale. This is due to their short wavelengths and isotropic, parabolic dispersion, meaning that smaller exchange spin wave devices should have faster computing speeds [4]. However, the generation of exchange spin waves can be challenging; a conventional microwave antenna must be at least as small as the wavelength of the generated wave [1], i.e. between 10-50nm, which can be difficult to fabricate.

Rather than creating an inhomogeneity in the source to excite waves in a uniform sample, one could instead create an inhomogeneity in the *sample* and use a uniform (but oscillatory) *source*, and this is considered in this Chapter. These inhomogeneities could take the form of a non-uniform internal field or magnetisation [19, 60], but for now we can simply consider a general inhomogeneity, or 'defect', in the magnetic anisotropy.

The control of spin waves via local defects has been studied in detail [61–65], particularly in relation to metamaterials and magnonic crystals [4, 42, 66]. Using the same techniques to fabricate such anisotropy profiles, spin wave *generation* could be possible via carefully designed excitation of them [67]. These anisotropy defects can either be etched or embedded into the magnetic sample [68], introduced by shaping or straining the material [64, 65, 69], or induced by external voltages [70]. Alternatively, they may simply occur naturally in the form of impurities [71, 72].

This Chapter is arranged as follows. Firstly, an analytical model is adapted

from Ref. [67], consisting of a generic anisotropy defect within an infinite ferromagnet. The dynamics of this system are described by the linearised Landau-Lifshitz equation, when the magnetic material is excited by a uniform, harmonic external field directed perpendicular to the magnetisation. In Section 3.3, solutions to this equation are sought for a rectangular profile, and the results are analysed. Gaussian units are used in the derivation for convenience.

3.2 General Method: Linearising the Landau-Lifshitz Equation

Let us model an effectively infinite ferromagnet in a homogeneous external magnetic field $\mathbf{H}_0$, which is directed along the z axis. The ferromagnet is uniaxially magnetised along z, but we introduce an anisotropy distribution[1]

$$\beta(x) = \beta_0 + \beta_1(x), \tag{3.2.1}$$

which varies only as a function of x. This is comprised of a uniaxial anisotropy term β_0, which is uniform everywhere, and $\beta_1(x)$, which describes the anisotropy defect. We keep the form of $\beta_1(x)$ general for now, but we investigate a particular case in due course.

We assume an applied external pumping magnetic field $\mathbf{h(t)} = h\exp(-i\omega t)\hat{\mathbf{x}}$, and impose that $\mathbf{h}(t)$ is a small perturbation to the static state. The precession of the magnetisation $\mathbf{M}$ in this situation is described by the Landau-Lifshitz equation, which is (ignoring relaxation)

$$\frac{\partial \mathbf{M}}{\partial t} = -\gamma[\mathbf{M} \times \mathbf{H}_{\text{eff}}], \tag{3.2.2}$$

where γ is the gyromagnetic ratio. As we saw in Chapter 2, the effective field $\mathbf{H}_{\text{eff}}$ is calculated from the free energy density W of the ferromagnet,

$$W = \frac{\alpha}{2}\left(\frac{\partial \mathbf{M}}{\partial x_i}\right)^2 - \frac{\beta(x)}{2}(\mathbf{M}\cdot\mathbf{n})^2 - \mathbf{M}\cdot\mathbf{H_0} - \mathbf{M}\cdot\mathbf{h}(t), \tag{3.2.3}$$

where the terms arise from the exchange interaction, anisotropy, Zeeman interaction with the aligning magnetic field $\mathbf{H}_0$, and the interaction with the exciting

[1] For reference, the magnetic anisotropy and its contribution to the energy was originally defined in Eq. (2.4.4).

magnetic field $\mathbf{h}(\mathbf{t})$, respectively. We have called α the exchange anisotropy constant, and $\mathbf{n}$ is a unit vector in the direction of the easy axis; in this case, $\mathbf{n} = n_z\hat{\mathbf{z}}$ due to the applied static magnetic field $\mathbf{H_0}$. We are working within the exchange approximation, so we have neglected the dipole-dipole contribution. Overall, the effective field is:

$$\mathbf{H}_{\text{eff}} = -\frac{\delta W}{\delta \mathbf{M}} = \alpha\nabla^2\mathbf{M} + \beta(x)M_z\hat{\mathbf{z}} + H_0\hat{\mathbf{z}} + h(t)\hat{\mathbf{x}}. \tag{3.2.4}$$

Now we can carry out the cross product in (3.2.2):

$$\begin{aligned}
\mathbf{M}\times\mathbf{H}_{\text{eff}} &= \begin{vmatrix} \hat{\mathbf{x}} & \hat{\mathbf{y}} & \hat{\mathbf{z}} \\ M_x & M_y & M_z \\ H_{\text{eff},x} & H_{\text{eff},y} & H_{\text{eff},z} \end{vmatrix} \\
&= \hat{\mathbf{x}}(M_yH_{\text{eff},z} - M_zH_{\text{eff},y}) + \hat{\mathbf{y}}(M_zH_{\text{eff},x} - M_xH_{\text{eff},z}) \\
&+ \hat{\mathbf{z}}(M_xH_{\text{eff},y} - M_yH_{\text{eff},x}) \\
&= \hat{\mathbf{x}}\Big(M_y\left[\alpha\nabla^2M_z + \beta(x)M_z + H_0(t)\right] - M_z\alpha\nabla^2M_y\Big) \\
&+ \hat{\mathbf{y}}\Big(M_z\left[\alpha\nabla^2M_x + h(t)\right] - M_x\left[\alpha\nabla^2M_z + \beta(x)M_z + H_0(t)\right]\Big) \\
&+ \hat{\mathbf{z}}\Big(M_x\alpha\nabla^2M_y - M_y\left[\alpha\nabla^2M_x + h(t)\right]\Big).
\end{aligned} \tag{3.2.5}$$

To linearise the Landau-Lifshitz equation of motion, we assume that the magnetisation $\mathbf{M}$ only undergoes a small deflection $\mathbf{m}$ from equilibrium [21], so that $\mathbf{M} = \mathbf{M_0} + \mathbf{m}$, with $\mathbf{M_0}$ the unperturbed magnetisation vector, i.e.

$$\mathbf{M} = \begin{pmatrix} m_x \\ m_y \\ M_0 + m_z \end{pmatrix}. \tag{3.2.6}$$

We substitute this into (3.2.2) to obtain 3 equations,

$$-\frac{1}{\gamma}\frac{\partial m_x}{\partial t} = m_y\left[\alpha\nabla^2(\cancel{M_0 + m_z}) + \beta(x)(M_0 + \cancel{m_z}) + H_0(t)\right] - (M_0 + \cancel{m_z})\alpha\nabla^2 m_y, \tag{3.2.7}$$

$$-\frac{1}{\gamma}\frac{\partial m_y}{\partial t} = (M_0 + \cancel{m_z})\left[\alpha\nabla^2 m_x + h(t)\right] - m_x\left[\alpha\nabla^2(\cancel{M_0 + m_z}) + \beta(x)(M_0 + \cancel{m_z}) + H_0(t)\right], \tag{3.2.8}$$

$$-\frac{1}{\gamma}\frac{\partial(\cancel{M_0} + m_z)}{\partial t} = \cancel{m_x\alpha\nabla^2 m_y} - \cancel{m_y\left[\alpha\nabla^2 m_x + h(t)\right]}. \tag{3.2.9}$$

Since $\mathbf{m}$ is a small perturbation, we have omitted terms in (3.2.7)-(3.2.9) which are second order in $\mathbf{m}$. Similarly, since $\mathbf{h}(t)$ is small (and by definition it is of order $\mathbf{m}$), then their product is also small enough to be neglected. Finally, the $\frac{\partial M_0}{\partial t}$ and $\nabla^2 M_0$ terms in (3.2.9) are zero, since M_0 is a constant.

Due to the omission of the higher order terms, (3.2.9) goes to $\frac{\partial m_z}{\partial t} = 0$, which fits with our requirement of $\mathbf{m}$ being a small perturbation; to the first order approximation, the length of $\mathbf{M}$ does not change. We can see this from Eq. (3.2.6), where to the first order $\frac{\partial M_z}{\partial t} = \frac{\partial M_0}{\partial t} = 0$, since M_0 is not time-dependent. We are therefore left with the following:

$$-\frac{1}{\gamma}\frac{\partial m_x}{\partial t} = -\alpha M_0\nabla^2 m_y + m_y\beta(x)M_0 + m_y H_0(t), \tag{3.2.10}$$

$$-\frac{1}{\gamma}\frac{\partial m_y}{\partial t} = \alpha M_0\nabla^2 m_x + M_0 h(t) - m_x\beta(x)M_0 - m_x H_0(t), \tag{3.2.11}$$

which we can convert to circular variables with $m_\pm(x,t) = m_x \pm i m_y$, to obtain

$$\pm\frac{i}{\gamma}\frac{\partial m_\pm(x,t)}{\partial t} = \alpha M_0\nabla^2 m_\pm(x,t) - [\beta(x)M_0 + H_0]m_\pm(x,t) + M_0 h(t). \tag{3.2.12}$$

This is starting to take the form of the Schrödinger-equation, but we will look at this in more detail after a little more manipulation. We now carry out a Fourier transform to convert from the time domain to the frequency domain. We use the result ([73] p.706) that the Fourier transform of the time derivative of $f(t)$ is given

by

$$F_1(\omega) = \int_{-\infty}^{+\infty} \frac{\mathrm{d}f(t)}{\mathrm{d}t} \exp(i\omega_0 t)\mathrm{d}t = -i\omega_0 F(\omega), \tag{3.2.13}$$

i.e. $-i\omega$ multiplied by the Fourier transform of $f(t)$. We also introduce

$$\tilde{m}_{\pm}(x,\omega) = \int_{-\infty}^{+\infty} \left[m_{\pm}(x,t)\exp(i\omega_0 t)\right] \mathrm{d}t\,, \tag{3.2.14}$$

$$\tilde{h}(\omega) = -\int_{-\infty}^{\infty} \left[h(t)\exp(i\omega_0 t)\right] \mathrm{d}t = -2\pi h\delta(\omega-\omega_0)\,, \tag{3.2.15}$$

$$\Omega = \frac{\omega}{\gamma M_0}\,, \tag{3.2.16}$$

where Ω is a dimensionless 'effective frequency'. We have incorporated a minus sign into the definition (3.2.15) for convenience, and notice that $\tilde{h}(\omega)$ and $\tilde{m}_{\pm}(x,\omega)$ are monochromatic, with angular frequency $\omega_0 = \omega$. Substituting these terms into (3.2.12), we obtain

$$\tilde{h}(\omega) = \left[\alpha\nabla^2 + \Omega - \beta(x) - (H_0/M_0)\right] \tilde{m}_{\pm}(x,\omega). \tag{3.2.17}$$

Note that we have only retained the positive solution for Ω, as it gives the only physically meaningful result, as we will see. In order to solve (3.2.17), we can write the magnetisation as a sum of two contributions:

$$\tilde{m}_{\pm}(x,\omega) = \tilde{m}_{\beta} + \tilde{m}_{h}\,, \tag{3.2.18}$$

where $\tilde{m}_{\beta}$ describes the excitation of the magnetisation due to the presence of the defect, and $\tilde{m}_h$ describes the excitation of the magnetisation in the homogeneous magnetic field. Note that each term will tend to zero if their respective sources, $\beta_1(x)$ or $\tilde{h}(\omega)$, tend to zero. We first substitute (3.2.18) into (3.2.17), and set $\beta_1(x)$ to zero (hence $\tilde{m}_{\beta}$ goes to zero), and this gives (3.2.19) below. We then substitute this back into (3.2.17), and obtain (3.2.20):

$$\left[\alpha\nabla^2 + \Omega - \beta_0 - (H_0/M_0)\right] \tilde{m}_h = \tilde{h}(\omega), \tag{3.2.19}$$

$$\left[\alpha\nabla^2 + \Omega - \beta(x) - (H_0/M_0)\right] \tilde{m}_{\beta} = \beta_1(x)\tilde{m}_h. \tag{3.2.20}$$

In our case, $\tilde{m}_h$ is not a function of x since we use a spatially-uniform harmonic source, so $\nabla^2 \tilde{m}_h = 0$, and the particular solution to (3.2.19) is

$$\tilde{m}_h = \frac{\tilde{h}(\omega)}{\Omega - \beta_0 - (H_0/M_0)}. \tag{3.2.21}$$

The solution to equation (3.2.20) is found for a rectangular profile of $\beta_1(x)$, in the following section. In the next Chapter, we solve a similar but slightly more complicated version of this equation for a magnetic domain wall.

Let us summarise the derivation so far. We have retained the linear terms from the Laudau-Lifshitz equation, which is built from the various terms in our energy density relating to the magnetisation, external field, and anisotropy. We have converted to circular variables, so that we only need to be concerned about the small amplitude magnetisation precession as a whole (rather than the x and y components separately). We then arrived at (3.2.17), which is a second-order differential equation reminiscent of the Schrödinger or Helmholtz equation. This is a very useful feature of working analytically with exchange spin waves; the linearised Landau-Lifshitz equation always reduces to a Schrödinger-like equation with a driving term, and a potential determined by the frequency, anisotropy and field/magnetisation ratio[2]. A host of exactly-solvable models can therefore be easily investigated for exchange spin waves, by mapping over the solutions from quantum mechanics (or optics), once the correct potential profile has been designed. In our case, since we are effectively driving the potential with an external field, the form of the potential also appears as part of the driving term (Eq. (3.2.21)). This is an intriguing difference from the usual form of the Schrödinger equation, and will likely lead to some interesting effects for more exotic potentials.

The next important feature of this derivation is in separating the contributions from the presence of the defect and from the uniform harmonic field. This was proposed in Ref. [67], and will allow us to untangle the uniform-precession waves caused by the field from the propagating spin waves originating from the defect, as we will see in the next section.

[2]Although we will be varying β_1 in this derivation to create the potential, we could technically vary H or M instead - although changing M would change the exchange constant α, according to Eq. (2.4.7), so this would make matters much more complicated.

3.3 Results for a Rectangular Profile

We assume that the anisotropy has a spatial distribution of:

$$\beta(x) = \beta_0 + \beta_1(x) = \beta_0 + \beta_1\{\Theta(x) - \Theta(x-a)\}, \tag{3.3.1}$$

where $\Theta(x)$ is the Heaviside step function. This corresponds to a rectangular local anisotropy 'defect', as shown in Fig. 3.1. Recall that β_0 is the constant of uniaxial anisotropy in the homogeneous material away from the defect, and we define β_1 as the amplitude of the defect. Although the theme of this thesis is on graded magnetic features, this investigation will serve as a 'proof of concept'; the solutions should be simple enough for us to focus more on the spin wave behaviour, and the spin wave excitation mechanism should still work for any other profile.

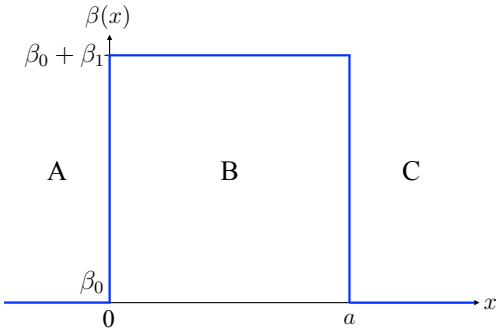

FIGURE 3.1: Magnetic anisotropy $\beta(x)$ distribution in the x axis. There is a local anisotropy defect of constant amplitude β_1 in region B where $0 < x \leq a$, and the anisotropy is a constant value β_0 in regions A ($x < 0$) and C ($x > a$).

3.3.1 Spin Wave Solutions

We seek plane wave solutions to (3.2.20) with the boundary condition that the waves are outgoing from the defect. The equation can be written separately in

each of the three regions A, B and C (also using (3.2.21)) as

$$\text{regions A and C}: \quad \left[\alpha\nabla^2 + \Omega - \beta_0 - (H_0/M_0)\right]\tilde{m}_\beta = 0, \tag{3.3.2}$$

$$\text{region B}: \quad \left[\alpha\nabla^2 + \Omega - \beta_0 - \beta_1 - (H_0/M_0)\right]\tilde{m}_\beta = \frac{\beta_1\tilde{h}(\omega)}{\Omega - \beta_0 - (H_0/M_0)}. \tag{3.3.3}$$

The same boundary conditions as the Schrödinger equation are imposed: that the function $\tilde{m}_\beta$ and its derivative are continuous across the boundaries. The solutions are

$$\tilde{m}_{\beta,\mathrm{A}} = A(\omega)\exp\left[-ik_0x\right], \tag{3.3.4}$$

$$\tilde{m}_{\beta,\mathrm{B}} = \eta + B_1(\omega)\exp\left[ik_1x\right] + B_2(\omega)\exp\left[-ik_1x\right], \tag{3.3.5}$$

$$\tilde{m}_{\beta,\mathrm{C}} = C(\omega)\exp\left[ik_0x\right], \tag{3.3.6}$$

where

$$A(\omega) = -\frac{\eta k_1(-1+\exp[ik_1a])}{k_0(1+\exp[ik_1a]) + k_1(1-\exp[ik_1a])}, \tag{3.3.7}$$

$$B_1(\omega) = \frac{k_0}{k_1(-1+\exp[ik_1a])}\cdot A(\omega), \tag{3.3.8}$$

$$B_2(\omega) = \exp[ik_1a]\cdot B_1(\omega), \tag{3.3.9}$$

$$C(\omega) = \exp[-ik_0a]\cdot A(\omega), \tag{3.3.10}$$

and with

$$\begin{aligned} k_0 &= \sqrt{\frac{\Omega - \beta_0 - (H_0/M_0)}{\alpha}}, \\ k_1 &= \sqrt{\frac{\Omega - \beta_0 - \beta_1 - (H_0/M_0)}{\alpha}}, \\ \eta &= \frac{\beta_1\tilde{h}(\omega)}{\alpha^2k_0^2k_1^2}. \end{aligned} \tag{3.3.11}$$

Note that the amplitudes A_1, B_1, B_2 and C_2 are written as functions of ω above, and this is via k_0, k_1 and η, although we do not write out this dependence for the latter variables, for brevity. We have also omitted the time-dependence in the exponentials, but we could equally have written the exponents as $i(\pm kx - \omega t)$. The term η is the inhomogeneous solution to (3.3.3), and can also be obtained by inspection; it is the solution to (3.3.3) if $\tilde{m}_\beta$ had no x dependence. Also note the form of $k_{0,1}$ justifies why the $-\Omega$ solution was dropped earlier: the wave numbers would be purely imaginary for all values of the parameters.

3.3.2 Frequency Regimes

We can see that we will have different solutions for the waves depending on whether the effective frequency Ω is smaller or larger than the strength of the anisotropies and the external field (as a proportion of the magnetisation), making k_1 and/or k_0 complex if Ω is too small. We will look at each situation separately. Note that we will use the following values for the various parameters, unless otherwise stated, to model a Permalloy-like material: $H_0 = 2$ kOe (≈ 160 kA/m), $M_0 = 800$ erg/G·cm^3 [74] (800 kA/m), $\alpha = 3.125 \times 10^{-12}$ cm^2 [23] ($= 3.125 \times 10^{-16}$ m^2), $\gamma = 1.76 \times 10^7$ rad·Hz/Oe ($= 1.76 \times 10^{11}$ rad·Hz/T), $\beta_0 = 1$, $\beta_1 = 1.5$, $a = 40 \times 10^{-7}$ cm (40 nm), and $h = 1$ Oe (≈ 80 A/m). The dimensionless anisotropy constants stated here can be related to the usual anisotropy constants[3] K via $\beta = 2K/M_0^2$, in which case we have a value corresponding to β_0 of $K_0 = 3.2 \times 10^5$ erg/cm^3 (32 kJ/m^3), which is reasonable for Permalloy [75].

If $\Omega < \beta_0 + (H_0/M_0)$, then according to Eq. (3.3.11) both k_0 and k_1 are imaginary, so the exponentials decay in all regions and no spin waves will propagate. We show a snapshot of $\tilde{m}_\beta$ for this case in Figure 3.2 (a). For our choice of variables, this corresponds to the condition that $\Omega < 3.5$.

If $\Omega = \beta_0 + (H_0/M_0) = 3.5$, then $k_0 = 0$ and $\eta \to \infty$, and so do A, B_1, B_2 and C in Eqs. (3.3.7)-(3.3.10) because this is now the dominant term in the numerator, and there is no solution in this case. Physically, this is the (undamped) ferromagnetic resonance condition of the material in the regions where the anisotropy constant is β_0: the amplitude of $\tilde{m}_\beta$ becomes large as $\Omega \to \beta_0 + (H_0/M_0)$.

When $\Omega > \beta_0 + (H_0/M_0)$ but $\Omega < \beta_1 + \beta_0 + (H_0/M_0)$, then $\tilde{m}_{\beta,\mathrm{A}}$ and $\tilde{m}_{\beta,\mathrm{C}}$ are both propagating solutions, since k_0 is real. However, k_1 is imaginary in this case, so there are no propagating solutions in the central region. This would suggest that spin waves are being emitted from the boundaries to inside or outside the defect, but do not propagate within it. We show a snapshot of the resulting waveform in Figure 3.2 (b). It is important to note however that the wavelength of the spin waves is >90nm in this (and the previously mentioned) regime(s). In reality, the magneto-dipole interaction is relevant in this regime, which we do not account for here. As we will soon see, the amplitude of the spin waves in this case will also be large, which is also not represented properly in our linearised model. So, we should only really be concerned with the behaviour of the spin

[3] since K is given in units of energy density, so this can be compared to the term containing β in the free energy density Eq. (3.2.3).

waves when the frequency Ω is much higher than the highest ferromagnetic resonance frequency in the model, which occurs when $\Omega = \beta_1 + \beta_0 + (H_0/M_0) = 5$ for the values stated above.

In the case that $\Omega > \beta_1 + \beta_0 + (H_0/M_0)$, there are propagating waves within and outwards from the defect region, as shown in Figure 3.2 (c). This is the regime that we are most interested in.

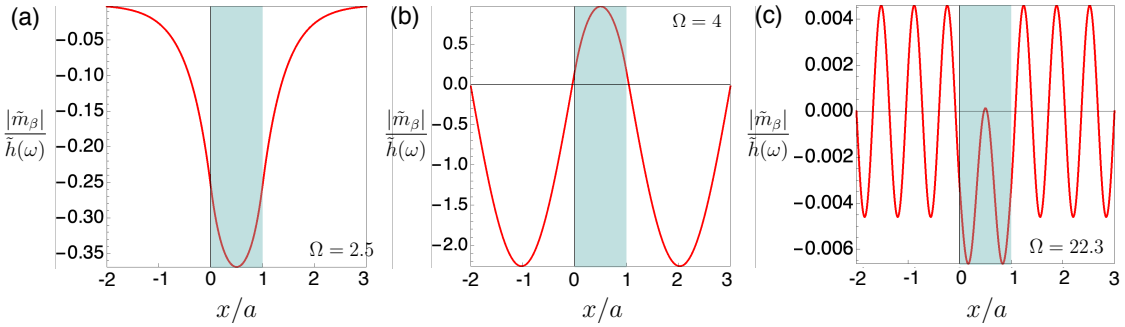

FIGURE 3.2: Solutions for $\tilde{m}_\beta$ for (a) $\Omega = 2.5$ ($f = 5.6$ GHz), so $\Omega < \beta_0 + (H_0/M_0)$, (b) $\Omega = 4$ ($f = 9.0$ GHz), so $\beta_0 + (H_0/M_0) < \Omega < \beta_1 + \beta_0 + (H_0/M_0)$, and (c) $\Omega = 22.3$ ($f = 50$ GHz), so $\Omega > \beta_1 + \beta_0 + (H_0/M_0)$. The shaded region indicates the anisotropy defect, and each image is taken at the same point in the phase ($3\pi/4$).

Emission and Suppression of Spin Waves

To understand how the amplitude of the emitted spin waves depends on the wave number outside of the defect, $A(\omega)$ is plotted (in red) against k_0 in Fig. 3.3. The amplitude of $\tilde{m}_h$ is also included (in blue) for comparison. The model is valid for the exchange-only regime, which is applicable around $\lambda < 50$ nm, and this corresponds to $k > 126$ rad/μm (and $\Omega \approx 8.4$, $f \approx 19$ GHz). This most relevant regime is highlighted on the graph[4] in Fig. 3.3.

We can firstly observe in Fig. 3.3 that the amplitude of both $A(\omega)$ and $\tilde{m}_h$ decreases quickly with increasing k_0 (and hence Ω). The amplitude of $\tilde{m}_h$ is however larger than $A(\omega)$ in the exchange regime, and remains so for all values of k_0. This does not necessarily mean that the spin waves will not be visible above the uniform precession; rather, they should appear as a moving ripple on top of a larger amplitude stationary wave. For a frequency of 50 GHz ($\Omega = 22.3$), the spin wave amplitude is approximately 9% of the uniform precession amplitude,

[4] Although it is out of the region of interest, it is worth noting that the amplitude increases strongly as $k_0 \to 0$ because since $\eta \to \infty$ as per (3.3.11). The amplitude would be finite (though large) in reality, and only occurs because we have neglected damping in our model for simplicity.

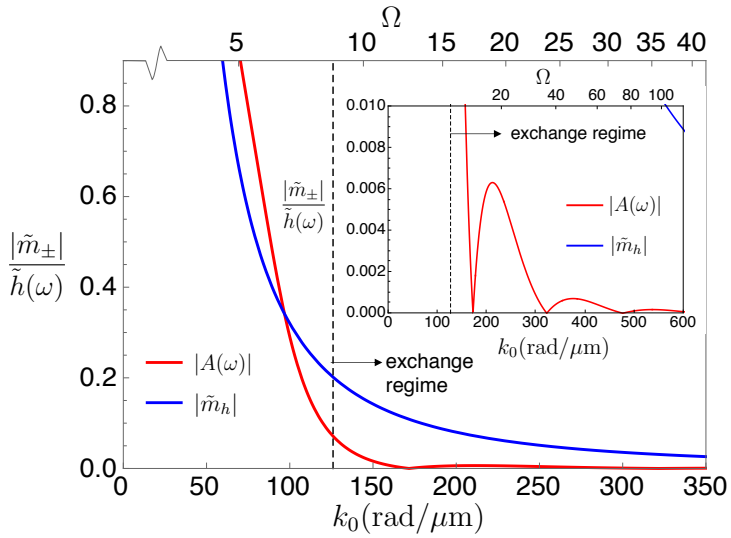

FIGURE 3.3: Amplitude of the magnetisation vs. wave vector outside the defect k_0 (bottom axis) or rather Ω (top axis). The red line is for the spin waves outside of the defect $A(\omega)$, and the blue line is for the uniform precession due to the harmonic field. The zeros of $A(\omega)$ correspond to standing waves within the defect region, shown more clearly for a larger range of k_0 in the inset.

which should still be visible, according to the experimental capabilities discussed in Chapter 2.8.

The second and most interesting observation is the zeros in emission at regular intervals. Looking at equations (3.3.7) and (3.3.10) for spin waves outside of the defect, we can see that zeros will occur when the numerator is equal to zero, i.e. for $\exp(iak_1) = 1$, which implies the condition for zero emission is:

$$ak_1 = 2n\pi \quad \text{where: } n = 0, 1, 2, \ldots . \tag{3.3.12}$$

The zeros on the graph are for k_0, not for k_1, but the two are related by the value of β_1 as per Eqs. (3.3.11). Checking this in *Mathematica*, we find that $ak_1 = 2n\pi$ is indeed fulfilled.

These zeros correspond to a standing wave within the defect region, due to a superposition of the left-travelling wave and the right-travelling wave within the defect. We can see in Eq. (3.3.12) that this is when the defect width a is a multiple of the spin wave wavelength $\lambda_1/2$ within the defect. To demonstrate that $\tilde{m}_\beta$ is a standing wave in this case, we can reintroduce the 'hidden' time-dependence in

our equation (3.3.5) for the case that B_1=B_2 = B (i.e. $\exp(iak_1) = 1$):

$$\begin{aligned}\tilde{m}_{\beta,B} &= \eta + B_1\exp[i(k_1x - \omega t)] + B_2\exp[-i(k_1x + \omega t)] \\ &= \eta + B\exp[-i\omega t]\Big\{\exp[+ik_1x] + \exp[-ik_1x]\Big\} \\ &= \eta + 2B\exp[-i\omega t]\cos[k_1x].\end{aligned}$$

This is the well-known form of a standing wave; the nodes in space are fixed. The energy is therefore confined within the defect region, and we see zero transmission of energy outside - hence the zeros.

3.3.3 Dependence of Spin Wave Amplitude on Defect Height

The value of β_1 determines whether the anisotropy defect forms a potential well (for $\beta_1 < 0$) or potential barrier (for $\beta_1 > 0$). We have only considered a potential barrier with a fixed value so far, but it would be interesting to see how varying β_1 changes the behaviour of the emitted spin waves.

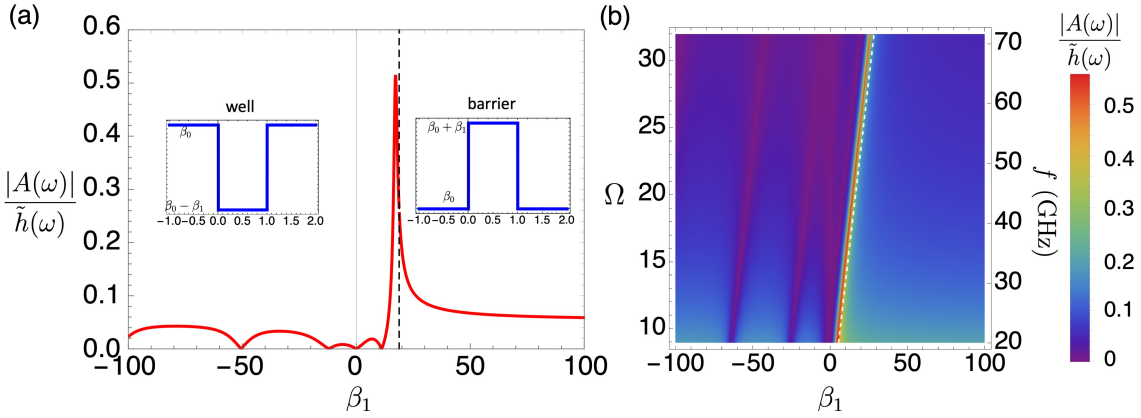

FIGURE 3.4: Dependence of the amplitude of the spin waves outside of the defect $A(\omega)$ on the defect height β_1, for (a) $\Omega = 22.3$ (f=50 GHz), and (b) a range of frequencies, where Ω is displayed on the left axis and f on the right.

The dependence of $A(\omega)$ on β_1 is shown in Figure 3.4, and we show a dashed line in panels (a) and (b) for $\beta_1 = \Omega - \beta_0 - H_0/M_0$. For $\beta_1 > \Omega - \beta_0 - H_0/M_0$, k_1 is imaginary, but waves can still propagate outwards from the region. In this case, the spin wave amplitude smoothly decays from the peak which is slightly to the left of the dashed line. In panel (a), the graph is plotted using 50 points, to ensure we do not obscure the point when $\beta_1 = \Omega - \beta_0 - H_0/M_0$ and thus $k_1 = 0$, as there will be no solution for $A(\omega)$. This is because $\eta \to \infty$ when $k_1 \to 0$, as we

can see in Eq. (3.3.11). The peak in amplitude is slightly away from this region due to the competition between the terms in the numerator and denominator of $A(\omega)$ defined in Eq. (3.3.7), which are oscillatory functions of β_1.

For $\beta_1 < \Omega - \beta_0 - H_0/M_0$ (and β_1 is less than the value leading to the emission peak), we observe zeros in the spin wave emission. The origin of the zeros is the same as we saw previously; when $ak_1 = 2n\pi$. In this case, since k_1 is changing with the square-root of β_1, the zeros are not evenly spaced. The dependence of these zeros with frequency is clear from panel (b). As Ω increases, the value of β_1 which leads to zeros must increase proportionally, for k_1 to still fulfil $ak_1 = 2n\pi$.

A final note is that the amplitude of spin waves emitted from the potential barrier is in general larger than those from a potential well. At large values of $|\beta_1|$ the amplitudes do tend towards the same value, but for reasonably small values ($|\beta_1| < 100$ for our choice of parameters) the barrier emits spin waves with a larger amplitude, and can thus be considered as more efficient, except when the emission is resonant around $\beta_1 \approx \Omega - \beta_0 - H_0/M_0$. The fact that the spin wave amplitude is still higher for $\beta_1 \gg \Omega - \beta_0 - H_0/M_0$ is likely because the spin waves are not propagating within the barrier in this case (since k_1 is imaginary), and so there is more energy to be emitted from the defect. From a more simple energy perspective, it is more energetically favourable to step down from a potential barrier than step up from a potential well; energy must be used up in the process of escaping the well. It is thanks to the Schrödinger-like equation which describes these spin waves in the linear, exchange regime, that we can make these analogies.

3.4 Conclusions

This work found solutions for spin wave emission from an anisotropy 'defect' region, purely as a result of the uniform, harmonic field combined with the presence of the defect. This defect could equally be in the magnetisation or external field, as these are otherwise just constants carried through the equation. The important point is that the parameters β, H_0 or M_0 form part of the potential in the Schrödinger-like equation, so the spatial manipulation of any one (or any combination) of these can lead to the creation of an effective potential barrier or well (or landscape). In addition, this potential also appears in the driving term of the equation, so the potential can therefore act as a spin wave emitter. However, spin wave emission can also be suppressed if standing waves are set up within the

defect region, depending on the properties of the potential and the wavevector inside it.

We have seen that there is a threshold frequency above which spin waves will be emitted from the defect, corresponding to $\Omega = \beta_0 + (H_0/M_0)$. This is the ferromagnetic resonance frequency of the material outside of the defect region. Spin wave suppression can also occur once the frequency Ω exceeds the ferromagnetic resonance frequency of the defect region, and only then when the defect width is a multiple of $\lambda/2$ inside the defect.

Overall, this method of spin wave generation offers an interesting alternative to the usual method of local antennas connected to an alternating current (AC). In this case, our antenna is the defect and the driving force is the uniform but harmonic external field; in both cases, it is a local inhomogeneity in the field which is driven to excite waves. This alternative form of a spin wave source may be easier to fabricate, and at the very least does not require a direct connection to an AC current. Our analysis is valid in the small-amplitude precession (linear) regime, and although some complexities may arise from any nonlinear effects, it is reasonable to assume that the mechanism is still valid even for a larger amplitude precession.

Chapter 4

Exchange Spin Wave Emission from a Bloch Domain Wall

4.1 Introduction

In the previous Chapter, we considered a generic defect in the anisotropy, and saw that it could be a source of spin waves when excited by a uniform, harmonic external field. Now, we consider a more complex, naturally-occuring graded index structure: the domain wall. These are the transition regions between domains of uniformly aligned magnetisation, and can have dimensions down to a few nanometers, depending on the material. Domain walls have been studied in great detail, due to a number of interesting properties: their magnetic field and current-driven motion [76, 77], their ability to channel spin waves [78–80], and the unusual reflectionless behavior for spin waves passing through them [81]. Recently, there have also been numerical [82, 83] and experimental [84, 85] reports of pinned domain walls *generating* spin waves, with wavelengths down to tens of nanometers [86]. The origin of the observed spin wave emission has typically been attributed to the domain wall oscillations, generated by the applied microwave magnetic field [82–85] or spin-polarized current [86, 87].

In this Chapter, we describe an analytical theory that demonstrates the emission of exchange spin waves from a Bloch domain wall driven by a uniform microwave magnetic field, as a result of a *linear* process. The problem is reduced to that of the Pöschl-Teller (P-T) potential in a Schrödinger-like equation - an exactly solvable model, of particular interest in quantum mechanics [88] and optics [89, 90]. This potential is mostly known for its peculiar property of 100% transmission of incident waves at *any* frequency, for certain parameters of the potential [91]. While forming such a potential in other systems is difficult, serendipitously

the reflectionless P-T potential *exactly* describes the graded magnonic index profile [12] due to a Bloch domain wall, allowing the peculiar behaviour to be naturally investigated in magnetic systems [92]. Furthermore, when the domain wall is driven by a uniform microwave magnetic field, the P-T profile happens to be present not only as the potential, but also as a driving term in the obtained Schrödinger-like equation. Strikingly, when we manipulate the aspect (height to width) ratio of the profile from that of a domain wall, we reveal novel effects on the waves in our system, which are not present for the quantum-mechanical analog (which has no driving term).

We study a thin film with infinite extent in the y-z plane containing two antiparallel domains separated by a Bloch domain wall, as shown in Figure 4.1. We are looking for conditions of spin wave emission from the domain wall, when a continuous wave magnetic field is applied perpendicular to it (along the y axis).

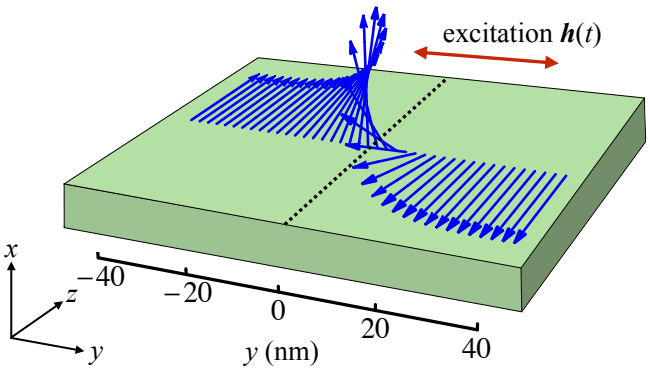

FIGURE 4.1: The studied system: a thin film with two antiparallel magnetic domains separated by a Bloch domain wall. The dotted line indicates the domain wall centre. The blue arrows represent the static magnetisation configuration $\mathbf{M}_0$, with its magnitude M_0 arbitrarily sized for clarity.

4.2 Energy Minimization

4.2.1 Energy Density

The magnetic energy density W of this system in Gaussian units is [21, 93]

$$W = \frac{\alpha}{2}\left(\frac{\partial \mathbf{M}}{\partial y}\right)^2 - \frac{\beta_{\parallel}}{2}(\mathbf{M}\cdot\hat{\mathbf{z}})^2 + \frac{\beta_{\perp}}{2}(\mathbf{M}\cdot\hat{\mathbf{x}})^2 - \mathbf{h}\cdot\mathbf{M}, \tag{4.2.1}$$

where α is the exchange constant (units of cm^2), $\beta_{\parallel}$ and $\beta_{\perp}$ are the constants of the easy axis and easy plane anisotropies respectively, $\hat{\mathbf{z}}$ and $\hat{\mathbf{x}}$ are unit vectors in the corresponding easy and hard magnetisation directions, and $\mathbf{h} = \mathbf{h}(t) = h\exp(-i\omega t)\hat{\mathbf{y}}$ is the driving microwave magnetic field at frequency ω. We only consider changes to the magnetisation in the y direction, which explains the form of the first term. The fact that the out-of-plane anisotropy term is positive indicates that x is a hard-axis, i.e. it is not energetically favourable for the magnetisation to align along this axis. We will find, of course, that the magnetisation must rotate into this axis in the Bloch domain wall; and this is an energetically-favourable configuration for domain walls in films which are not too thin [94]. The film thickness does not appear explicitly in W, and we only need to specify that its thickness in the x direction is much smaller than its (semi-infinite) extent in the $y-z$ plane, yet thick enough for a Bloch domain wall to be energetically favourable. We will refer to the film then as 'thin', in relation to its spatial extent in the $y-z$ plane.

4.2.2 Conversion to Spherical Coordinates

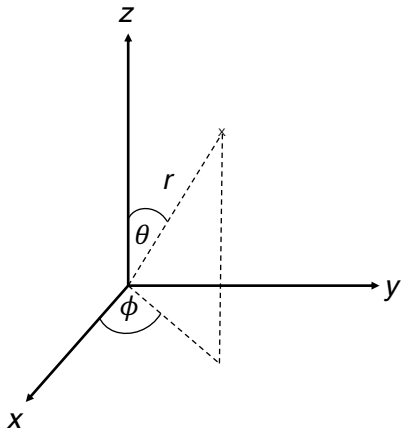

FIGURE 4.2: The spherical coordinate system

We want to find the equilibrium configuration of our domain wall system, so we must minimise the static energy density, omitting the final term in equation Eq. (4.2.1). It will be easier to work in the spherical coordinate system (Figure 4.2), so we introduce

$$\mathbf{M} = M_0(\sin\theta\cos\phi, \sin\theta\sin\phi, \cos\theta), \tag{4.2.2}$$

with M_0 the magnitude of the saturation magnetisation, which we will always assume to be a constant. We can substitute Eq. (4.2.2) into Eq. (4.2.1) (omitting

the driving field term) to convert to spherical coordinates, but we will need to expand the $\frac{1}{2}\alpha(\partial_y \mathbf{M})^2$ term. We assume that $\theta = \theta(y)$ and $\phi = \phi(y)$ for now, and then expand as follows:

$$
\begin{aligned}
&\frac{1}{2}\alpha(\partial_y \mathbf{M})^2 = \\
&= \frac{M_0}{2}\alpha\Big[\partial_y(\sin\theta\cos\phi\ \hat{\mathbf{x}} + \sin\theta\sin\phi\ \hat{\mathbf{y}} + \cos\theta\ \hat{\mathbf{z}})\Big]^2 \\
&\left(\text{using}\quad \partial_y = \frac{\partial}{\partial y} = \frac{\partial}{\partial\theta}\frac{\partial\theta}{\partial y} = \partial_\theta\partial_y\theta, \quad \therefore \partial_y = \partial_\phi\partial_y\phi\right): \\
&= \frac{M_0}{2}\alpha\Big[(\cos\theta\cos\phi\partial_y\theta - \sin\theta\sin\phi\partial_y\phi)\ \hat{\mathbf{x}} \\
&+ (\cos\theta\sin\phi\partial_y\theta + \sin\theta\cos\phi\partial_y\phi)\ \hat{\mathbf{y}} - \sin\theta\partial_y\theta\ \hat{\mathbf{z}}\Big]^2 \\
&= \frac{M_0}{2}\alpha\Big[\cos^2\theta\cos^2\phi(\partial_y\theta)^2 + \sin^2\theta\sin^2\phi(\partial_y\phi)^2 - 2\cos\theta\sin\theta\cos\phi\sin\phi\partial_y\theta\partial_y\phi \\
&+ \cos^2\theta\sin^2\phi(\partial_y\theta)^2 + \sin^2\theta\cos^2\phi(\partial_y\phi)^2 + 2\cos\theta\sin\theta\cos\phi\sin\phi\partial_y\theta\partial_y\phi \\
&+ \sin^2\theta(\partial_y\theta)^2\Big] \\
&= \frac{M_0}{2}\alpha\Big[\cos^2\theta(\partial_y\theta)^2 + \sin^2\theta(\partial_y\phi)^2 + \sin^2\theta(\partial_y\theta)^2\Big] \\
&= \frac{M_0}{2}\alpha\Big[(\partial_y\theta)^2 + \sin^2\theta(\partial_y\phi)^2\Big].
\end{aligned}
$$

We can now substitute the above result, along with Eq. (4.2.2), directly into the static energy density, to obtain

$$W_{\text{static}} = \frac{M_0}{2}\alpha\Big[(\partial_y\theta)^2 + \sin^2\theta(\partial_y\phi)^2\Big] - \frac{M_0}{2}\beta_{\parallel}\cos^2\theta + \frac{M_0}{2}\beta_{\perp}\sin^2\theta\cos^2\phi. \tag{4.2.3}$$

4.2.3 Euler-Lagrange Equations

The next step is to establish the Euler-Lagrange equations for the above energy density; this is carried out in Appendix B. We now specify that $\phi = \phi_0$ which is a constant, so only θ is a function of y. This means that each 'slice' along the y axis has components of M that only varies in the $x-z$ plane, having the same components out of that plane; it is not twisting along y. The resulting equations are:

$$[\beta_{\parallel} + \beta_{\perp}\cos^2\phi_0]\sin\theta\cos\theta = \alpha\theta'' \tag{4.2.4}$$

$$-\beta_{\perp}\sin^2\theta\sin\phi_0\cos\phi_0 = 0 \tag{4.2.5}$$

We can solve Eq. (4.2.5) directly; in order for the left hand side to equal zero, then either $\sin\phi_0 = 0$ or $\cos\phi_0 = 0$ (note that $\sin^2\theta$ cannot equal zero for all values of θ; θ is a function of y), which means that the solutions to this equation are $\phi_0 = 0$ or $\phi_0 = \pi/2$. These two solutions correspond to the two different domain wall types; a Néel or Bloch wall. We require a Bloch domain wall, where the magnetisation will rotate out-of-plane, around the y axis - in which case, $\phi_0 = 0$. Using this solution in Eq. (4.2.4), we find:

$$\begin{aligned}&[\beta_{\parallel} + \beta_{\perp}]\sin\theta\cos\theta - \alpha\theta'' = 0 \\ &\quad\implies \sin(2\theta) - 2\lambda_B^2\theta'' = 0, \quad \text{with:} \quad \lambda_B = \sqrt{\frac{\alpha}{\beta_{\parallel} + \beta_{\perp}}},\end{aligned} \tag{4.2.6}$$

where λ_B is the Bloch domain wall width. Equation (4.2.6) is a form of the sine-Gordon equation, well-studied due to its soliton-like solutions [95].

We now need to solve Eq. (4.2.6), to find the domain wall profile θ as a function of y and λ_B. This is carried out in full in Appendix C, and the result is:

$$\theta = +2\arctan\left[\exp\left(\frac{y - Y_0}{\lambda_B}\right)\right], \tag{4.2.7}$$

where Y_0 is the centre of the domain wall which we will position at $Y_0 = 0$. In the Appendix, we show that θ has a positive and a negative solution, which represents the two possible senses of rotation of the domain wall. In our case, we rotate from $\theta = 0 \to \pi$ as y increases, meaning that we take the positive, anti-clockwise solution. We can use our expression for θ to describe each component of the magnetisation, $\mathbf{M} = (M_x, M_y, M_z)$:

$$\begin{aligned}M_x = M_0\sin\theta\underbrace{\cos\phi_0}_{=1} &= M_0\sin\left[2\tan^{-1}\left[\exp\left(\frac{y - Y_0}{\lambda_B}\right)\right]\right] \\ &= M_0\text{sech}\left(\frac{y - Y_0}{\lambda_B}\right),\end{aligned} \tag{4.2.8}$$

$$M_y = M_0\sin\theta\underbrace{\sin\phi_0}_{=0} = 0, \tag{4.2.9}$$

$$M_z = M_0\cos\theta = -M_0\tanh\left(\frac{y - Y_0}{\lambda_B}\right). \tag{4.2.10}$$

Now we have found the static configuration of the magnetisation, we can now consider the dynamics in the next section.

4.3 Linearised L-L Equation in the Rotated Reference Frame

We now need to linearise the Landau-Lifshitz (L-L) equation, using the same method as in Chapter 3 but with the different contributions to the energy. We will include the expressions Eq. (4.2.8)-Eq. (4.2.10) in due course, but for now we can keep the magnetisation components general.

4.3.1 Linearisation

As we have seen in the previous Chapters, the Landau-Lifshitz equation without relaxation is:

$$\frac{\partial \mathbf{M}}{\partial t} = -\gamma[\mathbf{M} \times \mathbf{H}_{\text{eff}}], \tag{4.3.1}$$

where γ is the gyromagnetic ratio. We are considering the dynamic case, so we reintroduce the pumping magnetic field $\mathbf{h}(t) = h(t)\hat{\mathbf{y}} = h\exp(-i\omega t)\hat{\mathbf{y}}$. We expand the effective magnetic field $\mathbf{H}_{\text{eff}}$ into its components, remembering that W is given by equation Eq. (4.2.1), to find

$$\begin{aligned}\mathbf{H}_{\text{eff}} &= -\frac{\delta W}{\delta \mathbf{M}} = -\frac{\partial W}{\partial \mathbf{M}} + \frac{\partial}{\partial x_i}\frac{\partial W}{\partial\left(\frac{\partial \mathbf{M}}{\partial x_i}\right)} \\ &= \left[-\beta_{\perp} M_x + \alpha\partial_y^2 M_x\right]\hat{\mathbf{x}} + \left[\alpha\partial_y^2 M_y + h(t)\right]\hat{\mathbf{y}} + \left[\beta_{\parallel} M_z + \alpha\partial_y^2 M_z\right]\hat{\mathbf{z}}\end{aligned} \tag{4.3.2}$$

where we have used the chain rule to differentiate these terms, e.g.,

$$\frac{1}{2}\partial_{\mathbf{M}}\left[(\mathbf{M}\cdot\hat{\mathbf{z}})^2\right] = \mathbf{M}\cdot\hat{\mathbf{z}}\partial_{\mathbf{M}}(\mathbf{M}\cdot\hat{\mathbf{z}}) = M_z\hat{\mathbf{z}}.$$

This method will so far be reminiscent of the process we carried out in Chapter 3, though we now have both in-plane and out-of-plane anisotropies, contributing to different components of the effective field, since we are working with a thin film. As before, we now need to linearise the Landau-Lifshitz equation of motion, by assuming that the magnetisation $\mathbf{M}$ only undergoes a small deflection $\mathbf{m}$ from equilibrium, and that the pumping magnetic field, $\mathbf{h}(t)$ is also small. We therefore

impose that $\mathbf{M} = \mathbf{M}_0 + \mathbf{m}$, where $\mathbf{m}$ is a small, time-dependent perturbation to the static case $\mathbf{M}_0$ (not writing out the functional dependence, for brevity).

Before substituting $\mathbf{H}_{\text{eff}}$ into Eq. (4.3.1), we need to consider which terms will remain in our linear approximation. Firstly, we can see that the time differential on the left hand side will only affect $\mathbf{m}$. Next, in the cross product, we will only retain terms of the lowest order in our small quantities ($\mathbf{m}$ and $\mathbf{h}$). Notice that since the magnetisation appears in the effective field, this will now consist of static and time-dependent terms. We will write $\mathbf{H}_{\text{eff}} = \mathbf{H}_{\text{eff},0} + \delta\mathbf{H}_{\text{eff}}$, with the first term containing $\mathbf{M}_0$ (and *not* containing the small term $\mathbf{h}$) and the second term containing $\mathbf{m}$ along with $\mathbf{h}$. We will therefore have

$$\frac{\partial \mathbf{m}}{\partial t} = -\gamma\big[(\mathbf{M}_0 \times (\delta\mathbf{H}_{\text{eff}}) + (\mathbf{m} \times \mathbf{H}_{\text{eff},0})\big], \tag{4.3.3}$$

where

$$\delta\mathbf{H}_{\text{eff}} = [-\beta_\perp m_x + \alpha\partial_y^2 m_x]\,\hat{\mathbf{x}} + [\alpha\partial_y^2 m_y + h(t)]\,\hat{\mathbf{y}} + [\beta_\parallel m_z + \alpha\partial_y^2 m_z]\,\hat{\mathbf{z}} \tag{4.3.4}$$

$$\mathbf{H}_{\text{eff},0} = [-\beta_\perp M_{0,x} + \alpha\partial_y^2 M_{0,x}]\,\hat{\mathbf{x}} + [\alpha\partial_y^2 M_{0,y}]\,\hat{\mathbf{y}} + [\beta_\parallel M_{0,z} + \alpha\partial_y^2 M_{0,z}]\,\hat{\mathbf{z}} \tag{4.3.5}$$

Note that we have also omitted the term involving only the static magnetisation, i.e. $\mathbf{M}_0 \times \mathbf{H}_{\text{eff},0}$; this term is equal to zero. This can be seen by writing the Landau Lifshitz equation in the static case; the left hand side is equal to zero, and so must be this term on the right hand side.

We have a couple of cross products to carry out in Eq. (4.3.3). We'll start with the first term on the right hand side:

$$\begin{aligned}
\mathbf{M}_0 \times \delta\mathbf{H}_{\text{eff}} &= \begin{vmatrix} \hat{\mathbf{x}} & \hat{\mathbf{y}} & \hat{\mathbf{z}} \\ M_{0,x} & M_{0,y} & M_{0,z} \\ \delta H_{\text{eff},x} & \delta H_{\text{eff},y} & \delta H_{\text{eff},z} \end{vmatrix} \\
&= \hat{\mathbf{x}}(M_{0,y}\delta H_{\text{eff},z} - M_{0,z}\delta H_{\text{eff},y}) + \hat{\mathbf{y}}(M_{0,z}\delta H_{\text{eff},x} - M_{0,x}\delta H_{\text{eff},z}) \\
&+ \hat{\mathbf{z}}(M_{0,x}\delta H_{\text{eff},y} - M_{0,y}\delta H_{\text{eff},x}) \\
&= \hat{\mathbf{x}}\big[M_{0,y}(\beta_\parallel m_z + \alpha\partial_y^2 m_z) - M_{0,z}(h(t) + \alpha\partial_y^2 m_y)\big] \\
&+ \hat{\mathbf{y}}\big[M_{0,z}(-\beta_\perp m_x + \alpha\partial_y^2 m_x) - M_{0,x}(\beta_\parallel m_z + \alpha\partial_y^2 m_z)\big] \\
&+ \hat{\mathbf{z}}\big[M_{0,x}(h(t) + \alpha\partial_y^2 m_y) - M_{0,y}(-\beta_\perp m_x + \alpha\partial_y^2 m_x)\big].
\end{aligned} \tag{4.3.6}$$

For the second term, we have:

$$\begin{aligned}
\mathbf{m}\times\mathbf{H}_{\text{eff},0} &= \begin{vmatrix} \hat{\mathbf{x}} & \hat{\mathbf{y}} & \hat{\mathbf{z}} \\ m_x & m_y & m_z \\ H_{\text{eff,S},x} & H_{\text{eff,S},y} & H_{\text{eff,S},z} \end{vmatrix} \\
&= \hat{\mathbf{x}}(m_y H_{\text{eff,S},z} - m_z H_{\text{eff,S},y}) + \hat{\mathbf{y}}(m_z H_{\text{eff,S},x} - m_x H_{\text{eff,S},z}) \\
&+ \hat{\mathbf{z}}(m_x H_{\text{eff,S},y} - m_y H_{\text{eff,S},x}) \\
&= \hat{\mathbf{x}}\left[m_y(\beta_{\parallel} M_{0,z} + \alpha\partial_y^2 M_{0,z}) - m_z\alpha\partial_y^2 M_{0,y}\right] \\
&+ \hat{\mathbf{y}}\left[m_z(-\beta_{\perp} M_{0,x} + \alpha\partial_y^2 M_{0,x}) - m_x(\beta_{\parallel} M_{0,z} + \alpha\partial_y^2 M_{0,z})\right] \\
&+ \hat{\mathbf{z}}\left[m_x\alpha\partial_y^2 M_{0,y} - m_y(-\beta_{\perp} M_{0,x} + \alpha\partial_y^2 M_{0,x})\right]. \qquad (4.3.7)
\end{aligned}$$

We can collect these terms together to write Eq. (4.3.3) in full, as

$$\begin{aligned}
\frac{\partial\mathbf{m}}{\partial t} = -\gamma\Big\{ &\hat{\mathbf{x}}\left[M_{0,y}\beta_{\parallel} m_z + M_{0,y}\alpha\partial_y^2 m_z - M_{0,z}h(t) - M_{0,z}\alpha\partial_y^2 m_y + \right. \\
&\left. + m_y\beta_{\parallel} M_{0,z} + m_y\alpha\partial_y^2 M_{0,z} - m_z\alpha\partial_y^2 M_{0,y}\right] + \\
&+ \hat{\mathbf{y}}\left[- M_{0,z}\beta_{\perp} m_x + M_{0,z}\alpha\partial_y^2 m_x - M_{0,x}\beta_{\parallel} m_z - M_{0,x}\alpha\partial_y^2 m_z + \right. \\
&\left. - m_z\beta_{\perp} M_{0,x} + m_z\alpha\partial_y^2 M_{0,x} - m_x\beta_{\parallel} M_{0,z} - m_x\alpha\partial_y^2 M_{0,z}\right] + \\
&+ \hat{\mathbf{z}}\left[M_{0,x}h(t) + M_{0,x}\alpha\partial_y^2 m_y + M_{0,y}\beta_{\perp} m_x - M_{0,y}\alpha\partial_y^2 m_x + \right. \\
&\left. + m_x\alpha\partial_y^2 M_{0,y} + m_y\beta_{\perp} M_{0,x} - m_y\alpha\partial_y^2 M_{0,x}\right]\Big\}. \qquad (4.3.8)
\end{aligned}$$

This is clearly going to be quite difficult to work with; since our domain wall has static magnetisation components in all three directions, we have three equations to solve. It would be more convenient to work in a reference frame which follows the orientation of the domain wall as you move in the y direction, and this is investigated in the next section.

4.3.2 Rotating to the Local z' Frame

Converting Between the Reference Frames

We will rotate our old system anticlockwise around the y axis (the magnetisation rotates out of the $y-z$ plane; see Figure 4.3) using the rotation matrix

$$R_B = \begin{pmatrix} \cos\theta(y) & 0 & -\sin\theta(y) \\ 0 & 1 & 0 \\ \sin\theta(y) & 0 & \cos\theta(y) \end{pmatrix}. \qquad (4.3.9)$$

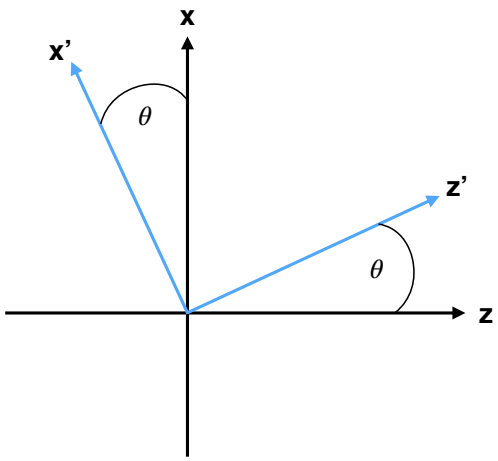

FIGURE 4.3: Relation between the new local frame of reference (where $\mathbf{M}_0$ always points along the z' direction), and the laboratory frame. The local frame rotates anticlockwise around the y axis (in this right-handed coordinate system).

To confirm that R_B does indeed make the magnetisation point in the z' direction, we apply it to $\mathbf{M}_0 = M_0(\sin\theta(y)\cos\phi_0, \sin\theta(y)\sin\phi_0, \cos\theta(y))$, where $\phi_0 = 0$ for a Bloch domain wall:

$$
\begin{aligned}
R_B\mathbf{M}_0 &= \begin{pmatrix} \cos\theta(y) & 0 & -\sin\theta(y) \\ 0 & 1 & 0 \\ \sin\theta(y) & 0 & \cos\theta(y) \end{pmatrix} \begin{pmatrix} M_0\sin\theta(y)\cos\phi_0 \\ M_0\sin\theta(y)\sin\phi_0 \\ M_0\cos\theta(y) \end{pmatrix} \\
&= \begin{pmatrix} M_0\sin\theta(y)\cos\theta(y)(\cos\phi_0 - 1) \\ M_0\sin\theta(y)\sin\phi_0 \\ M_0(\sin^2\theta(y)\cos\phi_0 + \cos^2\theta(y)) \end{pmatrix} = \begin{pmatrix} 0 \\ 0 \\ M_0 \end{pmatrix} = \begin{pmatrix} M'_{0,x} \\ M'_{0,y} \\ M'_{0,z} \end{pmatrix}.
\end{aligned}
$$

To be clear about the unit vectors here, the resulting vector is written in full as:

$$
\begin{aligned}
\mathbf{M}'_0 = R_B\mathbf{M}_0 &= M'_{0,x}\hat{\mathbf{x}}' + M'_{0,y}\hat{\mathbf{y}}' + M'_{0,z}\hat{\mathbf{z}}' \\
&= M_0\,\hat{\mathbf{z}}'.
\end{aligned}
$$

So this is a process of writing the vector in the rotated frame ($\mathbf{M}'_0$) in terms of the components of the original, unrotated vector ($\mathbf{M}_0$). The reverse transformation involves rotating $\mathbf{M}'_0$ from the local frame clockwise about the y axis into the lab frame. This results in $\mathbf{M}_0$ being expressed in terms of the components of $\mathbf{M}'_0$. To

do this, we apply the inverse rotation matrix to R_B^{-1} to $\mathbf{M}_0'$:

$$\begin{pmatrix} M_{0,x} \\ M_{0,y} \\ M_{0,z} \end{pmatrix} = R_B^{-1}\mathbf{M}_0' = \begin{pmatrix} \cos\theta(y) & 0 & \sin\theta(y) \\ 0 & 1 & 0 \\ -\sin\theta(y) & 0 & \cos\theta(y) \end{pmatrix} \begin{pmatrix} M_{0,x}' \\ M_{0,y}' \\ M_{0,z}' \end{pmatrix}$$
$$= \begin{pmatrix} \cos\theta(y)M_{0,x}' + \sin\theta(y)M_{0,z}' \\ M_{0,y}' \\ -\sin\theta(y)M_{0,x}' + \cos\theta(y)M_{0,z}' \end{pmatrix},$$

The resulting vector is written in full as:

$$\begin{aligned} \mathbf{M}_0 = R_B^{-1}\mathbf{M}_0' &= M_{0,x}\hat{\mathbf{x}} + M_{0,y}\hat{\mathbf{y}} + M_{0,z}\hat{\mathbf{z}} \\ &= \sin\theta(y)M_0\,\hat{\mathbf{x}} + \cos\theta(y)M_0\,\hat{\mathbf{z}} \end{aligned}$$

We can now apply this approach to our situation.

Rotation of the Linearised L-L Equation

The full derivation of applying the rotation matrices is quite lengthy, so the details are provided in Appendix D. To summarise the method, we first take Eq. (4.3.8) and rotate it anticlockwise around the y axis into the new local frame (the first transformation in the previous section). This means that the unit vectors point in the local frame's directions, but the resulting vector components are a function of our original lab frame components. However, since the precessional motion in the local frame is only in the $\hat{\mathbf{x}}' - \hat{\mathbf{y}}'$ plane, we would prefer to have the components written in terms of this more convenient local frame. To do this, we then carry out the second transformation from the previous section on $\mathbf{M}$ and $\mathbf{m}$, with $\mathbf{M}$ written in terms of $\theta(y)$ via Eqs. (4.2.8)-(4.2.10), and substitute the resulting components into the rotated Landau Lifshitz equation. We find that we can write equation Eq. (4.3.8) in the local frame as a system of two equations, now

expressed purely as a function of y:

$$\frac{\partial m'_x}{\partial t} = -\gamma M_0 \left\{ -h(t) + \left[\beta_{\parallel} - (\beta_{\parallel} + \beta_{\perp}) 2\text{sech}^2 \left(\frac{y - Y_0}{\lambda_B} \right) - \alpha \partial_y^2 \right] m'_y \right\}, \tag{4.3.10}$$

$$\frac{\partial m'_y}{\partial t} = -\gamma M_0 \left\{ \left[-(\beta_{\parallel} + \beta_{\perp}) + (\beta_{\parallel} + \beta_{\perp}) 2\text{sech}^2 \left(\frac{y - Y_0}{\lambda_B} \right) + \alpha \partial_y^2 \right] m'_x \right\}. \tag{4.3.11}$$

We can see that the terms in the square brackets are almost equal and opposite in sign, but with an extra factor of $-\beta_{\perp}$ in Eq. (4.3.11) (or rather, a missing factor of $\beta_{\perp}$ in Eq. (4.3.10)). We look at how to solve this equation in the next section.

4.4 Spin Wave Solutions

In order to solve Eq. (4.3.10) and Eq. (4.3.11), we'll first rewrite them in matrix form, also setting Y_0 to zero at this point,

$$\begin{aligned} \frac{1}{\gamma M_0} \begin{pmatrix} \partial_t m'_x \\ \partial_t m'_y \end{pmatrix} &= i \begin{pmatrix} 0 & -i \\ i & 0 \end{pmatrix} \left[\alpha \partial_y^2 - \beta_{\parallel} + (\beta_{\parallel} + \beta_{\perp}) 2\text{sech}^2 \left(\frac{y}{\lambda_B} \right) \right] \begin{pmatrix} m'_x \\ m'_y \end{pmatrix} \\ &\quad + \begin{pmatrix} 0 & 0 \\ \beta_{\perp} & 0 \end{pmatrix} \begin{pmatrix} m'_x \\ m'_y \end{pmatrix} + \begin{pmatrix} h(t) \\ 0 \end{pmatrix}, \\ \therefore \frac{1}{\alpha \gamma M_0} \partial_t \mathbf{m}' &= i\sigma_y \left[\partial_y^2 - \frac{\beta_{\parallel}}{\alpha} + \frac{2}{\lambda_B^2} \text{sech}^2 \left(\frac{y}{\lambda_B} \right) \right] \mathbf{m}' + \begin{pmatrix} 0 & 0 \\ \frac{\beta_{\perp}}{\alpha} & 0 \end{pmatrix} \mathbf{m}' + \\ &\quad + \begin{pmatrix} h(t) \\ 0 \end{pmatrix}, \end{aligned} \tag{4.4.1}$$

where σ_y is the Pauli matrix, and we have identified the domain wall width λ_B in the sech^2 term.

4.4.1 Homogeneous Equation

We'll first try to solve the homogeneous equation, i.e.

$$\frac{1}{\alpha \gamma M_0} \partial_t \mathbf{m}'_G = i\sigma_y \left[\partial_y^2 - \frac{\beta_{\parallel}}{\alpha} + \frac{2}{\lambda_B^2} \text{sech}^2 \left(\frac{y}{\lambda_B} \right) \right] \mathbf{m}'_G + \begin{pmatrix} 0 & 0 \\ \frac{\beta_{\perp}}{\alpha} & 0 \end{pmatrix} \mathbf{m}'_G. \tag{4.4.2}$$

We are calling the solution to the homogeneous equation $\mathbf{m}'_G$ to avoid confusion with the solution to the *inhomogeneous* equation (which we will leave as $\mathbf{m}'$). Again this is quite a long derivation, so we will continue in Appendix E. We find that there are two solutions to the homogeneous equation:

$$\mathbf{m}'_{\pm,G}(y,t) = \exp\left[\pm i \underbrace{\left(\alpha\gamma M_0 \Lambda^{\pm} \times \sqrt{1 - \frac{\beta_\perp}{\alpha\Lambda^{\pm}}}\right)}_{\omega} t\right] \underbrace{\begin{pmatrix} 1 \\ \pm i\sqrt{1 - \frac{\beta_\perp}{\alpha\Lambda^{\pm}}} \end{pmatrix}}_{\mathbf{a}^{\pm}} \varphi(y), \tag{4.4.3}$$

where the magnetisation is written as $\mathbf{m}'_{\pm,G}(y,t)$ as there is a positive and a negative solution, and the subscript G is used to show that this is the solution to the homogeneous equation (not the inhomogeneous equation). We have also highlighted the frequency[1], ω, but we'll find that $\Lambda^{\pm}$ is actually another important quantity, so rearranging, we obtain

$$\omega = \alpha\gamma M_0 \Lambda^{\pm} \times \sqrt{1 - \frac{\beta_\perp}{\alpha\Lambda^{\pm}}} \implies \Lambda^{\pm} = \frac{\beta_\perp}{2\alpha} \pm \sqrt{\frac{\beta_\perp^2}{4\alpha^2} + \frac{\Omega^2}{\alpha^2}}, \tag{4.4.4}$$

and we have introduced the dimensionless frequency $\Omega = \omega/\gamma M_0$. The function $\varphi(y)$ in Eq. (4.4.3) is the eigenfunction of the following equation:

$$\left[\partial_y^2 - \frac{\beta_\parallel}{\alpha} + \frac{2}{\lambda_B^2}\operatorname{sech}^2\left(\frac{y}{\lambda_B}\right)\right]\varphi(y) = \Lambda^{\pm}\varphi(y), \tag{4.4.5}$$

which we recognise as the Schrödinger equation with modified Pöschl-Teller potential [96–98]. This has been investigated in great detail in the topics of electromagnetism and quantum mechanics, due to the peculiar property that this potential is reflectionless for certain heights of the profile [91]. Indeed, it is well known [81] that spin waves incident on domain walls propagate through with 100% transmission, with only a phase shift. However, we are looking at this profile as a *source* of spin waves, so will we see an analogous effect?

We will solve equation Eq. (4.4.5) first in Appendix F, and once we consider the inhomogeneous equation we will be able to investigate any peculiarities of

[1] which must be equal to the driving field frequency ω in the linear regime.

this profile. We find that the solution to Eq. (4.4.5) is:

$$\varphi(y) = C^{\pm} w_1^{\pm} + D^{\pm} w_2^{\pm}, \tag{4.4.6}$$

where $C^{\pm}$ and $D^{\pm}$ are complex amplitudes, which we will be able to find expressions for later (when we solve the inhomogeneous equation), and:

$$w_1^{\pm} = (\cosh[y/\lambda_B])^{ik^{\pm}\lambda_B} F\left[-ik^{\pm}\lambda_B - 1, -ik^{\pm}\lambda_B + 2, -ik^{\pm}\lambda_B + 1; \frac{1-\tanh[y/\lambda_B]}{2}\right] \tag{4.4.7}$$

$$w_2^{\pm} = G_{12}\,(\cosh[y/\lambda_B])^{ik^{\pm}\lambda_B} \left(\frac{1-\tanh[y/\lambda_B]}{2}\right)^{ik^{\pm}\lambda_B} F\left[-1, 2, ik^{\pm}\lambda_B + 1; \frac{1-\tanh[y/\lambda_B]}{2}\right]$$
$$- G_{22}\,(\cosh[y/\lambda_B])^{ik^{\pm}\lambda_B} F\left[-ik^{\pm}\lambda_B - 1, -ik^{\pm}\lambda_B + 2, -ik^{\pm}\lambda_B + 1; \frac{1-\tanh[y/\lambda_B]}{2}\right] \tag{4.4.8}$$

$$\text{with:} \quad k^{\pm} = \sqrt{-\Lambda^{\pm} - \frac{\beta_{\parallel}}{\alpha}}, \quad \Lambda^{\pm} = \frac{\beta_{\perp}}{2\alpha} \pm \sqrt{\frac{\beta_{\perp}^2}{4\alpha^2} + \frac{\Omega^2}{\alpha^2}}, \tag{4.4.9}$$

$$G_{11} = \frac{\Gamma(-ik^{\pm}\lambda_B + 1)\Gamma(ik^{\pm}\lambda_B)}{\Gamma(-1)\Gamma(2)}, \quad G_{12} = \frac{\Gamma(-ik^{\pm}\lambda_B + 1)\Gamma(-ik^{\pm}\lambda_B)}{\Gamma(-ik^{\pm}\lambda_B - 1)\Gamma(-ik^{\pm}\lambda_B + 2)}, \tag{4.4.10}$$
$$G_{21} = \frac{\Gamma(ik^{\pm}\lambda_B + 1)\Gamma(ik^{\pm}\lambda_B)}{\Gamma(ik^{\pm}\lambda_B - 1)\Gamma(ik^{\pm}\lambda_B + 2)}, \quad G_{22} = \frac{\Gamma(ik^{\pm}\lambda_B + 1)\Gamma(-ik^{\pm}\lambda_B)}{\Gamma(-1)\Gamma(2)}.$$

The function $F[a, b, c; z]$ is the hypergeometric function [99] with parameters a, b, c and variable z, and $\Gamma(\cdots)$ is the Gamma function. The $\pm$ superscript in $w_{1,2}^{\pm}$ refers to the $\pm$ sign in $k^{\pm}$, and hence in $\Lambda^{\pm}$. We will find that k is actually the wave number (and we can see it has units of 1/length, since α is in units of length^2), so we will refer to it as such from now on.

We now have the solution to the homogeneous equation, and it is rather complicated. Let us summarise the steps from the lengthy derivation from Appendix F, so we can understand where these solutions come from and how best to interpret them. We primarily follow the derivation from Ref. [100], and the results are analogous to the standard solutions to the Schrödinger equation with a Pöschl-Teller potential. We then show that these functions tend to plane waves at the asymptotic limits — i.e. away from the domain wall region — which makes them

somewhat easier to process[2]. Next, we form a superposition of the fundamental solutions to suit our Gedankenexperiment; for waves being emitted from, rather than incident on, the P-T potential. These solutions are written as $w^{\pm}_{1,2}$ above. Finally, we use the asymptotic solutions to write out the Wronskian, which we need for the next part of the derivation: solving the inhomogeneous equation.

4.4.2 Inhomogeneous Equation

We now need to return to the inhomogeneous equation Eq. (4.4.1), repeated below:

$$\frac{1}{\alpha\gamma M_0}\partial_t \mathbf{m}' = i\sigma_y \left[\partial_y^2 - \frac{\beta_\parallel}{\alpha} + \frac{2}{\lambda_B^2}\operatorname{sech}^2\left(\frac{y}{\lambda_B}\right)\right]\mathbf{m}' + \begin{pmatrix} 0 & 0 \\ \frac{\beta_\perp}{\alpha} & 0 \end{pmatrix}\mathbf{m}' + \begin{pmatrix} \frac{h(t)}{\alpha} \\ 0 \end{pmatrix}.$$

We again keep the lengthy details in Appendix G, but let us summarise the key points. Firstly, we write the magnetisation $\mathbf{m}'$ as a sum of two contributions, which is the same approach as in [67] and Chapter 3,

$$\mathbf{m}' = \mathbf{m}'_\beta + \mathbf{m}'_h, \tag{4.4.11}$$

where $\mathbf{m}'_\beta$ is the magnetisation due to the presence of the domain wall, and $\mathbf{m}'_h$ is the magnetisation due to the external driving magnetic field. Substituting this into Eq. (4.4.1) and using the fact that $\mathbf{m}'_h$ has no y-dependence, and $\mathbf{m}'_\beta$ does not depend upon $h(t)$, we obtain two separate equations,

$$\begin{aligned}\frac{1}{\alpha\gamma M_0}\partial_t \mathbf{m}'_\beta = i\sigma_y \left[\partial_y^2 - \frac{\beta_\parallel}{\alpha} + \frac{2}{\lambda_B^2}\operatorname{sech}^2\left(\frac{y}{\lambda_B}\right)\right]\mathbf{m}'_\beta + i\sigma_y \frac{2}{\lambda_B^2}\operatorname{sech}^2\left(\frac{y}{\lambda_B}\right)\mathbf{m}'_h + \\ + \begin{pmatrix} 0 & 0 \\ \frac{\beta_\perp}{\alpha} & 0 \end{pmatrix}\mathbf{m}'_\beta,\end{aligned} \tag{4.4.12}$$

$$\frac{1}{\alpha\gamma M_0}\partial_t \mathbf{m}'_h = \begin{pmatrix} 0 & -\frac{\beta_\parallel}{\alpha} \\ \frac{\beta_\parallel+\beta_\perp}{\alpha} & 0 \end{pmatrix}\mathbf{m}'_h + \begin{pmatrix} \frac{h(t)}{\alpha} \\ 0 \end{pmatrix}. \tag{4.4.13}$$

[2]This is necessary for representing the hypergeometric functions properly in *Mathematica*, and there is a discussion in the Appendix of how to do this.

We solve Eq. (4.4.13) in Fourier space to obtain:

$$\tilde{\mathbf{m}}'_h = \frac{1}{-\Omega^2 + \beta_\parallel(\beta_\parallel + \beta_\perp)} \begin{pmatrix} -i\Omega\tilde{h}(\omega) \\ (\beta_\parallel + \beta_\perp)\tilde{h}(\omega) \end{pmatrix}, \tag{4.4.14}$$

where the tilde's indicate that this is the Fourier transform of the "un-tilde'd" quantity. The quantity $\tilde{h}(\omega)$ is the Fourier transform of $h(t)$, and has a magnitude of h.

The inhomogeneous equation that we thus need to solve is Eq. (4.4.12) in Fourier space:

$$i\sigma_y\left[\partial_y^2 - \frac{\beta_\parallel}{\alpha} + \frac{2}{\lambda_B^2}\operatorname{sech}^2\left(\frac{y}{\lambda_B}\right)\right]\tilde{\mathbf{m}}'_\beta + \begin{pmatrix} \frac{i\Omega}{\alpha} & 0 \\ \frac{\beta_\perp}{\alpha} & \frac{i\Omega}{\alpha} \end{pmatrix}\tilde{\mathbf{m}}'_\beta = -i\sigma_y\frac{2}{\lambda_B^2}\operatorname{sech}^2\left(\frac{y}{\lambda_B}\right)\tilde{\mathbf{m}}'_h = \mathbf{r}(y). \tag{4.4.15}$$

We already know the solution to the homogeneous form of this equation; it is the Fourier-transform of $\mathbf{m}'_{\pm,G}$, which is written as

$$\tilde{\mathbf{m}}'_{\pm,G} = \begin{pmatrix} 1 \\ \pm i\sqrt{1 - \frac{\beta_\perp}{\alpha\Lambda^\pm}} \end{pmatrix}\varphi(y). \tag{4.4.16}$$

We then solve the inhomogeneous equation Eq. (4.4.15) by using the method of variation of parameters ([101], pp. 99-102), and the solution can be written as

$$\begin{aligned}\tilde{\mathbf{m}}'_\beta = \mathbf{a}^+\Bigg\{ & C^+w_1^+ + D^+w_2^+ + \\ & + \frac{NA}{W^+}\left[w_1^+\int_{y_0}^{y}\frac{2}{\lambda_B^2}\operatorname{sech}^2\left(\frac{y'}{\lambda_B}\right)w_2^+\,dy' - w_2^+\int_{y_0}^{y}\frac{2}{\lambda_B^2}\operatorname{sech}^2\left(\frac{y'}{\lambda_B}\right)w_1^+\,dy'\right]\Bigg\} + \\ & + \mathbf{a}^-\Bigg\{ C^-w_1^- + D^-w_2^- + \\ & + \frac{NB}{W^-}\left[w_1^-\int_{y_0}^{y}\frac{2}{\lambda_B^2}\operatorname{sech}^2\left(\frac{y'}{\lambda_B}\right)w_2^-\,dy' - w_2^-\int_{y_0}^{y}\frac{2}{\lambda_B^2}\operatorname{sech}^2\left(\frac{y'}{\lambda_B}\right)w_1^-\,dy'\right]\Bigg\},\end{aligned} \tag{4.4.17}$$

where y_0 is an arbitrary point (we choose $y_0 = 0$), y is the value where we are seeking the solution, and $W^\pm = w_1^\pm\partial_y(w_2^\pm) - w_2^\pm\partial_y(w_1^\pm)$ is the Wronskian, which

was calculated in Appendix F.4 Eq. (F.4.4) as

$$W^{\pm} = \frac{ik^{\pm}G_{12}}{2^{ik^{\pm}\lambda_B}}. \tag{4.4.18}$$

Note that W^{+} uses Λ^{+} in k^{+}, and W^{-} uses Λ^{-} in k^{-}. The other variables in Eq. (4.4.17) are

$$\mathbf{a}^{\pm} = \begin{pmatrix} 1 \\ \pm i\sqrt{1 - \frac{\beta_\perp}{\alpha\Lambda^{\pm}}} \end{pmatrix}, \tag{4.4.19}$$

$$N = \frac{1}{-\frac{2}{i\Omega}\sqrt{\frac{\beta_\perp^2}{4} + \Omega^2}} \frac{\tilde{h}(\omega)}{-\Omega^2 + \beta_\parallel(\beta_\parallel + \beta_\perp)}, \tag{4.4.20}$$

$$A = \frac{\beta_\perp}{2} + \beta_\parallel - \sqrt{\frac{\beta_\perp^2}{4} + \Omega^2}, \tag{4.4.21}$$

$$B = -\frac{\beta_\perp}{2} - \beta_\parallel - \sqrt{\frac{\beta_\perp^2}{4} + \Omega^2}, \tag{4.4.22}$$

and we defined $w_1^{\pm}$ and $w_2^{\pm}$ earlier in Eqs. (4.4.7) and (4.4.8), respectively.

In due course, we investigate which solution of $\Lambda^{\pm}$ gives a real wave number, but at the moment we'll just keep both solutions of $k^{\pm}$ for generality.

4.4.3 Solution at Asymptotic Limits

We have not yet found expressions for $C^{\pm}$ and $D^{\pm}$, which are the complex amplitudes of the two solutions to the Schrödinger-like equation, introduced in Eq. (4.4.6). We can avoid the complication of the hypergeometric functions by looking at the form of the magnetisation away from the domain wall region, and use this to find the amplitudes $C^{\pm}$ and $D^{\pm}$. We know that the hypergeometric functions tend to plane waves away from the domain wall region, and so the spin waves must do as well. We will write the magnetisation $\tilde{\mathbf{m}}'_\beta$ at the asymptotic limits as

$$\lim_{y\to\pm\infty} \tilde{\mathbf{m}}'_\beta \approx \mathbf{S}^{+}(\omega)e^{\pm ik^{+}y} + \mathbf{S}^{-}(\omega)e^{\pm ik^{-}y}, \tag{4.4.23}$$

where the $\pm$ in the limit of $y \to \pm\infty$ corresponds to the $\pm$ in the exponent, since $e^{+ik^{\pm}y}$ is a right-travelling wave, and $e^{-ik^{\pm}y}$ is a left-travelling wave. We also suppose that there might be different amplitudes for the different wave numbers,

and that their contributions can be summed. So, we need to use the above condition in Eq. (4.4.17), along with the asymptotic expansions of $w_{1,2}^{\pm}$ from F.4 which are:

$$\lim_{y\to-\infty} w_1^{\pm} = \frac{G_{11}}{2^{ik^{\pm}\lambda_B}} e^{-ik^{\pm}y} + \frac{G_{12}}{2^{ik^{\pm}\lambda_B}} e^{+ik^{\pm}y}, \tag{4.4.24a}$$

$$\lim_{y\to+\infty} w_1^{\pm} = \frac{e^{+ik^{\pm}y}}{2^{ik^{\pm}\lambda_B}}, \tag{4.4.24b}$$

$$\lim_{y\to-\infty} w_2^{\pm} = \frac{e^{-ik^{\pm}y}}{2^{ik^{\pm}\lambda_B}}, \tag{4.4.24c}$$

$$\lim_{y\to+\infty} w_2^{\pm} = \frac{G_{12}}{2^{ik^{\pm}\lambda_B}} e^{-ik^{\pm}y} - \frac{G_{22}}{2^{ik^{\pm}\lambda_B}} e^{+ik^{\pm}y}. \tag{4.4.24d}$$

This is carried out in Appendix H, and we find:

$$C^+ = -I_{2,-}^+ \frac{NA}{\frac{ik^+G_{12}}{2^{ik^+\lambda_B}}}, \tag{4.4.25a}$$

$$D^+ = I_{1,+}^+ \frac{NA}{\frac{ik^+G_{12}}{2^{ik^+\lambda_B}}}, \tag{4.4.25b}$$

$$\mathbf{S}^+(\omega) = \mathbf{a}^+ \frac{NA}{ik^+G_{12}} \int_{-\infty}^{+\infty} \frac{2}{\lambda_B^2} \operatorname{sech}^2\left(\frac{y'}{\lambda_B}\right) w_1^+ \, \mathrm{d}y' \tag{4.4.25c}$$

$$= \mathbf{a}^+ \frac{NA}{ik^+G_{12}} \int_{-\infty}^{+\infty} \frac{2}{\lambda_B^2} \operatorname{sech}^2\left(\frac{y'}{\lambda_B}\right) w_2^+ \, \mathrm{d}y', \tag{4.4.25d}$$

$$C^- = -I_{2,-}^- \frac{NB}{\frac{ik^-G_{12}}{2^{ik^-\lambda_B}}}, \tag{4.4.26a}$$

$$D^- = I_{1,+}^- \frac{NB}{\frac{ik^-G_{12}}{2^{ik^-\lambda_B}}}, \tag{4.4.26b}$$

$$\mathbf{S}^-(\omega) = \mathbf{a}^- \frac{NB}{ik^-G_{12}} \int_{-\infty}^{+\infty} \frac{2}{\lambda_B^2} \operatorname{sech}^2\left(\frac{y'}{\lambda_B}\right) w_1^- \, \mathrm{d}y' \tag{4.4.26c}$$

$$= \mathbf{a}^- \frac{NB}{ik^-G_{12}} \int_{-\infty}^{+\infty} \frac{2}{\lambda_B^2} \operatorname{sech}^2\left(\frac{y'}{\lambda_B}\right) w_2^- \, \mathrm{d}y', \tag{4.4.26d}$$

where we call

$$I^{\pm}_{l,-} = \int_0^{-\infty} \frac{2}{\lambda_B^2}\text{sech}^2\left(\frac{y'}{\lambda_B}\right) w_l^{\pm}\, \mathrm{d}y', \qquad \text{with:} \quad l = 1, 2, \tag{4.4.27a}$$

$$I^{\pm}_{l,+} = \int_0^{+\infty} \frac{2}{\lambda_B^2}\text{sech}^2\left(\frac{y'}{\lambda_B}\right) w_l^{\pm}\, \mathrm{d}y', \qquad \text{with:} \quad l = 1, 2, \tag{4.4.27b}$$

so that the subscript "$l, +$" or "$l, -$" will denote the upper limit of the integral of $+\infty$ or $-\infty$, respectively.

4.4.4 The Wave Number

As a final note to this section, we look more closely at $k^{\pm}$, defined in Eq. (4.4.9), to confirm which solution is real and which is imaginary:

$$k^{\pm} = \sqrt{-\Lambda^{\pm} - \frac{\beta_{\parallel}}{\alpha}}, \quad \text{where:} \quad \Lambda^{\pm} = \frac{\beta_{\perp}}{2\alpha} \pm \sqrt{\frac{\beta_{\perp}^2}{4\alpha^2} + \frac{\Omega^2}{\alpha^2}}.$$

We can see that $-\Lambda^{+} - \frac{\beta_{\parallel}}{\alpha}$ will always be negative, so k^{+} is always imaginary. For the Λ^{-} solution, we get a real wave number for:

$$-\left(\frac{\beta_{\perp}}{2\alpha} + \frac{\beta_{\parallel}}{\alpha}\right) < \sqrt{\frac{\beta_{\perp}^2}{4\alpha^2} + \frac{\Omega^2}{\alpha^2}} \quad \Longrightarrow \quad \underline{\Omega > \sqrt{\beta_{\parallel}(\beta_{\parallel} + \beta_{\perp})}}. \tag{4.4.28}$$

Although only the real wave number (k^{-}) solutions will give us propagating waves beyond the domain wall, we will retain the imaginary wave number terms (we will see that they are useful in the next section).

4.5 Analysis of Results

In this section, we confirm the form of the dispersion relation, plot the form of the magnetisation, and analyse the behaviour of the spin waves in and around the domain wall region. We will use the following values of the material parameters, typical of a Permalloy-like material: $M_0 = 800$ erg·G^{-1}·cm^{-3} [74], $\gamma = 1.76 \times 10^7$ rad Hz·G^{-1}, $\alpha = 3.125 \times 10^{-12}$ cm^2 [23], $\beta_{\parallel} = 0.1$ ($K = 32 \times 10^3$erg·cm^{-3}), $\beta_{\perp} = 10$ ($K = 32 \times 10^5$erg·cm^{-3}) [75, 102]. This gives a domain wall width $\lambda_B = 5.6$ nm (although its full extent is around 40 nm), and a minimum driving frequency (required for k^{-} to be real) of $f_{\text{min}} = 2.3 \times 10^9$ Hz, but we will use a frequency

of $f = 5 \times 10^{10} = 50$ GHz. The resulting spin wave wavelength away from the domain wall is 26 nm. Finally, the excitation field is harmonic and uniform, with amplitude of 1 Oe.

4.5.1 Dispersion Relation

We will firstly check that the dispersion relation (f vs. k^-) is as we would expect; quadratic, for exchange spin waves (as we saw in Chapter 2, Eq. (2.5.4)). This is shown in Figure 4.4. We will not look at the k^+ solution because it is always imaginary. We can see that the dispersion is indeed quadratic, confirmed in the *Mathematica* calculations[3]. In addition, the minimum frequency required by Eq. (4.4.28) is $f_{\min} \approx 2.3 \times 10^9$ Hz, and the *Mathematica* code and graph confirms this.

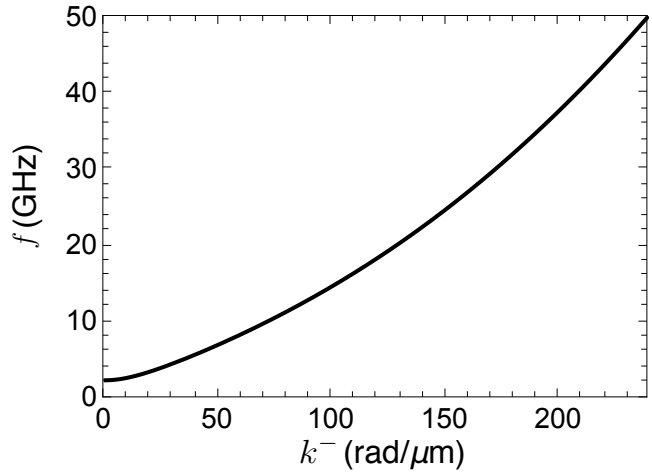

FIGURE 4.4: Dispersion relation, f vs. wave number k^-.

4.5.2 Form of the Magnetisation in the Rotated Frame

Let us now plot the entire solution for $\tilde{\mathbf{m}}'_\beta$, which is given by Eq. (4.4.17). We will first understand the contribution of the imaginary wavevector terms. Then, we can use the full solution (both real and imaginary terms) to compare the x and y components. Recall our convention that quantities are primed in the rotated reference frame, and also that the tilde denotes a Fourier-transformed quantity (i.e. it is written as a function of frequency).

[3]For the interested reader, the fit equation is $2.06516 + 6.97251 \times 10^{-8}k + 5.46103 \times 10^{-16}k^2$, (where k is k^-, written this way to avoid confusion with the squared term) and is a very close match except as $k \to 0$, which is out of the exchange regime anyway.

Contribution of the Imaginary Wavevector Components

Now we see what effect the k^+ contributions have on the final solution. Recall that $\tilde{\mathbf{m}}'_\beta$ defined in Eq. (4.4.17) contains variables with either a "$-$" superscript or "$+$" superscript, and that determines if k^- or k^+ is used, respectively. In Fig. 4.5, we plot the real and imaginary components of this expression with or without the "$+$" terms.

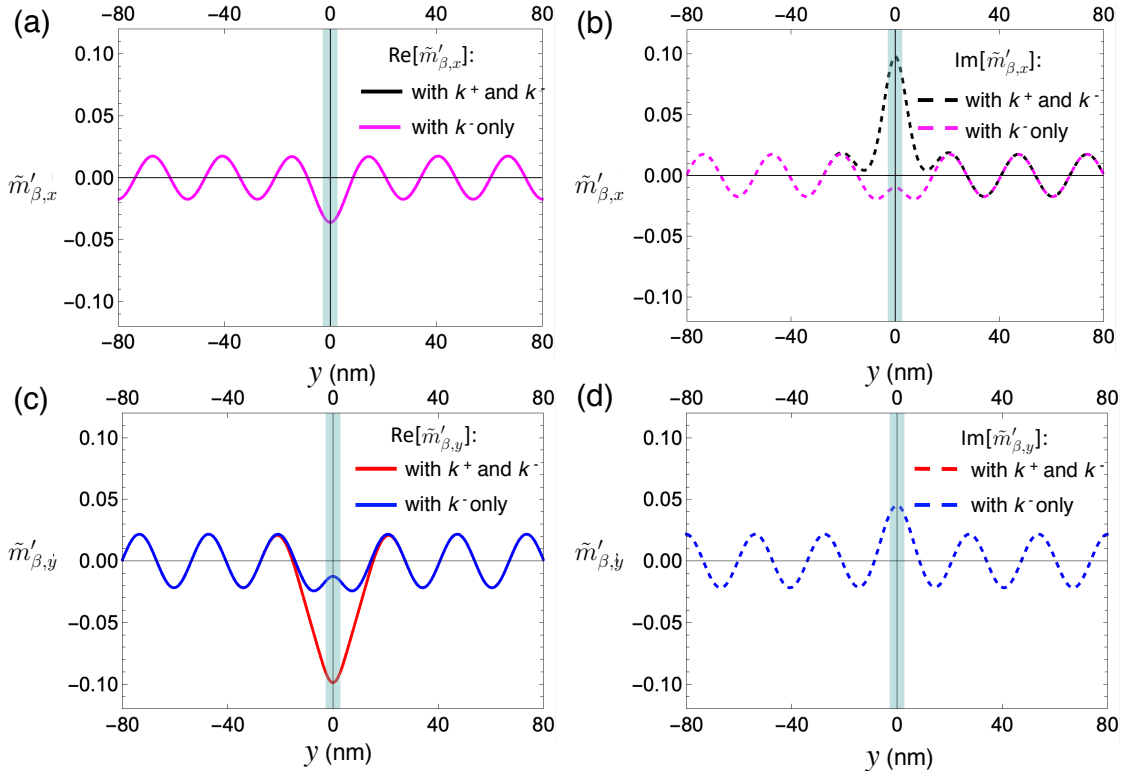

FIGURE 4.5: Comparison of the real (a, c) and imaginary (b, d) parts of $\tilde{\mathbf{m}}'_\beta$ defined in Eq. (4.4.17) with and without the terms containing k^+. In (a) and (b) the $\tilde{m}'_{\beta,x}$ component is shown, the black line contains both k^- and k^+ contributions, and the magenta line contains only k^- contributions. In (c) and (d) the $\tilde{m}'_{\beta,y}$ component is shown, the red line contains both k^- and k^+ contributions, and the blue line contains only k^- contributions. In each figure, the domain wall region defined by width λ_B is shown in turquoise.

In Figure 4.5 panels (a) and (d), both plots perfectly overlay each other, so only one of the lines is visible. This is also the case for (b) and (c) away from the domain wall. We can see that the contribution from k^+ is to affect the form of the magnetisation within and close to the domain wall. We thus retain the k^+ contributions in the following investigations, to ensure the magnetisation is represented accurately.

4.5.3 Comparision of x' and y' Components

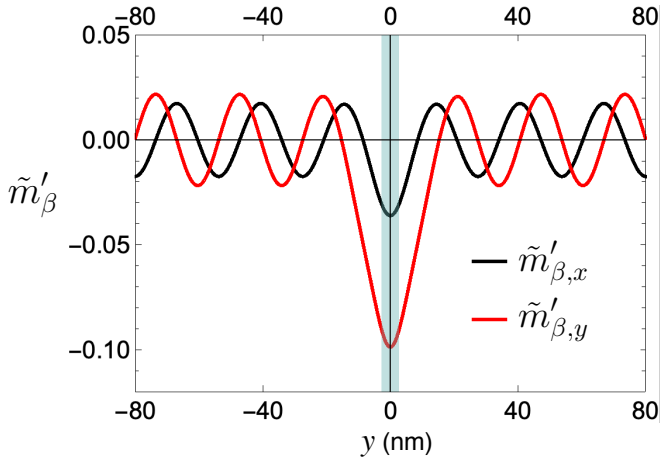

FIGURE 4.6: $\tilde{m}'_{\beta,x'}$ (black) and $\tilde{m}'_{\beta,y'}$ (red) vs. y.

Figure 4.6 shows the real part of the x' and y' components of the magnetisation. We see that the magnetisation is oscillating sinusoidally, and symmetrically about the domain wall centre. In addition, the x' and y' components are out of phase with each other; the x' component leading the y' component with a phase difference of $\pi/2$.

Importantly, Figure 4.6 shows the amplitude of the y' component of the magnetisation is larger than the amplitude of the x' component. As a result, the magnetisation has an elliptical precession, with a reduced amplitude in the out-of-plane, x' component, compared to the in-plane, y' component. It is energetically-favourable for the magnetisation to align in the $y-z$ plane, and so it is reasonable that the amplitude of precession in the out-of-plane direction is suppressed in this way.

4.5.4 Time-Dependent Precession

To effectively introduce time dependence into the *Mathematica* model, we need to multiply our functions $\tilde{m}'_{\beta,x'}$ and $\tilde{m}'_{\beta,y'}$ by e^{-iv}, where v is the phase which varies from $0 \rightarrow 2\pi$, and then take the real part[4].

Remember that we have been working in the rotated frame - in order to see what the domain wall is actually doing, we now need to convert back to the 'lab'

[4]We do not concern ourselves with the actual time elapsed in this model; since damping is neglected, the precession will oscillate with a period of 2π indefinitely.

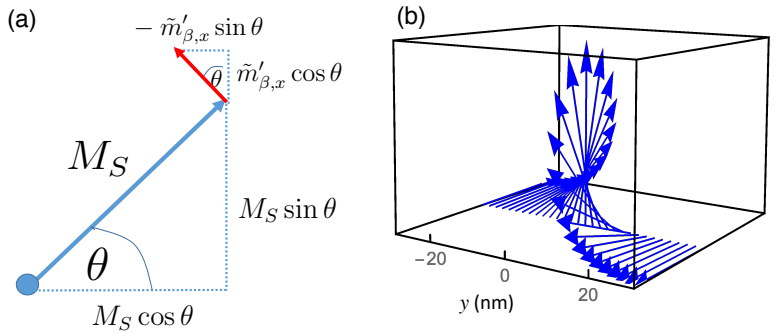

FIGURE 4.7: (a) Diagram showing the calculation of the static (blue) and dynamic (red) magnetisation components in the 'lab' or unprimed frame. Note that the horizontal components here in the z direction, vertical is x, and y is unchanged from y'. The central dot denotes the fixed position along the $x = z = 0$ line. (b) Plot of the static magnetisation in the unprimed (lab) frame.

frame. We convert via simple trigonometry, and choose to fix the end of the magnetisation arrows (as opposed to the tip, or the centre or anywhere else). The calculated angles are shown in Figure 4.7 (a) and the resulting static magnetisation is shown along the y direction in (b). To add the precession on top of this arrangement, we then need to convert $\tilde{m}'_{\beta,x'}$, which is perpendicular to the static magnetisation M_0, by resolving into its x (vertical) and z (horizontal) components. This is also shown in Figure 4.7, where $\tilde{m}'_{\beta,x'}$ is the red arrow.

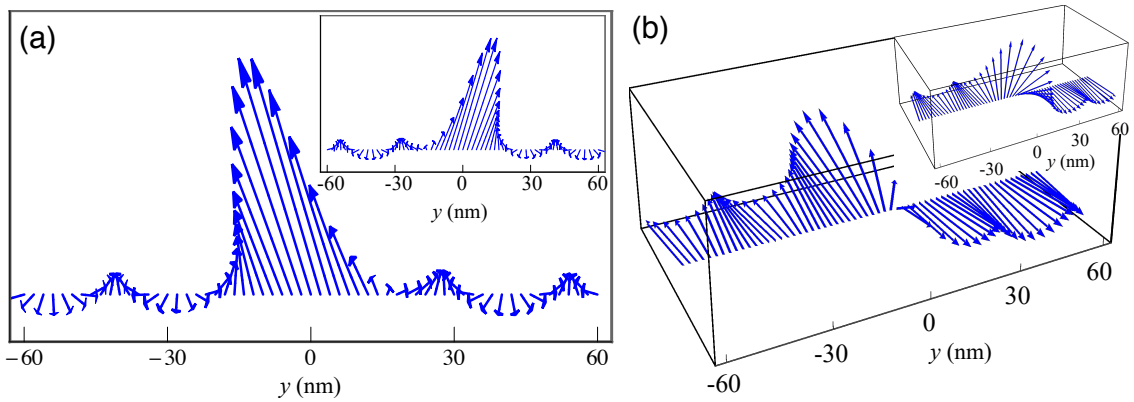

FIGURE 4.8: Visualisation of the magnetisation vectors (which have time-dependence described by $\tilde{m}_\beta$) in the unrotated frame, with (a) side $(x - y)$ projection and (b) axonometric view. Both for phase $v = 0$ (main image) and $v = \pi$ (inset). The y position and orientation of the vectors are accurate, while the static magnetisation length has been arbitrarily reduced for clarity.

In Figure 4.8, we visualise the precession of the magnetisation in the unprimed

(lab) frame. We can see that the magnetisation precession in the domain wall has a larger amplitude than in the adjacent domains. Moreover, the domain wall centre, which is the position of the magnetisation with the largest x component, appears to move back and forth along the y direction.

The apparent domain wall motion is not however the source of the emitted spin waves. Rather, this motion is the small amplitude precession given by the solution of the linearized Landau-Lifshitz equation, just as we saw in Chapter 3, and is of the same order as the emitted spin waves. The full non-linear Landau-Lifshitz equation would need to be solved to account for any interaction between different precessional modes, i.e. this would be at the next order. Examples of a non-linear generation of spin waves from a domain wall can be found in, for example, Refs. [82, 103] where the domain wall oscillations at frequency ω were observed to emit spin waves at twice the frequency, 2ω. This theory suggests that the spin wave emission from domain walls, at a frequency equal to that of the driving magnetic field [84, 85] or spin-polarized current [86] should rather be interpreted as a linear excitation due to the magnetic inhomogeneity [60] (or rather, “graded magnonic index" [12]) created by the domain wall, when excited by a uniform magnetic field.

4.5.5 Pöschl-Teller Potential Barrier vs. Potential Well

We know that the dynamics of a Bloch domain wall, in the linear regime, are described by a Schrödinger-like equation with Pöschl-Teller (P-T) potential well, given in Eq. (4.4.15). It would be interesting to see how these results compare to a P-T potential barrier[5], and through doing so, we discover that it is actually non-trivial that a domain wall emits spin waves. To elucidate this, we refer to the theory describing the Pöschl-Teller potential well for *incident* waves [91] - it is well-known to have “special" values of height at which it becomes reflectionless. If we write the profile as

$$\beta_l(y) = -\frac{l}{\lambda_B^2}\text{sech}^2\left(\frac{y}{\lambda_B}\right), \quad l = n(n+1), \tag{4.5.1}$$

the profiles that are reflectionless for incident waves can be identified as those with integer n. We do not consider incoming waves in this work, so we now use

[5] A Pöschl-Teller potential barrier would have to be formed by a suitable modification of the anisotropy, unless it is serendipitously formed of another natural, but as yet unknown/unexplored, magnetic structure.

Eq. (4.4.26c) to investigate how changing l affects the *emission* of spin waves from the profile.

In our *Mathematica* code, we need to change the height of the profile from 2 to l in the integrals, and we will also need to change s (introduced[6] in Appendix F) so that

$$s = \frac{1}{2}\left(-1 + \sqrt{1 - 4l\frac{1}{\lambda_B^2}\lambda_B^2}\right) = \frac{1}{2}\left(-1 + \sqrt{1-4l}\right). \tag{4.5.2}$$

The spin wave amplitude away from the domain wall is calculated using Eq. (4.4.26c) for both the well and barrier, and the results are shown in Figure 4.9 (a). The height l is swept through from negative values (which represent a potential barrier - there are no solutions for n in this case) through to positive values (a potential well, which has corresponding values of n). We can observe for the potential well that at certain values of l, which correspond to *even* n, the spin wave emission is zero, and the spin waves are confined within the domain wall region. Furthermore, profiles with odd n are local maxima. So, the presence of $\text{sech}^2(y/\lambda_B)$ in both the potential and the driving term in Eq. (4.4.15) leads to a different set of "special" values, corresponding to either strong wave emission or its complete suppression. The particular value of $l = 2$ ($n = 1$) for a domain wall happens to correspond to a local maximum condition for spin wave emission. However, a potential barrier of any height generates spin waves much more efficiently than the potential well solutions.

The peak at around $l = -3$ generates spin waves most efficiently compared to any other profile height, although this optimal value (along with the spin wave amplitude generally) depends on the frequency for a given set of the other parameters, as we show in Figure 4.9 (b). The minimum value of f in panel (b) corresponds to a wavelength $\lambda \approx 50\,\text{nm}$, which is approximately the upper wavelength limit of the exchange regime. We can see that the spin wave amplitude for all values of l (except for the zero conditions, of course) is larger for lower frequencies and thus smaller wave numbers. We explore this in more detail in the next section. In addition, we find that the spin waves emitted from a potential barrier always have a higher amplitude that those emitted from a potential well, for all values of frequency. The peak value of the amplitude, for a potential barrier, shifts slightly towards more negative values of l with increasing frequency,

[6] The parameter s was defined in Eq. (F.1.7), and is written in the hypergeometric functions in Eq. (F.1.19). For a P-T potential height of 2, $s = 1$, so we have not had to write it explicitly in the main text thus far.

although it does not exceed $l = -5$ in the frequency range we have used.

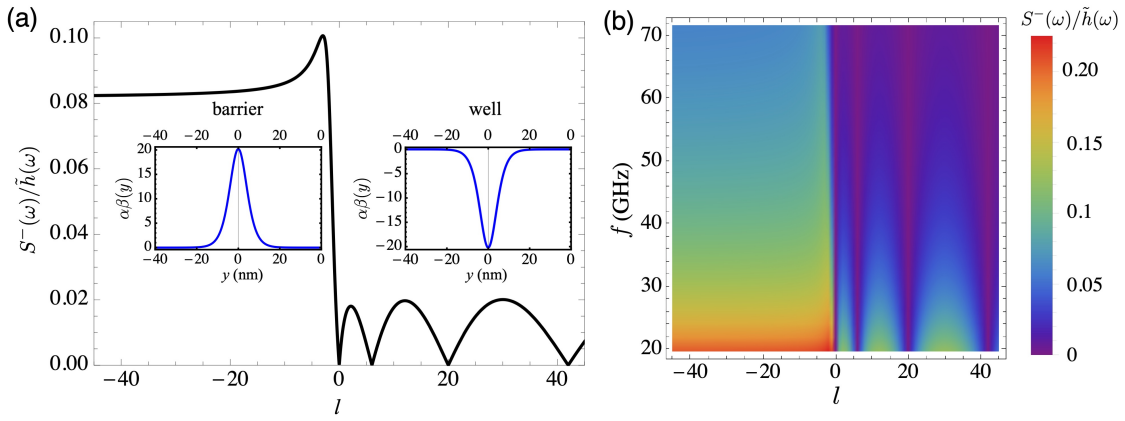

FIGURE 4.9: Spin wave amplitude vs. height of the P-T profile, for (a) $\Omega = 22$ (corresponding to $f \sim 50$ GHz) and (b) a range of frequencies from $8.7 \lesssim \Omega \lesssim 32$ (corresponding to $20 \lesssim f \lesssim 72$ GHz). Zeros of emission correspond to even values of n. In (a), the shape of the potentials is shown for $l = -2$ for the barrier (left inset) and $l = 2$ for the well (right inset).

4.5.6 Spin Wave Amplitude vs. Wave Number

Figure 4.10 compares the frequency dependence of the x' and y' components of the spin wave amplitude $\mathbf{S}^-(\omega)$, for both a P-T potential well (domain wall, $l = 2$) and barrier ($l = -2$). For comparison, we include the magnitude of the uniform precession $\tilde{\mathbf{m}}_h$, excited by the same field (defined in Eq. (4.4.14)). The start of the exchange regime (i.e. where the wavelength <50 nm) is also highlighted. The difference between $S^-_{x'}(\omega)$ and $S^-_{y'}(\omega)$ at small wave numbers shows that the precession is elliptical, with the ellipticity decreasing with increasing frequency. This difference in amplitudes arises purely due to the difference in the components of $\mathbf{a}_-$, defined in Eq. (4.4.19). We can see that, for large Ω', Λ^- is large, thus $\frac{\beta_\perp}{\alpha\Lambda^-}$ is small, so

$$\lim_{\Omega'\to\infty} \mathbf{a}^- = \lim_{\Omega'\to\infty} \begin{pmatrix} 1 \\ \pm i\sqrt{1 - \frac{\beta_\perp}{\alpha\Lambda^\pm}} \end{pmatrix} \approx \begin{pmatrix} 1 \\ -i \end{pmatrix},$$

and the amplitudes become equal; we recover the circular precession.

The frequency dependences of the precession amplitude far from the domain wall are different for propagating spin waves $\mathbf{S}^-(\omega)$ and the uniform precession $\tilde{\mathbf{m}}'_h$. As a result, for a domain wall (more generally, a P-T *well* profile) the out of

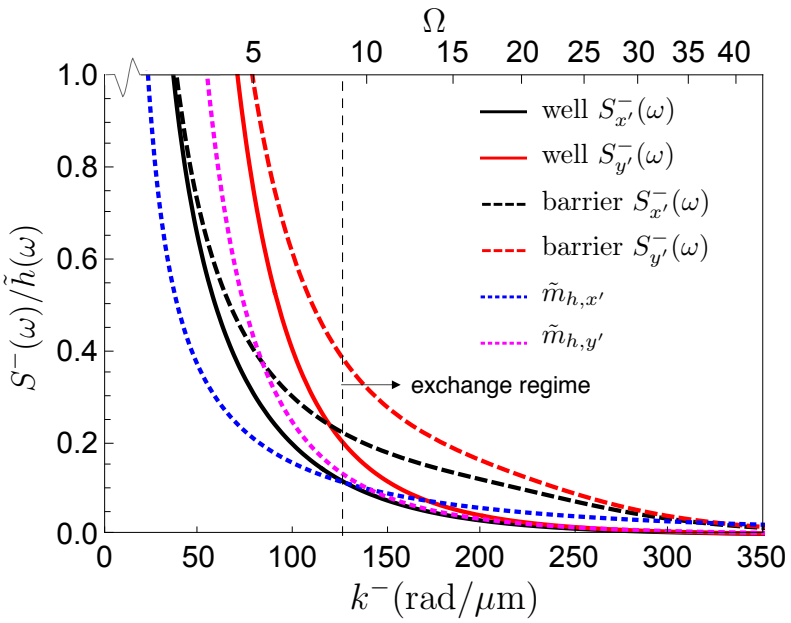

FIGURE 4.10: Amplitude of the spin waves generated by a P-T potential well (solid lines) and potential barrier (dashed lines), compared to the amplitude of uniform precession induced by the external field (dotted lines), showing x' and y' components (colours indicated on the graph). All quantities are normalized by the external field $\tilde{h}(\omega)$. $\mathbf{S}^-(\omega)$ is a function of k^- (bottom axis) and thus Ω (top axis), and $\tilde{\mathbf{m}}_h$ is only a function of Ω.

plane component $S^-_{x'}(\omega)$ is only larger in amplitude than $\tilde{\mathbf{m}}'_h$ at low frequencies, i.e., for $k^- < 125(\mu\mathrm{m})^{-1}$. However, for a P-T *barrier* profile, $S^-_{x'}(\omega)$ exceeds $\tilde{\mathbf{m}}'_h$ up to much higher frequencies, i.e., for $k^- < 300(\mu\mathrm{m})^{-1}$. This shows that, despite domain walls being such efficient magnonic emitters, an even better efficiency could be achieved by tailoring the local effective magnetic field (through modification of e.g. the anisotropy strength [67, 92, 104]) to form a P-T potential barrier instead.

Another point to note is that the frequency dependence of $\tilde{m}'_{h,x}$ is not the same as $\tilde{m}'_{h,y}$, and so we also observe a crossover between these quantities at around $k = 140(\mu\mathrm{m})^{-1}$, corresponding to $\Omega = \beta_\parallel + \beta_\perp$ in equation (4.4.14). This means that for low frequencies, the uniform precession is elliptical along the y direction, and as the frequency increases, the precession becomes circular, gradually becoming more elliptical in the x' direction when $\Omega \gg \beta_\parallel + \beta_\perp$. Importantly, the amplitude of the precession still decreases with increasing frequency. So, although the precession is restricted in the y' direction, it is not becoming enhanced in x', only less restricted in comparison (as we do not have a fast-switching field to restrict its motion in that direction).

Finally, it is worth comparing these results briefly to those for a rectangular potential, explored in the previous Chapter. The material parameters and main value of frequency used in each case are the same, except the material in Chapter 3 was considered to be an infinite slab, since we did not consider surface effects / competing anisotropy contributions (as we did in this Chapter). So, looking at Eq. (3.2.3) and Eq. (4.2.1) we can see that there are quite different contributions to the energy density in both cases, and so the results will only be approximately comparable.

The first feature to compare is how the spin wave emission amplitude depends on the wave number, comparing Fig. 3.3 for the rectangular potential barrier with Fig. 4.10 for the P-T potential. We see zeros in emission for the rectangular potential when $ak_1 = 2n\pi$. For the P-T potential barrier or well, there are no k^--dependent zeros of spin wave emission (when the potential height is not an even multiple of n, as per Eq. (4.5.1)). We would have to analyse other potentials to confirm this, but it may be related to the special property of the P-T potential; waves are transmitted through the potential (in our case, outwards in both directions) with 100% probability, for any value of frequency.

Next, we do observe a similar behaviour in both cases when we see how the emission amplitude depends on the height of the barrier, comparing Fig. 3.4 for the rectangular potential with Fig. 4.9 for the P-T potential. In both cases, we observe that a potential barrier is a more efficient emitter than a potential well. Although, the P-T potential barrier is significantly more efficient than the well, and the rectangular potential appears to be more efficient than either P-T potentials, if it is fair to compare the spin wave amplitudes. It is also interesting to note that the zeros of emission observed in these images for certain values of the potential height appear to have very different origins for either form of the potential. For the rectangular potential, the zeros occur when β_1 enables k_1 to fulfill the condition $ak_1 = 2n\pi$, i.e. when the potential width is a multiple of half a wavelength. As a result, the position of the zeros shifts with frequency, for this condition to still be fulfilled. For the P-T potential, however, the zeros are not a function of frequency, which implies that they are not related to standing waves in the same way as in a rectangular potential. So it seems that the P-T potential is either perfectly emitting or perfectly confining (i.e. for all values of frequency), for certain choices of the potential height, as discussed in Ref. [91].

4.6 Conclusions

In this Chapter, the origin and behaviour of exchange spin waves generated by a Bloch domain wall has been analysed, when excited by a uniform, harmonic magnetic field. The equations which describe the domain wall in the rotated frame are an interesting twist on the usual Schrödinger equation with a Pöschl-Teller potential, studied in detail in quantum mechanics. Since the excitation of the spin waves relies on the harmonic field combined with the presence of the domain wall itself, we see the P-T potential in the driving term of the Schrödinger-like equation. The interesting effect of this is observed when varying the "height" l of the potential, to reveal three things: firstly, that the natural "height" of a domain wall is a local maximum in terms of the spin wave emission amplitude. Secondly, certain heights of the profile correspond to complete suppression of spin wave emission from the barrier. The values of l which lead to this suppression do not correspond to the same values which allow perfect transmission in the usual P-T potential case (without the driving term, for incoming waves only). In addition, a potential barrier would be a much more efficient spin wave emitter, as we saw already in Chapter 3.

Another important point to emphasise is that the spin wave emission is the result of a linear theory, which implies that the apparent oscillation of the domain wall is not the source of spin waves. We also find the emission of spin waves is at the frequency of the driving uniform harmonic microwave field, and with amplitude scaling linearly with the field strength. This is clearly the result of a linear process, and thus the domain wall motion is not the cause of spin wave emission here. This contradicts the usual supposition that the domain wall is oscillating and thus emitting spin waves, for example in Refs. [84–86].

More generally, and in corroboration with the results of the previous Chapter, we have found that the domain wall acts as a source of spin waves simply because it is an inhomogeneity in the magnetisation, or rather a "graded magnonic index". This is the only source of spin waves in an otherwise uniform magnetisation / magnetic field landscape. The pumping magnetic field is of course required to inject energy into the system, but this field can be uniform as long as there is some form of material inhomogeneity present. This supports other recent studies which offer an alternative method of spin wave generation; instead of having to fabricate nanoscale antennas and excite spin waves via their local field, one can form a local inhomogeneity in the material (with its own local inhomogeneous field) and excite spin waves from it with a uniform (harmonic) global field. This

will be applicable for any other form of wave, of course, since it is just a wave phenomenon. Thus, although this theory is valid for exchange spin waves emitted from domain walls, it should also predict/explain the spin wave emission from other magnetic features, in any other regime (magnetostatic backward-volume, dipole-exchange,...).

Chapter 5

Graded Index Lenses for Spin Wave Focusing

5.1 Introduction

So far, we have investigated how profiles of the anisotropy or magnetisation — which have generally been described as a magnonic refractive index profile — can act as a source of spin waves when excited by a uniform, harmonic source. Now, we consider the more traditional use of a refractive index profile in controlling the propagation of incoming (spin) waves.

In this Chapter, we consider rotationally-symmetric refractive index profiles which are designed to focus spin waves. We primarily investigate the Luneburg lens [105], which is designed to focus a plane wave to a point, or conversely, to convert a point source to a plane wave. We also investigate how an index profile of parabolic shape can have similar focusing abilities. We make a parabolic fit to the Luneburg lens, and are able to vary the focusing strength and the position of the focal point by changing the 'height' of the profile. We use this to understand how effective the Luneburg lens is, and how robust it is to deviations in the profile.

The subject of spin wave lensing has been gaining interest recently, and many different techniques have been used to create a lensing effect. Simple magnonic lens designs with sharp boundaries were demonstrated in Refs. [106, 107]. However, such abrupt changes in the refractive index induce unnecessary reflection of spin waves, which is partly avoided in the case of smoothly changing a material parameter. Alternatively, focusing can be achieved using curved magnonic sources [108], in which case no modulation of the magnonic index is needed, and via reflection from a curved magnetic boundary [109]. One limitation is that these

non-rotationally-symmetric designs only work for a particular direction of incidence, which is not so easily reconfigurable.

Creating a rotationally-symmetric lens does not guarantee a rotationally- symmetric operation, however. For example, in Ref. [20] a graded decrease of the magnetisation was induced by locally heating an in-plane magnetised yttrium-iron-garnet (YIG) film via a laser spot. This heating profile acted as a focusing or defocusing lens for backward volume (BV) and Damon-Eshbach (DE) magnetostatic spin waves, respectively. Yet, despite being a rotationally-symmetric profile, it would not work for all angles of incidence since the BV and DE regimes are highly anisotropic. The focusing/defocusing only works when the propagation is parallel/perpendicular to the magnetisation orientation for BV / DE waves, respectively.

In contrast, rotationally-symmetric, graded-index lenses are most useful when dealing with an isotropic dispersion relation, since they will work equally well from any angle of incidence, whilst the graded profile avoids the issues of reflections from abrupt boundaries. The Luneburg profile, in particular, has been studied in many other areas of wave physics [110–113], in part due to its applications in future wave-based computing circuitry. The Luneburg lens could form a useful circuit component, to launch plane waves from an antenna, or to increase the amplitude of incoming plane waves to be read by the same antenna. To read-/launch a plane wave from/to a different direction, one only needs to move the antenna to the corresponding point on the lens edge, without having to reconfigure the lens.

We will begin by covering the theoretical formalism for creating a spin wave Luneburg lens in the forward-volume, magnetostatic regime. Then, we will analyse its operation in micromagnetic modelling, and compare it to a variable-profile parabolic lens. Finally, we will also see how to make a Luneburg lens for spin waves when the exchange interaction is taken into account.

5.2 Creating a Refractive Index Profile for Spin Waves

The refractive index profile $n(r)$ for a Luneburg lens is given by

$$n(r) = \begin{cases} \sqrt{2 - (r/R)^2}, & r \leq R, \\ 1, & r > R, \end{cases} \tag{5.2.1}$$

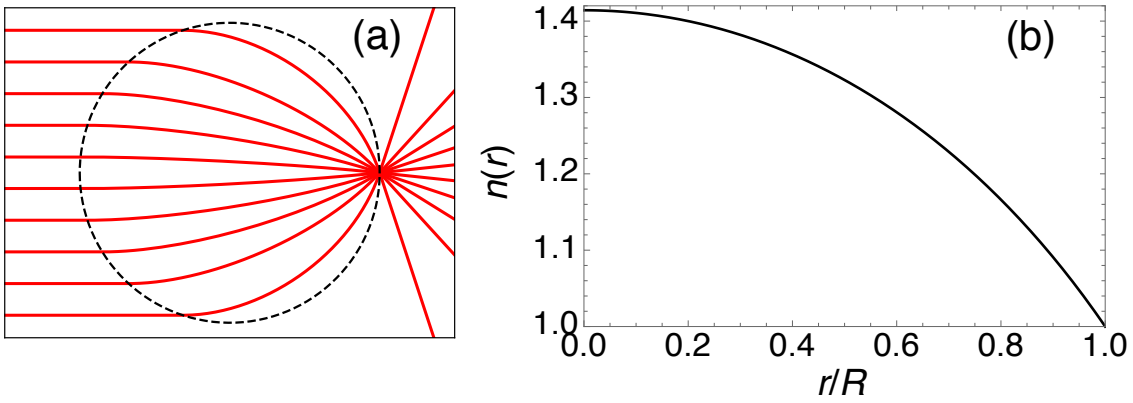

FIGURE 5.1: (a) The Luneburg lens, outlined by the dashed line, focuses rays (red lines) to a diffraction-limited spot on the opposite edge of the lens. (b) Refractive index profile described by Eq. (5.2.1).

where r is the radial coordinate and R is the radius of the lens. This profile, along with the ideal operation of the lens, is shown in Fig. 5.1.

For light propagating in an isotropic non-dispersive medium, the graded refractive index is given by

$$n(\mathbf{r}) \equiv \frac{k(\mathbf{r})}{k_0} = \frac{c}{v(\mathbf{r})}, \tag{5.2.2}$$

where k_0 (k) and c (v) are the wave number and the speed of light in vacuum (the graded medium) respectively. In this case, the dispersion relation $\omega(\mathbf{k})$, where ω is the angular frequency, is linear, isotropic and there is no band gap in the spectrum. As a result, the graded index has the same spatial profile for different frequencies.

For spin waves, the medium is always dispersive. Indeed, the spin wave dispersion relation $\omega(\mathbf{k})$ has a gap at $k = 0$, is non-linear, and may depend upon the mutual orientation of the wave vector and magnetisation. Hence, the magnonic refractive index can usually be defined only for a fixed frequency and perhaps its vicinity. So, any profile of the magnetic field or material parameters required to make a special graded profile of the index is generally frequency-dependent.

To make a Luneburg lens for spin waves at a particular frequency, we thus need to ensure that $k(r)/k_0$ obeys Eq. (5.2.1), where k_0 is now the reference wave number of the spin waves outside the lens. To avoid anisotropy, and also because

the results are most interesting[1], we choose to work with forward-volume magnetostatic spin waves (FVMSWs), propagating in the plane of a perpendicularly magnetised thin ferromagnetic film. As we saw in Chapter 2, when exchange effects can be neglected, these waves are described by the isotropic dispersion relation (given in SI units)

$$k = \frac{1}{s}\frac{2}{\sqrt{-(1+\kappa)}}\arctan\left(\frac{1}{\sqrt{-(1+\kappa)}}\right) \tag{5.2.3}$$

where

$$\kappa = \frac{\omega_H\omega_M}{\omega_H^2 - \omega^2}, \quad \omega_H = \gamma\mu_0 H_i, \quad \omega_M = \gamma\mu_0 M, \tag{5.2.4}$$

γ is the gyromagnetic ratio, μ_0 is the permeability of free space, M is the magnetization length, $H_i = H - M$ is the static internal magnetic field, H is the applied (external) magnetic field, and s is the film thickness.

There are three parameters in equations (5.2.3) and (5.2.4) that we can manipulate to vary the wave number and the magnonic index: s, M and H. Interestingly, if we vary the film thickness and fix all other parameters, there is a simple relation between the index and the thickness outside, s_R, and inside, $s(r)$, the lens

$$n(r) = s_R/s(r). \tag{5.2.5}$$

Surprisingly, this implies that *any* refractive index profile can be created by matching $n(r)$ to the ratio of the thicknesses inside and outside of the lens, for *any* frequency of dipolar spin wave described by (5.2.3). Note, however, that Eqs. (5.2.3)-(5.2.5) neglect changes in the static demagnetizing field due to the non-uniform thickness profile, which may be complicated if the thickness changes rapidly over a small distance [114–116]. Neglecting these effects should be valid if the thickness is changed gradually and smoothly (i.e. without steep gradients or steps).

In Chapter 7, we look in more detail at the properties of the magnonic refractive index and its dependence on these magnetic parameters, in different spin wave regimes. For now, we will establish the refractive index profiles required to

[1] We will look at how to create a Luneburg lens in the exchange and dipole-exchange regimes in Section 5.6, but this is a good opportunity to explore the dipole-dominated regime; not just because the results in this case are more interesting, but also because we have already investigated the purely exchange regime in great detail in earlier Chapters.

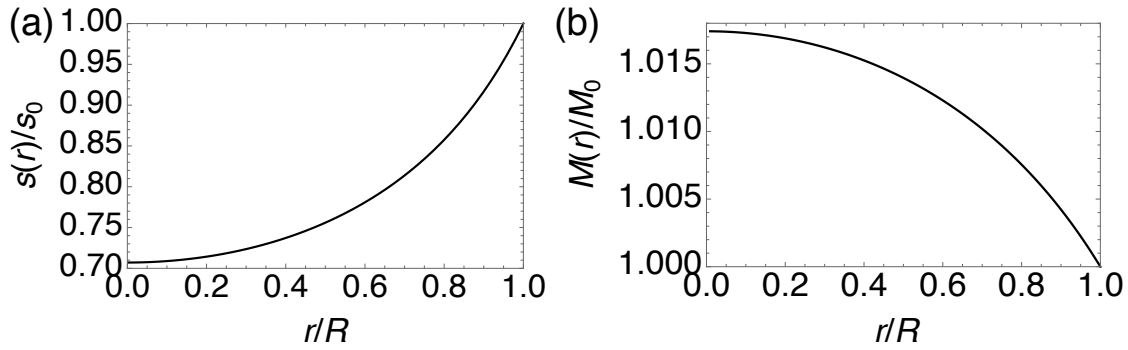

FIGURE 5.2: The thickness (a) and magnetisation (b) profiles required to make a Luneburg lens.

make the focusing lenses.

5.3 The Luneburg Lens

5.3.1 Refractive Index Profiles

The profile of the thickness $s(r)$ required to make a Luneburg lens is given in Fig. 5.2 (a). The film in the center of the profile needs to be $\sqrt{2}$ times thinner than outside of the lens, which suggests that the lens will not be too sensitive to small thickness variations.

The profile of the magnetisation or applied magnetic field required to make the Luneburg lens for spin waves cannot be written in an explicit form. However, in contrast to the thickness, it is significantly easier to model changes in these quantities in finite-difference micromagnetic simulations. So, to demonstrate the operation of a spin wave Luneburg lens, we vary the saturation magnetisation in space. We determine the magnetisation profile $M(r)$ required to produce the lens from Eqs. (5.2.3) and (5.2.4), and the resulting profile is shown in Fig. 5.2 (b). There are two features to notice. First, $M(r)$ needs to increase in the center of the lens. This cannot be achieved by a local heating of the sample [20] but instead requires a local cooling, or doping [117]. Second, the required maximum change in the magnetisation is just 1.7%, which is rather small. For a fixed thickness, this magnetisation change does depend on the frequency and external field, as detailed in Section 5.4.1. However, this tiny change in M required to make the lens is not an anomalous value originating from a lucky (or perhaps unlucky) choice of parameters; rather, it is just a surprising product of the magnetostatic spin wave dispersion, as we will see in later Chapters.

Next, we will demonstrate in micromagnetic modelling that the profile of Fig. 5.2 (b) can indeed make a very effective Luneburg lens.

5.3.2 Micromagnetic Method, Results & Analysis

We now describe how the lens is designed and tested in micromagnetic simulations using MuMax3 software [45]. We define a 1×0.5 mm^2 YIG-like film in the $x-y$ plane, with a fixed thickness of $s = 2$ μm. Periodic boundary conditions are applied in both in-plane directions. The Gilbert damping constant is $\alpha = 10^{-4}$. The saturation magnetisation is $M_0 = 140$ kA/m outside the lens and varies inside the lens as shown in Fig. 5.2 (b). The cell size is 0.5×0.5 μm^2 in the film plane, and is equal to the thickness in the z direction. The wavelength λ of the studied spin waves is much greater than both the cell size and the exchange length. So, any effects of the exchange interaction are irrelevant in our model.

First, we magnetise the sample by an out-of-plane magnetic field of 200 mT. Then, we apply a burst of microwave magnetic field in the region to the left of the lens profile. The microwave field is parallel to the x-axis and has central frequency of 1 GHz (corresponding to $\lambda = 33.9$ μm), bandwidth of 0.1 GHz and amplitude 0.1 mT. The spatiotemporal profile of the burst is designed to launch a Gaussian spin wave packet propagating towards the lens, detailed in Appendix I. The use of the wave packets in combination with a suitably long sample (in the direction of the wave packet travel) allows us to avoid using absorbing boundary conditions, [118] which can still cause spurious reflections from the gradients in the damping constant. This also means we can dedicate the limited number of material regions (256 in total, in MuMax3) solely to making the lens.

The Luneburg lens profile is designed in the geometrical optics approximation, [36] i.e. for $\lambda \ll 2R$. From comparisons with other studies, [119, 120] and to keep the simulation size reasonable, we use $R \approx 6\lambda$. We use Eqs. (5.2.1)-(5.2.4) to define 255 concentric circular regions in MuMax3, between which the saturation magnetisation changes in equal steps to form the $M(r)$ profile required for the Luneburg lens.

The snapshots of the x-component of the reduced dynamic magnetisation, $m_x = M_x/M_0$, are shown in Fig. 5.3 for different moments of time. The wavefronts behave as expected: the wavelength decreases in the region of increased refractive index, curving the wavefronts towards the lens's focus. In addition, the wavefronts are slowed within the lens. We see the effect of this after the wave has left the lens, when the focused energy is re-emitted from the focal spot.

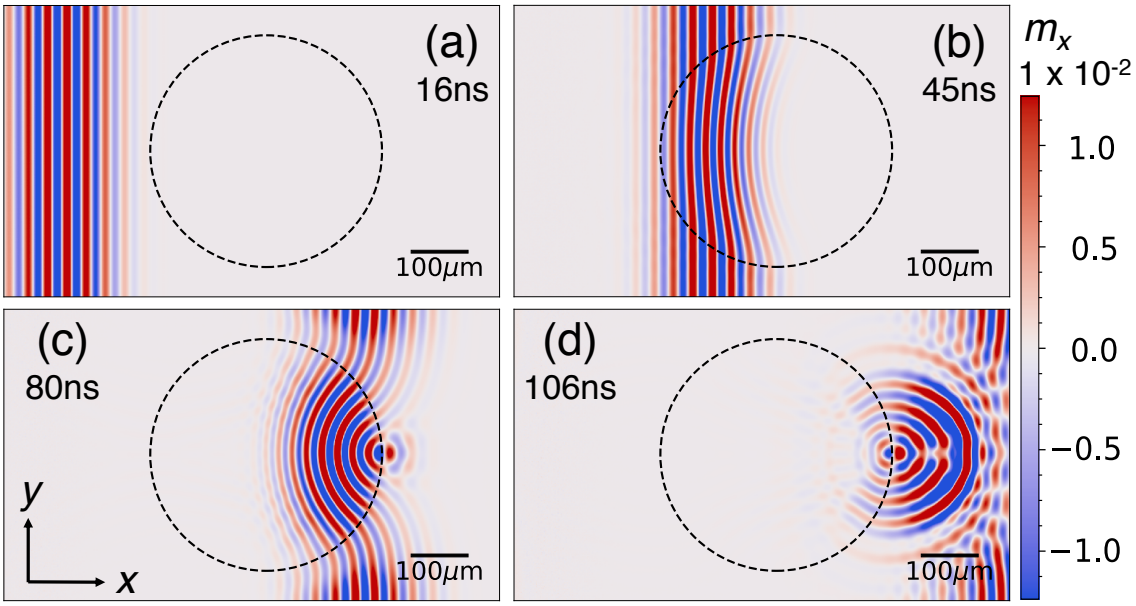

FIGURE 5.3: Snapshots of m_x are shown as the wave packet moves through the Luneburg lens (black circle) at times of (a) 16 ns, (b) 45 ns, (c) 80 ns, and (d) 106 ns.

To evaluate the degree of focusing, Fig. 5.4 (a) shows the maximum amplitude of m_x attained in each cell of the model over the entire duration of the simulation. The largest amplitude is indeed attained in the focus of the lens. Fig. 5.4 (b) shows the spin wave energy density near the focus at the time when the maximum amplitude over the simulation is achieved. The energy is mostly concentrated around $\pm\lambda/2$ of the ideal focus. However, the peak is shifted along x from the ideal position, similar to the results reported in Ref. [121]. Increasing the size of the lens with respect to λ should bring the focal spot closer to the lens edge. To evaluate the beam waist, Fig. 5.4 (c) shows the energy density cross-sections along y for the line i shown in panels (a) and (b) and for the x position of the actual focus peak. The waist, measured as the full width at half maximum (FWHM) of the peak at the actual focus, is around 23 μm or 0.67λ, which is reasonable for a diffraction-limited lens. At the actual and ideal focal points, the peak amplitudes of m_x are 5 and 4.7 times greater than the unfocused amplitude, respectively. This enhancement of the wave amplitude may be useful when reading an incoming plane wave using an antenna. There is little data on the amplitude at the focus of similar lenses outside of magnonics, however Ref. [113] and [122] reported an amplitude increase of 3-4 times for lens radii 2-3 times the wavelength.

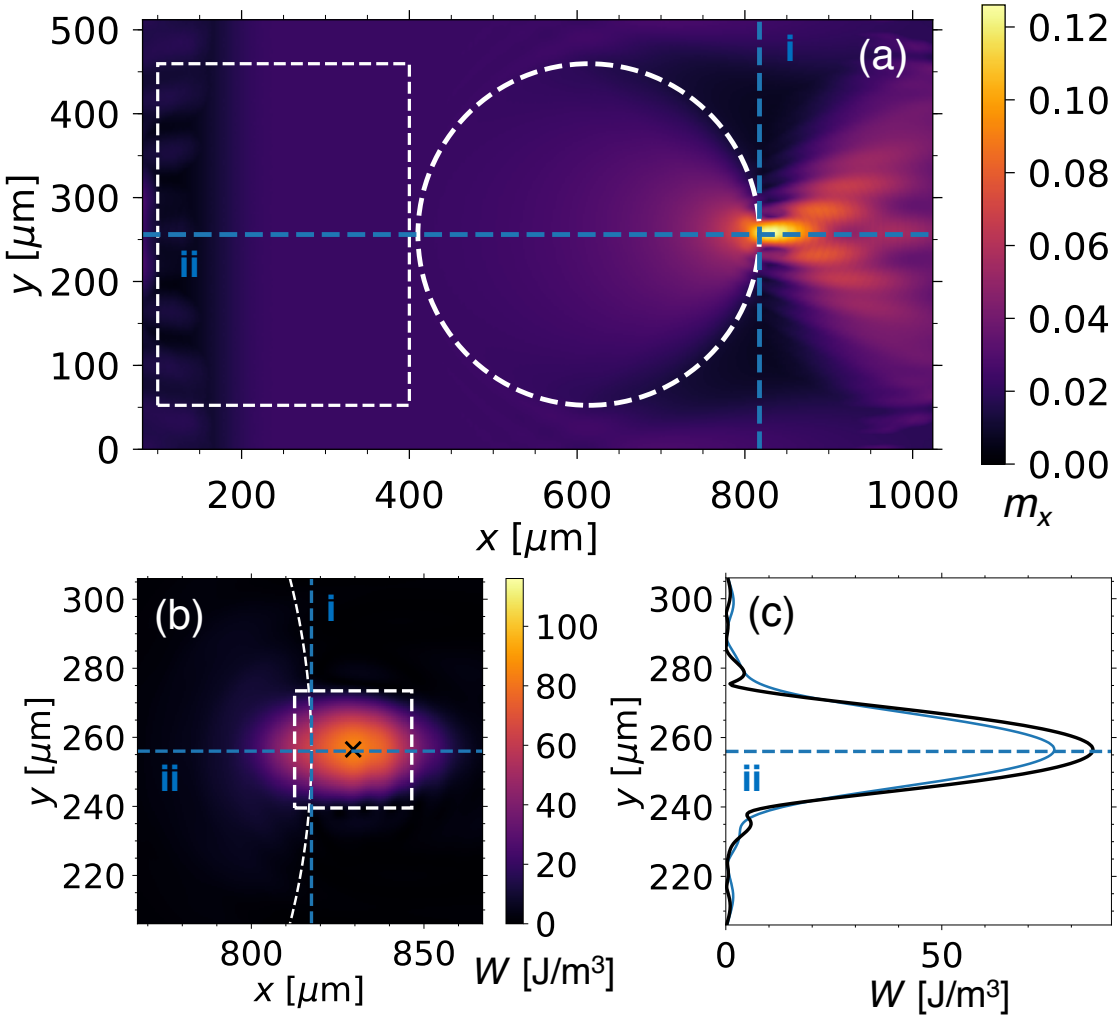

FIGURE 5.4: (a) Maximum amplitude of m_x attained across the model over the duration of the simulation. Rectangular box indicates the region used to calculate the incident spin wave energy. (b) Energy density, W, near focus region at the time of peak amplitude. The white square has a side of λ and is centered on the peak of the actual focus spot (black cross). (c) Energy density cross-sections for the line i from panels (a) and (b) (blue line) and at the x position of the actual focus (black line), at the times when the maximum amplitude occurs.

5.3.3 Lens Efficiency

Now, we evaluate the fraction of the wave packet energy that reaches the focal region. First, we sum the energy over the rectangular region before the lens, as shown in Fig. 5.4 (a), at 14 ns, i.e. once the packet starts moving and before it encounters the lens. The region has an x extent of 300 μm, which completely encompasses the wave packet length, and y extent of $2R$, so that only the portion of the wave packet that enters the lens is counted. Then, we sum the energy in the $\lambda \times \lambda$ region centered around the actual focus peak, as shown in Fig. 5.4 (b), at the time when the peak amplitude of the duration of the simulation is reached. As a result, we find that 46% of the incident energy arrives in the focal region. This is a pessimistic way to sum up the energy reaching the focus, since the wave experiences damping [16, 123], responsible for an energy loss of around 7% in our case.

An alternative way to quantify the reflection loss of the Luneburg lens is to consider the spin wave scattering in the reciprocal space. To do this, we Fourier transform the wave field in space, and compare the Fourier amplitudes for positive and negative k_x components of the wave vector. To account for the wave phase, we save the data from the simulations at time intervals separated by $\Delta t = \pi/(2\omega_0) = 1/(4f_0)$, and construct a complex wave field. The real and imaginary components of this field at each time step are given by the wave fields at adjacent time steps, $\pi/2$ out of phase.

If we sum the absolute values of the Fourier amplitudes across all k_y values and compare sums of the amplitudes calculated separately for all positive and all negative k_x values, we find that 13% of the wave is reflected in total. We would expect to see some reflection even for a perfect Luneburg lens anyway, due to reflections at each infinitesimal boundary where the refractive index changes. This effect would naturally be exacerbated in finite difference software, where comparatively large steps must be used. To confirm the origin of this reflection, Fig. 5.5 shows how the Fourier amplitude distribution in the reciprocal space changes in time as the wave moves through the lens. These shapshots of the Fourier amplitude in the $k_x - k_y$ plane are shown at times corresponding to the snapshots of m_x in real space in Fig. 5.3. We can see that the Fourier amplitude of non-zero k_y components emerges in panels (b) and (c), when the wavefronts become curved within the lens, and then spreads into a circle in panel (d), as the waves begin to emanate from the focus. The Fourier amplitude for negative k_x values is negligible until this point — the scale in panels (a-c) (ii) is around

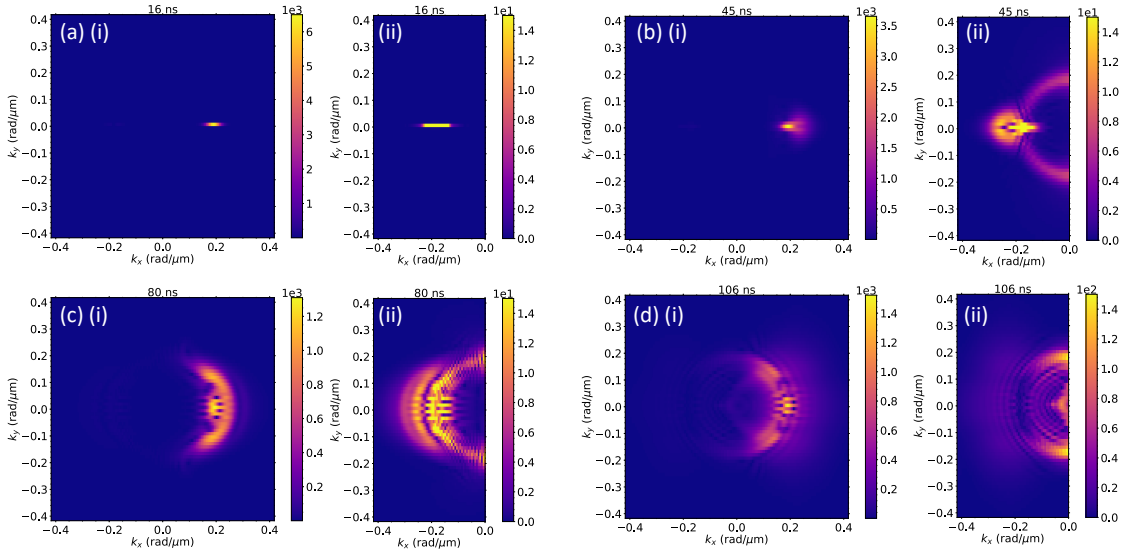

FIGURE 5.5: Fourier amplitude distribution (arbitrary units) in the (i) $k_x - k_y$ plane and the (ii) $(-k_x) - k_y$ plane, at (a) 16 ns, (b) 45 ns, (c) 80 ns and (d) 106 ns, which correspond to the same snapshots as in Fig. 5.3. Note that the colour scales in (i) differ in each image for clarity. The colour scales for the negative k_x amplitudes in (a-c) (ii) are all fixed at a maximum of 15, whereas the scale maximum in (d) (ii) is 150.

100 times lower than the scales in panels (a-c) (i). In panel (d), the negative k_x Fourier amplitude has increased by around a factor of 10, and is just noticeable in panel (d) (i). This suggests that it is not the quality of the lens that reduces the proportion of energy transmitted through it. Rather, as the pulse exits the focus of the lens (comparing to Fig. 5.3 (d)), the tips of the wavefronts seem to re-enter the lens as they spread out, and so travel in the negative x direction.

In Fig. 5.6, we show how the Fourier amplitude for negative k_x values accumulates over time, by summing the Fourier amplitude for all of the negative k_x values over all k_y, at each time step. We see a reasonably steady increase of the cumulative negative k_x amplitude as the wave moves through the lens, suggesting that this is the natural accumulation of reflections as the wave encounters each step change in index. When the peak of the wave packet is nearing the centre of the actual focus (comparing panel (b) with (a)), the rate of accumulation increases substantially. This confirms that the increase of the negative k_x amplitude that we observed in Fig. 5.5 is not due to the pulse moving through the lens, but instead is due to the wave spreading out and re-entering the lens after passing through the focus.

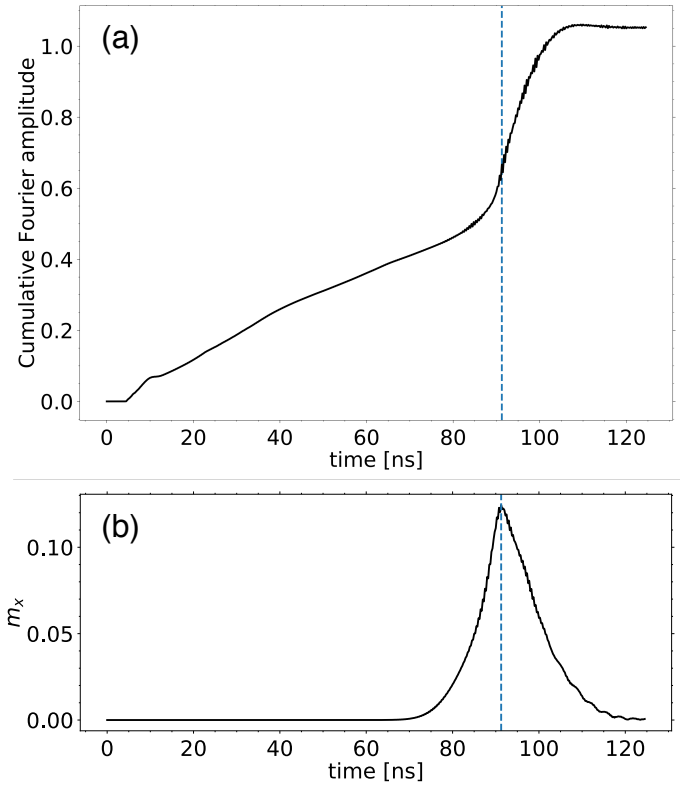

FIGURE 5.6: (a) Cumulative Fourier amplitude for negative k_x values (summed over all of k_y values) as a function of time. Blue dashed line indicates the time at which the peak of the wave packet encounters the actual focus, as shown in (b), where m_x amplitude is plotted at the center of the actual focus spot as a function of time.

5.4 Parabolic Lens

Next, we examine parabolic profiles, which can be fitted to the Luneburg lens profile and yet varied by tweaking their parameters. This is a way of understanding how sensitive the results for the Luneburg lens are to deviations from the ideal magnetisation profile. We run simulations for three parabolic profiles (Fig. 5.7(a)) obtained by fitting the Luneburg profile to $M(r)/M_0 = a - br^2$, where a and b are fitting parameters[2]. The best fit profile has an $M(0)$ error of 5% relative to the ideal value and still acts almost identically to the Luneburg profile, yielding a 5-times increase of the spin wave amplitude at the actual focal spot. We do not show this result here — rather, we present the results for the $\pm 30\%$ error profiles in Fig. 5.7 (b-d). If $M(0)$ is increased by 30% above the ideal value, the lensing effect is strengthened, creating a narrower focus and increasing the peak amplitude

[2]In this case, the lens radius R is 2.5% greater than before, to accommodate the parabolic fit and for the index to be equal to 1 at the lens edge.

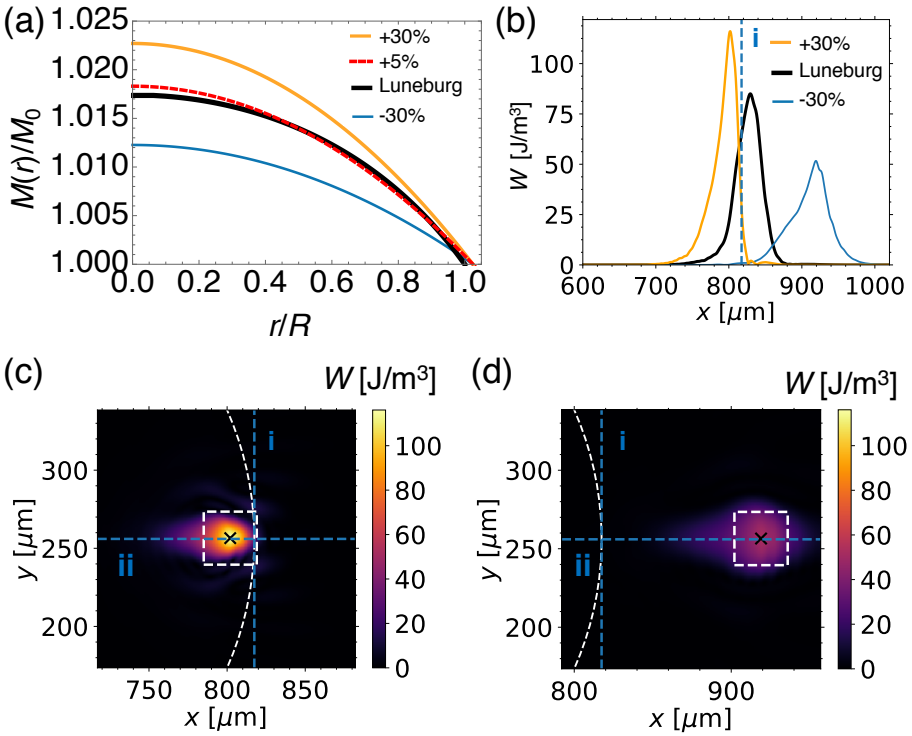

FIGURE 5.7: (a) The Luneburg profile (black) is shown with parabolas with either 5% (red, dashed), or $\pm 30\%$ (orange and blue, respectively) errors in $M(0)$. (b) Energy density cross-sections along x at the y position of the actual focus are shown for the lens profiles from (a). Spatial maps of the spin wave energy density are shown for (c) +30% and (d) -30% error profiles. Line i in (b) and intersections of lines i and ii in (c) and (d) show the ideal positions of the focus.

of m_x by 5.7 times. If $M(0)$ is decreased by 30% below the ideal value, the peak enhancement of the m_x amplitude decreases to 3.8 times of the incident wave's amplitude. Fig. 5.7 (b) compares the corresponding energy density cross-sections along the direction of incidence. We find that the +30% error, Luneburg, and -30% error profiles have FWHMs of 0.8λ, 1.1λ and 1.3λ, respectively. Comparing the energy of the wave packet before entering the lens with the energy in the $\lambda \times \lambda$ focus regions (Fig. 5.7 (c) and (d) [3]), we find that 49% and 37% of the incident energy arrives in the focus region for the +30% and -30% error profiles, respectively. Recall that the Luneburg profile received 46% of the incident energy at the focal region. So, if the magnetisation in the center is increased, the lens may produce a somewhat tighter focus than the Luneburg profile. This may be beneficial in a system where only the focusing power matters.

The analysis so far shows that the lens profile can deviate from the ideal Luneburg profile and still produce a reasonable lensing effect. However, only the actual Luneburg profile can both successfully focus a plane wave to a spot and convert a point source to a plane wave, as we show in Fig. 5.8. To create these images, we have used the same parameters as previously, except we have extended the size of the model (to suppress spurious interference) and introduced a source with a continuous-wave (CW) temporal and Gaussian spatial profile (details provided in Appendix I). The source is either located at the ideal focus on the edge of the lens, or at the actual focus determined from the focusing study. As before, we compare the ideal Luneburg lens to the $\pm$30% error profiles.

Fig. 5.8 shows that the Luneburg profile is the most successful in creating a plane wave, albeit with some interference due to reflections within the lens. The +30% and -30% profiles focus the outgoing wavefronts too much and too little for both source positions, respectively. Positioning the source at the actual focus of the -30% profile is a good improvement. However, the wavefronts are still not completely parallel to each other, and the wave amplitude is still lower than in the other two cases.

All the results presented here are valid for the specific choice of the frequency, applied magnetic field and film thickness. Next, we see how the required magnetisation profile depends on the applied field and frequency values used in the design.

[3] Note that, in Fig. 5.7 (c), (d), and Fig. 5.4 (b), the colour scale is set to the maximum value attained in Fig. 5.7 (c), for ease of comparison

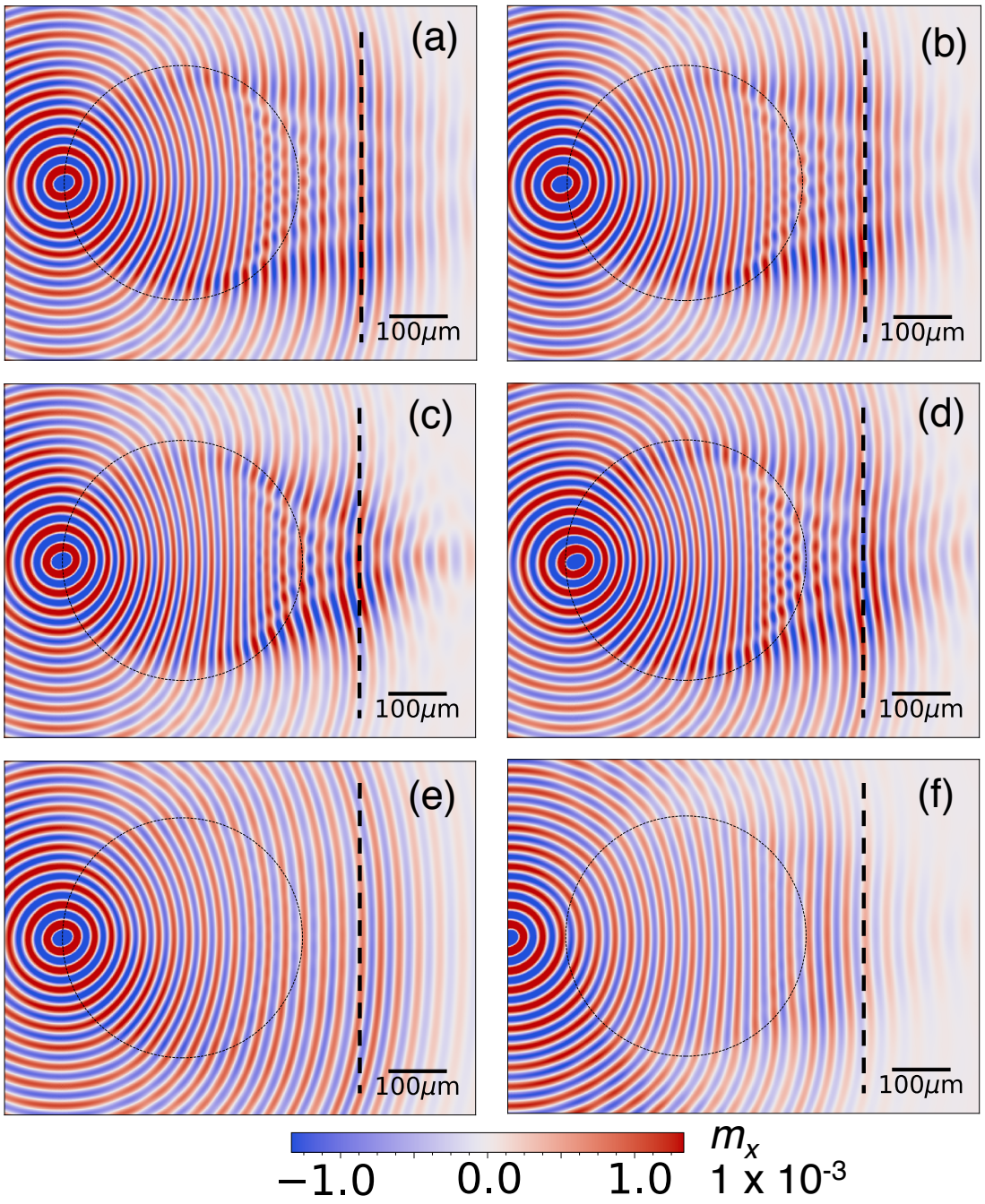

FIGURE 5.8: Snapshots of m_x at 82ns when a CW-Gaussian source is positioned near (a)-(b) the Luneburg lens, (c)-(d) the +30% error profile, and (e)-(f) the -30% error profile. The source is centered on the lens edge for (a), (c) and (e), and on the actual focus position for (b), (d) and (f). Vertical guide lines (black, dashed) are provided in the plane wave regions.

5.4.1 Dependence of the Magnetisation Profile on the Applied Field and Excitation Frequency

In this section, we explore how the peak value $M(0)$ of the optimal magnetisation profile required to create a Luneburg lens is affected by the choice of excitation frequency f and external field H.

Previously, we designed the lens to work most effectively for an incident wave with frequency $f_0 = 1$ GHz and external field of $\mu_0 H_0$ =200 mT. Changing the field shifts the dispersion curve, as shown in Fig. 5.9 (a). This gives us a different profile of the magnetisation required to make a Luneburg lens for the same incident wave frequency, as shown in Fig. 5.9 (b).

In addition, we can choose to design the lens for a different incident wave frequency, which will also affect the magnetisation profile for the lens. In Fig. 5.9 (c), we show how the value of the magnetisation at the center of the lens, $M(0)$, depends upon the frequency for different values of the field. Choosing a value of frequency close to the minimum or maximum frequency values of the FVMSW manifold (corresponding to ω_H and $\sqrt{\omega_H(\omega_H + \omega_M)}$, respectively) requires a small change in $M(0)$ from M_0 to create the profile (we are using $M_0 = 140$ kA/m). Note however that the geometrical optics approximation would be impractical to fulfill towards the minimum FVMSW frequency[4], while the exchange interaction can no longer be neglected near the maximum FVMSW frequency. We extend this analysis to consider the dipole-exchange regime in section 5.6 - so the dependence of $M(0)$ towards the high frequency end of the manifold is an approximation - but for now we will just consider the properties of the FVMSW manifold, for interest. The largest $M(0)$ for each fixed external field value is obtained somewhere around the central frequency in the manifold. We also show a plot of $M(0)$ for a range of f and H values in Fig. 5.10, and we can see that $M(0)$ increases as the field increases, for frequencies around the centre of the spin wave manifold. This means that a larger change in M is required to create the same change in the refractive index (from 1 to 1.4), and hence k, so the dispersion curve must be changing in shape for higher fields.

[4]since the lens must become increasingly large with the increasing wavelength, and would inevitably exceed the propagation length of the spin waves.

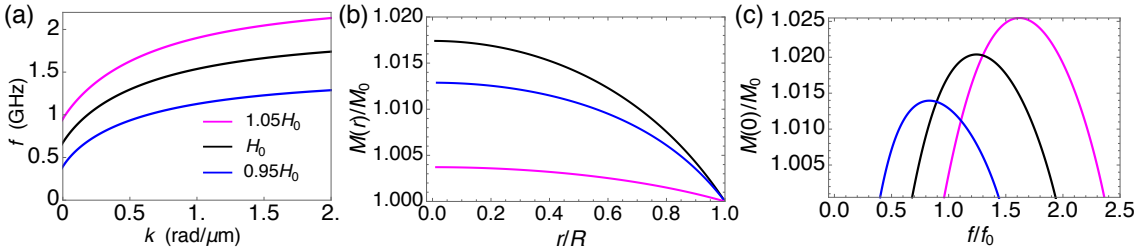

FIGURE 5.9: (a) Dispersion relation $f(k)$, (b) Luneburg lens magnetisation profile for $f_0 = 1$ GHz, and (c) the dependence of $M(0)/M_0$ on frequency, each for external field values of $0.95H_0$ (blue line), H_0 (black line) and $1.05H_0$ (magenta line), where $\mu_0 H_0 = 200$ mT is the external field used in the main text.

5.5 Lens Operation for Different Spin Wave Frequencies

Here, we briefly check how robust the focusing behavior of the lens is for different incident frequencies. We use the same lens as before, designed for an incident wave of frequency $f_0 = 1$ GHz. In Fig. 5.11 (a)-(d), we show the energy density around the focus region for incident wave packets with central frequencies $0.8f_0$, $0.9f_0$, $1.1f_0$ and $1.2f_0$. In each case, the bandwidth is still 10% of the central frequency and wave number.

We can see that a frequency of $0.9f_0$ achieves a slightly better focus amplitude than f_0, but is not as tightly focused. The fact that it resides slightly inside the lens rim (where the f_0 result lies slightly outside the lens) suggests that the actual optimal frequency for this lens — which compensates for not being perfectly in the geometrical optics regime — is somewhere between these values.

All the other incident wave packets suffer from a lower amplitude focus, although there is no clear correlation between the amplitude and the FWHM of the depth of focus. Overall, there is still focusing in each case, but the effect is greatly reduced when the frequency is beyond around $\pm 10\%$ of the optimal value.

5.6 Luneburg Lens in the Dipole-Exchange Regime

We have so far considered the strictly magnetostatic regime, where the spin wave solutions exist within a manifold described by Eq. (5.2.3). The properties of this dispersion relation, which we explore in much more detail later, enable a Luneburg lens to be created with just a 1.7% change in M at the centre of the lens. Now,

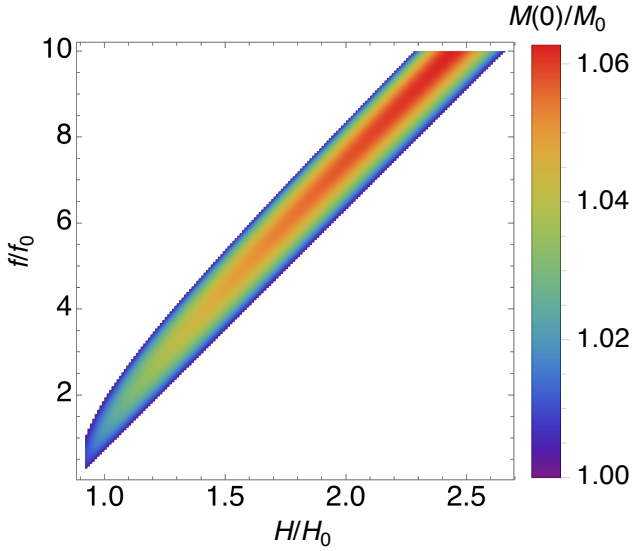

FIGURE 5.10: Dependence of $M(0)$ on the frequency and field, normalized to values used in the main text ($M_0 = 140$ kA/m, $f_0 = 1$ GHz and $\mu_0 H_0 = 200$ mT). The white region is outside of the FVMSW manifold, where no magnetostatic spin wave solutions exist. These results are amended for higher frequencies when incorporating the exchange interaction, which we see in section 5.6.

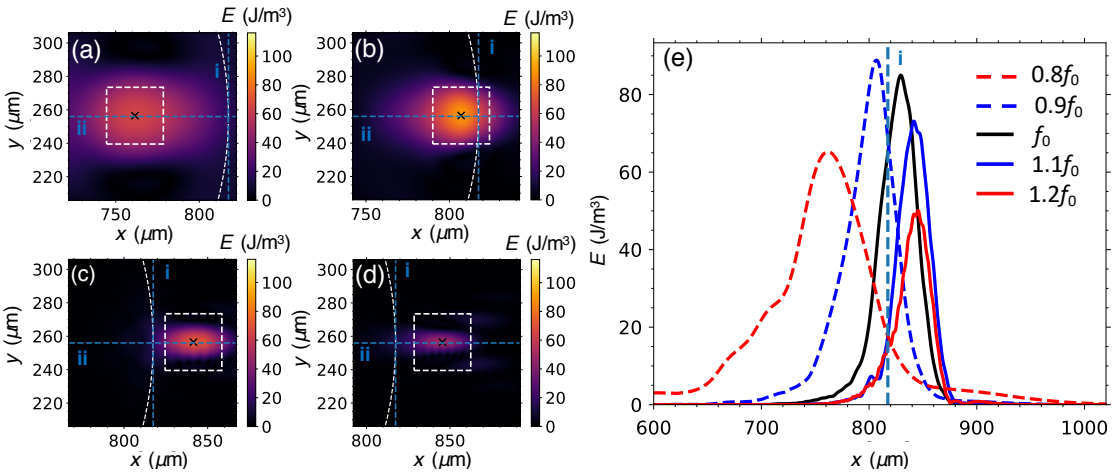

FIGURE 5.11: (a)-(d) Energy density, W, around the focus region for incident wave packets with central frequency of (a) $0.8f_0$, (b) $0.9f_0$, (c) $1.1f_0$ and (d) $1.2f_0$. In panel (e), each result is plotted along line ii (the depth of focus) in a red dashed line, blue dashed line, blue solid line and red solid line respectively. We also compare these to the actual Luneburg lens result with a black solid line.

we take into account the effects of the exchange interaction, and show the magnetisation profile required in the dipole-exchange regime.

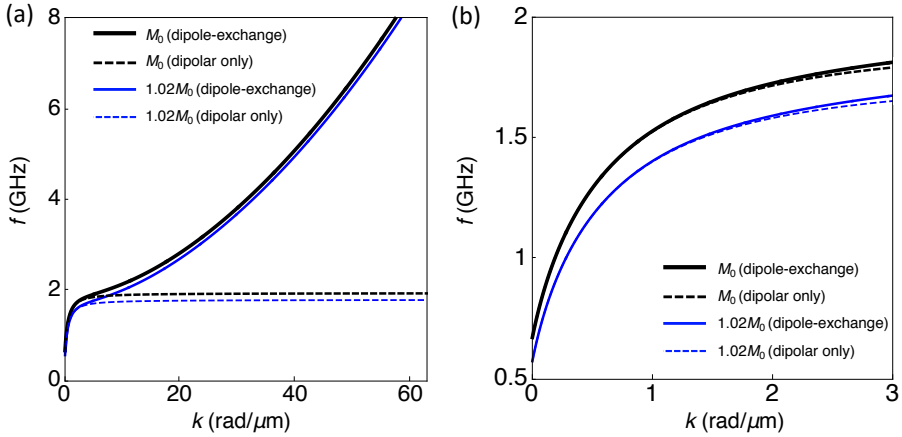

FIGURE 5.12: Dipole-exchange dispersion relation (solid lines), using the same parameters as before but now with the exchange constant $A_{ex} = 0.4 \times 10^{-11}$ J/m, compared to the dipolar dispersion relation (dashed lines), shown for (a) a large range of frequencies from the dipolar to dipole-exchange regimes, and (b) the dipolar regime.

In Fig. 5.12, the full dipole-exchange dispersion relation[5] (solid lines) is compared to the dipolar-dominated dispersion relation (dashed lines), for two different values of the magnetisation: M_0 and $1.02M_0$. In panel (a), the dispersion from the bottom of the magnetostatic spin wave manifold is shown up to the quadratic exchange regime. In panel (b), we show a zoom of the dipolar-dominated regime, up to the point that the dipolar and dipole-exchange graphs are clearly diverging. Panel (b) shows that neglecting exchange in the earlier model was certainly valid for $f = 1$ GHz, for our choice of material parameters.

Next, we show in Fig. 5.13 the equivalent versions of Figs. 5.9 (c) and 5.10, now incorporating the effect of the exchange interaction. In panel (a), the different regimes are highlighted with different line styles. The dashed black line shows where the dipolar contribution is dominant using the dipole-exchange dispersion relation (for wavelengths $\lambda \gtrapprox 6$ μm for our choice of parameters), and the solid black line shows where the exchange interaction becomes more dominant. For comparison, the dashed red line shows the dipolar-dominated dispersion relation (this is the black line in Fig. 5.9 (c)). We have limited the graph at $M(0) = H_0$, as beyond this point the internal field would be negative, and may lead to instability.

We can see that the peak $M(0)$ of the magnetisation profile to create the Luneburg lens needs to be much larger in the dipole-exchange regime, when $f > 2$ GHz. If we increase the value of H_0, as in Fig. 5.13 (b), even larger values of $M(0)$ are required. However, we have another restriction on the maximum value

[5]Given by equation (2.5.18) in Chapter 2.

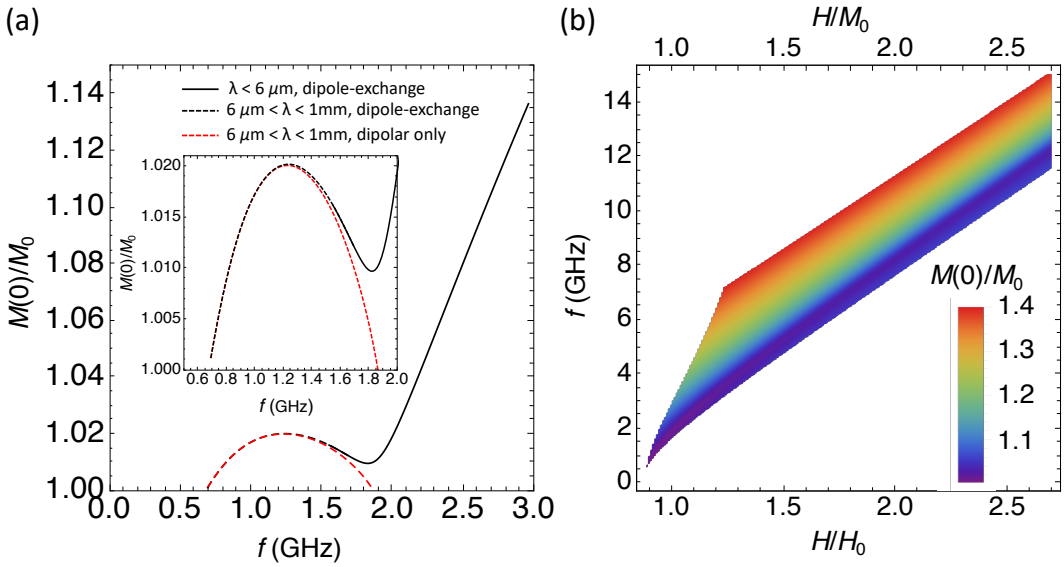

FIGURE 5.13: Dependence of $M(0)$ on (a) frequency, for $H = H_0$, and (b) frequency and H. The solid black line and dashed black line in panel (a), and the entire density plot in (b), are calculated using the dipole-exchange dispersion relation, whereas the dashed red line in (a) neglects the exchange interaction. In (b), the bottom axis shows H/H_0 and the top axis shows H/M_0. Note that the plot is limited to ensure M_0 is not greater than H_0, and also not greater than $1.4M_0$. Both these images can be compared to Figs. 5.9 (c) and 5.10 respectively.

of $M(0)$, and this is value of M for the chosen material at T=0 Kelvin. For YIG, $M(T = 0\,\text{K}) = 196\,\text{kA/m}$ [5]), which corresponds to $1.4M_0$. Therefore, we need to ensure that M is not larger than the external field *and* not larger than $1.4M_0$, so the white area at higher frequencies is where these conditions are not fulfilled. We can see that the Luneburg lens created by changing M is therefore not suitable for high-frequency, purely exchange spin waves (where the dipolar interaction can be neglected, typically for frequencies of tens of gigahertz) but could be feasible for dipole-exchange spin waves.

5.7 Conclusions

In this Chapter, we have demonstrated how to form a Luneburg lens in a magnetic material with perpendicular magnetisation, and analysed its effectiveness as a focusing device. This work also shows that magnetisation profiles which are different from the Luneburg profile could still focus spin waves. Yet, the Luneburg profile is still optimal for focusing a plane wave to a point and converting a

point source to a plane wave, with the detector / source positioned at the lens edge.

The simple relation between the refractive index and the magnetic film thickness — for purely dipolar waves — suggests that the thickness is the parameter of choice for designing broadband graded magnonic index profiles, valid for a range of field and magnetic parameter values. In contrast, the Luneburg profile of the saturation magnetisation is frequency and field dependent. Notably, the magnetisation change required to achieve Luneburg focusing may be rather small for dipolar-dominated spin waves. As the contribution from the exchange interaction increases, the required magnetisation change increases, and may become unrealistically large for higher frequencies. This means that these lenses cannot realistically be achieved in the exchange-dominated regime, when created by varying M only. This does not mean that the exchange regime is entirely incompatible with graded index lenses, however. Further work in this area may consider changing H or even a combination of s, M and H, or anisotropy (or any other parameter), to create a larger change in the index — but this is beyond the scope of this study.

Chapter 6

Spin Wave Steering Lenses

6.1 Introduction

We have seen in the previous Chapter that rotationally-symmetric, graded index lenses can be created to focus spin waves, provided that the dispersion relation is isotropic. Furthermore, we saw that these lenses could be created by a tiny change in the magnetisation, of $< 2\%$, in the (forward-volume) dipolar-dominated regime. It means that only a small change in M is required to change the refractive index by a modest amount. In this Chapter, we utilise this surprising result to make much more extreme refractive index profiles. We show that rotationally-symmetric *steering* lenses can easily be realised for spin waves in the same forward-volume, magnetostatic regime.

The challenge of steering spin waves has primarily been approached by confining waves along curved waveguides [78, 124–128]. However, these waveguides may suffer from losses/scattering in bends, and usually have a large spatial footprint. To reduce scattering losses, we could utilise a graded refractive index to steer spin waves. A number of groups have investigated this already by gradually changing a material parameter, such as the magnetisation [17, 20], the internal magnetic field through shape anisotropy [129] or the external magnetic field [16]. In each case however the steering effect is highly dependent on the direction of the incoming spin wave.

To overcome the issue of a large spatial footprint, and to avoid issues with directionality, we may again refer to the wealth of research in graded index optics. Rotationally-symmetric, graded index steering lenses offer a spatially-efficient way to direct light by a certain angle between 0° and 360°, from any direction of incidence [130–135]. As we have seen previously, although the lenses are designed to work with light, the same analysis applies to any other wave supposing that the dispersion relation is known.

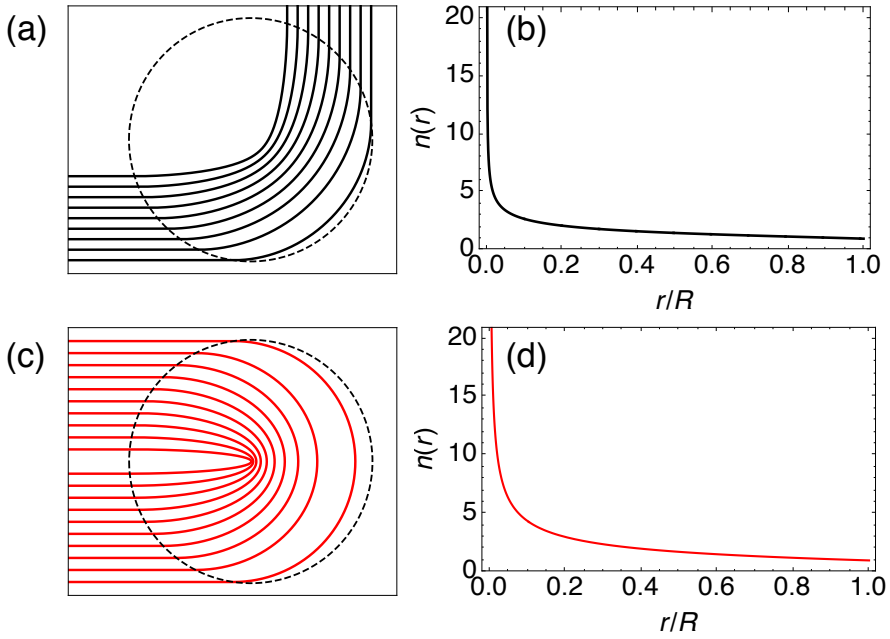

FIGURE 6.1: Images (a) and (c) show the ray paths, and images (b) and (d) give the refractive index profile for the 90° and Eaton lenses (lens radius R), respectively.

A practical problem with these steering lenses is that they require a singular refractive index in the centre, and even a moderately large refractive index is difficult to achieve in most areas of wave physics. One technique to avoid this problem is via transformation optics [136–138]. The profile can also be truncated, but this often results in an incorrect trajectory [111].

Here, we will see that an extremely high refractive index can quite easily be achieved for magnetostatic (dipolar) spin waves in the forward-volume geometry. Although a singular index is obviously still impossible, the refractive index can become high enough to closely match the required refractive index profile of these steering lenses. Micromagnetic modelling is used to demonstrate how two of these lenses can be realized for spin waves in the dipolar regime, and we analyse the lenses' robustness to profile deviations.

6.2 Theory of Spin Wave Steering Lenses

We first consider the properties of the steering lenses, and then see how they may be implemented for spin waves. We will be using the 90° lens [131, 133] and Eaton (180°) lens [130]. Fig. 6.1 compares their respective refractive index

profiles, defined as [135]

$$90^\circ \text{ lens:} \quad (r/R)n^4 - 2n + (r/R) = 0, \tag{6.2.1}$$

$$180^\circ \text{ (Eaton) lens:} \quad n(r) = \sqrt{\frac{2}{(r/R)} - 1}, \tag{6.2.2}$$

where r is the radial coordinate and R is the radius of the lens in each case. Note that the profile for the 90° lens (6.2.1) is defined implicitly here.

As we have seen in the previous Chapter, defining a refractive index profile for spin waves is non-trivial, since the dispersion relation is strongly dependent on the geometry, and is always nonlinear. In some geometries it is also highly anisotropic. The simplest way to implement the rotationally-symmetric profiles is via a geometry with an isotropic dispersion relation, and design each lens for a fixed incident wave frequency, although it should work also for a wave packet with a small frequency spread. The refractive index is defined as the ratio of the wave number inside the lens, $k(r)$, to that outside the lens, k_{ref},

$$n(r) = \frac{k(r)}{k_{\text{ref}}}. \tag{6.2.3}$$

To change the wave number and thus the index for the given wave frequency, we need to change the dispersion relation by varying one of the bulk material parameters, or film thickness.

We then need to choose an isotropic dispersion relation that enables a large change in k, and thus n. This requirement is satisfied in the dipolar-dominated regime, in the forward-volume geometry, where the magnetization is directed normal to the film plane. As we saw in Chapter 2, the dipole-dipole interaction dominates the dispersion for spin wave wavelengths λ of millimeters to micrometers. At the other end of the spectrum, the short-range exchange interaction dominates, for wavelengths from tens to hundreds of nanometers. In the crossover regime, the dispersion curve flattens out before the exchange interaction begins to have a stronger influence. It is this shallow gradient in the crossover regime that enables a large index to be obtained. As per Eq. (2.5.10), the forward-volume dipole-exchange dispersion relation can be written for the angular frequency $\omega(k)$ as

$$\omega(k) = \sqrt{(\omega_H + l_{\text{ex}}^2 \omega_M k^2)\,(\omega_H + l_{\text{ex}}^2 \omega_M k^2 + \omega_M f(k))}, \tag{6.2.4}$$

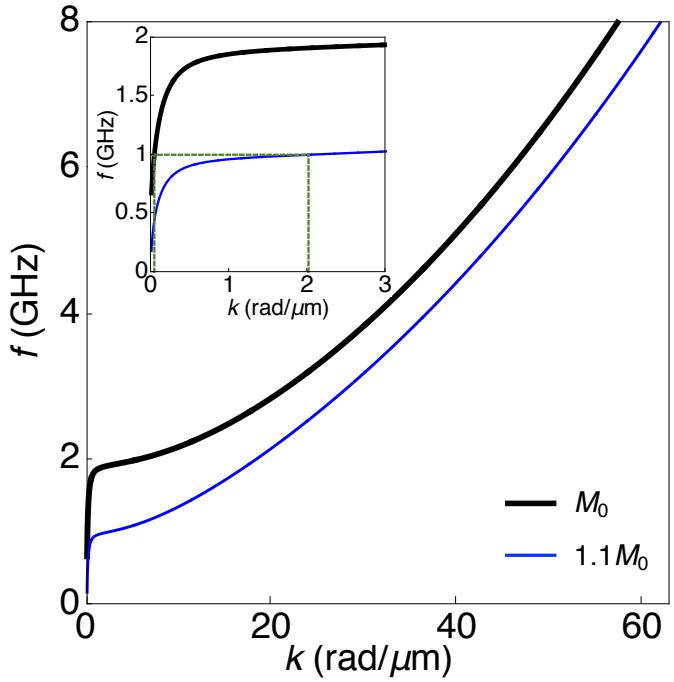

FIGURE 6.2: Dispersion relation $f(k)$ for dipole-exchange spin waves, with a zoom of the dipolar-dominated region shown in the inset. The curves use $M = M_0 = 140$ kA/m (black) or $M = 1.1M_0 = 154$ kA/m (blue). The green dashed line in the inset indicates how much the wave number changes for a fixed frequency of 1 GHz.

where $\omega_H = \mu_0\gamma(H - M)$, $\omega_M = \mu_0\gamma M$, and $f(k) = 1 - \frac{1-\exp(-ks)}{ks}$. Here, μ_0 is the permeability of free space, γ is the gyromagnetic ratio, H is the applied external magnetic field, M is the saturation magnetization, s is the film thickness and $l_{\text{ex}} = \sqrt{\frac{2A_{\text{ex}}}{\mu_0 M_0^2}}$ is the exchange length, where $A_{\text{ex}} = 0.4 \times 10^{-11}$ J/m is the exchange constant. In this Chapter, we will use the following values outside of the lens for the magnetization, applied magnetic field and thickness, respectively, characteristic of yttrium-iron garnet (YIG): $M_0 = 140$kA/m, $\mu_0 H_0 = 200$mT, and $s_0 = 10\mu$m. Also, we neglect any magnetocrystalline anisotropy. The resulting value of exchange length is $l_{\text{ex}} \approx 18$ nm. These values determine k_{ref}, and thus the index will be 1 when $M = M_0$, $H = H_0$ and $s = s_0$. We choose to study a YIG-like material due to YIG's low damping, but the results here should be relevant for any other material (with suitable choice of wave frequency), supposing that the waves obey the dispersion relation (6.2.4).

Using the material parameters listed above, the dipole-exchange dispersion relation is plotted in Fig. 6.2, where the effect of increasing M by 10% is also shown. This small change in M leads to a large change in k, and thus n, due to the shallow gradient in the crossover region between the dipolar-dominated

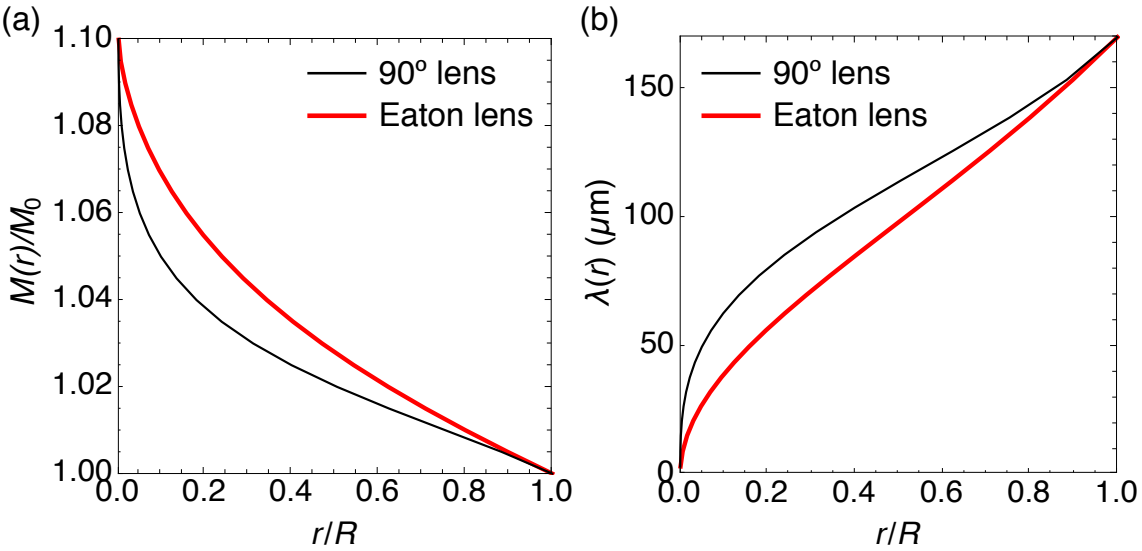

FIGURE 6.3: (a) Magnetization profiles and (b) value of the wavelength along the radius of each lens, for the 90° (black) and Eaton (red) lenses. This is valid for an incident wave frequency of 1 GHz, and other parameters listed in the text.

and exchange-dominated regimes, which we explore in more detail in Chapter 7. The corresponding change in the index in this case is from 1 to 54 for a fixed frequency of 1 GHz. The use of a thick film of 10μm enables a particularly large index to be achieved, because the shallow gradient extends to larger k values. In comparison, a thinner film of 2 μm leads to an index change from 1 to 28 for the same 10% increase in M. Note that the value of f at $k = 0$ marks the lower threshold of the spin wave 'manifold', which corresponds to the ferromagnetic resonance frequency. In Eq. (6.2.4), this occurs when $H = M$ and thus $\omega_H = 0$.

Changing the saturation magnetization is more straightforward in micromagnetic modelling, so we will vary M to vary the index. Using the steering lens profiles (6.2.1)-(6.2.2), along with the dipole-exchange dispersion relation (6.2.4), we can establish numerically the magnetization profile to create each lens. For the choice of material / incident wave parameters listed below, we show the required magnetization profiles in Fig. 6.3 (a), and the corresponding wavelength profiles in (b). For clarity, we show the profiles up to $M = 1.1M_0$, which corresponds to a value of r/R of 1×10^{-5} and 7×10^{-4} for the 90° and Eaton lenses, respectively. So, the majority of the profile is shown except for the singular index region in the very centre.

6.3 Micromagnetic Modelling

6.3.1 Method and Parameters

In order to verify the above analysis, micromagnetic simulations are performed using MuMax3 software [45]. We model a YIG film with thickness $s_0 = 10\mu$m in the z direction, and extent of around 6mm×6mm in the $x-y$ plane. The $x-y$ axes are defined in Fig. 6.4. As before, the saturation magnetization outside each lens is set to $M_0 = 140$kA/m and the bias magnetic field is $\mu_0 H_0 = 200$mT in the z direction. The Gilbert damping parameter is set to $\alpha = 1 \times 10^{-4}$.

We use a cell size of $1.5 \times 1.5 \times 10\mu$m with $4096 \times 4096 \times 1$ cells in the (x, y, z) directions. This choice of cell size is a compromise between resolving the smallest possible wavelength, and being able to represent a large enough lens. From Fig. 6.3 (b), we can see that if we direct the incident waves to avoid the region $r/R < 0.1$, then the smallest wavelength should easily be greater than 15μm, which is 10 times larger than the cell size in the film plane. This approach is a necessity for the modelling, but should not be a limitation for any future experiments. If the profile in Fig. 6.3 can be created, this should represent the refractive index profile almost exactly, except for the very central region. In Appendix J we confirm that this cell size is valid for our choice of parameters, by ensuring that the analytical and numerical dispersions are equal in the $f-k$ range of interest.

We now describe the form of the incident waves[1]. The lenses are primarily designed to steer a collimated beam, and we create this with a magnetic field of the form $[1 - \exp(-0.1\omega_0 t)]\sin(\omega_0 t)$ in time, where $\omega_0 = 2\pi f_0$ and f_0 is the excitation frequency. The prefactor ensures that the beam is gradually ramped up to full amplitude, to maintain the packet's spectral purity. Spatially, this magnetic field is Gaussian in y and has a step profile in x, 8 cells wide, similar to the approach in Ref. [139]. The magnetic field is directed along x, with an amplitude of 0.2 mT, and a frequency of $f_0 = 1$ GHz. The lenses also work well with a wave packet, which we can position to be partly steered by the lens and partly unaffected by it, similar to the approach in Ref. [140]. We create the wave packet by amending the driving magnetic field profile to be of the form $G[x]G[y]G[t]\sin(\omega_0 t - k_0 x)$, where G is a Gaussian in x, y or t, $k_0 = 2\pi/\lambda_0$, and $\lambda_0 \approx 170\mu$m is the spin wave wavelength outside of the lens for excitation frequency f_0. This wavelength is much shorter than the wavelength of light at 1 GHz, justifying the use of the

[1] The details of their implementation in MuMax3 can be found in Appendix I, which describes how to create the wave forms from this and the previous Chapter.

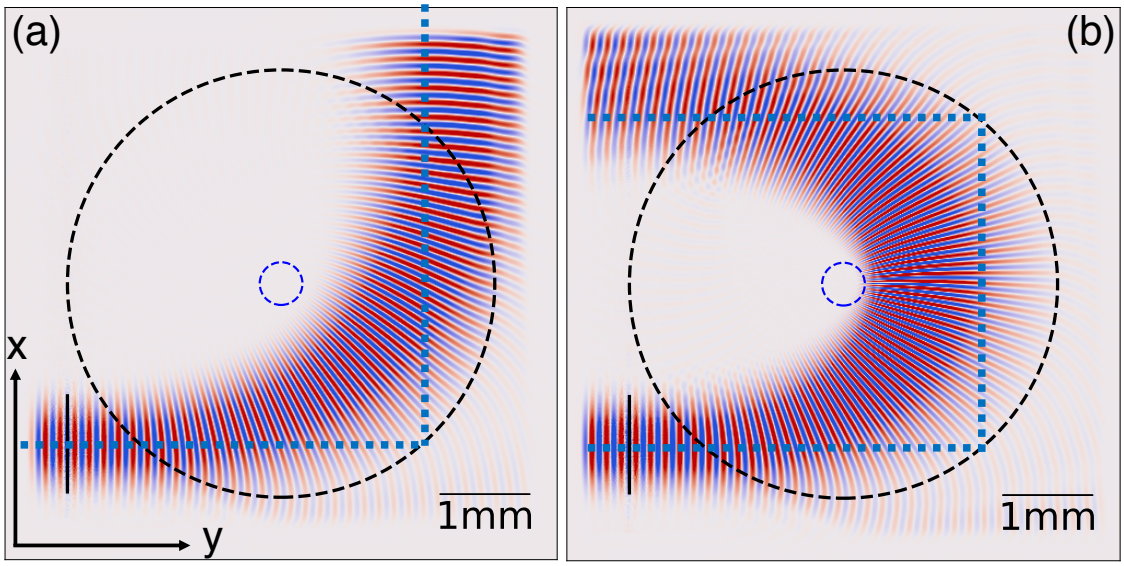

FIGURE 6.4: Steady-state snapshot of beams travelling through the (a) 90° and (b) Eaton lens, sized at $r = 14\lambda$. The inner dashed circle indicates $r/R = 0.1$, and blue dotted guide lines are shown to indicate the 90°/180° angles. The black line on the lower left in each image indicates the source region for the beam.

magnetostatic approximation [21, 141]. Absorbing boundary layers are also employed along the edges in the x and y directions [118], created by increasing the damping constant parabolically to $1 + \alpha$ at the edge.

A perfectly graded index is not possible in finite difference simulations, but a stepped profile can work effectively if the steps are much smaller than the wavelength. This also holds true in experiments, as per the metamaterial approach [142]. In the model, we allocate 235 concentric circular regions to the lens, where the radius of each region is sized to ensure that M steps up by equal amounts each time, until reaching $1.1M_0$ as per Fig. 6.3. However, this stepped profile will not be matched exactly in the numerical model due to the cell size, especially where M is required to change substantially on a length scale which is smaller than the cell size. This means that the index will be changing in large steps towards the centre of the lens, which would lead to strong scattering if the wave encounters these interfaces. More details can be found in Appendix J. This is a limitation of the modelling, and the scattering should be mitigated somewhat by avoiding the central region of $r/R < 0.1$.

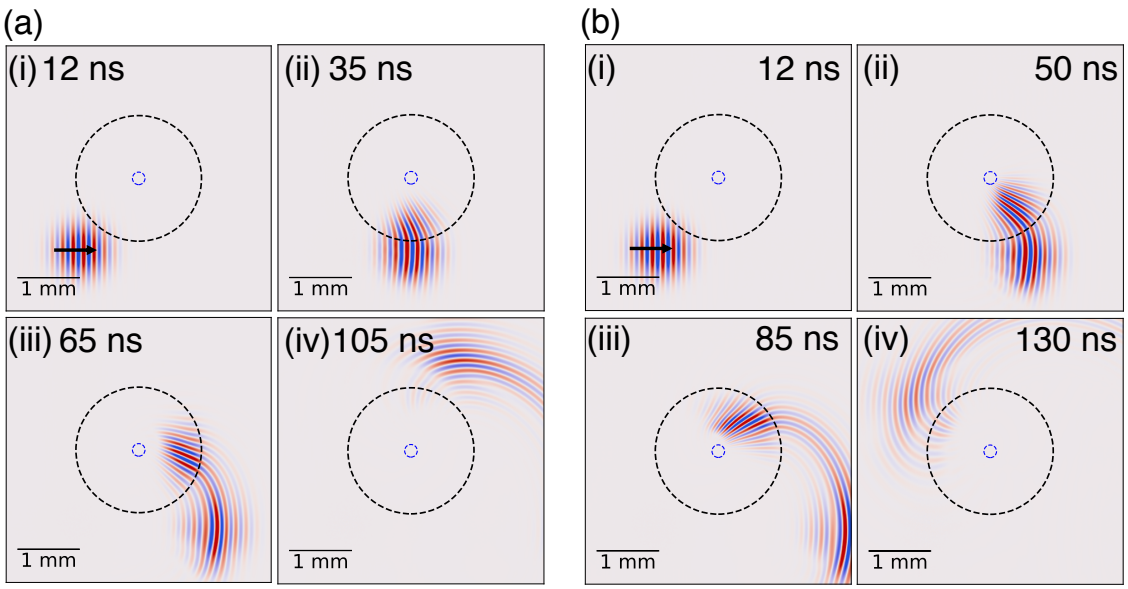

FIGURE 6.5: Consecutive snapshots of the wave packet moving through the (a) 90° and (b) Eaton lenses with $R = 6\lambda$, shown from (i)-(iv). The m_x component is shown, saturated for clarity. The inner circle indicates $r/R = 0.1$. The black arrow in panels (i) indicates the initial propagation direction of the wave packet.

6.3.2 Results: Steering and Beam-Dividing

In Fig. 6.4, we show the beam's trajectory through each lens, after a long enough time has elapsed for a large number of wavelengths of the beam to have moved completely through the lens. Both lenses are sized at $R = 14\lambda_0$, to ensure the beam is mostly contained within the lens. We can see that the 90° lens works particularly well to bend the beam by the required angle, although there is some expected spreading of the beam within and on exiting the lens, making it difficult to see if the trajectory follows the required angle exactly. The Eaton lens is quite sensitive to the placement of the beam, as the beam tends to spread into the central region, where the cell size limits how well we can represent the refractive index profile. By positioning the beam towards the edge of the lens, the central region is mostly avoided and the trajectory is around 175°. Note for both images that the absorbing boundaries have absorbed the edge of the outgoing beam, so the actual outgoing beam is a little wider than shown.

We show the results for the wave packet incident on the 90° and Eaton lenses in Fig. 6.5. We can see that in each case, the portion of the wave packet that enters the lens is steered approximately by the required angle, and remains 'connected' to the other portion of the packet that does not enter the lens and hence continues

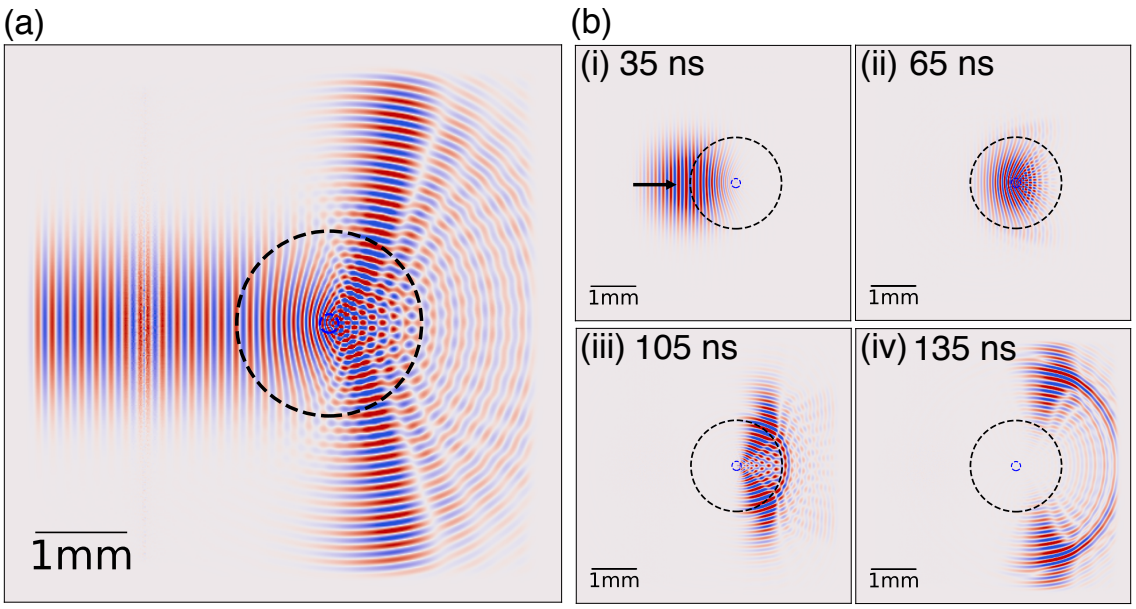

FIGURE 6.6: (a) Steady state snapshot of the beam and (b) snapshots in time of the wave packet moving through the 90° lens ($R = 6\lambda$) to demonstrate its use as a beam divider. The m_x component is shown, saturated for clarity. The inner circle indicates $r/R = 0.1$.

on the original trajectory. Interestingly, this implies that the part of the wave joining these two portions of the wave packet experiences an effective graded index, despite being in a homogeneous medium; its wavefronts must be curved, to bridge the two diverging parts of the wave packet [143]. The use of the lenses in this way is similar to a beam divider, and may be a way to send different portions of the same wave (beam or packet) to more than one output, albeit with some loss en route.

In Fig. 6.6, we show another use for the 90° lens when the beam is instead positioned to enter the lens symmetrically about the centre. In this case, the lens acts as a ±90° half-power beam divider, proposed by Ref. [131]. This works well for both a beam (Fig. 6.6 (a)) and wave packet (Fig. 6.6 (b)), albeit with some scattering from the central region. Note that we have broadened the excitation width across the y direction, to ensure that the beam is exposed to as much of the lens as possible, without having to reduce the lens size. In addition, the excitation amplitude has been reduced to 0.1mT in both cases, to avoid a nonlinear response when the wave encounters the high-index central region. There are a few issues that can lead to the spin angle becoming larger than the tolerable limit of 0.35 rads (20 degrees). Firstly, close to the centre, the index increases rapidly over a small distance, leading to the wave amplitude increasing rapidly as the wave

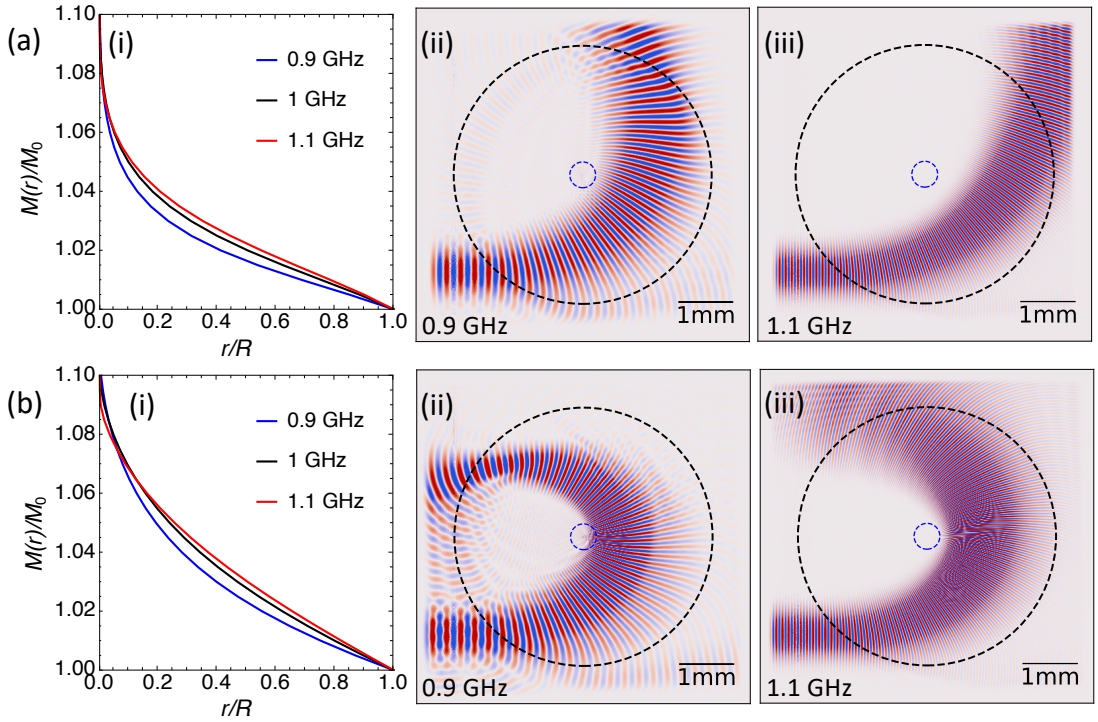

FIGURE 6.7: Demonstration of the effectiveness of the (a) 90° and (b) Eaton lenses from Fig. 6.4, for different incident wave frequencies (ii) $f = 0.9f_0$ and (iii) $f = 1.1f_0$, with $f_0 = 1$ GHz. For comparison, the magnetization profiles which would be required to make the lenses for each frequency are shown in (i). The inner circle indicates $r/R = 0.1$.

is confined to a smaller area (as the wavelength shortens). This is compounded by the following issues related to the cell size: steep steps in M and therefore the index (leading to strong scattering and interference), and poor representation of wavelengths which are smaller than the cell size (which we would expect to create numerical noise). The rationale for reducing the excitation amplitude is to minimise these effects and ensure that, although the spin wave amplitude will necessarily increase, the maximum spin angle is within tolerable limits. The maximum spin angle reached is 0.16 rads, and although the scattering is unavoidable, the majority of the wave packet will pass close to this region without reaching too high an amplitude.

6.3.3 Robustness of the Steering Profile

So far, we have seen the results for each lens when the refractive index profile is designed correctly for the incident wave. However, we would now like to demonstrate that the lenses still work reasonably well when the incident wave frequency is slightly different from the optimal value. As we will see, this is equivalent to designing a slightly incorrect magnetization profile for a certain choice of frequency. In Fig. 6.7, we change the frequency of the incident wave by $\pm 10\%$ from f_0 =1 GHz, and these waves travel along the profile designed to work for an incident wave frequency of f_0, for the 90° lens in Fig. 6.7 (a) and Eaton lens in Fig. 6.7 (b). In panel (i), we show the magnetization profiles that would be required to make the lenses for each frequency. We then show the results for the 0.9 GHz and the 1.1 GHz beams in panels (ii) and (iii), respectively. Recall that these 0.9 GHz and 1.1 GHz beams should rotate by 90°/180° only when they encounter their respective magnetization profiles in panel (i), but they are instead traversing the profile designed for the 1 GHz wave. As a result, we see that the 0.9 GHz beam rotates too much, and the 1.1 GHz beam does not rotate enough in each case. The angles are again difficult to quantify exactly due to the beam spreading, but are around 10°-20° away from the target angle in each case. This suggests that if the wave trajectory is not quite right, then the correct trajectory may be recovered by adjusting the wave frequency accordingly.

6.4 Conclusions

In summary, the work in this Chapter has demonstrated how steering lenses with singular graded index profiles can be almost exactly realized for spin waves with a 10% change in either the external magnetic field or magnetization, in the dipole-dominated regime. The operation of two such lenses (90° and 180° rotation) has been shown in micromagnetic modelling by changing the magnetization, but the theory is applicable for rotation by any angle, and these lenses work from any angle of incidence. As long as the index is smoothly graded, the lenses should be robust to small deviations in the profile, and small deviations in rotation angle may be corrected by changing the incident wave frequency.

We have also highlighted a few different uses for these lenses: to steer beams (the usual application), to act as a wave packet divider (which will also work for a beam), and a $\pm 90°$ half-power beam (or packet) divider. These lenses could

thus have a number of different uses in a future spin wave circuit, by simply positioning an incoming beam or packet appropriately.

More generally, these results demonstrate the potential of magnonics, and in particular the higher-k end of the dipolar dispersion, for realising extreme ranges of the refractive index. It is worth reiterating that this is far more difficult to achieve in other areas of wave physics, making a magnetic film a useful playground to study waves traversing high-range index landscapes.

Chapter 7

Properties of the Magnonic Index

7.1 Introduction

In the previous two Chapters, we explored well-known refractive index profiles from optics, and saw how they can be realised for spin waves, primarily by changing the magnetisation. We have not yet gone into detail about the magnonic refractive index in the forward-volume geometry, particularly how it is governed by the shape of the dispersion relation at different frequencies, which is in turn influenced by the choice of magnetic parameters. This is the topic of this Chapter.

7.2 Dipole-Dominated and Dipole-Exchange Regime

We have already seen that forward-volume spin waves have 3 distinct (yet continuous) dispersion regimes. In this section, we investigate the regimes which extend for the largest range of spin wave wavelengths: the dipolar / magnetostatic regime (wavelengths between mm and a few μm) and dipole-exchange regime (wavelengths of a few μm down to around 50 nm). In particular, we will focus on the interesting crossover region between these two regimes. Let us write out the full dipole-exchange dispersion relation again for clarity:

$$\omega(k) = \sqrt{(\omega_H + l_{\text{ex}}^2 \omega_M k^2)\,(\omega_H + l_{\text{ex}}^2 \omega_M k^2 + \omega_M f(k))}, \tag{7.2.1}$$

where $\omega_H = \mu_0 \gamma (H - M)$, $\omega_M = \mu_0 \gamma M$, $l_{\text{ex}} = \sqrt{\frac{2A_{\text{ex}}}{\mu_0 M_0^2}}$ and $f(k) = 1 - \frac{1-\exp(-ks)}{ks}$. We saw in the previous Chapter that the shallow gradient in the crossover region between the dipolar and dipole-exchange regimes can lead to a large change in k, and thus a large change in the index n. Now we analyse how changing the 3 parameters in Eq. (7.2.1) (M, H and s) modifies the dipole-exchange dispersion curve, and hence the index for a choice of frequency.

Firstly, Fig. 7.1 shows how the dispersion relation changes when varying the parameters from the values $M = M_0 = 140$ kA/m, $\mu_0 H = \mu_0 H_0 = 200$ mT, and $s = s_0 = 10$ μm. These parameters are the same as in the previous Chapter, chosen to show how a large index can be achieved. In panels (a) and (b), we can see that an increase in M is akin to a similar decrease in H, and vice versa, at least for smaller wave numbers. The dispersion in each case shifts downwards or upwards by a similar amount, hence changing k for a fixed value of (incident) wave frequency. The shift of the dispersion is not identical in each case, due to the slightly different contributions of M and H in Eq. (7.2.1). In addition, the dispersion curve is not just being shifted; the shape of the dispersion relation also subtly changes for different values of M_0 or H_0. We saw the consequences of this in Chapter 5 for the Luneburg lens: the magnetisation profile required to make the lens would change for a different choice of fixed external field H_0. So, the change in the shape of the dispersion, and hence the refractive index profile created via a change in M or H, would strongly depend on the choice of the initial parameters. However, as we saw in Chapter 6, there may be some leeway in how 'perfect' the profile must be; a small change in the incident wave frequency might compensate for a slightly incorrect profile, thanks to the curvature of the dispersion relation.

The change of the dispersion relation with s is more complicated, because s only appears in $f(k)$, and only has a significant contribution to the dipolar dispersion when k is small. The effect of reducing the thickness from 10 μm is a steeper gradient of the dispersion curve in the crossover region, which is not beneficial for creating a high index. The thicker the film (in general), the more shallow the slope of the crossover region, although this has little effect beyond 10 μm. As the film thickness reduces, particularly from hundreds to tens of nanometers, the dipolar contribution is far less dominant at low wave numbers and the dispersion curve is exchange-dominated.

In Fig. 7.2, we show how n depends on M, H and s, for different incident wave frequencies f. The index is 1 by definition for $M = M_0$, $H = H_0$ and $s = s_0$, for any value of frequency chosen. In Fig. 7.2 (a)-(c), we can see the distinct dipole-dominated and exchange-dominated regimes, for $f \lesssim 1.9$ GHz and $f \gtrsim 1.9$ GHz, respectively (for this choice of parameters). The transition region between these two regimes is where the dispersion curve flattens. The white regions in panels (a) and (b) correspond to values of M or H for which there are no spin wave solutions for the given value of frequency, i.e. when the bottom of the spin wave manifold is above the chosen value of frequency. Note that M/M_0 in (a) and (d)

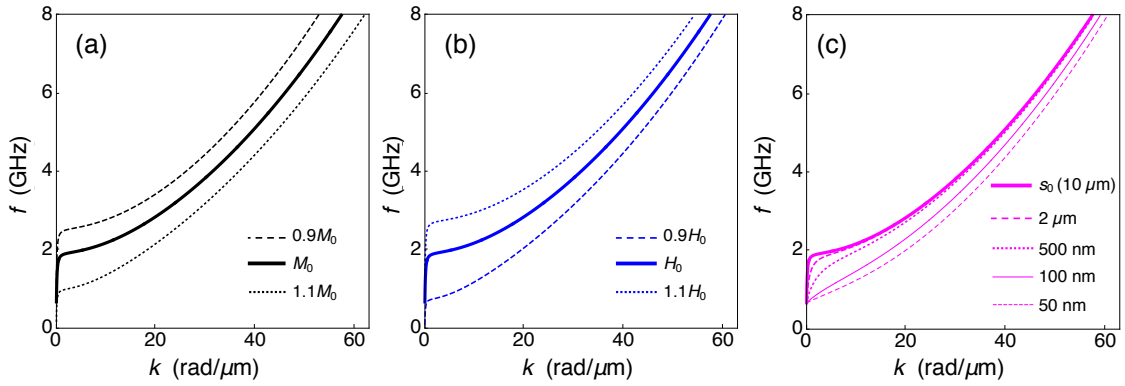

FIGURE 7.1: Dispersion relation for the dipole-exchange regime, showing the change in the dispersion curve when varying (a) magnetisation, (b) external field, or (c) film thickness.

and H/H_0 in (b) and (e) are limited to ensure that $M \leq H$, i.e. to keep the internal magnetic field positive and thus avoid any instability. In addition, the smallest value of f corresponds to a maximum wavelength of 1mm when the index is equal to 1.

We can see from Fig. 7.2 that an increase in the magnetization or a decrease in the magnetic field / thickness is required to increase the index, for any value of frequency. For the former case, this may be achieved via cooling (as heating naturally reduces the magnetization [144]) or doping [117]. Strikingly, Fig. 7.2 shows that just a relatively small change in M or H is required to produce a dramatic change in the index in the dipolar regime. The index may even exceed 100 for very low frequencies, but this occurs as $M \to H$, so the magnetic system is likely to be less stable in this case. As we saw in the previous Chapter, the dipolar regime is therefore ideal to create extreme refractive index profiles; even an index change of around 50 can form the majority of the Eaton lens profile very well. In addition, refractive index profiles that require only a small change in the index may be created in this geometry by a tiny change in the same parameters, as we saw in Chapter 6.

Although we show the variation of the index with thickness according to (7.2.1), a graded index profile created in this way may induce complicated static or dynamic demagnetising fields, though these effects may be reduced by slowly changing the thickness over a large distance. Theoretically, an index up to 100 may be achieved by shrinking s by a factor > 100, according to Fig. 7.2. In Fig. 7.1, we see that this occurs because the dispersion curve arches outwards to adopt a k^2-dependence for thinner films, leading to a very large change in k for a fixed

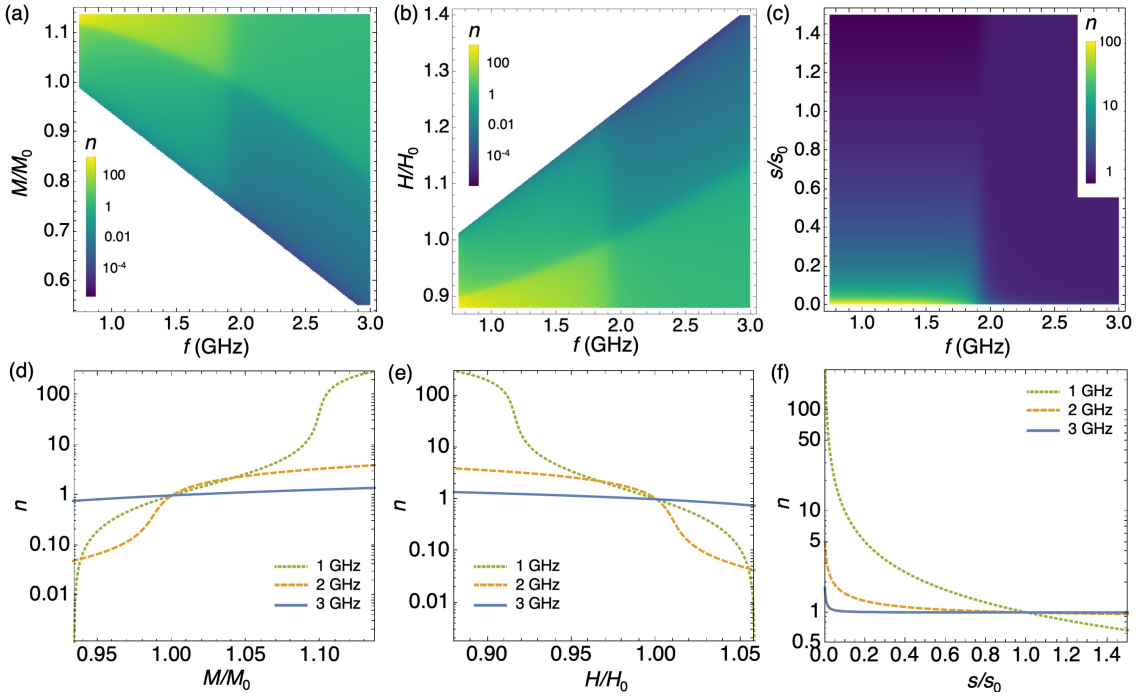

FIGURE 7.2: The dependence of the magnonic refractive index on (a, d) magnetization, (b, e) magnetic field and (c, f) film thickness. In (d)-(f), this dependence is shown for waves with frequencies of 1 GHz (green, dotted), 2 GHz (orange, dashed) and 3 GHz (blue). In (a)-(c), the colour scale is logarithmic, along with the n axis in (d)-(f).

incident wave frequency in the dipolar regime. Also, as mentioned in Chapter 5, the index is directly proportional to the change in the thickness for purely dipolar spin waves, regardless of the values of M or H. So, changing s would be much more useful than changing the other parameters, as long as the gradient is smooth and slowly changing. This is the main issue with changing the thickness: it is not clear how slowly-changing the graded index would need to be to avoid complex demagnetising fields (which in turn change the index). Although beyond the scope of this work, it would form an interesting, yet computationally challenging, micromagnetics study to test this; requiring a great deal of computational power for good resolution in all 3 spatial dimensions (for each time step of the simulation).

Although the usual procedure is to increase the refractive index, it is also possible to *reduce* the index, and thus k value (i.e. lengthen the wavelength) by a factor of 100 by a 6-7% decrease of M or increase of H, in this dipolar regime. This is not quite as interesting as the case for light, where $n = c/v$ and $n = 1$ always corresponds to the universal speed limit c, so the (phase) velocity in the material may exceed that of light[1]. However, it does mean that we can increase or decrease the spin wave wavelength significantly by a small change in the parameters.

Let us consider the dipole-exchange regime before we move on to the purely exchange regime. This is where we choose an incident wave frequency that resides at/just after the crossover region of the dispersion curve, which is around 2 GHz for our choice of parameters. In this case, the index may be increased from 1 up to around 3 via a 10% change in the parameters, which is not quite as dramatic as the results for the dipolar regime. We can see from Fig. 7.1 that the dispersion graphs curve upwards for higher frequencies (towards a parabolic dependence on k), so it is increasingly more difficult to achieve a larger change in k with larger frequencies. Due to the shallow gradient for smaller k values, the index can be decreased from 1 to 0.05 with a small (6-7%) change in M or H, or even more for a larger change in these parameters.

Note that we have not included anisotropy in our calculations here or in previous Chapters, when studying dipolar or dipole-exchange spin waves. According to Ref. [145], the inclusion of cubic anisotropy (such as for YIG [5]) in a

[1] In our case, the index is set to 1 arbitrarily; we choose it to be the index of the unmodified material that we are working with. This is perfectly acceptable because only the *change* in n is important. We also do not have a cosmically significant reference material or speed limit to refer to for spin waves.

perpendicularly-magnetised film can lead to the addition of a linear term (in H) in the internal field, corresponding to a shift in frequency of the dipole-exchange dispersion curve. Therefore, we would expect the results to be similar to changing H for dipole-exchange spin waves in YIG. The situation is much more complicated for other forms of anisotropy, and this is not relevant for this work.

7.3 Exchange-Dominated Spin Waves

For the 3 GHz wave frequencies in Fig. 7.2, we saw that the growing contribution of the exchange interaction means that a larger change in one of the parameters is required, for a comparatively modest change in n. We encountered this earlier in our brief analysis in Section 5.6, where we saw how much $M(r = 0)$ would have to change to create the Luneburg lens (with a maximum index of 1.4), for different values of field and frequency. We concluded that an index of 1.4 would be unfeasible for exchange-dominated spin waves when changing M only, because M would have to change by an amount larger than the zero-temperature magnetisation value. However, we did not consider the properties of the index in this regime, nor its dependence on H. We do so in this Section.

Note that we will use the same parameters for YIG as before (with M_0, H_0 and s_0), although there may be better materials to use for exchange spin waves, such as Permalloy (used for our earlier studies in the exchange regime). The results should be equivalent for any other material; it just means a different choice of M_0 or H_0, and perhaps a different wavelength limit where the dipolar contribution can be completely neglected. Just to elucidate this point, recall from Chapter 2 that the dispersion relation Eq. (7.2.1) in the exchange regime is quadratic in k, given by Eq. (2.5.4). However, the dipole / dipole-exchange / exchange regimes are continuous spectra, without clear boundaries where one finishes and another commences, and the approximate 'boundaries' differ strongly with material parameters. For this thin film of YIG, Eq. (2.5.4) is most accurate for wavelengths less than around 15 nm; the dipolar contribution still has a small but noticeable effect down to this wavelength. The following results using either dispersion relation still only differ by a few percent, but for comparison with the results in the previous section we only use Eq. (7.2.1) in what follows[2].

[2]For wavelengths around 15 nm and below, the dispersions given by Eq. (7.2.1) and Eq. (2.5.4) are mostly indistinguishable, although the frequency is rather impractically high (hundreds of GHz) — this is one good reason why a thick sample of Permalloy is preferable for ultra-short wavelengths, since the frequencies are lower (typically below 100 GHz, as we saw in Chapter 3).

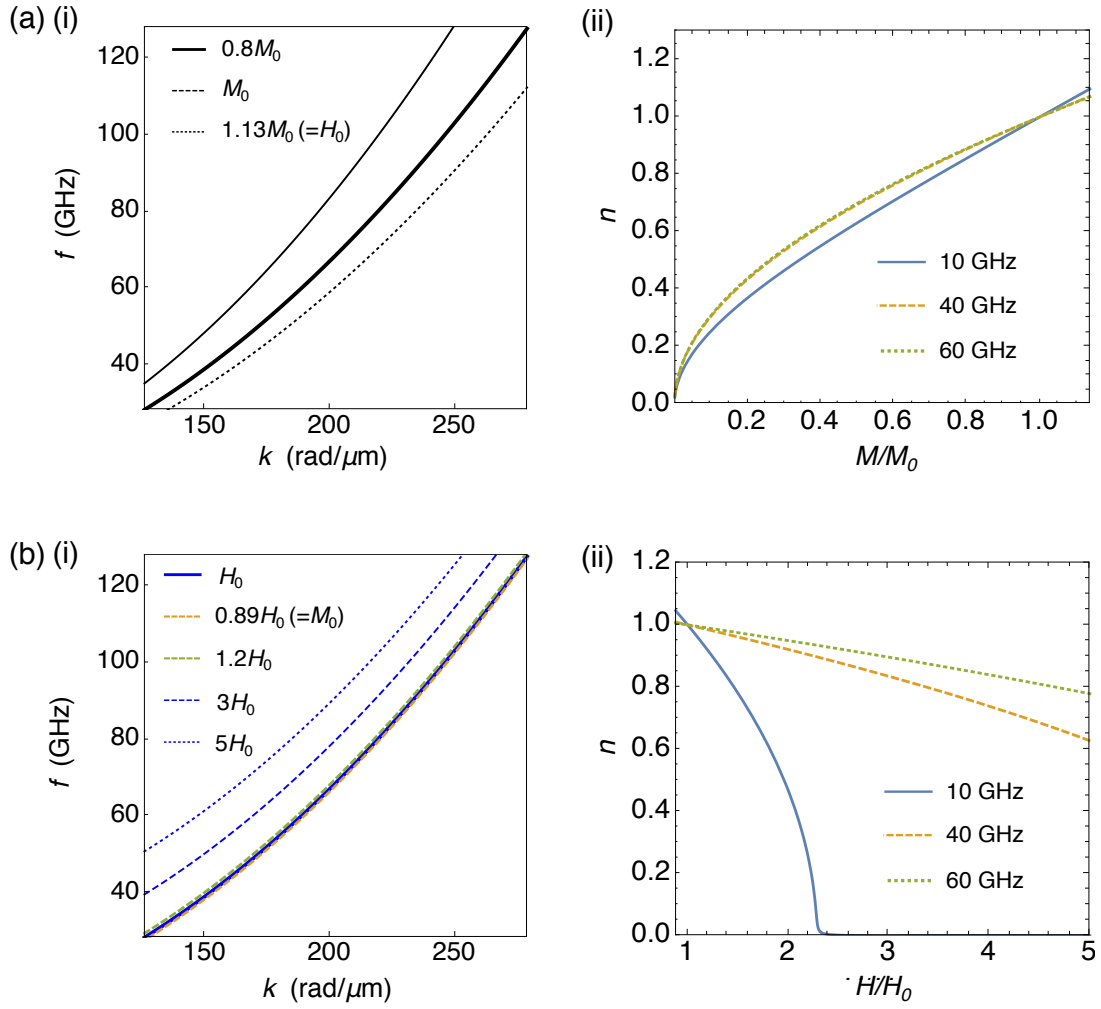

FIGURE 7.3: The dependence of the (i) high-frequency range of the dispersion relation and (ii) magnonic refractive index (for different values of incident wave frequency) on (a) the magnetization and (b) magnetic field for exchange-dominated spin waves (wavelengths $\lesssim 50$ nm). For both graphs in (i), the minimum and maximum wave number corresponds to wavelengths of 50 nm and 23 nm respectively, the latter corresponding to l_{ex} for $M = 0.8M_0$. The largest value of M used in (a) is H_0, and the smallest value of H used in (b) is M_0, to ensure that $M < H$.

In Fig. 7.3, we can see how the dispersion (panel (a)) and n (panel (b)) varies with M and H for exchange spin waves. Panels (a,b) are equivalent to the earlier Figures 7.1 (a,b) and 7.2 (d,e), but for much larger frequencies and for a much smaller (non-logarithmic) range in the index, respectively. In panels (a) (ii) and (b) (ii), the result for a 10 GHz incident wave frequency is included for comparison. All graphs are plotted using the dipole-exchange dispersion relation Eq. (7.2.1). Since we are studying a thin film here, we do still have the requirement of $M < H$, and this is accounted for in the graphs[3]. The range of wave numbers corresponds to wavelengths between 50 nm and 23 nm, and the latter is the exchange length for $M = 0.8M_0$.

As mentioned in the previous section, it becomes increasingly difficult in the exchange-dominated regime to achieve a large change in k for a small change in the material parameters, because the dispersion graph curves unfavourably (with k^2). For example, a realistic increase in M from M_0 to $1.1M_0$, for a 40 GHz spin wave, shifts the wavelength by about 5%, from 41 nm to 39 nm, for our choice of parameters. As we can see from Fig. 7.3, for our choice of M_0 and H_0 we can reduce the index much more than we can increase it, but we also have to change M or H by a comparatively large amount, especially as the frequency increases (panel (b)). In the case of changing M by such a large amount, it is not clear that A_{ex} would remain a constant, and we discuss this in the following subsection. The field is more easy to increase in principle (M and H can only ever decrease to 0), but the graph is limited at $\mu_0 H$ =1 T which is around the experimental limit. In both cases, the index might only be reduced[4] to around 0.8 for a reasonable change in M or H.

This sounds much less impressive than the results for the dipolar waves, but it must be emphasised that the exchange regime only occupies a small range of wavelengths. Furthermore, the wavelengths under consideration are the smallest possible wavelengths for spin waves. So, although a large change in the index may be unfeasible, this is not entirely surprising since the wavelengths cannot be reduced by, say, 100 or even 10 times anyway; the spin wave wavelength may be less than the exchange length in that case. Perhaps beneficially, exchange spin waves are therefore not likely to be sensitive to small modifications in material

[3]For an infinite sample, this is not necessarily the case since the demagnetising film can be neglected - see the discussion in Chapter (2.4.1).

[4]Of course, we are assuming here that M and H start from the values we have given them; M_0 and H_0. We could of course make M_0 smaller, and H_0 larger, and thus *increase* the index by an equivalent amount, it is all a matter of perspective!

parameters, which will occur naturally on smaller length scales (through material defects).

7.3.1 Form of n for Exchange-Only Regime

The work above is for exchange-dominated spin waves, and the results include the small contribution from the dipolar interaction, which reduces with increasing k. Here, we will see that when the dipolar contribution can be completely neglected, then there is an analytical expression for the index in terms of the material parameters. In this case for large k, the term $\omega_M f(k)$ in Eq. (7.2.1) is negligible, and ω simplifies to the expression Eq. (2.5.4),

$$\begin{aligned} \omega &= \omega_H + l_{\text{ex}}^2 \omega_M k^2 = \gamma\mu_0(H_0 - M_0) + \frac{2A_{\text{ex}}}{\mu_0 M^2}\gamma\mu_0 M k^2 \\ \therefore \omega &= \gamma\mu_0(H_0 - M_0) + \frac{2\gamma A_{\text{ex}}}{M}k^2, \end{aligned} \tag{7.3.1}$$

where we have expanded l_{ex}, ω_H and ω_M to be clear about the functional dependences. We can see that H_0 will have less influence on the dispersion for large k, unlike M. Let us now rearrange for k, since we can then obtain an analytical expression for the index:

$$k = \sqrt{\frac{M(\omega/\gamma - \mu_0(H_0 - M_0))}{2A_{\text{ex}}}}. \tag{7.3.2}$$

We can see that this is equivalent to Eq. (3.3.11) from Chapter 3, if we convert from SI units (above) to Gaussian units (in Eq. (3.3.11)), and recognise that $\alpha = 2A_{\text{ex}}/(\mu_0 M^2) = l_{\text{ex}}^2$ in SI units. Also, we considered an infinite sample in Eq. (3.3.11), so there is no demagnetising field in that case. We varied the anisotropy (and thus defined it separately) in that Chapter, but we know that we could vary H to have the same effect.

So, we now have an analytical expression for k in terms of the frequency, and we can use the familiar expression (2.6.1) to define the index (and writing that M and H are our variable parameters),

$$n = \frac{k(r)}{k_0} = \sqrt{\frac{M(r)}{M_0}\left(\frac{\omega/\gamma - \mu_0[H(r) - M(r)]}{\omega/\gamma - \mu_0[H_0 - M_0]}\right)}. \tag{7.3.3}$$

We can see in the numerator that as ω increases, the effect of H on the index will become less significant, as we saw earlier. Notice that the exchange constant has been cancelled through here, because we assume it is constant in space. This should be valid if M is varied gradually and by a small amount [21] (p.179-180), but certainly the results here are an approximation. A far more detailed study would need to be carried out to consider the full effect on the exchange constant[5] for large changes in M.

Note that for an infinite sample (studied in Chapter 3 for example), taking into account the assumptions above, then for a fixed external field (or rather, effective field, if anisotropy is considered)

$$n = \sqrt{\frac{M(r)}{M_0}} \quad \textit{(infinite sample)}, \tag{7.3.4}$$

which is valid for any frequency. We saw that in the magnetostatic regime $n = s_0/s(r)$, with s_0 the fixed (reference) thickness. It is pleasing that there is another frequency-independent method of varying the refractive index, although it is only accurate in an infinite sample for the small range of exchange-only spin waves, and also for small and gradual changes in M. However, it is likely that it could remain approximately valid as long as the exchange term dominates.

As a final note, it is worth highlighting that the index n can be extracted from the exchange regime Linearised Landau-Lifshitz equation that we saw in Chapters 3 and 4 (showing a simple version of the homogeneous equation here from Eq. (3.2.17)),

$$\Bigg[\nabla^2 - \underbrace{\frac{\beta(r)}{\alpha} + \frac{\Omega}{\alpha} - \frac{H(r)}{\alpha M(r)}}_{k^2(r)}\Bigg]\varphi(x,y) = 0. \tag{7.3.5}$$

since we can compare it directly to the Helmholtz equation,

$$\left[\nabla^2 + k_0^2 n(x,y)^2\right]\varphi(x,y) = 0. \tag{7.3.6}$$

Using the definition $n = \frac{k(r)}{k_0}$, one simply needs to divide the expression for $k(r)$ by k_0 as before.

[5] An interesting study which considers the spatial dependence of A_{ex} and M in magnonic crystals can be found in Ref. [146], for example. The parameters in magnonic crystals vary far more abruptly and rapidly than in our situation, however there is a detailed discussion about the effect on the exchange energy in that case.

7.4 Conclusions

In this Chapter, we have analysed how the properties of the forward-volume dispersion relation can be changed to vary the index, in the dipolar to exchange regimes.

The dipolar regime is the most unusual. For thicker films (around 10 μm), the shallow gradient of the dispersion curve extends for large k values, meaning that a huge refractive index, even exceeding 100, may be achieved for spin waves when changing M or H by a small amount (around 10 %). Such large values of n may be achieved by changing the thickness also, but by a much greater proportion of the original value, from micrometres to tens of nanometres. However, it is likely that demagnetising fields will interfere with this index profile, unless the profile is changed very gradually. Further study would be required to confirm the viability of changing s to change the index.

For dipole-exchange spin waves, a much more modest increase in the index of around 3 can be achieved for the same change in the parameters. However, it is much easier to reduce the index (i.e. lengthen the wavelength) by a factor of 100 in this case, by a similarly small change in M or H as in the dipolar regime (around 10%). This is just the reverse operation of increasing the index by 100 times from the dipolar to the dipole-exchange regimes[6]. Whether the index is increased or decreased depends on the choice of frequency f_0 for the reference values M_0, H_0 or s_0, or vice versa.

The exchange regime only occupies a small range of spin wave wavelengths, and due to the k^2 dependence of the dispersion curve, only a very small increase in the index (around 5%) can be achieved with a 10% change in the parameters. This might mean at least that exchange spin waves are less affected by small defects, but may imply that graded refractive index profiles, created by varying one parameter, are best used with dipolar or dipole-exchange spin waves instead.

[6]By choosing a fixed frequency in the dipolar regime for reference values M_0, H_0 and s_0 (for which $n = 1$), the dispersion curve must be shifted downwards to increase the index. When choosing a fixed frequency in the dipole-exchange regime for the same values of M_0, H_0 and s_0, the dispersion curve must be shifted downwards by the same amount to reduce the index by the same amount.

Chapter 8

Concluding Remarks and Future Work

In this thesis, the variation of magnetic parameters has been investigated in ferromagnetic materials, to create a 'magnonic refractive index profile'. These profiles have been investigated either as a source of spin waves in Chapters 3 and 4, or as a focusing / steering device in Chapters 5 and 6 respectively. The final investigation in Chapter 7 studies the magnonic refractive index itself, and its dependence on the magnetic parameters in different frequency regimes. In each case, we have considered waves described by an isotropic dispersion relation.

Let us first reflect on the observations from Chapters 3 and 4. By studying exchange-dominated spin waves, we have seen that any feature in a magnetic material, where the magnetic parameter is varied in space (gradually or sharply), may act as a source of spin waves when excited by a uniform, harmonic magnetic field. We may extrapolate this mechanism to other spin wave regimes, or indeed any other wave; it could be considered as the complementary operation to the excitation of propagating waves in a uniform sample by a local, non-uniform source (i.e. via an antenna).

Exciting a magnonic index profile does not guarantee spin wave emission, however. Certain conditions could lead to standing waves within the potential, and thus complete suppression of spin waves from it, and we saw this clearly for the rectangular potential barrier in Chapter 3. The situation for the Pöschl-Teller (P-T) potential well profile, which is naturally formed from a Bloch domain wall (with a fixed potential height) studied in Chapter 4, is somewhat different. The unusual properties which make it a frequency-independent transmitter of incoming waves seem also to make it either emit or suppress (spin) waves of any frequency, depending on the choice of the potential height. Despite the height being a fixed quantity for domain walls, this gives a unique insight into the unusual

situation of the Schrödinger-like equation with a P-T potential well *and* source. Although we observed the effect of the frequency-independent spin wave confinement in this case, its analytical origins have not been probed, and could form an interesting additional investigation, perhaps extending the study in Ref. [91].

It also appears from this work that potential barriers are more efficient spin wave emitters than potential wells, judging by the spin wave amplitude emitted from the two profiles studied here. Further work in this area may include extending the theory to different profiles to test this. In addition, it would be interesting to confirm that the spin wave emission mechanism is valid in other spin wave regimes, or for the generation of any other wave, as we would presume. It would also be interesting to see if a Neél domain wall exhibits similar behaviours to the Bloch domain wall, or perhaps the study could be extended to other magnetic textures, such as vortices, skyrmions or Bloch points.

In Chapters 5 and 6, a gradual change in the magnetisation M of a YIG-like film was created to focus / steer *propagating* spin waves. We saw that an increase in the magnetisation is required to increase the index, which may be achieved by local cooling, for example. The results of the micromagnetic modelling showed that the focusing and steering lenses worked as the theory predicted, even for a lens radius of only 6 times the wavelength. There are many more graded index lenses to choose from (see for example Refs. [131, 135]), and the results from this work should form a general blueprint of how to make them for spin waves. The starting point is having an isotropic dispersion relation, at least for rotationally-symmetric lenses, and this was achieved in this work in the forward-volume geometry.

These lenses were designed for magnetostatic (dipolar) spin waves, of wavelengths from tens to hundreds of micrometres. Surprisingly, the Luneburg lens (requiring a change in the refractive index from 1 to 1.4) can be made in this regime by increasing M by less than than 2%. The steering lenses require a singularity in the centre, and although this is not physically achievable, the lens profiles can be made almost exactly with just a 10% increase in M, except for the central $< 0.1\%$ of the lens. The index for this change in M reaches 54, and it is due to the shape of the dispersion curve for these spin waves.

In Chapter 7, we saw how the form of the dispersion relation influences the magnonic refractive index, for a range of spin wave frequencies. We saw how the dispersion curve could be changed when varying the parameters M, external magnetic field H and thickness s, and analysed the resulting effect on the index. As we saw in Chapters 5 and 6, the most interesting regime, as far as the index

is concerned, is for dipolar spin waves. In this case, due to the shallow gradient in the crossover region between the dipolar and dipole-exchange regimes, a huge change in k and hence n can be achieved when the material parameters are modified by just a small amount. An index in excess of 100 is theoretically achievable in this regime by changing M, H, or even s, although the latter may induce complicated demagnetising fields unless changed very gradually with position. Further work would need to confirm if changing s is practically possible.

The dipole-exchange regime offers a moderate increase in the index up to about 3, but the index can more easily be reduced by 100 times by a 10% change in M or H. As the influence of the exchange interaction increases, the k^2 dependence of the dispersion relation means it is increasingly difficult to achieve a larger change in k for a fixed frequency, by changing M or H; a 10% change in M now only leads to a 5% change in n. The change in H required is also much greater, since M has a stronger influence on the exchange dispersion relation for exchange spin waves. On the plus side, these waves may therefore be less sensitive to changes in M, H or s, which may occur naturally on small length scales.

This work has covered the main influences on the refractive index for spin waves in various frequency regimes, but has not investigated the vast parameter space that could be manipulated to vary the index further; such as the various forms of anisotropy, or a combination of different parameters. Future work may also consider extending these analyses to other spin wave regimes, such as for anisotropic backward-volume or surface spin waves. However, the directional-dependence combined with the nonlinear dispersion relation means that the index will be even more narrowly defined in those cases.

Overall, this work aims to support and extend the existing literature, to show that interesting and — above all — *useful* phenomena can arise from what might ordinarily be deemed a 'defect'; a nonuniformity of the material parameters. Magnetic nonuniformities excited by a spatially uniform harmonic field may emit or confine spin waves. Careful shaping of magnetic nonuniformities can result in extreme changes in the spin wave properties. Finally, spin wave research may have an important role to play in wave-based physics research more broadly, especially in realising nonuniform (graded index) profiles which are much more challenging to create in other areas of wave physics, such as the Pöschl-Teller potential and steering lenses.

Appendix A

Forward Volume Magnetostatic Modes of a Thin Film

A.1 Derivation

In this Appendix, we describe the derivation of the Walker equation, which originates from the magnetostatic Maxwell equations. The Walker equation contains the electrostatic scalar potential, and this is the function which describes the magnetostatic spin waves. We find the form of these spin waves which fit the boundary conditions at the ferromagnet-dielectric interfaces of a thin film, and establish the dispersion relation for forward volume spin waves.

A.1.1 The Walker Equation

We loosely follow the approach in [5, 147, 148], where our geometry is shown in Figure A.1: we have a perpendicularly magnetised, infinite (in the $x-y$ plane) *thin* (in the z plane) film. We start with the Magnetostatic Maxwell equations in Gaussian units:

$$\nabla \times \mathbf{H} = 0, \tag{A.1.1a}$$

$$\nabla \cdot \mathbf{B} = 0. \tag{A.1.1b}$$

We then write the magnetisation $\mathbf{M}$ and internal magnetic field $\mathbf{H}$ as a static component plus a small time-dependent component, i.e.

$$\mathbf{M} = \mathbf{M_0} + \mathbf{m}\exp(i\omega t), \tag{A.1.2a}$$

$$\mathbf{H} = \mathbf{H_i} + \mathbf{h}\exp(i\omega t), \tag{A.1.2b}$$

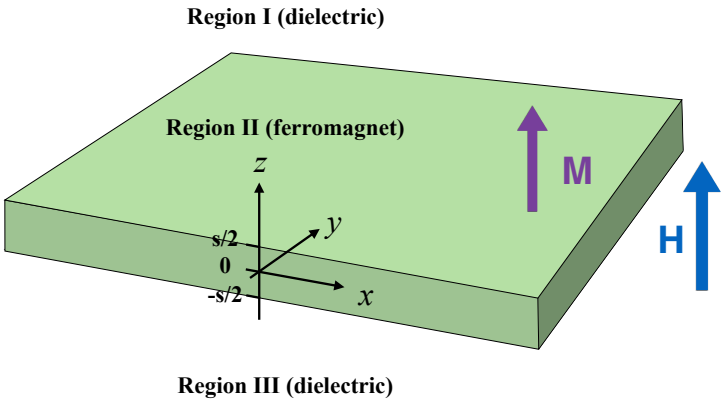

FIGURE A.1: The system under consideration, with thickness s and infinite extent in the $x-y$ plane.

where $\mathbf{M}_0$ and $\mathbf{H}_i$ are directed along z (this is the usual convention), $\mathbf{m}$ can only have x and y components (in the linear excitation regime, the length of the magnetisation does not change) and $\mathbf{h}$ may have x, y and z components. We know that these small quantities must also obey Maxwell's equations Eq. (A.1.1a) and Eq. (A.1.1b). Using the relation ([5], p.113) $\mathbf{B} = \hat{\mu} \cdot \mathbf{H}_i$, we rewrite Eq. (A.1.1b) as

$$\nabla \cdot (\hat{\mu} \cdot \mathbf{h}) = 0, \tag{A.1.3}$$

with $\hat{\mu}$ the permeability tensor. Next, from Eq. (A.1.1a), since the curl of a gradient is always zero, i.e. $\nabla \times (\nabla \phi) = 0$, we can write

$$\mathbf{h} = -\nabla \psi, \tag{A.1.4}$$

where ψ is a magnetic scalar potential (the choice of sign is arbitrary - and is chosen to match the form of the electrostatic scalar potential). We can substitute this into Eq. (A.1.3) to find

$$\nabla \cdot (\hat{\mu} \cdot \nabla \psi) = 0, \tag{A.1.5}$$

and this is the general form of the Walker equation ([5] p.140).

Now, we need to understand the form of $\hat{\mu}$ which goes into the Walker equation — this is usually done by linearising the Landau-Lifshitz equation (c.f. [147–149]), and results in the following form of μ (given in Gaussian units - the SI

version is obtained by multiplying $\hat{\mu}$ by μ_0):

$$\hat{\mu} = \begin{pmatrix} 1+\kappa & -i\nu & 0 \\ +i\nu & 1+\kappa & 0 \\ 0 & 0 & 1 \end{pmatrix}, \tag{A.1.6}$$

with

$$\begin{aligned} \kappa = \frac{\omega_H \omega_M}{\omega_H^2 - \omega^2}, \quad \nu = \frac{\omega \omega_M}{\omega_H^2 - \omega^2}, \\ \text{(Gaussian units:)} \quad \omega_M = 4\pi\gamma M_0, \qquad \text{(SI units:)} \quad \omega_M = \gamma\mu_0 M_0, \\ \text{(Gaussian units:)} \quad \omega_H = \gamma H_i, \qquad \text{(SI units:)} \quad \omega_H = \gamma\mu_0 H_i, \end{aligned} \tag{A.1.7}$$

where all of the details of the demagnetising field are now 'hidden' in $\mathbf{H}_i$ in ω_H. This is the same approach as in Ref. [148], and the equations so far apply to an arbitrary shape with a *uniform internal magnetic field*.

Now, as per the approach in Ref. [148], we can specify that the demagnetising factor $N_z = 4\pi$ (in Gaussian units, or 1 in SI units) for a ferromagnetic slab, and because it is effectively infinite in the $x-y$ plane then $N_x = N_y = 0$. This is important in determining the internal field $\mathbf{H}_i = \mathbf{H}_0 + \mathbf{H}_\mathrm{D}$, which is

$$\mathbf{H}_i = \mathbf{H}_0 - 4\pi\mathbf{M} \quad \text{(Gaussian units)}, \qquad \mathbf{H}_i = \mathbf{H}_0 - \mathbf{M} \quad \text{(SI units)}, \tag{A.1.8}$$

with $\mathbf{H}_0$ the external ('bias') field and $\mathbf{H}_\mathrm{D}$ the demagnetising field.

A.1.2 Form of the Magnetostatic Potential in each Region

Next, we need to establish our boundary conditions. We require the tangential component of $\mathbf{h}$ to be continuous (due to Ampere's law - see [150] Section 6.3.3, p.273). We will call the tangential component $\mathbf{h}_t = -\nabla_t \psi$ where

$$\nabla_t = \frac{\partial}{\partial x}\hat{\mathbf{x}} + \frac{\partial}{\partial y}\hat{\mathbf{y}}. \tag{A.1.9}$$

So, let us specify at the boundaries between region I and II, and region II and III:

Boundary Condition 1:

$$\nabla_t \psi^I\Big|_{z=s/2} = \nabla_t \psi^{II}\Big|_{z=s/2}, \tag{A.1.10}$$

$$\nabla_t \psi^{II}\Big|_{z=-s/2} = \nabla_t \psi^{III}\Big|_{z=-s/2}. \tag{A.1.11}$$

The second boundary condition is for the normal component of $\mathbf{b} = \hat{\mu}\mathbf{h} = -\hat{\mu}\nabla\psi$ to be continuous along z (magnetic field lines are closed loops), so

$$\underline{\text{Boundary Condition 2:}} \qquad \left.\frac{\partial\psi}{\partial z}^{I}\right|_{z=s/2} = \left.\frac{\partial\psi}{\partial z}^{II}\right|_{z=s/2}, \tag{A.1.12}$$

$$\left.\frac{\partial\psi}{\partial z}^{II}\right|_{z=-s/2} = \left.\frac{\partial\psi}{\partial z}^{III}\right|_{z=-s/2}. \tag{A.1.13}$$

Finally,

$$\underline{\text{Boundary Condition 3:}} \qquad \psi \to 0 \text{ as } z \to \pm\infty. \tag{A.1.14}$$

We will follow the approach in [5] p.152. We will suppose that the solution for ψ in the ferromagnet consists of propagating waves in the $x-y$ directions, and waves which propagate in the z direction - but because of the boundaries, we could have waves propagating towards one surface ($\psi_z \sim \exp[ik_z z]$), then reflecting off it ($\psi_z \sim \exp[-ik_z z]$). These multiply reflected waves will superpose to form a standing wave[1]. We write

$$\psi_{\text{II}} = \psi_0 \exp[i\mathbf{k}_{\text{t}}\cdot\mathbf{r}]\left(\frac{\exp[ik_z z]+\exp[-ik_z z]}{2}\right) \psi_{\text{II}} = \psi_0 \exp[i\mathbf{k}_{\text{t}}\cdot\mathbf{r}]\cos[k_z z], \tag{A.1.15}$$

where ψ_0 is an arbitrary constant, $\mathbf{k}_{\text{t}} = k_x\hat{\mathbf{x}} + k_y\hat{\mathbf{y}}$ is the tangential wavevector and k_z is the (modulus of the) z-direction wavevector.

Outside the ferromagnet, $\hat{\chi} = 0$ and the Walker equation just turns into the Laplace equation, $\nabla^2\psi_{\text{d}} = 0$. We don't instinctively know the form of ψ outside the ferromagnet, but we do know that it should tend to zero at large $\pm z$ - we don't have the same constraints for the x or y directions. If we then suppose that $\psi_{\text{d}} \sim \exp[i\mathbf{k}_{\text{t,d}}\cdot\mathbf{r} \pm k_{z,\text{d}} z]$ then, with $\nabla^2\psi_{\text{d}} = 0$, we have

$$\begin{aligned}\nabla^2 \exp[i\mathbf{k}_{\text{t,d}}\cdot\mathbf{r} \pm k_{z,\text{d}} z] &= 0 \\ \implies -k_{\text{t,d}}^2 + k_{z,\text{d}}^2 = 0 \quad &\implies k_{z,\text{d}} = \pm k_{\text{t,d}},\end{aligned} \tag{A.1.16}$$

where the subscript d is used for the dielectric regions (I and III)[2]. So we can use

[1] see Griffiths [150] p. 410 for a description of the form of waves in a waveguide -an analogous situation.

[2] in [5], they assume a generic form of $\psi_{\text{d}} \sim \exp(i\mathbf{k}_{\text{t,d}}\cdot\mathbf{r})$, and then the condition is that $k_{z,\text{d}} = \pm ik_{\text{t,d}}$. But since we specified this in the first place, we just automatically have that $k_{z,\text{d}} = \pm k_{\text{t,d}}$.

the same wavevector for the z and tangential components of ψ_d. We will then make the replacement $k_{z,\mathrm{d}} \to k_{\mathrm{t,d}}$, and write out ψ in each region for completeness:

$$\psi_\mathrm{I} = C\exp[i\mathbf{k}_{\mathrm{t,d}}\cdot\mathbf{r} - k_{\mathrm{t,d}}z], \tag{A.1.17}$$
$$\psi_\mathrm{II} = \psi_0\exp[i\mathbf{k}_\mathrm{t}\cdot\mathbf{r}]\cos[k_z z], \tag{A.1.18}$$
$$\psi_\mathrm{III} = D\exp[i\mathbf{k}_{\mathrm{t,d}}\cdot\mathbf{r} + k_{\mathrm{t,d}}z]. \tag{A.1.19}$$

We now impose the boundary conditions on these solutions. Applying boundary condition 1 (and remembering $\mathbf{h}_t = -\nabla_t\psi$), we have

$$-\mathbf{k}_{\mathrm{t,d}}\psi_\mathrm{I}(z = s/2) = -\mathbf{k}_\mathrm{t}\psi_\mathrm{II}(z = s/2), \tag{A.1.20}$$
$$-\mathbf{k}_\mathrm{t}\psi_\mathrm{II}(z = -s/2) = -\mathbf{k}_{\mathrm{t,d}}\psi_\mathrm{III}(z = -s/2). \tag{A.1.21}$$

We can see that $\mathbf{k}_{\mathrm{t,d}}$ and $\mathbf{k}_\mathrm{t}$ must then be equal[3], in order for the above equations to be satisfied for all values of x and y. We can then make the replacement $\mathbf{k}_{\mathrm{t,d}} \to \mathbf{k}_\mathrm{t}$ write the full versions of Eq. (A.1.20) and Eq. (A.1.21) as

$$C\exp[-k_\mathrm{t}s/2] = \psi_0\cos[k_z s/2], \tag{A.1.22}$$
$$D\exp[-k_\mathrm{t}s/2] = \psi_0\cos[-k_z s/2] = \psi_0\cos[k_z s/2]. \tag{A.1.23}$$

Since the right hand sides are both the same, clearly $C = D$.

Let us apply boundary condition 2 (cancelling the $\exp[i\mathbf{k}_\mathrm{t}\cdot\mathbf{r}]$ terms on both sides, now we know they are equal):

$$-k_\mathrm{t}C\exp[-k_{\mathrm{t,d}}s/2] = -k_z\psi_0\sin[k_z s/2], \tag{A.1.24}$$
$$-k_z\psi_0\sin[-k_z s/2] = k_\mathrm{t}D\exp[-k_{\mathrm{t,d}}s/2]. \tag{A.1.25}$$

Since $\sin(-x) = -\sin(x)$ then, if $C = D$, these two equations are equal. So, if we use one of them, say Eq. (A.1.26), and substitute Eq. (A.1.22) into it, we get

$$\begin{aligned} k_\mathrm{t}\cancel{\psi_0}\cos[k_z s/2] &= k_z\cancel{\psi_0}\sin[k_z s/2] \\ \implies \frac{k_z}{k_\mathrm{t}} &= \tan[k_z s/2]. \end{aligned} \tag{A.1.26}$$

[3] since C, D, ψ_0 and $z = \pm s/2$ are fixed, a change in $\mathbf{r}$ must give the same change to both ψ_I and ψ_II - this can only be the case if $\mathbf{k}_{\mathrm{t,d}} = \mathbf{k}_\mathrm{t}$. This can more simply be justified via conservation of momentum - the tangential momentum should not change if it changes its direction in z.

To summarise:

- The z component and tangential component of the wavevector in the dielectric are related by $\mathbf{k}_{z,\mathrm{d}} = \pm i\mathbf{k}_{\mathrm{t,d}}$.
- The tangential wavevector in the ferromagnet is equal to the tangential wavevector in the dielectric, $\mathbf{k}_{\mathrm{t}} = \mathbf{k}_{\mathrm{t,d}}$.
- The final expressions for ψ are given by:

$$\psi_{\mathrm{I}} = C\exp[i\mathbf{k}_{\mathrm{t}}\cdot\mathbf{r} - k_{\mathrm{t}}z], \tag{A.1.27}$$
$$\psi_{\mathrm{II}} = \psi_0\exp[i\mathbf{k}_{\mathrm{t}}\cdot\mathbf{r}]\cos[k_z z], \tag{A.1.28}$$
$$\psi_{\mathrm{III}} = C\exp[i\mathbf{k}_{\mathrm{t}}\cdot\mathbf{r} + k_{\mathrm{t}}z]. \tag{A.1.29}$$

A.1.3 Obtaining the Dispersion Relation

Now, let us substitute our expressions for ψ in the ferromagnet, Eq. (A.1.28), into the Walker equation:

$$\begin{aligned}
\nabla\cdot(\hat{\mu}\nabla\{\psi_0\exp[i\mathbf{k}_{\mathrm{t}}\cdot\mathbf{r}]\cos[k_z z]\}) &= 0\\
\nabla\cdot\left(\hat{\mu}\left[\left\{\cos[k_z z](ik_x\hat{\mathbf{x}} + ik_y\hat{\mathbf{y}}) - \sin[k_z z]k_z\hat{\mathbf{z}}\right\}\psi_0\exp[i\mathbf{k}_{\mathrm{t}}\cdot\mathbf{r}]\right]\right) &= 0\\
\nabla\cdot\Big[\left\{(1+\kappa)ik_x\psi_{\mathrm{II}} + i^2\nu k_y\psi_{\mathrm{II}}\right\}\hat{\mathbf{x}} + \left\{-i^2\nu k_x\psi_{\mathrm{II}} + (1+\kappa)ik_y\psi_{\mathrm{II}}\right\}\hat{\mathbf{y}} +&\\
+\left\{-k_z\psi_0\exp[i\mathbf{k}_t\cdot\mathbf{r}]\sin(k_z z)\right\}\hat{\mathbf{z}}\Big] &= 0\\
-(1+\kappa)k_x^2\psi_{\mathrm{II}} - \cancel{i\nu k_y k_x\psi_{\mathrm{II}}} + \cancel{i\nu k_x k_y\psi_{\mathrm{II}}} - (1+\kappa)k_y^2\psi_{\mathrm{II}} - k_z^2\underbrace{\psi_0\exp[i\mathbf{k}_t\cdot\mathbf{r}]\cos(k_z z)}_{\psi_{\mathrm{II}}} &= 0\\
\left\{-(1+\kappa)(k_x^2+k_y^2) - k_z^2\right\}\psi_{\mathrm{II}} &= 0\\
(1+\kappa)(k_x^2+k_y^2) + k_z^2 &= 0\\
\implies (1+\kappa)k_t^2 + k_z^2 &= 0.
\end{aligned} \tag{A.1.30}$$

Rearranging this result, we obtain

$$\frac{k_t}{k_z} = \frac{1}{\sqrt{-(1+\kappa)}}, \tag{A.1.31}$$

and we can use this in Eq. (A.1.26) to obtain the dispersion relation for the *even* modes in the z direction (i.e. with cosine dependence on z) , which relates ω

(hidden in κ) to the tangential wavevector $\mathbf{k}_t$:

$$\frac{1}{\sqrt{-(1+\kappa)}} = \tan\left[\frac{k_t s}{2}\sqrt{-(1+\kappa)}\right]. \tag{A.1.32}$$

But clearly this is not a usual dispersion relation - we need to plot both functions and find their intersection, to obtain solutions. But this still only identifies the *even* solutions (with nodes at the top and bottom surfaces, thus cosine-dependence) - we really need both. We will just extract the solution[4] from Ref. [5] p. 155:

$$\frac{1}{\sqrt{-(1+\kappa)}} = \tan\left[\frac{k_t s}{2}\sqrt{-(1+\kappa)} - \frac{n\pi}{2}\right], \tag{A.1.33}$$

where $n = 0, 1, 2, ...$ is the order of the mode, which corresponds to the number of zeros across the thickness. In this thesis, we will always consider the $n = 0$ mode, which is the most easy to detect experimentally. We can rearrange Eq. (A.1.33) to obtain k_t as a function of all the other variables:

$$k_t = \frac{1}{s}\left[\arctan\left(\frac{1}{\sqrt{-(1+\kappa)}}\right) + \frac{n\pi}{2}\right]\frac{2}{\sqrt{-(1+\kappa)}}. \tag{A.1.34}$$

This result is repeated at Eq. (2.5.10). A similar process can be carried out for the backward volume and surface wave geometries, with more details in Ref. [5].

A.2 The Spin Wave Manifold

Magnetostatic (volume) spin waves exist within a manifold of frequencies. To see where this originates from (following Ref. [5], p.140) let us go back to the final line of the derivation Eq. (A.1.30), and expand $k_t^2 = k_x^2 + k_y^2$:

$$(1+\kappa)(k_x^2 + k_y^2) + k_z^2 = 0. \tag{A.2.1}$$

[4] which is obtained by repeating the previous analysis with $\psi_{II} = \psi_0 \exp[i\mathbf{k}_t \cdot \mathbf{r}] \sin[k_z z]$, to obtain $-\cot[k_t\sqrt{-(1+\kappa)}(s/2)] = 1/\sqrt{-(1+\kappa)}$. This relation and the other are combined into a single equation using the fact that $\tan(\theta - \pi/2) = -\cot\theta$, and then the following equation can be obtained.

If we now write that these wavevector components in terms of the angle θ that they make with the $\hat{\mathbf{z}}$ direction[5], then

$$k_x^2 + k_y^2 = k^2 \sin^2\theta, \tag{A.2.2}$$

$$k_z^2 = k^2 \cos^2\theta, \tag{A.2.3}$$

and if we substitute these into our previous equation Eq. (A.2.1), we obtain:

$$\begin{aligned}
(1+\kappa)k^2\sin^2\theta + k^2\cos^2\theta &= 0 \\
k^2 + \kappa k^2 \sin^2\theta &= 0 \\
\kappa \sin^2\theta &= -1 \\
\frac{\omega_H \omega_M}{\omega_H^2 - \omega^2}\sin^2\theta &= -1 \\
\omega_H\omega_M \sin^2\theta + \omega_H^2 &= \omega^2 \\
\implies \sqrt{\omega_H(\omega_H + \omega_M\sin^2\theta)} &= \omega.
\end{aligned} \tag{A.2.4}$$

This is the dispersion relation for magnetostatic waves in an *infinite* material (i.e. no boundaries anywhere). The smallest value of ω corresponds to an angle of $\theta = 0$, i.e. the wavevector is purely along the z (bias magnetic field) direction and $\omega = \omega_H$. The largest possible frequency is for when $\theta = \pi/2$; the wavevector is purely in the $x-y$ plane, and $\omega = \sqrt{\omega_H^2 + \omega_H\omega_M}$. Note that this approach (for an infinite material) implies a continuous range of possible frequencies. In our previous analysis, we saw that the boundaries of the film only allow certain modes to exist — those which have an integer number of half wavelengths in the z direction. In addition, an infinite sample also has a dispersion relation which does not depend on the magnitude of k, so waves at frequency ω can have any wavelength! This degeneracy is again removed when boundaries (or the exchange contributions) are considered.

[5] recalling that $x = r\sin\theta\cos\phi$, $y = r\sin\theta\sin\phi$, and $z = r\cos\theta$ in spherical coordinates.

Appendix B

Minimising The Domain Wall Energy

Here we minimise the static energy density, which is (4.2.1) without the driving term. Generally, for a functional:

$$J = \int_{x_1}^{x_2} f[x, y(x), y'(x)]\mathrm{d}x,$$

the Euler-Lagrange equation is

$$\frac{\partial f}{\partial y} - \frac{\mathrm{d}}{\mathrm{d}x}\frac{\partial f}{\partial y'} = 0.$$

Before we proceed to write f in our case, we need to impose that $\phi = \phi_0$ which is a constant[1]. As a result, the term $\sin^2\theta(\partial_y\phi_0)^2$ in (4.2.3) is equal to zero, and we therefore write:

$$f[\theta(y), \theta'(y), \phi_0] = \frac{M_0}{2}\alpha(\partial_y\theta)^2 - \frac{M_0}{2}\beta_{\parallel}\cos^2\theta + \frac{M_0}{2}\beta_{\perp}\sin^2\theta\cos^2\phi_0.$$

Since we have two arguments, θ and ϕ_0, we have two separate Euler-Lagrange equations, as follows:

$$\frac{\partial f}{\partial \theta} - \frac{\mathrm{d}}{\mathrm{d}y}\frac{\partial f}{\partial \theta'} = 0, \tag{B.0.1}$$

$$\frac{\partial f}{\partial \phi_0} - \cancel{\frac{\mathrm{d}}{\mathrm{d}y}\frac{\partial f}{\partial \phi_0'}} = 0. \tag{B.0.2}$$

[1] This can be justified quite easily; a change in ϕ, as shown in Figure 4.2, just means a change in the direction of the component of the magnetisation out of the $y-z$ plane, which we have said will be constant for all subsequent slices in that plane. A change in θ, however, is necessary to get from the $+z$ to $-z$ orientation.

We will first look at (B.0.1). The first and second terms are, respectively,

$$\frac{\partial f}{\partial \theta} = M_0 \beta_{\parallel} \cos\theta \sin\theta + M_0 \beta_{\perp} \sin\theta \cos\theta \cos^2\phi_0.$$
$$\frac{\mathrm{d}}{\mathrm{d}y}\frac{\partial f}{\partial \theta'} = \partial_y[\alpha M_0 \partial_y \theta] = \alpha M_0 \partial_y^2 \theta = \alpha M_0 \theta''.$$

Substituting these into (B.0.1) we find,

$$[\beta_{\parallel} + \beta_{\perp} \cos^2\phi_0] \sin\theta \cos\theta = \alpha\theta''. \tag{B.0.3}$$

We now carry out the same approach for (B.0.2). The second term will be equal to zero, since we have no differentials in ϕ_0. In which case, we find:

$$-\beta_{\perp} \sin^2\theta \sin\phi_0 \cos\phi_0 = 0. \tag{B.0.4}$$

These are the two Euler-Lagrange equations, repeated in the main text.

Appendix C

Derivation of the Domain Wall Profile

To solve (4.2.6), we use the same method as in [7]. Multiplying (4.2.6) by $-\frac{\partial\theta}{\partial y}$, we find:

$$-\frac{\partial\theta}{\partial y}\sin[2\theta] + 2\lambda_B^2 \frac{\partial\theta}{\partial y}\frac{\mathrm{d}^2\theta}{\mathrm{d}y^2} = 0.$$

If we recognise that

$$-\frac{\partial\theta}{\partial y}\sin[2\theta] = \frac{1}{2}\frac{\partial}{\partial y}\cos[2\theta],$$

$$\text{and:} \qquad \frac{\partial\theta}{\partial y}\frac{\mathrm{d}^2\theta}{\mathrm{d}y^2} = \frac{1}{2}\frac{\partial}{\partial y}\left(\frac{\partial\theta}{\partial y}\right)^2,$$

then we can write the equation as

$$\frac{1}{2}\frac{\partial}{\partial y}\cos[2\theta] + \lambda_B^2\frac{\partial}{\partial y}\left(\frac{\partial\theta}{\partial y}\right)^2 = 0$$

$$\implies \frac{\partial}{\partial y}\left(\frac{1}{2}\cos[2\theta] + \lambda_B^2\left(\frac{\partial\theta}{\partial y}\right)^2\right) = 0.$$

If $\frac{\partial A}{\partial y} = 0$, it means that A must be equal to a constant, i.e.

$$\frac{1}{2}\cos[2\theta] + \lambda_B^2\left(\frac{\partial\theta}{\partial y}\right)^2 = C. \tag{C.0.1}$$

We can now solve for C using the boundary conditions. Firstly, we know that the magnetisation far from the wall, at say $y \to -\infty$ must be aligned in the $+z$

direction, so that $\theta = 0$. In addition, the derivative of this must be zero (it is unchanging). The boundary conditions are therefore

$$\theta(y \to -\infty) = 0, \tag{C.0.2}$$

$$\left.\frac{\partial\theta}{\partial y}\right|_{y\to-\infty} = 0. \tag{C.0.3}$$

If we substitute (C.0.2) and (C.0.3) into (C.0.1), we find that $C = \frac{1}{2}$. We can now use this, along with the relation $\frac{1}{2}[\cos(2\theta - 1)] = -\sin^2\theta$ in (C.0.1) to find:

$$\begin{aligned} 0 &= \lambda_B^2 \left(\frac{\partial\theta}{\partial y}\right)^2 - \sin^2\theta \\ \implies \frac{\partial\theta}{\partial y} &= \pm\frac{1}{\lambda_B}\sin\theta. \end{aligned} \tag{C.0.4}$$

Equation (C.0.4) describes the chirality of the domain wall; the $+$ solution for the anticlockwise rotation, and the $-$ solution for the clockwise rotation. This equation can be solved simply by rearranging and integrating:

$$\begin{aligned} \int_{\theta(Y_0)}^{\theta} \frac{\mathrm{d}\theta}{\sin\theta} &= \pm\frac{1}{\lambda_B}\int_{Y_0}^{y}\mathrm{d}y, \\ \left[-\log\left(\cot\left[\frac{\theta}{2}\right]\right)\right]_{\theta(Y_0)}^{\theta} &= \pm\frac{1}{\lambda_B}(y - Y_0). \end{aligned}$$

If we choose Y_0 to be the centre of the domain wall, then the magnetisation points out of plane in the $+x$ direction, i.e. $\theta(Y_0) = \pi/2$. Then, conveniently, $\log(\cot[\pi/4]) = \log(1) = 0$, and we find

$$\begin{aligned} -\log\left(\cot\left[\frac{\theta(y)}{2}\right]\right) &= \pm\exp\left(\frac{y - Y_0}{\lambda_{B,N}}\right), \\ \theta(y) &= \pm 2\arctan\left[\exp\left(\frac{y - Y_0}{\lambda_{B,N}}\right)\right], \end{aligned}$$

which is the well-known result for a domain wall.

Appendix D

Rotating to the Local z' Frame: Full Derivation

We now carry out the rotation of the Landau-Lifshitz equation (4.3.8) to get the resulting vector in terms of $\hat{\mathbf{x}}'$, $\hat{\mathbf{y}}'$ and $\hat{\mathbf{z}}'$. We will use the fact that we have set the z' axis to point along the static magnetisation direction in the domain wall: in the linear approximation (i.e. no change in the length of $\mathbf{m}$) we will only have components of the oscillation in the x' and y' directions, so $\mathbf{m}' = (m'_x, m'_y, 0)$. So, applying the rotation matrix to (4.3.8) we obtain:

$$
\begin{aligned}
R_B\left[\frac{\partial \mathbf{m}}{\partial t}\right] &= \frac{\partial m'_x}{\partial t}\,\hat{\mathbf{x}}' + \frac{\partial m'_y}{\partial t}\,\hat{\mathbf{y}}' + 0\,\hat{\mathbf{z}}' \\
&= -\gamma\Big\{\hat{\mathbf{x}}'\big[\cos\theta\big\{M_{0,y}\beta_{\parallel}m_z + M_{0,y}\alpha\partial_y^2 m_z - M_{0,z}h(t) - M_{0,z}\alpha\partial_y^2 m_y + \\
&+ m_y\beta_{\parallel}M_{0,z} + m_y\alpha\partial_y^2 M_{0,z} - m_z\alpha\partial_y^2 M_{0,y}\big\} - \sin\theta\big\{M_{0,x}h(t) + \\
&+ M_{0,x}\alpha\partial_y^2 m_y + M_{0,y}\beta_{\perp}m_x - M_{0,y}\alpha\partial_y^2 m_x + m_x\alpha\partial_y^2 M_{0,y} + \\
&+ m_y\beta_{\perp}M_{0,x} - m_y\alpha\partial_y^2 M_{0,x}\big\}\big] + \\
&+ \hat{\mathbf{y}}'\big[-M_{0,z}\beta_{\perp}m_x + M_{0,z}\alpha\partial_y^2 m_x - M_{0,x}\beta_{\parallel}m_z - M_{0,x}\alpha\partial_y^2 m_z + \\
&- m_z\beta_{\perp}M_{0,x} + m_z\alpha\partial_y^2 M_{0,x} - m_x\beta_{\parallel}M_{0,z} - m_x\alpha\partial_y^2 M_{0,z}\big] + \\
&+ \hat{\mathbf{z}}'\big[\sin\theta\big\{M_{0,y}\beta_{\parallel}m_z + M_{0,y}\alpha\partial_y^2 m_z - M_{0,z}h(t) - M_{0,z}\alpha\partial_y^2 m_y + \\
&+ m_y\beta_{\parallel}M_{0,z} + m_y\alpha\partial_y^2 M_{0,z} - m_z\alpha\partial_y^2 M_{0,y}\big\} + \cos\theta\big\{M_{0,x}h(t) + \\
&+ M_{0,x}\alpha\partial_y^2 m_y + M_{0,y}\beta_{\perp}m_x - M_{0,y}\alpha\partial_y^2 m_x + m_x\alpha\partial_y^2 M_{0,y} + \\
&+ m_y\beta_{\perp}M_{0,x} - m_y\alpha\partial_y^2 M_{0,x}\big\}\big]\Big\}. \qquad \text{(D.0.1)}
\end{aligned}
$$

We can see that, conveniently, the $\hat{\mathbf{z}}'$ term on the 'right-hand side' (i.e. in the $\mathbf{m} \times \mathbf{H}_{\text{eff}}$ term) must be equal to zero to match the 'left-hand side', so this can be omitted in the next step. We have now rotated the vector $(\mathbf{M}_0 \times \delta\mathbf{H}_{\text{eff}}) +$

$(\mathbf{m} \times \mathbf{H}_{\text{eff},S})$ so that $\hat{\mathbf{x}} \to \hat{\mathbf{x}}'$, $\hat{\mathbf{y}} \to \hat{\mathbf{y}}'$ and $\hat{\mathbf{z}} \to \hat{\mathbf{z}}'$ (though the latter is null), but we would like to have the components expressed in terms of the local (primed) frame components. To do this, we use the general approach outlined in Section 4.3.2; we apply the inverse rotation matrix R_B^{-1} to $\mathbf{M}_0'$ and $\mathbf{m}'$, and obtain $\mathbf{M}_0$ and $\mathbf{m}$, respectively. Let us look at $\mathbf{m}$ first:

$$\begin{aligned}\mathbf{m} &= \begin{pmatrix} m_x \\ m_y \\ m_z \end{pmatrix} \\ &= R_B^{-1}\mathbf{m}' = \begin{pmatrix} \cos\theta & 0 & \sin\theta \\ 0 & 1 & 0 \\ -\sin\theta & 0 & \cos\theta \end{pmatrix} \begin{pmatrix} m_x' \\ m_y' \\ 0 \end{pmatrix} = \begin{pmatrix} \cos\theta m_x' \\ m_y' \\ -\sin\theta m_x' \end{pmatrix}, \end{aligned} \tag{D.0.2}$$

i.e. $m_x = \cos\theta m_x'$, etc, so we can now convert the components of $\mathbf{m}$ from the lab frame to the local frame. Now we express the components of $\mathbf{M}_0$ in terms of the rotated frame, using the same approach as above:

$$\begin{aligned}\mathbf{M}_0 &= \begin{pmatrix} M_{0,x} \\ M_{0,y} \\ M_{0,z} \end{pmatrix} = \begin{pmatrix} M_0 \sin\theta\cos\phi_0 \\ M_0 \sin\theta \sin\phi_0 \\ M_0\cos\theta \end{pmatrix} \\ &= R_B^{-1}\mathbf{M}' = \begin{pmatrix} \cos\theta & 0 & \sin\theta \\ 0 & 1 & 0 \\ -\sin\theta & 0 & \cos\theta \end{pmatrix} \begin{pmatrix} 0 \\ 0 \\ M_0 \end{pmatrix} = \begin{pmatrix} M_0\sin\theta \\ 0 \\ M_0\cos\theta \end{pmatrix}, \end{aligned} \tag{D.0.3}$$

which means that $M_{0,x} = M_0 \sin\theta\cos\phi_0$ in the lab frame corresponds to $M_{0,x}' = M_0\sin\theta$ in the local frame, etc. We need to be careful here, remembering that we have no 'markers' in the final expression for $\mathbf{M}_0$ in (D.0.3) which denote the coordinate system we are working in. We will just have to bear this in mind when we make the substitution.

We can now return to equation (D.0.1), and substitute (D.0.2) and (D.0.3) in:

$$
\begin{aligned}
&\frac{\partial m'_x}{\partial t}\,\hat{\mathbf{x}}' + \frac{\partial m'_y}{\partial t}\,\hat{\mathbf{y}}' + 0\,\hat{\mathbf{z}}' \\
&= -\gamma M_0 \Big\{ \hat{\mathbf{x}}' \big[\cos\theta \{ -\cos\theta h(t) - \cos\theta\alpha\partial_y^2 m'_y + m'_y\beta_\parallel \cos\theta + m'_y\alpha\partial_y^2(\cos\theta) \} \\
&- \sin\theta \{ \sin\theta h(t) + \sin\theta\alpha\partial_y^2 m'_y + m'_y\beta_\perp \sin\theta - m'_y\alpha\partial_y^2(\sin\theta) \} \big] \\
&+ \hat{\mathbf{y}}' \big[-\cos\theta\beta_\perp \cos\theta m'_x + \cos\theta\alpha\partial_y^2(\cos\theta m'_x) + \sin\theta\beta_\parallel \sin\theta m'_x + \sin\theta\alpha\partial_y^2(\sin\theta m'_x) \\
&+ \sin\theta m'_x\beta_\perp \sin\theta - \sin\theta m'_x\alpha\partial_y^2(\sin\theta) - \cos\theta m'_x\beta_\parallel \cos\theta - \cos\theta m'_x\alpha\partial_y^2(\cos\theta) \big] \Big\}
\end{aligned}
$$

$$
\begin{aligned}
&= -\gamma M_0 \Big\{ \hat{\mathbf{x}}' \big[-\cos^2\theta h(t) - \cos^2\theta\alpha\partial_y^2 m'_y + m'_y\beta_\parallel \cos^2\theta + \cos\theta m'_y\alpha\partial_y^2(\cos\theta) \\
&- \sin^2\theta h(t) - \sin^2\theta\alpha\partial_y^2 m'_y - m'_y\beta_\perp \sin^2\theta + \sin\theta m'_y\alpha\partial_y^2(\sin\theta) \big] \\
&+ \hat{\mathbf{y}}' \big[-\cos^2\theta\beta_\perp m'_x + \cos\theta\alpha\partial_y^2(\cos\theta m'_x) + \sin^2\theta\beta_\parallel m'_x + \sin\theta\alpha\partial_y^2(\sin\theta m'_x) \\
&+ \sin^2\theta m'_x\beta_\perp - \sin\theta m'_x\alpha\partial_y^2(\sin\theta) - \cos^2\theta m'_x\beta_\parallel - \cos\theta m'_x\alpha\partial_y^2(\cos\theta) \big] \Big\}
\end{aligned}
$$

$$
\begin{aligned}
&= -\gamma M_0 \Big\{ \hat{\mathbf{x}}' \big[-h(t) - \alpha\partial_y^2 m'_y + m'_y[\beta_\parallel \cos^2\theta - \beta_\perp \sin^2\theta \\
&+ \cos\theta\alpha\partial_y^2(\cos\theta) + \sin\theta\alpha\partial_y^2(\sin\theta)] \big] \\
&+ \hat{\mathbf{y}}' \big[m'_x[(\sin^2\theta - \cos^2\theta)\beta_\perp + (\sin^2\theta - \cos^2\theta)\beta_\parallel - \sin\theta\alpha\partial_y^2(\sin\theta) \\
&- \cos\theta\alpha\partial_y^2(\cos\theta)] + \cos\theta\alpha\partial_y^2(\cos\theta m'_x) + \sin\theta\alpha\partial_y^2(\sin\theta m'_x) \big] \Big\}.
\end{aligned}
$$

We now need to simplify the differential terms. We will write them out as follows:

$$
\partial_y^2(\cos\theta) = \partial_y[\partial_y(\cos\theta)] = \partial_y[-\sin\theta\partial_y\theta] = -\cos\theta(\partial_y\theta)^2 - \sin\theta\partial_y^2\theta, \quad \text{(D.0.4)}
$$

$$
\begin{aligned}
\partial_y^2(\cos\theta m'_x) &= \partial_y[\partial_y(\cos\theta m'_x)] = \partial_y[-\sin\theta\partial_y\theta m'_x + \cos\theta\partial_y m'_x] \\
&= -\cos\theta(\partial_y\theta)^2 m'_x - \sin\theta\partial_y^2\theta m'_x - 2\sin\theta\partial_y\theta\partial_y m'_x + \cos\theta\partial_y^2 m'_x,
\end{aligned} \quad \text{(D.0.5)}
$$

$$
\partial_y^2(\sin\theta) = \partial_y[\partial_y(\sin\theta)] = \partial_y[\cos\theta\partial_y\theta] = -\sin\theta(\partial_y\theta)^2 + \cos\theta\partial_y^2\theta, \quad \text{(D.0.6)}
$$

$$
\begin{aligned}
\partial_y^2(\sin\theta m'_x) &= \partial_y[\partial_y(\sin\theta m'_x)] = \partial_y[\cos\theta\partial_y\theta m'_x + \sin\theta\partial_y m'_x] \\
&= -\sin\theta(\partial_y\theta)^2 m'_x + \cos\theta\partial_y^2\theta m'_x + 2\cos\theta\partial_y\theta\partial_y m'_x + \sin\theta\partial_y^2 m'_x.
\end{aligned} \quad \text{(D.0.7)}
$$

We can now substitute these back into our equation:

$$
\begin{aligned}
&\frac{\partial m'_x}{\partial t}\,\hat{\mathbf{x}}' + \frac{\partial m'_y}{\partial t}\,\hat{\mathbf{y}}' + 0\,\hat{\mathbf{z}}' \\
&= -\gamma M_0 \Big\{ \hat{\mathbf{x}}' \big[-h(t) - \alpha\partial_y^2 m'_y + m'_y \{ \beta_\parallel \cos^2\theta - \beta_\perp \sin^2\theta \\
&+ \cos\theta\alpha(-\cos\theta(\partial_y\theta)^2 - \sin\theta\partial_y^2\theta) + \sin\theta\alpha(-\sin\theta(\partial_y\theta)^2 + \cos\theta\partial_y^2\theta) \} \big] \\
&+ \hat{\mathbf{y}}' \big[m'_x \{ (\sin^2\theta - \cos^2\theta)\beta_\perp + (\sin^2\theta - \cos^2\theta)\beta_\parallel \\
&- \sin\theta\alpha(-\sin\theta(\partial_y\theta)^2 + \cos\theta\partial_y^2\theta) - \cos\theta\alpha(-\cos\theta(\partial_y\theta)^2 - \sin\theta\partial_y^2\theta) \} \\
&+ \cos\theta\alpha(-\cos\theta(\partial_y\theta)^2 m'_x - \sin\theta\partial_y^2\theta m'_x - 2\sin\theta\partial_y\theta\partial_y m'_x + \cos\theta\partial_y^2 m'_x) \\
&+ \sin\theta\alpha(-\sin\theta(\partial_y\theta)^2 m'_x + \cos\theta\partial_y^2\theta m'_x + 2\cos\theta\partial_y\theta\partial_y m'_x + \sin\theta\partial_y^2 m'_x) \big] \Big\}
\end{aligned}
$$

$$
\begin{aligned}
&= -\gamma M_0 \Big\{ \hat{\mathbf{x}}' \big[-h(t) - \alpha\partial_y^2 m'_y + m'_y \{ \beta_\parallel \cos^2\theta - \beta_\perp \sin^2\theta \\
&- \cos^2\theta\alpha(\partial_y\theta)^2 - \cancel{\cos\theta\sin\theta\alpha\partial_y^2\theta} - \sin^2\theta\alpha(\partial_y\theta)^2 + \cancel{\sin\theta\cos\theta\alpha\partial_y^2\theta} \} \big] \\
&+ \hat{\mathbf{y}}' \big[m'_x \{ (\sin^2\theta - \cos^2\theta)\beta_\perp + (\sin^2\theta - \cos^2\theta)\beta_\parallel \\
&+ \sin^2\theta\alpha(\partial_y\theta)^2 - \cancel{\sin\theta\cos\theta\alpha\partial_y^2\theta} + \cos^2\theta\alpha(\partial_y\theta)^2 + \cancel{\cos\theta\sin\theta\alpha\partial_y^2\theta} \} \\
&- \cos^2\theta\alpha(\partial_y\theta)^2 m'_x - \cancel{\cos\theta\sin\theta\alpha\partial_y^2\theta m'_x} - \cancel{2\cos\theta\sin\theta\alpha\partial_y\theta\partial_y m'_x} + \cos^2\theta\alpha\partial_y^2 m'_x \\
&- \sin^2\theta\alpha(\partial_y\theta)^2 m'_x + \cancel{\sin\theta\cos\theta\alpha\partial_y^2\theta m'_x} + \cancel{2\sin\theta\cos\theta\alpha\partial_y\theta\partial_y m'_x} + \sin^2\theta\alpha\partial_y^2 m'_x \big] \Big\}
\end{aligned}
$$

$$
\begin{aligned}
&= -\gamma M_0 \Big\{ \hat{\mathbf{x}}' \big[-h(t) - \alpha\partial_y^2 m'_y + m'_y \{ \beta_\parallel \cos^2\theta - \beta_\perp \sin^2\theta - \alpha(\partial_y\theta)^2 \} \big] \\
&+ \hat{\mathbf{y}}' \big[m'_x \{ (\sin^2\theta - \cos^2\theta)\beta_\perp + (\sin^2\theta - \cos^2\theta)\beta_\parallel + \cancel{\alpha(\partial_y\theta)^2} \} - \cancel{\alpha(\partial_y\theta)^2 m'_x} + \alpha\partial_y^2 m'_x \big] \Big\}
\end{aligned}
$$

$$
\begin{aligned}
&= -\gamma M_0 \Big\{ \hat{\mathbf{x}}' \big[-h(t) - \alpha\partial_y^2 m'_y + m'_y \{ \beta_\parallel \cos^2\theta - \beta_\perp \sin^2\theta - \alpha(\partial_y\theta)^2 \} \big] \\
&\quad + \hat{\mathbf{y}}' \big[\alpha\partial_y^2 m'_x + m'_x \{ \beta_\parallel (2\sin^2\theta - 1) + \beta_\perp (2\sin^2\theta - 1) \} \big] \Big\}.
\end{aligned}
$$

We can now use (4.2.7)-(4.2.10) in place of θ, so we have:

$$\sin^2\theta = \operatorname{sech}^2\left(\frac{y - Y_0}{\lambda_B}\right), \tag{D.0.8}$$

$$\cos^2\theta = \tanh^2\left(\frac{y - Y_0}{\lambda_B}\right). \tag{D.0.9}$$

Substituting these in, and rearranging slightly:

$$\begin{aligned}
&\frac{\partial m'_x}{\partial t}\,\hat{\mathbf{x}}' + \frac{\partial m'_y}{\partial t}\,\hat{\mathbf{y}}' \\
&= -\gamma M_0 \Bigg\{ \hat{\mathbf{x}}' \left[-h(t) + \left\{ \beta_\parallel \tanh^2\left(\frac{y-Y_0}{\lambda_B}\right) - \beta_\perp \operatorname{sech}^2\left(\frac{y-Y_0}{\lambda_B}\right) - \alpha(\partial_y\theta)^2 - \alpha\partial_y^2 \right\} m'_y \right] \\
&\quad + \hat{\mathbf{y}}' \left[\left\{ \beta_\parallel \left(2\operatorname{sech}^2\left(\frac{y-Y_0}{\lambda_B}\right) - 1 \right) + \beta_\perp \left(2\operatorname{sech}^2\left(\frac{y-Y_0}{\lambda_B}\right) - 1 \right) + \alpha\partial_y^2 \right\} m'_x \right] \Bigg\}.
\end{aligned} \tag{D.0.10}$$

Now we can expand the $\alpha(\partial_y\theta)^2$ term in the $\hat{\mathbf{x}}$ component:

$$\begin{aligned}
\alpha(\partial_y\theta)^2 &= \alpha \left(\partial_y \left\{ 2\arctan\left[\exp\left(\frac{y-Y_0}{\lambda_B}\right) \right] \right\} \right)^2 \\
&= \frac{\alpha}{\lambda_B^2} \operatorname{sech}^2\left(\frac{y-Y_0}{\lambda_B}\right).
\end{aligned} \tag{D.0.11}$$

Substituting this in, and recognising that $\frac{\alpha}{\lambda_B^2} = \frac{\alpha}{\alpha/(\beta_\parallel+\beta_\perp)} = \beta_\parallel + \beta_\perp$:

$$\begin{aligned}
&\frac{\partial m'_x}{\partial t}\,\hat{\mathbf{x}}' + \frac{\partial m'_y}{\partial t}\,\hat{\mathbf{y}}' \\
&= -\gamma M_0 \Bigg\{ \hat{\mathbf{x}}' \Bigg[-h(t) + \Bigg\{ \beta_\parallel \tanh^2\left(\frac{y-Y_0}{\lambda_B}\right) - \beta_\perp \operatorname{sech}^2\left(\frac{y-Y_0}{\lambda_B}\right) \\
&\quad - (\beta_\parallel + \beta_\perp) \operatorname{sech}^2\left(\frac{y-Y_0}{\lambda_B}\right) - \alpha\partial_y^2 \Bigg\} m'_y \Bigg] \\
&\quad + \hat{\mathbf{y}}' \left[\left\{ \beta_\parallel \left(2\operatorname{sech}^2\left(\frac{y-Y_0}{\lambda_B}\right) - 1 \right) + \beta_\perp \left(2\operatorname{sech}^2\left(\frac{y-Y_0}{\lambda_B}\right) - 1 \right) + \alpha\partial_y^2 \right\} m'_x \right] \Bigg\} \\
&= -\gamma M_0 \Bigg\{ \hat{\mathbf{x}}' \left[-h(t) + \left\{ \beta_\parallel \left(1 - 2\operatorname{sech}^2\left(\frac{y-Y_0}{\lambda_B}\right) \right) - 2\beta_\perp \operatorname{sech}^2\left(\frac{y-Y_0}{\lambda_B}\right) - \alpha\partial_y^2 \right\} m'_y \right] \\
&\quad + \hat{\mathbf{y}}' \left[\left\{ \beta_\parallel \left(2\operatorname{sech}^2\left(\frac{y-Y_0}{\lambda_B}\right) - 1 \right) + \beta_\perp \left(2\operatorname{sech}^2\left(\frac{y-Y_0}{\lambda_B}\right) - 1 \right) + \alpha\partial_y^2 \right\} m'_x \right] \Bigg\}.
\end{aligned} \tag{D.0.12}$$

The $\hat{\mathbf{x}}'$ and $\hat{\mathbf{y}}'$ terms are almost equal and opposite, except for the $-h(t)$ term in the $\hat{\mathbf{x}}'$ direction and the $-2\beta_\perp$ term in the $\hat{\mathbf{y}}'$ direction.

We will rewrite (D.0.12) as a system of two equations and rearrange slightly:

$$\frac{\partial m'_x}{\partial t} = -\gamma M_0 \Bigg\{ -h(t) + \left[\beta_{\parallel} - (\beta_{\parallel} + \beta_{\perp}) 2\text{sech}^2 \left(\frac{y - Y_0}{\lambda_B} \right) - \alpha \partial_y^2 \right] m'_y \Bigg\} \tag{D.0.13}$$

$$\frac{\partial m'_y}{\partial t} = -\gamma M_0 \Bigg\{ \left[-(\beta_{\parallel} + \beta_{\perp}) + (\beta_{\parallel} + \beta_{\perp}) 2\text{sech}^2 \left(\frac{y - Y_0}{\lambda_B} \right) + \alpha \partial_y^2 \right] m'_x \Bigg\} \tag{D.0.14}$$

These equations are repeated and discussed in the main text.

Appendix E

Solving the Homogeneous Equation

We will rewrite (4.3.10) and (4.3.11) (which are the same as (D.0.13) and (D.0.14) from the previous Appendix) in matrix form:

$$\begin{aligned}\frac{1}{\gamma M_0}\begin{pmatrix}\partial_t m'_x\\ \partial_t m'_y\end{pmatrix} &= i\begin{pmatrix}0 & -i\\ i & 0\end{pmatrix}\left[\alpha\partial_y^2 - \beta_\parallel + (\beta_\parallel+\beta_\perp)2\mathrm{sech}^2\left(\frac{y}{\lambda_B}\right)\right]\begin{pmatrix}m'_x\\ m'_y\end{pmatrix}\\ &\quad + \begin{pmatrix}0 & 0\\ \beta_\perp & 0\end{pmatrix}\begin{pmatrix}m'_x\\ m'_y\end{pmatrix} + \begin{pmatrix}h(t)\\ 0\end{pmatrix},\\ \therefore \frac{1}{\alpha\gamma M_0}\partial_t \mathbf{m}' &= i\sigma_y\left[\partial_y^2 - \frac{\beta_\parallel}{\alpha} + \frac{2}{\lambda_B^2}\mathrm{sech}^2\left(\frac{y}{\lambda_B}\right)\right]\mathbf{m}' + \begin{pmatrix}0 & 0\\ \frac{\beta_\perp}{\alpha} & 0\end{pmatrix}\mathbf{m}' + \begin{pmatrix}\frac{h(t)}{\alpha}\\ 0\end{pmatrix},\end{aligned} \tag{E.0.1}$$

where σ_y is the Pauli matrix given on the line above. Note that we have divided through by α in the second step, as this will make things easier for when we solve the inhomogeneous equation. We will first solve the homogeneous equation, i.e.:

$$\frac{1}{\alpha\gamma M_0}\partial_t \mathbf{m}'_G = i\sigma_y\left[\partial_y^2 - \frac{\beta_\parallel}{\alpha} + \frac{2}{\lambda_B^2}\mathrm{sech}^2\left(\frac{y}{\lambda_B}\right)\right]\mathbf{m}'_G + \begin{pmatrix}0 & 0\\ \frac{\beta_\perp}{\alpha} & 0\end{pmatrix}\mathbf{m}'_G, \tag{E.0.2}$$

where we have called the magnetisation here $\mathbf{m}'_G$; since we are solving the *homogeneous* equation, we want to avoid confusion with the solution to the *inhomogeneous* equation (which we will leave as $\mathbf{m}'$). First, we can construct an eigenvalue equation out of this central term:

$$\left[\partial_y^2 - \frac{\beta_\parallel}{\alpha} + \frac{2}{\lambda_B^2}\mathrm{sech}^2\left(\frac{y}{\lambda_B}\right)\right]\varphi(y) = \Lambda^{\pm}\varphi(y), \tag{E.0.3}$$

i.e. we assume that if the operator on the left acts on some function $\varphi(y)$, it will return an eigenvalue and the original $\varphi(y)$. We know that this is valid, because it is actually a modified Schrödinger equation with a Pöschl-Teller potential [100].

We know that there are two solutions to this eigenvalue equation, and we should assume for now that there are two eigenvalues $\Lambda^{\pm}$. We solve for $\varphi(y)$ in the next Appendix. For now, we postulate that our magnetisation $\mathbf{m}'_G$ is comprised of a time-dependent vector $\mathbf{a}(t)$ multiplied by this function $\varphi(y)$, i.e.:

$$\mathbf{m}'_G(y,t) = \mathbf{a}(t)\varphi(y). \tag{E.0.4}$$

If we substitute this into (E.0.2), we find:

$$\begin{aligned}
\frac{1}{\alpha\gamma M_0}\partial_t(\mathbf{a}(t)\cancel{\varphi(y)}) &= i\sigma_y\Lambda^{\pm}\cancel{\varphi(y)}\mathbf{a}(t) + \begin{pmatrix} 0 & 0 \\ \frac{\beta_\perp}{\alpha} & 0 \end{pmatrix}\mathbf{a}(t)\cancel{\varphi(y)} \\
\therefore \dot{\mathbf{a}}(t) &= \begin{pmatrix} 0 & \alpha\gamma M_0\Lambda^{\pm} \\ -\alpha\gamma M_0\Lambda^{\pm} + \gamma M_0\beta_\perp & 0 \end{pmatrix}\cdot\mathbf{a}(t) = \boldsymbol{A}\cdot\mathbf{a}(t),
\end{aligned}$$

which has a general solution of

$$\mathbf{a}(t) = \exp[\boldsymbol{A}t]\cdot\mathbf{a}(0), \tag{E.0.5}$$

where $\mathbf{a}(0)$ is the arbitrary magnetisation vector at $t = 0$. Using our definition (E.0.4), we can therefore write the magnetisation as:

$$\mathbf{m}'_G(y,t) = \exp[\boldsymbol{A}t]\cdot\mathbf{a}(0)\varphi(y). \tag{E.0.6}$$

Now, to deal with the term $\mathbf{a}(0)$, we can specify that it is an eigenvector of $\boldsymbol{A}$, i.e.:

$$\boldsymbol{A}\mathbf{a}(0) = \varepsilon_{\pm}\mathbf{a}(0). \tag{E.0.7}$$

We will solve this eigenvalue equation as normal; first finding the eigenvalues, then the eigenvectors. For the eigenvalues, we solve the characteristic determinant:

$$\begin{aligned}
\begin{vmatrix} -\varepsilon_{\pm} & \alpha\gamma M_0\Lambda^{\pm} \\ -\alpha\gamma M_0\Lambda^{\pm} + \gamma M_0\beta_\perp & -\varepsilon_{\pm} \end{vmatrix} = 0 \implies \varepsilon_{\pm}^2 &= \gamma^2 M_0^2(-\alpha^2(\Lambda^{\pm})^2 + \alpha\beta_\perp\Lambda^{\pm}) \\
\implies \varepsilon_{\pm} &= \pm i\gamma M_0\sqrt{\alpha^2(\Lambda^{\pm})^2 - \alpha\beta_\perp\Lambda^{\pm}} \\
\implies \varepsilon_{\pm} &= \pm i\alpha\gamma M_0\Lambda^{\pm}\sqrt{1 - \frac{\beta_\perp}{\alpha\Lambda^{\pm}}}.
\end{aligned} \tag{E.0.8}$$

For the eigenvectors, we solve the eigenvalue equation:

$$\begin{pmatrix} -\varepsilon_\pm & \alpha\gamma M_0\Lambda^\pm \\ -\alpha\gamma M_0\Lambda^\pm + \gamma M_0\beta_\perp & -\varepsilon_\pm \end{pmatrix}\begin{pmatrix} a_1 \\ a_2 \end{pmatrix} = 0,$$
$$\therefore \begin{cases} -\varepsilon_\pm a_1 + \alpha\gamma M_0\Lambda^\pm a_2 = 0 \\ (-\alpha\gamma M_0\Lambda^\pm + \gamma M_0\beta_\perp)a_1 - \varepsilon_\pm a_2 = 0. \end{cases} \tag{E.0.9}$$

From the first equation we find the eigenvector (this also works for the second equation, but you need to use the definition of $\epsilon_\pm$) remembering that there are two solutions, since $\varepsilon_\pm$ consists of a positive and negative solution. We call the resulting eigenvector $\mathbf{a}_\pm(0)$:

$$\varepsilon_\pm a_1 = \alpha\gamma M_0\Lambda^\pm a_2 \implies a_2 = a_1\frac{\varepsilon_\pm}{\alpha\gamma M_0\Lambda^\pm}$$
$$\therefore \mathbf{a}_\pm(0) = \begin{pmatrix} 1 \\ \frac{\varepsilon_\pm}{\alpha\gamma M_0\Lambda^\pm} \end{pmatrix}. \tag{E.0.10}$$

In the case where the perpendicular anisotropy $\beta_\perp = 0$, then from (E.0.8) we find that $\varepsilon_\pm = \pm i\alpha\gamma M_0\Lambda^\pm$, and we see the circularly polarised case emerging, where the eigenvectors would be $m_x \pm im_y$.

If we return to (E.0.6), we can replace for $\mathbf{a}_\pm(0)$, but we also want to rewrite the matrix $\boldsymbol{A}$ in the exponential. Here we use the power series representation of an exponential:

$$\exp[\boldsymbol{A}t] = \sum_{n=0}^{\infty}\left\{\frac{t^n}{n!}\boldsymbol{A}^n\right\} = \mathbb{1} + t\boldsymbol{A} + \frac{1}{2!}t^2\boldsymbol{A}^2 + \cdots,$$

so substituting this into (E.0.6) we have:

$$
\begin{aligned}
\mathbf{m}'_G(y,t) &= \left[\mathbb{1} + t\boldsymbol{A} + \frac{1}{2!}t^2\boldsymbol{A}^2 + \cdots\right] \cdot \mathbf{a}(0)\varphi(y) \\
&= \left[\begin{array}{l} \mathbb{1}\mathbf{a}(0) + t[\underbrace{\boldsymbol{A}\mathbf{a}_\pm(0)}_{=\varepsilon_\pm\mathbf{a}_\pm(0)}] + \frac{1}{2!}t^2[\underbrace{\boldsymbol{A}^2\mathbf{a}_\pm(0)}_{\substack{=\boldsymbol{A}\varepsilon_\pm\mathbf{a}_\pm(0) \\ =\varepsilon_\pm^2\mathbf{a}_\pm(0)}}] + \cdots \end{array}\right] \varphi(y) \\
&= \left[\mathbb{1} + t\varepsilon_\pm + \frac{1}{2!}t^2\varepsilon_\pm^2 + \cdots\right] \cdot \mathbf{a}_\pm(0)\varphi(y) \\
&= \exp[\varepsilon_\pm t]\mathbf{a}_\pm(0)\varphi(y) \\
\therefore \mathbf{m}'_{\pm,G}(y,t) &= \exp\left[\pm i\left(\alpha\gamma M_0\Lambda^\pm\sqrt{1-\frac{\beta_\perp}{\alpha\Lambda^\pm}}\right)t\right]\begin{pmatrix} 1 \\ \pm i\sqrt{1-\frac{\beta_\perp}{\alpha\Lambda^\pm}} \end{pmatrix}\varphi(y),
\end{aligned}
$$

where we have represented the two solutions (positive and negative) as $\mathbf{m}'_{\pm,G}(y,t)$ in the last step. These solutions show ellipticity due to $\beta_\perp$ as mentioned previously. We continue with the derivation in the main text.

Appendix F

Solutions to the Schrödinger Eq. with P-T Potential Well

F.1 Obtaining the Solutions

We are trying to find the solution to (4.4.5), which we repeat here and rearrange slightly:

$$\partial_y^2\varphi(y) + \left[-\Lambda^{\pm} - \frac{\beta_{\|}}{\alpha} + \frac{2}{\lambda_B^2}\operatorname{sech}^2\left(\frac{y}{\lambda_B}\right)\right]\varphi(y) = 0. \tag{F.1.1}$$

We will compare this to the standard form of the Schrödinger equation for a Pöschl-Teller potential well ([100], pp.72-73):

$$\frac{\mathrm{d}^2\psi}{\mathrm{d}x^2} + \frac{2m}{\hbar^2}\left[E + U_0\operatorname{sech}^2(\delta x)\right]\psi = 0. \tag{F.1.2}$$

We will work with (F.1.2), but we can easily convert back to (F.1.1) at the end, since

$$\psi \to \varphi(y), \quad E \to \left(-\Lambda^{\pm} - \frac{\beta_{\|}}{\alpha}\right), \quad \frac{2m}{\hbar^2} \to 1, \quad U_0 \to \frac{2}{\lambda_B^2}, \quad \delta \to \frac{1}{\lambda_B}, \quad x \to y. \tag{F.1.3}$$

We follow the approach outlined in [100] (pp. 72-73 & 79-80). Firstly, we rearrange (F.1.2) to take the form of Legendre's differential equation, which is

$$\frac{\mathrm{d}}{\mathrm{d}\xi}\left[(1-\xi^2)\frac{\mathrm{d}\psi}{\mathrm{d}\xi}\right] + \left[s(s+1) - \frac{\epsilon^2}{1-\xi^2}\right]\psi = 0 = \frac{\mathrm{d}^2\psi}{\mathrm{d}\xi^2} - 2\xi\frac{\mathrm{d}\psi}{\mathrm{d}\xi} + \left[s(s+1) - \frac{\epsilon^2}{1-\xi^2}\right]\psi, \tag{F.1.4}$$

where the left and right hand side are just different forms of the same equation. We introduce $\xi = \tanh(\delta x)$ into (F.1.2), and to do so we need to use the chain rule,

$$\frac{d\psi}{dx} = \frac{d\psi}{d\xi}\frac{d\xi}{dx} \quad \Longrightarrow \quad \frac{d^2\psi}{dx^2} = \underbrace{\frac{d}{dx}}_{=\frac{d}{d\xi}\frac{d\xi}{dx}}\left(\frac{d\psi}{d\xi}\right)\frac{d\xi}{dx} + \frac{d^2\xi}{dx^2}\frac{d\psi}{d\xi}$$

$$\therefore \frac{d^2\psi}{dx^2} = \frac{d^2\psi}{d\xi^2}\left(\frac{d\xi}{dx}\right)^2 + \frac{d^2\xi}{dx^2}\frac{d\psi}{d\xi}.$$

We can now replace this in (F.1.2), using the fact that

$$\frac{d\xi}{dx} = \frac{d}{dx}\tanh(\delta x) = \delta \mathrm{sech}^2(\delta x) = \delta(1 - \tanh^2(\delta x) = \delta(1-\xi^2),$$
$$\frac{d^2\xi}{dx^2} = \frac{d^2}{dx^2}\tanh(\delta x) = -2\delta^2 \tanh(\delta x)\mathrm{sech}^2(\delta x) = -2\delta^2\xi(1-\xi^2).$$

Therefore, (F.1.2) goes to

$$\frac{d^2\psi}{d\xi^2}\delta^2(1-\xi^2)^2 - 2\frac{d\psi}{d\xi}[\delta^2\xi(1-\xi^2)] + \frac{2m}{\hbar^2}\left(E + U_0(1-\xi^2)\right)\psi = 0, \tag{F.1.5}$$

where we have used $1/\cosh^2(\delta x) = \mathrm{sech}^2(\delta x) = 1-\xi^2$. Dividing through by $\delta^2(1-\xi^2)$ we find

$$\frac{d^2\psi}{d\xi^2}(1-\xi^2) - 2\frac{d\psi}{d\xi}\xi + \frac{2m}{\delta^2\hbar^2}\left(\frac{E}{(1-\xi^2)} + U_0\right)\psi = 0, \tag{F.1.6}$$

and we now call

$$\frac{2mE}{\hbar^2} = k^2, \qquad \frac{2mU_0}{\delta^2\hbar^2} = s(s+1), \tag{F.1.7}$$

which is actually using the substitution for the inverted Pöschl-Teller potential from [100] p.79-80 (we are currently following the derivation on p.72-73), but it is more straightforward to introduce the wavevector k immediately in this way. We shall replace for (F.1.7) in the equation above, and arrive at Legendre's equation:

$$(1-\xi^2)\frac{d^2\psi}{d\xi^2} - 2\xi\frac{d\psi}{d\xi} + \left[s(s+1) + \frac{k^2}{\delta^2(1-\xi^2)}\right]\psi = 0. \tag{F.1.8}$$

We convert this to the hypergeometric equation by calling $\psi = (1-\xi^2)^{-ik/2\delta}w(\xi)$ $= fw_\xi$, and changing the argument to $u = \frac{1}{2}(1-\xi)$. We will process the differentials first using our new form of ψ, and then substitute in for u. Our differentials

are thus

$$\psi' = f'w_\xi + fw'_\xi,$$
$$\psi'' = f''w_\xi + 2f'w'_\xi + fw''_\xi.$$

w'_ξ and w''_ξ are just $\frac{\mathrm{d}w}{\mathrm{d}\xi}$ and $\frac{\mathrm{d}^2w}{\mathrm{d}\xi^2}$, but f' and f'' are more complicated:

$$f' = \frac{\mathrm{d}}{\mathrm{d}\xi}(1-\xi^2)^{-ik/2\delta} = +\frac{ik\xi}{\delta(1-\xi^2)}f,$$
$$f'' = -\frac{k^2\xi^2}{\delta^2(1-\xi^2)^2}f + \frac{ik}{\delta(1-\xi^2)}f + \frac{2ik\xi^2}{\delta(1-\xi^2)^2}f.$$

So let us substitute the above into (F.1.8):

$$-2\xi[f'w_\xi + fw'_\xi] + (1-\xi^2)[f''w_\xi + 2f'w'_\xi + fw''_\xi] + \left[s(s+1) + \frac{k^2}{\delta^2(1-\xi^2)}\right] = 0$$

$$\Longrightarrow$$

$$-2\xi\left[\frac{ik\xi}{\delta(1-\xi^2)}fw_\xi + fw'_\xi\right] + (1-\xi^2)\left[-\frac{k^2\xi^2}{\delta^2(1-\xi^2)^2}fw_\xi + \frac{ik}{\delta(1-\xi^2)}fw_\xi + \frac{2ik\xi^2}{\delta(1-\xi^2)^2}fw_\xi + \frac{2ik\xi}{\delta(1-\xi^2)}fw'_\xi + fw''_\xi\right] + \left[s(s+1) + \frac{k^2}{\delta^2(1-\xi^2)}\right]fw_\xi = 0. \quad \text{(F.1.9)}$$

Dividing through by f and multiplying out the brackets:

$$\cancel{\frac{-2ik\xi^2}{\delta(1-\xi^2)}}w_\xi - 2\xi w'_\xi - \frac{k^2\xi^2}{\delta^2(1-\xi^2)}w_\xi + \frac{ik}{\delta}w_\xi + \cancel{\frac{2ik\xi^2}{\delta(1-\xi^2)}}w_\xi + \frac{2ik\xi}{\delta}w'_\xi + (1-\xi^2)w''_\xi + s(s+1)w_\xi + \frac{k^2}{\delta^2(1-\xi^2)}w_\xi = 0. \quad \text{(F.1.10)}$$

Factoring into terms of w'', w', and w:

$$(1-\xi^2)w''_\xi - 2\xi w'_\xi\left(1 - \frac{ik}{\delta}\right) + w_\xi\left(-\frac{k^2\xi^2}{\delta^2(1-\xi^2)} + \frac{ik}{\delta} + s(s+1) + \frac{k^2}{\delta^2(1-\xi^2)}\right) = 0. \quad \text{(F.1.11)}$$

If we group together the two terms in the right-hand bracket with the denominator $\delta^2(1-\xi^2)$, we see that

$$-\frac{k^2\xi^2}{\delta^2(1-\xi^2)} + \frac{k^2}{\delta^2(1-\xi^2)} = \frac{k^2\cancel{(1-\xi^2)}}{\delta^2\cancel{(1-\xi^2)}} = \frac{k^2}{\delta^2}, \quad \text{(F.1.12)}$$

so overall we have

$$(1-\xi^2)w''_\xi - 2\xi w'_\xi\left(1-\frac{ik}{\delta}\right) + w_\xi\left(\frac{k^2}{\delta^2}+\frac{ik}{\delta}+s(s+1)\right)=0. \tag{F.1.13}$$

Now we need to convert to functions of u, recalling that $u=\frac{1}{2}(1-\xi)$. Note that so far, we have been working with w_ξ, and so we need to remember that

$$\begin{aligned} w'_\xi &= \frac{\mathrm{d}w}{\mathrm{d}\xi} = \frac{\mathrm{d}u}{\mathrm{d}\xi}\frac{\mathrm{d}w}{\mathrm{d}u} = -\frac{1}{2}\frac{\mathrm{d}w}{\mathrm{d}u} = -\frac{1}{2}w'_u, \\ w''_\xi &= \frac{\mathrm{d}^2w}{\mathrm{d}\xi^2} = \frac{\mathrm{d}}{\mathrm{d}\xi}\frac{\mathrm{d}w}{\mathrm{d}\xi} = \frac{\mathrm{d}}{\mathrm{d}u}\frac{\mathrm{d}u}{\mathrm{d}\xi}\left(\frac{\mathrm{d}u}{\mathrm{d}\xi}\frac{\mathrm{d}w}{\mathrm{d}u}\right) = +\frac{1}{4}\frac{\mathrm{d}^2w}{\mathrm{d}u^2} = +\frac{1}{4}w''_u, \end{aligned} \tag{F.1.14}$$

and of course $w_\xi \to w_u$ directly, since w is a function of ξ which is a function of u. Let us substitute (F.1.14) into (F.1.13) to find

$$\begin{aligned} \cancel{4}\tfrac{1}{\cancel{4}}(u-u^2)w''_u + \cancel{2}\tfrac{1}{\cancel{2}}\left(1-\frac{ik}{\delta}\right)(1-2u)w'_u - \left(-\frac{ik}{\delta}-s\right)\left(-\frac{ik}{\delta}+s+1\right)w_u = 0, \\ u(1-u)w''_u + \left(1-\frac{ik}{\delta}\right)(1-2u)w'_u - \left(-\frac{ik}{\delta}-s\right)\left(-\frac{ik}{\delta}+s+1\right)w_u = 0. \end{aligned} \tag{F.1.15}$$

This is the hypergeometric equation, in the same form as in [100] p.73. The general solution to the hypergeometric equation of the form

$$z(1-z)y'' + [c-(a+b+1)z]y' - aby = 0 \tag{F.1.16}$$

is a sum of two linearly independent solutions ([99], p.630):

$$y(z) = AF[a,b,c;z] + Bz^{1-c}F[a-c+1,b-c+1,2-c;z], \tag{F.1.17}$$

where A and B are constants to be found by considering the boundary conditions, and $F[a,b,c;z]$ is the hypergeometric function[1]. The arbitrary complex numbers a,b and c are known as the *parameters*, and z is the *variable* of the hypergeometric function. It can be written as

$$F[a,b,c;z] = \frac{\Gamma(c)}{\Gamma(a)\Gamma(b)}\sum_{n=0}^{\infty}\frac{\Gamma(a+n)\Gamma(b+n)}{\Gamma(c+n)}\frac{z^n}{n!}. \tag{F.1.18}$$

The full details of these functions are discussed in a variety of textbooks, for

[1] Also denoted ${}_2F_1[a,b,c;z]$ - see footnote in [99], p.630.

example [99] (pp.628-632) or [151] (Chapter II), and will not be discussed here. First, let us confirm that our equation (F.1.15) is of the same form as (F.1.16), and thus has solutions (F.1.17). We can see straight away that u takes the role of z. We can also assume that a and b are given by the two brackets multiplying w_u in (F.1.15), which must mean that:

$$\begin{aligned} c-(a+b+1)u &\stackrel{!}{=} \left(1-\frac{ik}{\delta}\right)(1-2u) \\ \therefore c-\left[\left(-\frac{ik}{\delta}-s\right)+\left(-\frac{ik}{\delta}+s+1\right)+1\right]u &\stackrel{!}{=} \left(1-\frac{ik}{\delta}\right)(1-2u) \\ \therefore c+\frac{2ik}{\delta}u-2u &\stackrel{!}{=} 1-2u-\frac{ik}{\delta}+\frac{2ik}{\delta}u \\ \implies c &= 1-\frac{ik}{\delta}. \end{aligned}$$

Now we know a, b and c, we can say that the solution to the hypergeometric equation (F.1.15) is

$$\begin{aligned} \psi = A(1-\xi^2)^{-ik/2\delta}F\left[-\frac{ik}{\delta}-s,-\frac{ik}{\delta}+s+1,-\frac{ik}{\delta}+1,\frac{1}{2}(1-\xi)\right]+ \\ B(1-\xi^2)^{-ik/2\delta}\left(\frac{1}{2}(1-\xi)\right)^{ik/\delta}F\left[-s,s+1,\frac{ik}{\delta}+1;\frac{1}{2}(1-\xi)\right]. \end{aligned} \tag{F.1.19}$$

We can now convert to our original variables, using (F.1.3) and (F.1.7) (although we will keep k in the equation; conveniently, it is the wave number!) so we just need to find s:

$$\begin{aligned} \frac{2mU_0}{\delta^2\hbar^2} = s(s+1) \implies s &= \frac{1}{2}\left(-1+\sqrt{1+\frac{8mU_0}{\delta^2\hbar^2}}\right) \\ &= \frac{1}{2}\left(-1+\sqrt{1+4\frac{2}{\cancel{\lambda_B^2}}\cancel{\lambda_B^2}}\right) = \frac{1}{2}\left(-1+\sqrt{1+8}\right) = 1. \end{aligned} \tag{F.1.20}$$

Now we replace these in (F.1.19), remembering that $\xi = \tanh[y/\lambda_B]$, and using the fact that $\left(1-\tanh^2[y/\lambda_B]\right)^{-1/2} = \left(\operatorname{sech}^2[y/\lambda_B]\right)^{-1/2} = \cosh[y/\lambda_B]$:

$$\varphi(y) = \overbrace{A\left(\cosh[y/\lambda_B]\right)^{ik\lambda_B} F\left[-ik\lambda_B - 1, -ik\lambda_B + 2, -ik\lambda_B + 1, \frac{1-\tanh[y/\lambda_B]}{2}\right]}^{m_1} + \underbrace{B\left(\cosh[y/\lambda_B]\right)^{ik\lambda_B}\left(\frac{1-\tanh[y/\lambda_B]}{2}\right)^{ik\lambda_B} F\left[-1, 2, ik\lambda_B + 1; \frac{1-\tanh[y/\lambda_B]}{2}\right]}_{m_2}, \quad \text{(F.1.21)}$$

with

$$k = \sqrt{-\Lambda^{\pm} - \frac{\beta_{\|}}{\alpha}} = k^{\pm}.$$

The notation $k^{\pm}$ is introduced because it actually represents two solutions; a solution corresponding to Λ^+ and one corresponding to Λ^-. **We will use this new notation in the main text, but for ease of reading we will omit this subscript in the rest of this Appendix.** Notice also that we define m_1 and m_2 in (F.1.21), for brevity.

F.2 Representing the Hypergeometric Function in *Mathematica*

In plotting m_1 and m_2 for some arbitrary values of all the variables, we find that the graph ends abruptly just away from the domain wall region, and is, according to *Mathematica*, indeterminate beyond these points. It turns out that, because of the behaviour of $\tanh(y/\lambda_B)$ and the hypergeometric function (which depends on the former), you have to resort to taking the asymptotic limits of the entire function in order to get a reasonable solution. Let us see briefly why the function becomes 'indeterminate' in *Mathematica*, and how to overcome this issue.

At the positive limit, the second term in $\varphi(y)$ is indeterminate, and something to bear in mind in *Mathematica* is that any indeterminate term 'poisons' the entire expression. This second term is indeterminate simply because $(1 - \tanh[y/\lambda_B]) \to 0$ as y/λ_B becomes large and positive, as shown in Figure F.1, and $0^{ik\lambda_B}$ has no solution[2].

[2]Although the expression becomes indeterminate at seemingly small (positive or negative) values of x, this is just due to *Mathematica* rounding the function to exactly 0 or 1; in reality, these values are asymptotes - they never exactly get there.

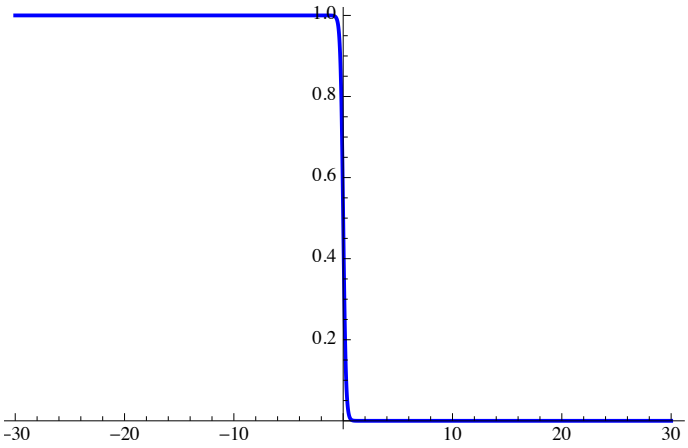

FIGURE F.1: Plot of $\frac{1}{2}(1-\tanh[4y])$ vs. y. The behaviour at $\pm\infty$ means that we must consider the 'asymptotic form' of $\varphi(y)$ away from the domain wall region.

For negative y, $\frac{1}{2}(1-\tanh[y/\lambda_B]) \to 1$, and *Mathematica* seems to round this value to 1. The hypergeometric function $F[a,b,c;1]$ is indeterminate, due to our values of a, b and c; it seems that *Mathematica* can only find the solution to $F[a,b,c;1]$ if[3] $\mathrm{Re}\{c-a-b\} > 0$ - which is not fulfilled in our case. It turns out that there is a legitimate conversion formula that we can force *Mathematica* to use, to avoid it automatically assuming that our function is indeterminate away from the domain wall region.

Firstly, we correct the plotting issue at $y \to +\infty$ by combining the $\cosh(y/\lambda_B)$ and $\frac{1}{2}(1-\tanh[y/\lambda_B])$ terms together:

$$\begin{aligned}\cosh[y/\lambda_B]^{ik\lambda_B}\left(\frac{1-\tanh[y/\lambda_B]}{2}\right)^{ik\lambda_B} &= \left\{\frac{1}{2}\left(\cosh[y/\lambda_B] - \cancel{\cosh[y/\lambda_B]}\cdot\frac{\sinh[y/\lambda_B]}{\cancel{\cosh[y/\lambda_B]}}\right)\right\}^{ik\lambda_B} \\ &= \left(\frac{e^{y/\lambda_B}+e^{-y/\lambda_B}-e^{y/\lambda_B}+e^{-y/\lambda_B}}{4}\right)^{i\lambda_B} \\ &= \left(\frac{e^{-y/\lambda_B}}{2}\right)^{ik\lambda_B}.\end{aligned}$$

Now we will have no problems with $0^{ik\lambda_B}$ terms, although imaginary k values may cause issues at large values of y. We also need to plot the function in a piecewise manner; keeping the original solution for where the function is 'well-behaved' (near and in the domain wall), and using a conversion formula for when $y \to -\infty$. As $y \to -\infty$, $z \to 1$, and for $F[a,b,c;z \to 1]$ we need to use the relation

[3] see http://functions.wolfram.com/HypergeometricFunctions/Hypergeometric2F1/03/02/

([100], p.606, and [151], p.108):

$$F[a,b,c;z] = \frac{\Gamma(c)\Gamma(c-a-b)}{\Gamma(c-a)\Gamma(c-b)}F[a,b,a+b-c+1;1-z]+$$
$$+\frac{\Gamma(c)\Gamma(a+b-c)}{\Gamma(a)\Gamma(b)}(1-z)^{c-a-b}F[c-a,c-b,c-a-b+1;1-z]. \tag{F.2.1}$$

For $z = 1$, we specify that *Mathematica* should use (F.2.1), otherwise it uses the original solution - and this works well.

F.3 Form of the Two Solutions at Asymptotic Limits

We have that m_1 and m_2 are the two, linearly independent solutions to the hypergeometric equation. To understand what these actually look like, we need to take the limit as $y \to \pm\infty$. We will look at the two limits separately.

Negative Limit of $\varphi(y)$

We rewrite (F.1.21) using (F.2.1)[4], including s even though we know it is equal to 1, to keep it general:

$$\begin{aligned}\lim_{y\to-\infty}\varphi(y) &= A(\cosh[y/\lambda_B])^{ik\lambda_B}\left\{\frac{\Gamma(c)\Gamma(c-a-b)}{\Gamma(c-a)\Gamma(c-b)}+(1-z)^{c-a-b}\frac{\Gamma(c)\Gamma(a+b-c)}{\Gamma(a)\Gamma(b)}\right\}\\
&+B(\cosh[y/\lambda_B])^{ik\lambda_B}\left(\frac{1-\tanh[y/\lambda_B]}{2}\right)^{ik\lambda_B}\left\{\frac{\Gamma(c')\Gamma(c'-a'-b')}{\Gamma(c'-a')\Gamma(c'-b')}+\right.\\
&\left.+(1-z)^{c'-a'-b'}\frac{\Gamma(c')\Gamma(a'+b'-c')}{\Gamma(a')\Gamma(b')}\right\}\\
&= A(\cosh[y/\lambda_B])^{ik\lambda_B}\left\{\frac{\Gamma(-ik\lambda_B+1)\Gamma(ik\lambda_B)}{\Gamma(1+s)\Gamma(-s)}+\right.\\
&\left.+\left(\frac{e^{2y/\lambda_B}}{e^{2y/\lambda_B}+1}\right)^{ik\lambda_B}\frac{\Gamma(-ik\lambda_B+1)\Gamma(-ik\lambda_B)}{\Gamma(-ik\lambda_B-s)\Gamma(-ik\lambda_B+s+1)}\right\}\\
&+B(\cosh[y/\lambda_B])^{ik\lambda_B}\left(\frac{1}{e^{2y/\lambda_B}+1}\right)^{ik\lambda_B}\left\{\frac{\Gamma(ik\lambda_B+1)\Gamma(ik\lambda_B)}{\Gamma(ik\lambda_B+s+1)\Gamma(ik\lambda_B-s)}+\right.\\
&\left.+\left(\frac{e^{2y/\lambda_B}}{e^{2y/\lambda_B}+1}\right)^{ik\lambda_B}\frac{\Gamma(ik\lambda_B+1)\Gamma(-ik\lambda_B)}{\Gamma(-s)\Gamma(1+s)}\right\},\end{aligned} \tag{F.3.1}$$

[4]Remember that the expression for $\varphi(y)$ in (F.1.21) is the sum of two terms, m_1 and m_2 each with a different hypergeometric function. The parameters for the second hypergeometric equation are therefore primed, to avoid confusion.

where we have expanded $1-z = 1-\frac{1}{2}(1-\tanh[y/\lambda_B]) = \frac{e^{2y/\lambda_B}}{e^{2y/\lambda_B}+1}$. Let us multiply out the brackets, and take the limits of these terms as $y \to -\infty$. Writing $\cosh[y/\lambda_B] = \frac{1}{2}(e^{y/\lambda_B} + e^{-y/\lambda_B})$, we therefore have:

$$\begin{aligned}
\lim_{y\to-\infty}\varphi(y) =& A\frac{1}{2^{ik\lambda_B}}\underbrace{\big(\overbrace{e^{y/\lambda_B}}^{\to 0}+e^{-y/\lambda_B}\big)^{ik\lambda_B}}_{\approx e^{-iky}}\frac{\Gamma(-ik\lambda_B+1)\Gamma(ik\lambda_B)}{\Gamma(1+s)\Gamma(-s)}+\\
&+A\frac{1}{2^{ik\lambda_B}}\underbrace{\underbrace{\big(e^{y/\lambda_B}+e^{-y/\lambda_B}\big)^{ik\lambda_B}}_{\approx e^{-iky}}\underbrace{\left(\frac{\overbrace{e^{2y/\lambda_B}}^{\text{dominates}}}{\underbrace{e^{2y/\lambda_B}}_{\to 0}+1}\right)^{ik\lambda_B}}_{\approx e^{2iky}}}_{\approx e^{+iky}}\frac{\Gamma(-ik\lambda_B+1)\Gamma(-ik\lambda_B)}{\Gamma(-ik\lambda_B-s)\Gamma(-ik\lambda_B+s+1)}\\
&+B\frac{1}{2^{ik\lambda_B}}\underbrace{\underbrace{\big(e^{y/\lambda_B}+e^{-y/\lambda_B}\big)^{ik\lambda_B}}_{\approx e^{-iky}}\underbrace{\left(\frac{1}{e^{2y/\lambda_B}+1}\right)^{ik\lambda_B}}_{\to 1^{ik\lambda_B}}}_{\approx e^{-iky}}\frac{\Gamma(ik\lambda_B+1)\Gamma(ik\lambda_B)}{\Gamma(ik\lambda_B+s+1)\Gamma(ik\lambda_B-s)}+\\
&+B\Bigg\{\frac{1}{2^{ik\lambda_B}}\underbrace{\big(e^{y/\lambda_B}+e^{-y/\lambda_B}\big)^{ik\lambda_B}\left(\frac{1}{e^{2y/\lambda_B}+1}\right)^{ik\lambda_B}\left(\frac{e^{2y/\lambda_B}}{e^{2y/\lambda_B}+1}\right)^{ik\lambda_B}}_{\approx e^{+iky}}\times\\
&\times\frac{\Gamma(ik\lambda_B+1)\Gamma(-ik\lambda_B)}{\Gamma(-s)\Gamma(1+s)}\Bigg\}
\end{aligned}$$

$$\begin{aligned}
\therefore \lim_{x\to-\infty}\varphi(y) \approx& \frac{A}{2^{ik\lambda_B}}e^{-iky}\overbrace{\frac{\Gamma(-ik\lambda_B+1)\Gamma(ik\lambda_B)}{\Gamma(1+s)\Gamma(-s)}}^{G_{11}}+\frac{A}{2^{ik\lambda_B}}e^{+iky}\overbrace{\frac{\Gamma(-ik\lambda_B+1)\Gamma(-ik\lambda_B)}{\Gamma(-ik\lambda_B-s)\Gamma(-ik\lambda_B+s+1)}}^{G_{12}}\\
&+\frac{B}{2^{ik\lambda_B}}e^{-iky}\underbrace{\frac{\Gamma(ik\lambda_B+1)\Gamma(ik\lambda_B)}{\Gamma(ik\lambda_B+s+1)\Gamma(ik\lambda_B-s)}}_{G_{21}}+\frac{B}{2^{ik\lambda_B}}e^{+iky}\underbrace{\frac{\Gamma(ik\lambda_B+1)\Gamma(-ik\lambda_B)}{\Gamma(-s)\Gamma(1+s)}}_{G_{22}}.
\end{aligned}\tag{F.3.2}$$

This matches up with the result in [100], except for a factor of $\lambda_B = 1/\alpha$ (note that "$1/\alpha$" is in the notation of [100] and does not relate to α in this work) which is missing from the gamma factors in [100] - we can assume this is a typo, as these are directly obtained from a, b and c. In addition, we will retain the factor of $\frac{1}{2^{ik\lambda_B}}$, since this provides an important imaginary contribution to the function (clearly seen when plotting).

Positive Limit of $\varphi(y)$

Let us look at the other limit, for $y \to +\infty$. In this case, $F[a,b,c;z\to 0] = 1$ and $\varphi(y)$ from (F.1.21) just consists of $\cosh(y/\lambda_B)$ and $\tanh(y/\lambda_B)$ terms:

$$\begin{aligned}\lim_{x\to+\infty}\varphi(y) &= A(\cosh[y/\lambda_B])^{ik\lambda_B} + B(\cosh[y/\lambda_B])^{ik\lambda_B}\left(\frac{1-\tanh[y/\lambda_B]}{2}\right)^{ik\lambda_B} \\ &= A\frac{1}{2^{ik\lambda_B}}\underbrace{\left(e^{y/\lambda_B}+\overbrace{e^{-y/\lambda_B}}^{\to 0}\right)^{ik\lambda_B}}_{\approx e^{+iky}} + B\frac{1}{2^{ik\lambda_B}}\underbrace{\underbrace{\left(e^{y/\lambda_B}+\overbrace{e^{-y/\lambda_B}}^{\to 0}\right)^{ik\lambda_B}}_{\approx e^{+iky}}\underbrace{\left(\frac{1}{e^{2y/\lambda_B}+1}\right)^{ik\lambda_B}}_{\approx e^{-2iky}}}_{\approx e^{-iky}} \\ &\approx \frac{A}{2^{ik\lambda_B}}e^{+iky} + \frac{B}{2^{ik\lambda_B}}e^{-iky}. \end{aligned} \tag{F.3.3}$$

This matches up with the result in [100] (though again they omit the second solution to the hypergeometric equation, so they do not include the term containing B).

F.4 Asymptotic Limits & the Wronskian

So far, we have been working with the fundamental solutions to the hypergeometric equation in their original forms. However, we need to design solutions to the equation which are a linear superposition of these two fundamental solutions; these would physically just correspond to a different experiment being carried out. The current 'experiment' is shown in Figure F.2a, and this is compared to the 'experiment' we would rather represent in Figure F.2b. This way, we should more easily be able to choose A and B so that the waves fulfill the boundary conditions. Note that we will now call these amplitudes C and D, to avoid confusion.

In Figure F.2b we have made a convenient superposition of m_1 and m_2, to form:

$$w_1 = m_1, \qquad \text{and} \qquad w_2 = G_{12}m_2 - G_{22}m_1. \tag{F.4.1}$$

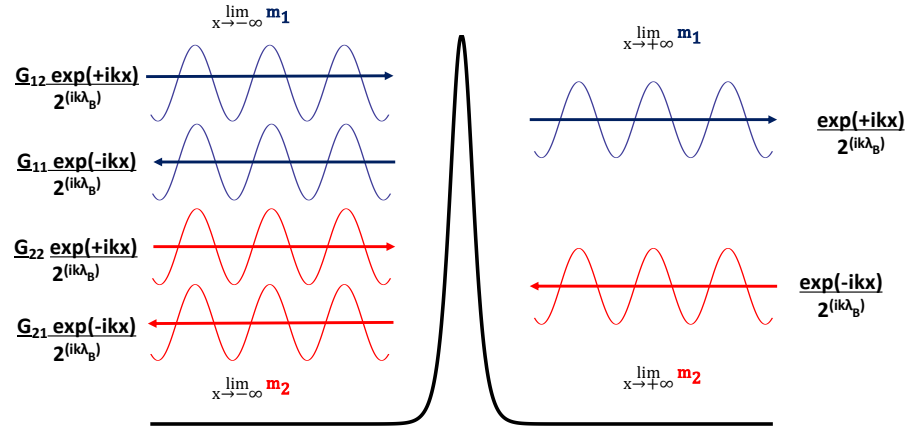

(A) Current situation, with m_1 and m_2 in their unaltered forms.

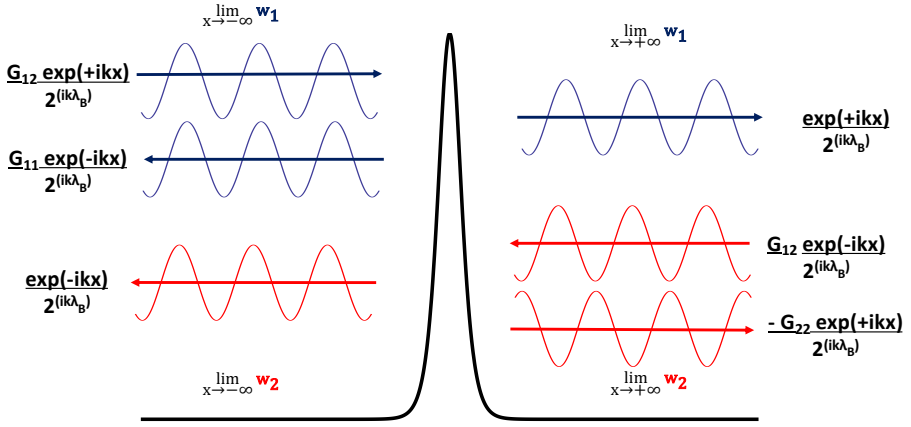

(B) Preferred situation: making a superposition of m_1 and m_2 to form w_1 and w_2. This makes it easier to remove solutions which do not fit our boundary conditions.

FIGURE F.2: Pictorial representation of waves impinging on the domain wall.

As a result (as shown in Figure F.2b):

$$\begin{aligned}
\lim_{y\to-\infty} w_2 &= G_{12}m_2 - G_{22}m_1 \\
&= G_{12}\left(\frac{G_{21}}{2^{ik\lambda_B}}e^{-iky} + \frac{G_{22}}{2^{ik\lambda_B}}\cancel{e^{+iky}}\right) - G_{22}\left(\frac{G_{11}}{2^{ik\lambda_B}}e^{-iky} + \frac{G_{12}}{2^{ik\lambda_B}}\cancel{e^{+iky}}\right) \\
&= \underbrace{\left(G_{12}G_{21} - G_{11}G_{22}\right)}_{=1}\frac{e^{-iky}}{2^{ik\lambda_B}} \\
&= \frac{e^{-iky}}{2^{ik\lambda_B}},
\end{aligned}$$

$$\lim_{y\to+\infty} w_2 = G_{12}m_2 - G_{22}m_1$$
$$= \frac{G_{12}}{2^{ik\lambda_B}}e^{-iky} - \frac{G_{22}}{2^{ik\lambda_B}}e^{+iky}.$$

We adapt (F.1.21) by replacing m_1 by w_1 (although they are the same, we will use the new notation) and m_2 by w_2. In the main text, we shall call these $w_1^{\pm}$ and $w_2^{\pm}$ since they are a function of $k^{\pm}$ (these superscripts have been omitted in this Appendix for brevity). This are written in the main text as Eq. (4.4.6).

Finally, let us use the asymptotic limits to work out the Wronskian, W, for this situation. This is a quantity which will be required later to solve the inhomogeneous equation, and is defined as

$$W = y_1y_2' - y_2y_1',$$

where y_1 and y_2 are the two linearly independent solutions of the homogeneous, second order differential equation $y''(x) + p(x)y'(x) + q(x)y(x) = 0$. We will look at W for each limit separately, and they should be equal. Just for now, we call our solutions to the homogeneous equation at each limit $w_{1+/-}$ and $w_{2+/-}$, where the $+$ or $-$ subscript indicates that it is for the $+\infty$ or $-\infty$ limit, respectively. Let us first look at the Wronskian for $x \to +\infty$:

$$\begin{aligned} W_{x\to+\infty} &= (w_{2+})(w_{1+})' - (w_{1+})(w_{2+})' \\ &= \left(\frac{G_{12}}{2^{ik\lambda_B}}e^{-ikx} - \cancel{\frac{G_{22}}{2^{ik\lambda_B}}e^{+ikx}}\right)\left(\frac{ik}{2^{ik\lambda_B}}e^{+ikx}\right) \\ &- \left(\frac{1}{2^{ik\lambda_B}}e^{+ikx}\right)\left(\frac{-ikG_{12}}{2^{ik\lambda_B}}e^{-ikx} - \cancel{\frac{ikG_{22}}{2^{ik\lambda_B}}e^{+ikx}}\right) \\ &= \frac{2ikG_{12}}{2^{2ik\lambda_B}} = \frac{ikG_{12}}{2^{ik\lambda_B}}. \end{aligned} \tag{F.4.2}$$

For $x \to -\infty$ we have:

$$\begin{aligned} W_{x\to-\infty} &= (w_{2-})(w_{1-})' - (w_{1-})(w_{2-})' \\ &= \left(\frac{1}{2^{ik\lambda_B}}e^{-ikx}\right)\left(\frac{ikG_{12}}{2^{ik\lambda_B}}e^{+ikx} - \cancel{\frac{ikG_{11}}{2^{ik\lambda_B}}e^{-ikx}}\right) \\ &- \left(\frac{G_{12}}{2^{ik\lambda_B}}e^{+ikx} + \cancel{\frac{G_{11}}{2^{ik\lambda_B}}e^{-ikx}}\right)\left(\frac{-ik}{2^{ik\lambda_B}}e^{-ikx}\right) \\ &= \frac{ikG_{12}}{2^{ik\lambda_B}}. \end{aligned} \tag{F.4.3}$$

So the Wronskian is the same at both limits. We will write out the final result in the form we use in the main text (including the superscripts):

$$W^{\pm} = \frac{ik^{\pm}G_{12}}{2^{ik^{\pm}\lambda_B}}. \tag{F.4.4}$$

Appendix G

Solving the Inhomogeneous Matrix Equation

G.1 Magnetisation as a Sum of Two Contributions

We are trying to solve

$$\frac{1}{\alpha\gamma M_0}\partial_t \mathbf{m}' = i\sigma_y \left[\partial_y^2 - \frac{\beta_\parallel}{\alpha} + \frac{2}{\lambda_B^2}\operatorname{sech}^2\left(\frac{y}{\lambda_B}\right)\right]\mathbf{m}' + \begin{pmatrix} 0 & 0 \\ \frac{\beta_\perp}{\alpha} & 0 \end{pmatrix}\mathbf{m}' + \begin{pmatrix} \frac{h(t)}{\alpha} \\ 0 \end{pmatrix}, \tag{G.1.1}$$

which is Eq. (4.4.1) in the main text. As per the approach in [67], we can write that the magnetisation is the sum of two contributions:

$$\mathbf{m}' = \mathbf{m}'_\beta + \mathbf{m}'_h, \tag{G.1.2}$$

where $\mathbf{m}'_\beta$ is the magnetisation due to the presence of the domain wall, and $\mathbf{m}'_h$ is the magnetisation due to the external driving magnetic field. Substituting this into (G.1.1) we find:

$$\begin{aligned}\frac{1}{\alpha\gamma M_0}\partial_t\left[\mathbf{m}'_\beta + \mathbf{m}'_h\right] = i\sigma_y\left[\partial_y^2 - \frac{\beta_\parallel}{\alpha} + \frac{2}{\lambda_B^2}\operatorname{sech}^2\left(\frac{y}{\lambda_B}\right)\right]\left[\mathbf{m}'_\beta + \mathbf{m}'_h\right] \\ + \begin{pmatrix} 0 & 0 \\ \frac{\beta_\perp}{\alpha} & 0 \end{pmatrix}\left[\mathbf{m}'_\beta + \mathbf{m}'_h\right] + \begin{pmatrix} \frac{h(t)}{\alpha} \\ 0 \end{pmatrix}.\end{aligned}$$

The purpose of separating the magnetisation into two distinct contributions will now become clear: we can compare each side of the equation, and use the fact

that $\mathbf{m}'_h$ has no y-dependence[1], and that $\mathbf{m}'_\beta$ has no dependence on $h(t)$, to extract two equations from the single equation above[2]:

$$\begin{aligned}\frac{1}{\alpha\gamma M_0}\partial_t \mathbf{m}'_\beta = i\sigma_y\left[\partial_y^2 - \frac{\beta_\parallel}{\alpha} + \frac{2}{\lambda_B^2}\operatorname{sech}^2\left(\frac{y}{\lambda_B}\right)\right]\mathbf{m}'_\beta \\ + i\sigma_y\frac{2}{\lambda_B^2}\operatorname{sech}^2\left(\frac{y}{\lambda_B}\right)\mathbf{m}'_h + \begin{pmatrix} 0 & 0 \\ \frac{\beta_\perp}{\alpha} & 0\end{pmatrix}\mathbf{m}'_\beta,\end{aligned} \tag{G.1.3}$$

$$\begin{aligned}\frac{1}{\alpha\gamma M_0}\partial_t \mathbf{m}'_h &= i\sigma_y\left[-\frac{\beta_\parallel}{\alpha}\right]\mathbf{m}'_h + \begin{pmatrix} 0 & 0 \\ \frac{\beta_\perp}{\alpha} & 0\end{pmatrix}\mathbf{m}'_h + \begin{pmatrix} \frac{h(t)}{\alpha} \\ 0\end{pmatrix} \\ &= \begin{pmatrix} 0 & -\frac{\beta_\parallel}{\alpha} \\ \frac{\beta_\parallel+\beta_\perp}{\alpha} & 0\end{pmatrix}\mathbf{m}'_h + \begin{pmatrix} \frac{h(t)}{\alpha} \\ 0\end{pmatrix}.\end{aligned} \tag{G.1.4}$$

These two equations are much easier to deal with. Firstly, (G.1.3) is just the inhomogenous form of the equation that we solved in the previous Appendix, and now the driving term (which depends on $\mathbf{m}'_h$) is not uniform in space; it is moderated by the sech^2 term. Secondly, equation (G.1.4) can be solved easily once we have carried out a Fourier transform.

G.2 Fourier Transform to Frequency Domain

We will now carry out a Fourier transform to convert from the time domain to the frequency domain. Generally, the definition of a Fourier transform for this situation is ([73], p.690):

$$F(\omega') = \int_{-\infty}^{+\infty} f(t)\exp(i\omega' t)\mathrm{d}t, \tag{G.2.1}$$

where the factor of $\frac{1}{\sqrt{2\pi}}$ has been omitted, if it is understood that the inverse function (which we will conveniently not need to obtain) will have an extra factor of $\frac{1}{2\pi}$. We apply the Fourier transform to both sides of (G.1.3) and (G.1.4), i.e. we multiply by $\exp(i\omega t)$ and integrate over t. This means that we transform $\mathbf{m}'_\beta(t) \to \tilde{\mathbf{m}}'_\beta(\omega)$, and $h(t) \to \tilde{h}(\omega)$.

[1] $h(t)$ is applied in the y direction, but it is invariant in this direction. We specified that it is of the form $h(t) = h\exp(-i\tilde{\omega}t)$, so only the amplitude varies in time.

[2] Though both equations can be obtained by reasoning which terms should be on the right hand side of each equation, you can also obtain (G.1.3) by substituting (G.1.4) back into (G.1.1).

On the left hand side of each equation (G.1.3) and (G.1.4), we will need to use the result ([73] p.706) that the Fourier transform of the time derivative of $f(t)$ is given by:

$$F_1(\omega) = \int_{-\infty}^{+\infty} \frac{\mathrm{d}f(t)}{\mathrm{d}t} \exp(i\omega t)\mathrm{d}t = -i\omega F(\omega), \tag{G.2.2}$$

where $F(\omega)$ is given in (G.2.1). We therefore convert $\partial_t \mathbf{m}'_\beta(t) \rightarrow -i\omega\tilde{\mathbf{m}}'_\beta(\omega)$. Substituting these results into our equations, we find equation (G.1.3) goes to:

$$\begin{aligned} -\frac{i\omega}{\alpha\gamma M_0}\tilde{\mathbf{m}}'_\beta = i\sigma_y \left[\partial_y^2 - \frac{\beta_\parallel}{\alpha} + \frac{2}{\lambda_B^2}\operatorname{sech}^2\left(\frac{y}{\lambda_B}\right)\right]\tilde{\mathbf{m}}'_\beta \\ + i\sigma_y \frac{2}{\lambda_B^2}\operatorname{sech}^2\left(\frac{y}{\lambda_B}\right)\tilde{\mathbf{m}}'_h + \begin{pmatrix} 0 & 0 \\ \frac{\beta_\perp}{\alpha} & 0 \end{pmatrix}\tilde{\mathbf{m}}'_\beta, \end{aligned} \tag{G.2.3}$$

and similarly for (G.1.4):

$$\begin{aligned} -\frac{i\omega}{\alpha\gamma M_0}\tilde{\mathbf{m}}'_h &= \begin{pmatrix} 0 & -\frac{\beta_\parallel}{\alpha} \\ \frac{\beta_\parallel}{\alpha} + \frac{\beta_\perp}{\alpha} & 0 \end{pmatrix}\tilde{\mathbf{m}}'_h + \begin{pmatrix} \frac{\tilde{h}(\omega)}{\alpha} \\ 0 \end{pmatrix} \\ \implies \mathbb{1}\begin{pmatrix} \frac{\tilde{h}(\omega)}{\alpha} \\ 0 \end{pmatrix} &= \left\{\mathbb{1}\begin{pmatrix} 0 & \frac{\beta_\parallel}{\alpha} \\ -\frac{\beta_\parallel}{\alpha} - \frac{\beta_\perp}{\alpha} & 0 \end{pmatrix} - \mathbb{1}\frac{i\omega}{\alpha\gamma M_0}\right\}\tilde{\mathbf{m}}'_h \\ \therefore \begin{pmatrix} \frac{\tilde{h}(\omega)}{\alpha} \\ 0 \end{pmatrix} &= \begin{pmatrix} -\frac{i\omega}{\alpha\gamma M_0} & \frac{\beta_\parallel}{\alpha} \\ -\frac{\beta_\parallel}{\alpha} - \frac{\beta_\perp}{\alpha} & -\frac{i\omega}{\alpha\gamma M_0} \end{pmatrix}\tilde{\mathbf{m}}'_h \\ \therefore \tilde{\mathbf{m}}'_h &= \frac{\alpha^2}{-\frac{\omega^2}{\gamma M_0^2} + \beta_\parallel(\beta_\parallel + \beta_\perp)} \begin{pmatrix} -\frac{i\omega}{\alpha\gamma M_0} & -\frac{\beta_\parallel}{\alpha} \\ \frac{\beta_\parallel + \beta_\perp}{\alpha} & -\frac{i\omega}{\alpha\gamma M_0} \end{pmatrix}\begin{pmatrix} \frac{\tilde{h}(\omega)}{\alpha} \\ 0 \end{pmatrix} \\ \therefore \tilde{\mathbf{m}}'_h &= \frac{1}{\frac{-\omega^2}{\gamma M_0^2} + \beta_\parallel(\beta_\parallel + \beta_\perp)} \begin{pmatrix} -\frac{i\omega}{\gamma M_0}\tilde{h}(\omega) \\ (\beta_\parallel + \beta_\perp)\tilde{h}(\omega) \end{pmatrix}. \end{aligned} \tag{G.2.4}$$

Note that in the second step, we multiply by the identity matrix $\mathbb{1}$, which does not affect the existing matrices, but converts the term $\frac{i\omega}{\gamma M_0}$ into a diagonal matrix, so we can simplify the term in the curly bracket into one matrix. We then inverted this matrix, using the standard procedure ([73], p.185) that

$$\text{if} \quad \boldsymbol{A} = \begin{pmatrix} a_{11} & a_{12} \\ a_{21} & a_{22} \end{pmatrix}, \quad \text{then the inverse} \quad \boldsymbol{A}^{-1} = \frac{1}{\det(A)}\begin{pmatrix} a_{22} & -a_{12} \\ -a_{21} & a_{11} \end{pmatrix}.$$

After finding the inverse, the equation is rearranged using the rule that for $\boldsymbol{A}\mathbf{x} = \mathbf{b}$, the solution is $\mathbf{x} = \boldsymbol{A}^{-1}\mathbf{b}$ ([73], p.185) - remembering that the order matters in

matrix multiplication.

G.3 Solving for $\tilde{\mathbf{m}}'_\beta$

We therefore have an expression for $\tilde{\mathbf{m}}'_h$, and we now need to return to (G.2.3) to solve for $\tilde{\mathbf{m}}'_\beta$. We will rearrange (G.2.3) to take a more familiar form:

$$i\sigma_y\left[\partial_y^2 - \frac{\beta_\parallel}{\alpha} + \frac{2}{\lambda_B^2}\operatorname{sech}^2\left(\frac{y}{\lambda_B}\right)\right]\tilde{\mathbf{m}}'_\beta + \begin{pmatrix} \frac{i\omega}{\alpha\gamma M_0} & 0 \\ \frac{\beta_\perp}{\alpha} & \frac{i\omega}{\alpha\gamma M_0}\end{pmatrix}\tilde{\mathbf{m}}'_\beta = -i\sigma_y\frac{2}{\lambda_B^2}\operatorname{sech}^2\left(\frac{y}{\lambda_B}\right)\tilde{\mathbf{m}}'_h = \mathbf{r}(y). \tag{G.3.1}$$

For completeness, we compare this equation to the homogeneous equation in the main text (4.4.2), which we will repeat here

$$\frac{1}{\alpha\gamma M_0}\partial_t\mathbf{m}'_G = i\sigma_y\left[\partial_y^2 - \frac{\beta_\parallel}{\alpha} + \frac{2}{\lambda_B^2}\operatorname{sech}^2\left(\frac{y}{\lambda_B}\right)\right]\mathbf{m}'_G + \begin{pmatrix} 0 & 0 \\ \frac{\beta_\perp}{\alpha} & 0\end{pmatrix}\mathbf{m}'_G, \tag{G.3.2}$$

and now Fourier transform to the frequency domain:

$$i\sigma_y\left[\partial_y^2 - \frac{\beta_\parallel}{\alpha} + \frac{2}{\lambda_B^2}\operatorname{sech}^2\left(\frac{y}{\lambda_B}\right)\right]\tilde{\mathbf{m}}'_{\pm,G} + \begin{pmatrix} \frac{i\omega}{\alpha\gamma M_0} & 0 \\ \frac{\beta_\perp}{\alpha} & \frac{i\omega}{\alpha\gamma M_0}\end{pmatrix}\tilde{\mathbf{m}}'_{\pm,G} = 0. \tag{G.3.3}$$

We can clearly see, as we discussed earlier, that the equation for $\tilde{\mathbf{m}}'_\beta$ given by (G.3.1) is the same as the homogeneous equation (G.3.3) but with a driving term, which we have called $\mathbf{r}(y)$. Therefore $\tilde{\mathbf{m}}'_{\pm,G}$, the Fourier transform of $\mathbf{m}'_{\pm,G}$, is just the solution to the homogeneous equation for $\tilde{\mathbf{m}}'_\beta$. We will therefore convert $\mathbf{m}'_{\pm,G}(y,t)$ to the frequency domain (noting that only the exponential has time dependence). Carrying out the usual Fourier transform procedure:

$$\begin{aligned}
\tilde{\mathbf{m}}'_{\pm,G} &= \int_{-\infty}^{+\infty}\mathbf{m}'_{\pm,G}(y,t)\exp(i\omega t)\mathrm{d}t \\
&= \begin{pmatrix} 1 \\ \pm i\sqrt{1-\frac{\beta_\perp}{\alpha\Lambda^\pm}}\end{pmatrix}\varphi(y)\int_{-\infty}^{+\infty}\mathrm{d}t\left\{\exp(i\omega t)\exp\left[\pm i\left(\gamma M_0\alpha\Lambda^\pm\sqrt{1-\frac{\beta_\perp}{\alpha\Lambda^\pm}}\right)t\right]\right\} \\
&= \begin{pmatrix} 1 \\ \pm i\sqrt{1-\frac{\beta_\perp}{\alpha\Lambda^\pm}}\end{pmatrix}\varphi(y)\int_{-\infty}^{+\infty}\mathrm{d}t\left\{\exp\left[i\left(\omega \pm \gamma M_0\alpha\Lambda^\pm\sqrt{1-\frac{\beta_\perp}{\alpha\Lambda^\pm}}\right)t\right]\right\} \\
&= \begin{pmatrix} 1 \\ \pm i\sqrt{1-\frac{\beta_\perp}{\alpha\Lambda^\pm}}\end{pmatrix}\varphi(y).
\end{aligned} \tag{G.3.4}$$

Normally we would just write the Fourier transformed variable in its shorthand notation, not being concerned with the integral it contains. In the second step, however, we wrote it out in full since we are interested in the function $\phi(y)$ and the matrix. So, the integral is zero unless $\omega \pm \gamma M_0 \alpha \Lambda^{\pm} \sqrt{1 - \frac{\beta_\perp}{\alpha \Lambda^{\pm}}} = 0$, in which case the integral is equal to a delta function, centred at:

$$\omega = \gamma M_0 \alpha \Lambda^{\pm} \sqrt{1 - \frac{\beta_\perp}{\alpha \Lambda^{\pm}}}, \tag{G.3.5}$$

where we drop the negative solution, since we can only have positive frequencies. Of course, this corresponds to our earlier result (4.4.4). Testing this final form of $\tilde{\mathbf{m}}'_{\pm,G}$ in Eq. (G.3.3), we do indeed find it is a solution.

G.4 Variation of Parameters

We can solve the inhomogeneous equation for $\tilde{\mathbf{m}}'_{\beta}$ by using the method of variation of parameters ([101], pp. 99-102). For an inhomogeneous linear ordinary differential equation (ODE) of the form:

$$y''(x) + p(x)y'(x) + q(x)y(x) = r(x),$$

the general solution $y(x)$ is the sum of the general solution to the homogeneous equation, $y_G(x)$ and the particular solution to the inhomogeneous equation $y_p(x)$:

$$\begin{aligned} y(x) =& y_G(x) + y_p(x) = Ay_1(x) + By_2(x) + y_2(x) \int \left(\frac{y_1(x) r(x)}{W} \right) \mathrm{d}x + \\ & - y_1(x) \int \left(\frac{y_2(x) r(x)}{W} \right) \mathrm{d}x, \end{aligned} \tag{G.4.1}$$

where y_1 and y_2 are the two linearly independent solutions of the homogeneous equation $y''(x) + p(x)y'(x) + q(x)y(x) = 0$, and W is the Wronskian, given by:

$$W = y_1 y_2' - y_2 y_1'.$$

Our two linearly independent solutions to the homogeneous equation are slightly complicated. We will write out (G.3.4) in full here, for clarity:

$$\tilde{\mathbf{m}}'_{\pm,G} = \underbrace{\begin{pmatrix} 1 \\ \pm i\sqrt{1-\frac{\beta_\perp}{\alpha\Lambda^\pm}} \end{pmatrix}}_{\mathbf{a}^\pm} \phi(y), \tag{G.4.2}$$

where:

$$\phi(y) = C^\pm w_1^\pm + D^\pm w_2^\pm, \tag{G.4.3}$$

and

$$w_1^\pm = (\cosh[y/\lambda_B])^{ik^\pm\lambda_B} F\left[-ik^\pm\lambda_B - 1, -ik^\pm\lambda_B + 2, -ik^\pm\lambda_B + 1; \frac{1-\tanh[y/\lambda_B]}{2}\right],$$

$$w_2^\pm = G_{12}\,(\cosh[y/\lambda_B])^{ik^\pm\lambda_B}\left(\frac{1-\tanh[y/\lambda_B]}{2}\right)^{ik^\pm\lambda_B} F\left[-1, 2, ik^\pm\lambda_B + 1; \frac{1-\tanh[y/\lambda_B]}{2}\right]$$

$$- G_{22}\,(\cosh[y/\lambda_B])^{ik^\pm\lambda_B} F\left[-ik^\pm\lambda_B - 1, -ik^\pm\lambda_B + 2, -ik^\pm\lambda_B + 1; \frac{1-\tanh[y/\lambda_B]}{2}\right],$$

$$\text{with:}\quad k^\pm = \sqrt{-\Lambda^\pm - \frac{\beta_\parallel}{\alpha}}, \qquad \Lambda^\pm = \frac{\beta_\perp}{2\alpha} \pm \sqrt{\frac{\beta_\perp^2}{4\alpha^2} + \frac{\omega^2}{\alpha^2}},$$

$$G_{11} = \frac{\Gamma(-ik^\pm\lambda_B + 1)\Gamma(ik^\pm\lambda_B)}{\Gamma(-1)\Gamma(2)}, \quad G_{12} = \frac{\Gamma(-ik^\pm\lambda_B + 1)\Gamma(-ik^\pm\lambda_B)}{\Gamma(-ik^\pm\lambda_B - 1)\Gamma(-ik^\pm\lambda_B + 2)},$$

$$G_{21} = \frac{\Gamma(ik^\pm\lambda_B + 1)\Gamma(ik^\pm\lambda_B)}{\Gamma(ik^\pm\lambda_B - 1)\Gamma(ik^\pm\lambda_B + 2)}, \quad G_{22} = \frac{\Gamma(ik^\pm\lambda_B + 1)\Gamma(-ik^\pm\lambda_B)}{\Gamma(-1)\Gamma(2)}.$$

The problem with the variation of parameters equation (G.4.1) is that the functions $y_{1,2}$ and $r(x)$ are scalars. In our case, we can't just substitute the matrices in place of these functions because matrix multiplication is more complicated. So, we can either re-derive variation of parameters for matrices, or we could work out how to adapt variation of parameters for our particular situation. We will use the latter approach.

Firstly, we assume that the solution to the inhomogeneous equation (G.3.1) can be written as:

$$\begin{aligned}\tilde{\mathbf{m}}'_\beta =& \mathbf{a}^+[C^+w_1^+ + D^+w_2^+] + \mathbf{a}^-[C^-w_1^- + D^-w_2^-] + \\ &+ \underbrace{\frac{\mathbf{A}^+}{W^+}\left[w_1^+\int_{y_0}^{y} A(y')w_2^+\,\mathrm{d}y' - w_2^+\int_{y_0}^{y} A(y')w_1^+\,\mathrm{d}y'\right]}_{\tilde{\mathbf{m}}'^+_\beta} + \\ &+ \underbrace{\frac{\mathbf{B}^-}{W^-}\left[w_1^-\int_{y_0}^{y} B(y')w_2^-\,\mathrm{d}y' - w_2^-\int_{y_0}^{y} B(y')w_1^-\,\mathrm{d}y'\right]}_{\tilde{\mathbf{m}}'^-_\beta},\end{aligned} \tag{G.4.4}$$

where $W^\pm$ is the Wronskian for $w^\pm_{1,2}$. This form of the solution uses the basic idea of variation of parameters, but introduces some unknown matrices - which must be present since the left hand side is a matrix. To work out what $\boldsymbol{A}^+$,$\boldsymbol{B}^-$, and the scalars $A(y)$ and $B(y)$ are, we can substitute this solution (G.4.4) back into (G.3.1). We will try the process with $C^\pm = D^\pm = 0$ for now; indeed, since they are the solutions to the homogeneous equation, when substituted into the inhomogeneous equation they contribute zero to the solution (as they have been designed to!), so it is fine to leave them out for now. The inhomogeneous equation is then:

$$\mathbf{r}(y) = i\sigma_y\left[\partial_y^2 - \frac{\beta_\parallel}{\alpha} + \frac{2}{\lambda_B^2}\operatorname{sech}^2\left(\frac{y}{\lambda_B}\right)\right](\tilde{\mathbf{m}}'^+_\beta + \tilde{\mathbf{m}}'^-_\beta) + \begin{pmatrix} \frac{i\omega}{\alpha} & 0 \\ \frac{\beta_\perp}{\alpha} & \frac{i\omega}{\alpha}\end{pmatrix}(\tilde{\mathbf{m}}'^+_\beta + \tilde{\mathbf{m}}'^-_\beta). \tag{G.4.5}$$

Now, when we apply the square bracket to $\tilde{\mathbf{m}}'^\pm_\beta$ in (G.4.5), we need to remember that the differential will act on the function $w^\pm_{1,2}$ outside of the integral, and also on the integral. Let us first find:

$$
\begin{aligned}
\hat{L}\tilde{\mathbf{m}}'^{+}_{\beta} =& \overbrace{\left[\partial_y^2 - \frac{\beta_{\|}}{\alpha} + \frac{2}{\lambda_B^2}\operatorname{sech}^2\left(\frac{y}{\lambda_B}\right)\right]}^{\hat{L}} \frac{\mathbf{A}^+}{W^+}\left[w_1^+\int_{y_0}^{y} A(y')w_2^+\,\mathrm{d}y' - w_2^+\int_{y_0}^{y} A(y')w_1^+\,\mathrm{d}y'\right] \\
=& \frac{\mathbf{A}^+}{W^+}\partial_y^2\left[w_1^+\int_{y_0}^{y} A(y')w_2^+\,\mathrm{d}y' - w_2^+\int_{y_0}^{y} A(y')w_1^+\,\mathrm{d}y'\right] + \left[-\frac{\beta_{\|}}{\alpha} + \frac{2}{\lambda_B^2}\operatorname{sech}^2\left(\frac{y}{\lambda_B}\right)\right]\tilde{\mathbf{m}}'^{+}_{\beta} \\
=& \frac{\mathbf{A}^+}{W^+}\partial_y\Bigg[\left(\partial_y w_1^+\right)\int_{y_0}^{y} A(y')w_2^+\,\mathrm{d}y' + w_1^+\partial_y\int_{y_0}^{y} A(y')w_2^+\,\mathrm{d}y' - \left(\partial_y w_2^+\right)\int_{y_0}^{y} A(y')w_1^+\,\mathrm{d}y' + \\
& - w_2^+\partial_y\int_{y_0}^{y} A(y')w_1^+\,\mathrm{d}y'\Bigg] + \left[-\frac{\beta_{\|}}{\alpha} + \frac{2}{\lambda_B^2}\operatorname{sech}^2\left(\frac{y}{\lambda_B}\right)\right]\tilde{\mathbf{m}}'^{+}_{\beta} \\
=& \frac{\mathbf{A}^+}{W^+}\partial_y\Bigg[\left(\partial_y w_1^+\right)\int_{y_0}^{y} A(y')w_2^+\,\mathrm{d}y' + \cancel{w_1^+ A(y) w_2^+} + \\
& - \left(\partial_y w_2^+\right)\int_{y_0}^{y} A(y')w_1^+\,\mathrm{d}y' - \cancel{w_2^+ A(y) w_1^+}\Bigg] + \left[-\frac{\beta_{\|}}{\alpha} + \frac{2}{\lambda_B^2}\operatorname{sech}^2\left(\frac{y}{\lambda_B}\right)\right]\tilde{\mathbf{m}}'^{+}_{\beta} \\
=& \frac{\mathbf{A}^+}{W^+}\Bigg[\left(\partial_y^2 w_1^+\right)\int_{y_0}^{y} A(y')w_2^+\,\mathrm{d}y' + \left(\partial_y w_1^+\right)A(y)w_2^+ + \\
& - \left(\partial_y^2 w_2^+\right)\int_{y_0}^{y} A(y')w_1^+\,\mathrm{d}y' - \left(\partial_y w_2^+\right)A(y)w_1^+\Bigg] + \left[-\frac{\beta_{\|}}{\alpha} + \frac{2}{\lambda_B^2}\operatorname{sech}^2\left(\frac{y}{\lambda_B}\right)\right]\tilde{\mathbf{m}}'^{+}_{\beta} \\
=& \mathbf{A}^+A(y) + \frac{\mathbf{A}^+}{W^+}\left[\left(\partial_y^2 w_1^+\right)\int_{y_0}^{y} A(y')w_2^+\,\mathrm{d}y' - \left(\partial_y^2 w_2^+\right)\int_{y_0}^{y} A(y')w_1^+\,\mathrm{d}y'\right] \\
& + \left[-\frac{\beta_{\|}}{\alpha} + \frac{2}{\lambda_B^2}\operatorname{sech}^2\left(\frac{y}{\lambda_B}\right)\right]\tilde{\mathbf{m}}'^{+}_{\beta} \\
=& \mathbf{A}^+A(y) + \left(\int_{y_0}^{y} A(y')w_2^+\,\mathrm{d}y'\right)\left[\partial_y^2 - \frac{\beta_{\|}}{\alpha} + \frac{2}{\lambda_B^2}\operatorname{sech}^2\left(\frac{y}{\lambda_B}\right)\right]w_1^+ \\
& - \left(\int_{y_0}^{y} A(y')w_1^+\,\mathrm{d}y'\right)\left[\partial_y^2 - \frac{\beta_{\|}}{\alpha} + \frac{2}{\lambda_B^2}\operatorname{sech}^2\left(\frac{y}{\lambda_B}\right)\right]w_2^+ \\
=& \mathbf{A}^+A(y) + \frac{\mathbf{A}^+}{W^+}\Lambda^+\tilde{\mathbf{m}}'^{+}_{\beta}.
\end{aligned}
$$

In the third-to-last step, we have recognised that $w_2^+\partial_y w_1^+ - w_1^+\partial_y w_2^+ = W^+$ and so separated out the $\mathbf{A}^+A(y)$ term. In the last step we used the result:

$$
\left[\partial_y^2 - \frac{\beta_{\|}}{\alpha} + \frac{2}{\lambda_B^2}\operatorname{sech}^2\left(\frac{y}{\lambda_B}\right)\right]w_{1,2}^+ = \Lambda^+ w_{1,2}^+. \tag{G.4.6}
$$

We can carry out the same process for the $\mathbf{B}^- \cdots$ term, to find that we can write (G.4.5) as:

$$\mathbf{r}(y) = i\sigma_y \mathbf{A}^+ A(y) + i\sigma_y \mathbf{B}^- B(y) + i\sigma_y \Lambda^+ \tilde{\mathbf{m}}_\beta'^+ + i\sigma_y \Lambda^- \tilde{\mathbf{m}}_\beta'^- + \begin{pmatrix} \frac{i\omega}{\alpha} & 0 \\ \frac{\beta_\perp}{\alpha} & \frac{i\omega}{\alpha} \end{pmatrix} (\tilde{\mathbf{m}}_\beta'^+ + \tilde{\mathbf{m}}_\beta'^-). \tag{G.4.7}$$

Since we know $\mathbf{r}(y)$ does not contain $\tilde{\mathbf{m}}_\beta'^\pm$, this leads to two conditions:

$$\underline{\text{Condition 1:}} \quad i\sigma_y \Lambda^+ \tilde{\mathbf{m}}_\beta'^+ + i\sigma_y \Lambda^- \tilde{\mathbf{m}}_\beta'^- + \begin{pmatrix} \frac{i\omega}{\alpha} & 0 \\ \frac{\beta_\perp}{\alpha} & \frac{i\omega}{\alpha} \end{pmatrix} (\tilde{\mathbf{m}}_\beta'^+ + \tilde{\mathbf{m}}_\beta'^-) = 0, \tag{G.4.8}$$

$$\underline{\text{Condition 2:}} \quad \mathbf{r}(y) = i\sigma_y \mathbf{A}^+ A(y) + i\sigma_y \mathbf{B}^- B(y). \tag{G.4.9}$$

Let us require that, from (G.4.8):

$$\begin{pmatrix} \frac{i\omega}{\alpha} & 0 \\ \frac{\beta_\perp}{\alpha} & \frac{i\omega}{\alpha} \end{pmatrix} \tilde{\mathbf{m}}_\beta'^+ = -i\sigma_y \Lambda^+ \tilde{\mathbf{m}}_\beta'^+ \implies \begin{pmatrix} \frac{\beta_\perp}{\alpha} & \frac{i\omega}{\alpha} \\ -\frac{i\omega}{\alpha} & 0 \end{pmatrix} \tilde{\mathbf{m}}_\beta'^+ = \Lambda^+ \tilde{\mathbf{m}}_\beta'^+, \tag{G.4.10a}$$

$$\begin{pmatrix} \frac{i\omega}{\alpha} & 0 \\ \frac{\beta_\perp}{\alpha} & \frac{i\omega}{\alpha} \end{pmatrix} \tilde{\mathbf{m}}_\beta'^- = -i\sigma_y \Lambda^- \tilde{\mathbf{m}}_\beta'^- \implies \begin{pmatrix} \frac{\beta_\perp}{\alpha} & \frac{i\omega}{\alpha} \\ -\frac{i\omega}{\alpha} & 0 \end{pmatrix} \tilde{\mathbf{m}}_\beta'^- = \Lambda^- \tilde{\mathbf{m}}_\beta'^-, \tag{G.4.10b}$$

where we have multiplied both sides by $i\sigma_y$ to obtain the eigenvalue equations. We already know the eigenvalues, but let us check that they give the same result:

$$\begin{vmatrix} \frac{\beta_\perp}{\alpha} - \Lambda^\pm & \frac{i\omega}{\alpha} \\ -\frac{i\omega}{\alpha} & -\Lambda^\pm \end{vmatrix} = 0 \implies \begin{cases} \Lambda^+ = \frac{\beta_\perp}{2\alpha} + \sqrt{\frac{\beta_\perp^2}{4\alpha^2} + \frac{\omega^2}{\alpha^2}} \\ \\ \Lambda^- = \frac{\beta_\perp}{2\alpha} - \sqrt{\frac{\beta_\perp^2}{4\alpha^2} + \frac{\omega^2}{\alpha^2}} \end{cases}. \tag{G.4.11}$$

this is the same definition as we had before in (4.4.4), so we can now find the eigenvectors. Looking at how $\tilde{\mathbf{m}}_\beta'^+$ was defined in (G.4.4), we see that we can cancel everything except $\mathbf{A}^+$ on both sides of the eigenvalue equation. $\mathbf{A}^+$ is therefore the eigenvector in (G.4.10a), and similarly $\mathbf{B}^-$ is the eigenvector in (G.4.10b).

So, from (G.4.10a):

$$\begin{pmatrix} \frac{\beta_\perp}{\alpha} - \Lambda^+ & \frac{i\omega}{\alpha} \\ -\frac{i\omega}{\alpha} & -\Lambda^+ \end{pmatrix} \begin{pmatrix} A_1^+ \\ A_2^+ \end{pmatrix} = 0 \quad \Longrightarrow \quad \begin{cases} \left(\frac{\beta_\perp}{\alpha} - \Lambda^+\right) A_1^+ + \frac{i\omega}{\alpha} A_2^+ & = 0 \\ -\frac{i\omega}{\alpha} A_1^+ - \Lambda^+ A_2^+ & = 0 \end{cases}$$

$$\therefore \text{ from the first equation: } \quad \mathbf{A}^+ = \begin{pmatrix} 1 \\ -\frac{\alpha}{i\omega}\left(\frac{\beta_\perp}{\alpha} - \Lambda^+\right) \end{pmatrix}$$

$$= \begin{pmatrix} 1 \\ \frac{1}{i\omega}\left(-\frac{\beta_\perp}{2} + \sqrt{\frac{\beta_\perp^2}{4} + \omega^2}\right) \end{pmatrix}. \tag{G.4.12}$$

Similarly for $\mathbf{B}^-$, we can carry out the same process as above to find:

$$\mathbf{B}^- = \begin{pmatrix} 1 \\ \frac{1}{i\omega}\left(-\frac{\beta_\perp}{2} - \sqrt{\frac{\beta_\perp^2}{4} + \omega^2}\right) \end{pmatrix}. \tag{G.4.13}$$

How do these compare with the vectors $\mathbf{a}^\pm$ from (G.4.2)? We will write out $\mathbf{a}^+$ in full:

$$\mathbf{a}^+ = \begin{pmatrix} 1 \\ +i\sqrt{1 - \frac{\beta_\perp}{\alpha\Lambda^+}} \end{pmatrix} = \begin{pmatrix} 1 \\ -\frac{i\omega}{\alpha\Lambda^+} \end{pmatrix}.$$

We just need to find $1/\Lambda^+$:

$$\frac{1}{\Lambda^+} = \frac{1}{\left(\frac{\beta_\perp}{2\alpha} + \sqrt{\frac{\beta_\perp^2}{4\alpha^2} + \frac{\omega^2}{\alpha^2}}\right)} \frac{\frac{\beta_\perp}{2\alpha} - \sqrt{\frac{\beta_\perp^2}{4\alpha^2} + \frac{\omega^2}{\alpha^2}}}{\frac{\beta_\perp}{2\alpha} - \sqrt{\frac{\beta_\perp^2}{4\alpha^2} + \frac{\omega^2}{\alpha^2}}} = -\frac{\alpha^2}{\omega^2}\left(\frac{\beta_\perp}{2\alpha} - \sqrt{\frac{\beta_\perp^2}{4\alpha^2} + \frac{\omega^2}{\alpha^2}}\right). \tag{G.4.14}$$

Substituting into our expression for $\mathbf{a}^+$:

$$\mathbf{a}^+ = \begin{pmatrix} 1 \\ -\frac{i\omega}{\alpha}\left(-\frac{\alpha^2}{\omega^2}\right)\left(\frac{\beta_\perp}{2\alpha} - \sqrt{\frac{\beta_\perp^2}{4\alpha^2} + \frac{\omega^2}{\alpha^2}}\right) \end{pmatrix} = \begin{pmatrix} 1 \\ \frac{1}{i\omega}\left(-\frac{\beta_\perp}{2} + \sqrt{\frac{\beta_\perp^2}{4} + \omega^2}\right) \end{pmatrix},$$

where we have used the fact that $1/i = -i$. We compare this result to (G.4.12) and deduce that $\mathbf{a}^+ = \mathbf{A}^+$ and similarly $\mathbf{a}^- = \mathbf{B}^-$. We will adopt the original notation when we substitute everything back into (G.4.4), but for now we will continue with this current notation.

All that is left now is to solve (G.4.9). We will write it out in full:

$$\begin{aligned}
\mathbf{r}(y) &= i\sigma_y \mathbf{A}^+ A(y) + i\sigma_y \mathbf{B}^- B(y) \\
\begin{pmatrix} r_1(y) \\ r_2(y) \end{pmatrix} &= \begin{pmatrix} A_1^+ \\ A_2^+ \end{pmatrix} A(y) + \begin{pmatrix} B_1^- \\ B_2^- \end{pmatrix} B(y) \\
&\implies \begin{pmatrix} A_1^+ & B_1^- \\ A_2^+ & B_2^- \end{pmatrix} \begin{pmatrix} A(y) \\ B(y) \end{pmatrix} = \begin{pmatrix} r_1(y) \\ r_2(y) \end{pmatrix} \\
\implies \begin{pmatrix} A(y) \\ B(y) \end{pmatrix} &= \frac{1}{A_1^+ B_2^- - B_1^- A_2^+} \begin{pmatrix} B_2^- & -B_1^- \\ -A_2^+ & A_1^+ \end{pmatrix} \begin{pmatrix} r_1(y) \\ r_2(y) \end{pmatrix} \\
&= \frac{1}{A_1^+ B_2^- - B_1^- A_2^+} \begin{pmatrix} B_2^- r_1(y) - B_1^- r_2(y) \\ -A_2^+ r_1(y) + A_1^+ r_2(y) \end{pmatrix}.
\end{aligned} \tag{G.4.15}$$

Notice that we have cancelled the $i\sigma_y$ from both sides, so $r_1(y)$ and $r_2(y)$ do not include this factor. We will first calculate:

$$\begin{aligned}
\frac{1}{A_1^+ B_2^- - B_1^- A_2^+} &= \frac{1}{\frac{\alpha}{i\omega}\left(-\frac{\beta_\perp}{2\alpha} - \sqrt{\frac{\beta_\perp^2}{4\alpha^2} + \frac{\omega^2}{\alpha^2}}\right) - \frac{\alpha}{i\omega}\left(-\frac{\beta_\perp}{2\alpha} + \sqrt{\frac{\beta_\perp^2}{4\alpha^2} + \frac{\omega^2}{\alpha^2}}\right)} \\
&= \frac{1}{-\frac{2}{i\omega}\sqrt{\frac{\beta_\perp^2}{4} + \omega^2}},
\end{aligned}$$

and next we will find the components of the matrix:

$$\begin{aligned}
B_2^- r_1(y) - B_1^- r_2(y) = \frac{1}{\cancel{i\omega}}&\left(-\frac{\beta_\perp}{2} - \sqrt{\frac{\beta_\perp^2}{4} + \omega^2}\right)\left(\cancel{2}\frac{2}{\lambda_B^2}\operatorname{sech}^2\left(\frac{y}{\lambda_B}\right)\frac{\cancel{i\omega}\tilde{h}(\omega)}{-\omega^2 + \beta_\parallel(\beta_\parallel + \beta_\perp)}\right) + \\
&- \left(-\frac{2}{\lambda_B^2}\operatorname{sech}^2\left(\frac{y}{\lambda_B}\right)\frac{(\beta_\parallel + \beta_\perp)\tilde{h}(\omega)}{-\omega^2 + \beta_\parallel(\beta_\parallel + \beta_\perp)}\right) \\
&= \left\{-\frac{\beta_\perp}{2} - \sqrt{\frac{\beta_\perp^2}{4} + \omega^2} + \beta_\parallel + \beta_\perp\right\}\left(\frac{2}{\lambda_B^2}\operatorname{sech}^2\left(\frac{y}{\lambda_B}\right)\frac{\tilde{h}(\omega)}{-\omega^2 + \beta_\parallel(\beta_\parallel + \beta_\perp)}\right).
\end{aligned}$$

The other matrix component is:

$$\begin{aligned}
-A_2^+ r_1(y) + A_1^+ r_2(y) = -\frac{1}{\cancel{i\omega}}&\left(-\frac{\beta_\perp}{2} + \sqrt{\frac{\beta_\perp^2}{4} + \omega^2}\right)\left(\cancel{2}\frac{2}{\lambda_B^2}\operatorname{sech}^2\left(\frac{y}{\lambda_B}\right)\frac{\cancel{i\omega}\tilde{h}(\omega)}{-\omega^2 + \beta_\parallel(\beta_\parallel + \beta_\perp)}\right) + \\
&+ \left(-\frac{2}{\lambda_B^2}\operatorname{sech}^2\left(\frac{y}{\lambda_B}\right)\frac{(\beta_\parallel + \beta_\perp)\tilde{h}(\omega)}{-\omega^2 + \beta_\parallel(\beta_\parallel + \beta_\perp)}\right) \\
&= \left\{\frac{\beta_\perp}{2} - \sqrt{\frac{\beta_\perp^2}{4} + \omega^2} - \beta_\parallel - \beta_\perp\right\}\left(\frac{2}{\lambda_B^2}\operatorname{sech}^2\left(\frac{y}{\lambda_B}\right)\frac{\tilde{h}(\omega)}{-\omega^2 + \beta_\parallel(\beta_\parallel + \beta_\perp)}\right).
\end{aligned}$$

We can substitute these results back into (G.4.15) to find:

$$A(y) = \frac{2}{\lambda_B^2}\operatorname{sech}^2\left(\frac{y}{\lambda_B}\right)\underbrace{\left(\frac{1}{-\frac{2}{i\omega}\sqrt{\frac{\beta_\perp^2}{4}+\omega^2}}\frac{\tilde{h}(\omega)}{-\omega^2+\beta_\parallel(\beta_\parallel+\beta_\perp)}\right)}_{N}\underbrace{\left\{\frac{\beta_\perp}{2}+\beta_\parallel-\sqrt{\frac{\beta_\perp^2}{4}+\omega^2}\right\}}_{A}, \tag{G.4.16}$$

$$B(y) = \frac{2}{\lambda_B^2}\operatorname{sech}^2\left(\frac{y}{\lambda_B}\right)\underbrace{\left(\frac{1}{-\frac{2}{i\omega}\sqrt{\frac{\beta_\perp^2}{4}+\omega^2}}\frac{\tilde{h}(\omega)}{-\omega^2+\beta_\parallel(\beta_\parallel+\beta_\perp)}\right)}_{N}\underbrace{\left\{-\frac{\beta_\perp}{2}-\beta_\parallel-\sqrt{\frac{\beta_\perp^2}{4}+\omega^2}\right\}}_{B}. \tag{G.4.17}$$

Let us substitute these all back into (G.4.4), using the fact that $\mathbf{a}^+ = \mathbf{A}^+$, $\mathbf{a}^- = \mathbf{B}^-$ as discussed previously:

$$\begin{aligned}\tilde{\mathbf{m}}'_\beta = \quad & \mathbf{a}^+\Bigg\{C^+w_1^+ + D^+w_2^+ + \\ & + \frac{NA}{W^+}\left[w_1^+\int_{y_0}^{y}\frac{2}{\lambda_B^2}\operatorname{sech}^2\left(\frac{y'}{\lambda_B}\right)w_2^+\,\mathrm{d}y' - w_2^+\int_{y_0}^{y}\frac{2}{\lambda_B^2}\operatorname{sech}^2\left(\frac{y'}{\lambda_B}\right)w_1^+\,\mathrm{d}y'\right]\Bigg\} \\ & + \mathbf{a}^-\Bigg\{C^-w_1^- + D^-w_2^- + \\ & + \frac{NB}{W^-}\left[w_1^-\int_{y_0}^{y}\frac{2}{\lambda_B^2}\operatorname{sech}^2\left(\frac{y'}{\lambda_B}\right)w_2^-\,\mathrm{d}y' - w_2^-\int_{y_0}^{y}\frac{2}{\lambda_B^2}\operatorname{sech}^2\left(\frac{y'}{\lambda_B}\right)w_1^-\,\mathrm{d}y'\right]\Bigg\}.\end{aligned} \tag{G.4.18}$$

This result is repeated in the main text as Eq. (4.4.17).

Appendix H

Finding the Constants $C^{\pm}$ and $D^{\pm}$

Here we establish the constants $C^{\pm}$ and $D^{\pm}$ by using the asymptotic form of the magnetisation, away from the domain wall. Remember that $\tilde{\mathbf{m}}'_{\beta}$ was defined in equation (4.4.17) from Section 4.4.3 as:

$$\begin{aligned}\tilde{\mathbf{m}}'_{\beta} = \quad & \mathbf{a}^{+}\Bigg\{C^{+}w_1^{+} + D^{+}w_2^{+} + \\ & + \frac{NA}{W^{+}}\left[w_1^{+}\int_{y_0}^{y}\frac{2}{\lambda_B^2}\operatorname{sech}^2\left(\frac{y'}{\lambda_B}\right)w_2^{+}\,\mathrm{d}y' - w_2^{+}\int_{y_0}^{y}\frac{2}{\lambda_B^2}\operatorname{sech}^2\left(\frac{y'}{\lambda_B}\right)w_1^{+}\,\mathrm{d}y'\right]\Bigg\} \\ & + \mathbf{a}^{-}\Bigg\{C^{-}w_1^{-} + D^{-}w_2^{-} + \\ & + \frac{NB}{W^{-}}\left[w_1^{-}\int_{y_0}^{y}\frac{2}{\lambda_B^2}\operatorname{sech}^2\left(\frac{y'}{\lambda_B}\right)w_2^{-}\mathrm{d}y' - w_2^{-}\int_{y_0}^{y}\frac{2}{\lambda_B^2}\operatorname{sech}^2\left(\frac{y'}{\lambda_B}\right)w_1^{-}\mathrm{d}y'\right]\Bigg\}.\end{aligned}$$

For both limits, the magnetisation should tend to plane waves moving outwards from the domain wall. We can use the assumed form of $\tilde{\mathbf{m}}'_{\beta}$ given in Eq. (4.4.23), and establish the amplitudes $\mathbf{S}_{\pm}(\omega)$ by using the asymptotic forms of $w_{1,2}^{\pm}$ (Eqs. (4.4.24a) to (4.4.24d)) in (4.4.17). We first look at the limit of $y \to -\infty$:

$$\lim_{y\to-\infty}\tilde{\mathbf{m}}'_{\beta} \approx \mathbf{S}_{+}(\omega')e^{-ik^{+}y} + \mathbf{S}_{-}(\omega')e^{-ik^{-}y} \tag{H.0.1}$$

$$\begin{aligned}
&= \mathbf{a}^{+}\Bigg\{C^{+}\left(\frac{G_{11}}{2^{ik^{+}\lambda_B}}e^{-ik^{+}y} + \frac{G_{12}}{2^{ik^{+}\lambda_B}}e^{+ik^{+}y}\right) + D^{+}\frac{e^{-ik^{+}y}}{2^{ik^{+}\lambda_B}} \\
&+ \frac{NA}{\frac{ik^{+}G_{12}}{2^{ik^{+}\lambda_B}}}\left[\left(\frac{G_{11}}{2^{ik^{+}\lambda_B}}e^{-ik^{+}y} + \frac{G_{12}}{2^{ik^{+}\lambda_B}}e^{+ik^{+}y}\right)I^{+}_{2,-} - \frac{e^{-ik^{+}y}}{2^{ik^{+}\lambda_B}}I^{+}_{1,-}\right]\Bigg\} \\
&+ \mathbf{a}^{-}\Bigg\{C^{-}\left(\frac{G_{11}}{2^{ik^{-}\lambda_B}}e^{-ik^{-}y} + \frac{G_{12}}{2^{ik^{-}\lambda_B}}e^{+ik^{-}y}\right) + D^{-}\frac{e^{-ik^{-}y}}{2^{ik^{-}\lambda_B}} \\
&+ \frac{NB}{\frac{ik^{-}G_{12}}{2^{ik^{-}\lambda_B}}}\left[\left(\frac{G_{11}}{2^{ik^{-}\lambda_B}}e^{-ik^{-}y} + \frac{G_{12}}{2^{ik^{-}\lambda_B}}e^{+ik^{-}y}\right)I^{-}_{2,-} - \frac{e^{-ik^{-}y}}{2^{ik^{-}\lambda_B}}I^{-}_{1,-}\right]\Bigg\},
\end{aligned} \tag{H.0.2}$$

where we call:

$$\int_{0}^{-\infty}\frac{2}{\lambda_B^2}\mathrm{sech}^2\left(\frac{y'}{\lambda_B}\right)w_l^{\pm}\,\mathrm{d}y' = I^{\pm}_{l,-}\,, \qquad \text{with:} \quad l = 1,2, \tag{H.0.3}$$

and for the other limit:

$$\int_{0}^{+\infty}\frac{2}{\lambda_B^2}\mathrm{sech}^2\left(\frac{y'}{\lambda_B}\right)w_l^{\pm}\,\mathrm{d}y' = I^{\pm}_{l,+}\,, \qquad \text{with:} \quad l = 1,2, \tag{H.0.4}$$

so that the subscript "$l,+$" or "$l,-$" denotes the upper limit of the integral of $+\infty$ or $-\infty$, respectively. Notice that the limits of the integral in our original equation (4.4.17) are from an arbitrary point, y_0, to the value of y of interest[1]. We will always choose our arbitrary point as $y_0 = 0$, and y in these asymptotic expansions will be $\pm\infty$.

We can separate out (H.0.2) into two equations; one each for k^{-} and k^{+}. Since they are exactly the same except for the subscripts in $k^{\pm}$, $\mathbf{a}^{\pm}$ and in the integrals, and for the factors A and B, we will just look at the k^{+} case, then we should be able to write down the solution for the k^{-} case. Extracting the equation for k^{+}

[1]When, after finding the constants $C^{\pm}$ and $D^{\pm}$, we plot out the full solution $\tilde{\mathbf{m}}'_{\beta}$ vs. y, we will need to (numerically) solve these integrals, from $y_0 = 0$ up to the point at which the solution is produced.

then, we get:

$$\begin{aligned}
\mathbf{S}_+(\omega')e^{-ik^+y} &= \mathbf{a}^+\Bigg\{e^{-ik^+y}\left[\frac{G_{11}}{2^{ik^+\lambda_B}}\left(C^+ + I^-_{2,+}\frac{NA}{\frac{ik^+G_{12}}{2^{ik^+\lambda_B}}}\right) + \frac{D^+}{2^{ik^+\lambda_B}} - \frac{NA}{\frac{ik^+G_{12}}{2^{ik^+\lambda_B}}}\frac{I^-_{1,+}}{2^{ik^+\lambda_B}}\right] \\
&\quad + e^{+ik^+y}\frac{G_{12}}{2^{ik^+\lambda_B}}\left(C^+ + I^-_{2,+}\frac{NA}{\frac{ik^+G_{12}}{2^{ik^+\lambda_B}}}\right)\Bigg\} \\
\implies \mathbf{S}_+(\omega') &= \mathbf{a}^+\left[\frac{G_{11}}{2^{ik^+\lambda_B}}\left(C^+ + I^-_{2,+}\frac{NA}{\frac{ik^+G_{12}}{2^{ik^+\lambda_B}}}\right) + \frac{D^+}{2^{ik^+\lambda_B}} - \frac{NA}{\frac{ik^+G_{12}}{2^{ik^+\lambda_B}}}\frac{I^-_{1,+}}{2^{ik^+\lambda_B}}\right], \qquad \text{(H.0.5a)} \\
\&\quad 0 &= \mathbf{a}^+\frac{G_{12}}{2^{ik^+\lambda_B}}\left(C^+ + I^-_{2,+}\frac{NA}{\frac{ik^+G_{12}}{2^{ik^+\lambda_B}}}\right) \implies C^+ = -I^-_{2,+}\frac{NA}{\frac{ik^+G_{12}}{2^{ik^+\lambda_B}}}. \qquad \text{(H.0.5b)}
\end{aligned}$$

We can do the same for the limit of $y \to +\infty$:

$$\begin{aligned}
\lim_{y\to+\infty}\tilde{\mathbf{m}}'_\beta &\approx \mathbf{S}_+(\omega')e^{+ik^+y} + \mathbf{S}_-(\omega')e^{+ik^-y} \\
&= \mathbf{a}^+\Bigg\{C^+\frac{e^{+ik^+y}}{2^{ik^+\lambda_B}} + D^+\left(\frac{G_{12}}{2^{ik^+\lambda_B}}e^{-ik^+y} - \frac{G_{22}}{2^{ik^+\lambda_B}}e^{+ik^+y}\right) \\
&\quad + \frac{NA}{\frac{ik^+G_{12}}{2^{ik^+\lambda_B}}}\left[\frac{e^{+ik^+y}}{2^{ik^+\lambda_B}}I^+_{2,+} - I^+_{1,+}\left(\frac{G_{12}}{2^{ik^+\lambda_B}}e^{-ik^+y} - \frac{G_{22}}{2^{ik^+\lambda_B}}e^{+ik^+y}\right)\right]\Bigg\} \\
&\quad + \mathbf{a}^-\Bigg\{C^-\frac{e^{+ik^-y}}{2^{ik^-\lambda_B}} + D^-\left(\frac{G_{12}}{2^{ik^-\lambda_B}}e^{-ik^-y} - \frac{G_{22}}{2^{ik^-\lambda_B}}e^{+ik^-y}\right) \\
&\quad + \frac{NB}{\frac{ik^-G_{12}}{2^{ik^-\lambda_B}}}\left[\frac{e^{+ik^-y}}{2^{ik^-\lambda_B}}I^+_{2,-} - I^+_{1,-}\left(\frac{G_{12}}{2^{ik^-\lambda_B}}e^{-ik^-y} - \frac{G_{22}}{2^{ik^-\lambda_B}}e^{+ik^-y}\right)\right]\Bigg\},
\end{aligned}$$

which means that (again just looking at the k^+ case):

$$\begin{aligned}
\mathbf{S}_+(\omega')e^{+ik^+y} &= \mathbf{a}^+\Bigg\{e^{+ik^+y}\left[\frac{C^+}{2^{ik^+\lambda_B}} + \frac{NA}{\frac{ik^+G_{12}}{2^{ik^+\lambda_B}}}\frac{I^+_{2,+}}{2^{ik^+\lambda_B}} + \frac{G_{22}}{2^{ik^+\lambda_B}}\left(I^+_{1,+}\frac{NA}{\frac{ik^+G_{12}}{2^{ik^+\lambda_B}}} - D^+\right)\right] \\
&\quad + e^{-ik^-y}\frac{G_{12}}{2^{ik^+\lambda_B}}\left(D^+ - I^+_{1,+}\frac{NA}{\frac{ik^+G_{12}}{2^{ik^+\lambda_B}}}\right)\Bigg\} \\
\implies \mathbf{S}_+(\omega') &= \mathbf{a}^+\left[\frac{C^+}{2^{ik^+\lambda_B}} + \frac{NA}{\frac{ik^+G_{12}}{2^{ik^+\lambda_B}}}\frac{I^+_{2,+}}{2^{ik^+\lambda_B}} + \frac{G_{22}}{2^{ik^+\lambda_B}}\left(I^+_{1,+}\frac{NA}{\frac{ik^+G_{12}}{2^{ik^+\lambda_B}}} - D^+\right)\right] \qquad \text{(H.0.6a)} \\
\&\quad 0 &= \mathbf{a}^+\frac{G_{12}}{2^{ik^+\lambda_B}}\left(D^+ - I^+_{1,+}\frac{NA}{\frac{ik^+G_{12}}{2^{ik^+\lambda_B}}}\right) \implies D^+ = I^+_{1,+}\frac{NA}{\frac{ik^+G_{12}}{2^{ik^+\lambda_B}}}. \qquad \text{(H.0.6b)}
\end{aligned}$$

We can now substitute (H.0.5b) and (H.0.6b) into either (H.0.5a) or (H.0.6a) to find an expression for $\mathbf{S}(\omega')$ - we will first try (H.0.5a):

$$\begin{aligned}
\mathbf{S}_+(\omega') &= \mathbf{a}^+ \left[\frac{G_{11}}{2^{ik^+\lambda_B}} \left(-I^-_{2,+} \frac{NA}{\frac{ik^+G_{12}}{2^{ik^+\lambda_B}}} + I^-_{2,+} \frac{NA}{\frac{ik^+G_{12}}{2^{ik^+\lambda_B}}} \right) + \frac{1}{2^{ik^+\lambda_B}} I^+_{1,+} \frac{NA}{\frac{ik^+G_{12}}{2^{ik^+\lambda_B}}} - \frac{NA}{\frac{ik^+G_{12}}{2^{ik^+\lambda_B}}} \frac{I^-_{1,+}}{2^{ik^+\lambda_B}} \right] \\
&= \mathbf{a}^+ \frac{NA}{ik^+G_{12}} \left[I^+_{1,+} - I^-_{1,+} \right] \\
&= \mathbf{a}^+ \frac{NA}{ik^+G_{12}} \left[\int_0^{+\infty} \frac{2}{\lambda_B^2} \operatorname{sech}^2\left(\frac{y'}{\lambda_B}\right) w_1^+ \, \mathrm{d}y' - \int_0^{-\infty} \frac{2}{\lambda_B^2} \operatorname{sech}^2\left(\frac{y'}{\lambda_B}\right) w_1^+ \, \mathrm{d}y' \right] \\
\implies \mathbf{S}_+(\omega') &= \mathbf{a}^+ \frac{NA}{ik^+G_{12}} \int_{-\infty}^{+\infty} \frac{2}{\lambda_B^2} \operatorname{sech}^2\left(\frac{y'}{\lambda_B}\right) w_1^+ \, \mathrm{d}y', \qquad \text{(H.0.7)}
\end{aligned}$$

and trying (H.0.6a):

$$\begin{aligned}
\mathbf{S}_+(\omega') &= \mathbf{a}^+ \left[-\frac{I^-_{2,+}}{2^{ik^+\lambda_B}} \frac{NA}{\frac{ik^+G_{12}}{2^{ik^+\lambda_B}}} + \frac{NA}{\frac{ik^+G_{12}}{2^{ik^+\lambda_B}}} \frac{I^+_{2,+}}{2^{ik^+\lambda_B}} + \frac{G_{22}}{2^{ik^+\lambda_B}} \left(I^+_{1,+} \frac{NA}{\frac{ik^+G_{12}}{2^{ik^+\lambda_B}}} - I^+_{1,+} \frac{NA}{\frac{ik^+G_{12}}{2^{ik^+\lambda_B}}} \right) \right] \\
&= \mathbf{a}^+ \frac{NA}{ik^+G_{12}} \left[I^+_{2,+} - I^-_{2,+} \right] \\
\implies \mathbf{S}_+(\omega') &= \mathbf{a}^+ \frac{NA}{ik^+G_{12}} \int_{-\infty}^{+\infty} \frac{2}{\lambda_B^2} \operatorname{sech}^2\left(\frac{y'}{\lambda_B}\right) w_2^+ \, \mathrm{d}y'. \qquad \text{(H.0.8)}
\end{aligned}$$

We can use the results above to write down the k^- solutions:

$$C^- = -I^-_{2,-} \frac{NB}{\frac{ik^-G_{12}}{2^{ik^-\lambda_B}}}, \qquad \text{(H.0.9)}$$

$$D^- = I^+_{1,-} \frac{NB}{\frac{ik^-G_{12}}{2^{ik^-\lambda_B}}}, \qquad \text{(H.0.10)}$$

$$\mathbf{S}_-(\omega') = \mathbf{a}^- \frac{NB}{ik^-G_{12}} \int_{-\infty}^{+\infty} \frac{2}{\lambda_B^2} \operatorname{sech}^2\left(\frac{y'}{\lambda_B}\right) w_1^- \, \mathrm{d}y', \qquad \text{(H.0.11)}$$

$$= \mathbf{a}^- \frac{NB}{ik^-G_{12}} \int_{-\infty}^{+\infty} \frac{2}{\lambda_B^2} \operatorname{sech}^2\left(\frac{y'}{\lambda_B}\right) w_2^- \, \mathrm{d}y'. \qquad \text{(H.0.12)}$$

These results are reproduced in the main text.

Appendix I

Creating Spin Wave Sources in MuMax3 software

This Appendix provides the details of how to create the spin wave sources in MuMax3 software which are used in this Thesis: the wave packet with uniform amplitude in the y direction (Gaussian & moving in the x direction), the wave packet which is Gaussian in both x and y and moving in x, the spin wave beam, and the point source. The use of a vector mask (and other basic features) was adapted from the MuMax3 documentation, the implementation of the 1-way spin wave packet in MuMax3 (by superposing two counterpropagating fields) was discovered by my colleague Fedor Mushenok, and the spin wave beam is based on the excitation method given in Ref. [139], though adapted somewhat for our use.

We aim to excite spin waves with a small Gaussian spread in (angular) frequency ω and wavevector k, so we inverse Fourier Transform the following functions,

$$F(k) = 2\sqrt{a_1}\sqrt{\pi}\exp\left[-a_1(k-k0)^2\right] \quad \Longrightarrow \; f(x) = \exp(-ik_0x)\exp\left[-\frac{x^2}{4a_1}\right], \tag{I.0.1}$$

$$F(\omega) = 2\sqrt{b_1}\sqrt{\pi}\exp\left[-b_1(\omega-\omega_0)^2\right] \quad \Longrightarrow \; f(t) = \exp(i\omega_0t)\exp\left[-\frac{t^2}{4b_1}\right], \tag{I.0.2}$$

which we can easily shift in space and time by replacing $x \to x - x_0$ and $t \to t - t_0$ in the Gaussians, as we show below in the code snippet.

The width of the Gaussian in space is quantified by a_1, where $a_1 = 1/(2c_k^2)$ and $c_k = 0.1k_0$ is the standard deviation in k, with k_0 the wavevector corresponding to the central excitation frequency. Notice that a_1 represents the usual denominator

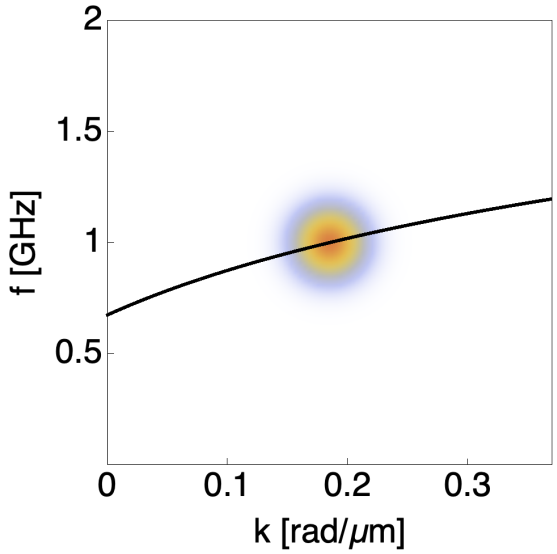

FIGURE I.1: Dispersion f vs. k for the forward-volume spin waves where $M = M_0 = M_R$ and $H = H_0$, showing the absolute value of the excitation function (red is high Fourier amplitude, blue is low Fourier amplitude), centred on $f = f_0$ and $k = k_0$. Only a small range of frequencies and wave numbers are excited.

in the k-space Gaussian $F(k)$. Similarly for the time/frequency-dependent terms: the width of the Gaussian in time is quantified by $b_1 = 1/(2c_\omega^2)$, with the standard deviation in angular frequency $c_\omega = 0.1\omega_0$, and ω_0 the central excitation angular frequency ($\omega_0 = 2\pi f_0$). The resulting function $F(k)F(\omega)$ is superposed on the dispersion relation in Fig. I.1.

To create the wave packet which moves in one direction, we need to rewrite the real component of the plane wave $\sin(\omega_0 t \mp k_0 x)$ (sign referring to right-/left-travelling respectively) as

$$\sin(\omega_0 t \mp k_0 x) = \cos(k_0 x)\cos(\omega_0 t) \pm \sin(k_0 x)\sin(\omega_0 t), \tag{I.0.3}$$

since the space and time functions must be applied separately in Mumax3. We multiply (I.0.3) by the Gaussian in space (I.0.1) and time (I.0.2) and the stimulation field amplitude $H_{\text{stim}} = 0.1\text{mT}$, and add this small dynamic contribution to the fixed external field. The code used in Chapter 5 for the Luneburg lens is given below.

LISTING I.1: Mumax code snippet to make a 1-way wavepacket (Gaussian in x and constant in y)

```
// lens properties:
r_lens := wavelength*6 // wavelength calculated from dispersion relation
source_position := 1.5*r_lens // positive value => 'left of centre'
```

```
lensoffsetx := r_lens/2
lensoffsety := 0

//Run:
c_k := 0.1*k; // standard deviation in k
c_w := 0.1*omega; // standard deviation in omega_0, with omega_0 = 2*pi*f_0
a1 := 1/(2*pow((c_k),2));
b1 := 1/(2*pow((c_w),2));
t0 := 1e-8; // delay time

// field in space
field1 := newVectorMask(Nx, Ny, Nz)
field2 := newVectorMask(Nx, Ny, Nz)

for xInd := 0; xInd < Nx; xInd++ {
   r := index2coord(xInd, 0, 0)
   \\ make Gaussian in x only:
  gaussx := exp(- pow(r.X()+source_position, 2) /(4*a1))
        for yInd := 0; yInd < Ny; yInd++ {
                for zInd := 0; zInd < Nz; zInd++ {
                      field1.setVector(xInd,yInd,zInd,
                      vector(stimAmp*sin(k*r.X())*gaussx, 0, 0))
                      //
                      field2.setVector(xInd,yInd,zInd,
                          vector(stimAmp*cos(k*r.X())*gaussx, 0, 0))
                }
        }
}

// Apply time dependence to spatial field, and add to existing B_ext field:
// (must be added after relaxing/minimising)

B_ext.add(field1, sin(omega*t)*exp(-pow(t-t0, 2)/(4*b1)))
B_ext.add(field2, cos(omega*t)*exp(-pow(t-t0, 2)/(4*b1)))
```

The code above is changed slightly for the Gaussian (in x and y) wave packet used in Chapter 6, and the amended code snippet is written below (note that the lens radius and source position differ depending on the source chosen, so this is omitted here).

LISTING I.2: Mumax code snippet to make a 1-way wavepacket (Gaussian in x and y)

```
...
// field
field1 := newVectorMask(Nx, Ny, Nz)
field2 := newVectorMask(Nx, Ny, Nz)

for xInd := 0; xInd < Nx; xInd++ {
  for yInd := 0; yInd < Ny; yInd++ {
    r := index2coord(xInd, yInd, 0)
    // make Gaussian in x:
    gaussx := exp(- pow(r.X()+source_positionx, 2) /(4*a1))
    // make Gaussian in y:
```

```
    gaussy := exp(- pow(r.Y()+source_positiony, 2) /(4*a1))
      for zInd := 0; zInd < Nz; zInd++ {
            field1.setVector(xInd,yInd,zInd,
            vector(stimAmp*sin(k*r.X())*gaussx*gaussy, 0, 0))
                    field2.setVector(xInd,yInd,zInd,
                        vector(stimAmp*cos(k*r.X())*gaussx*gaussy, 0, 0))
      }
        }
}

// Apply time dependence to spatial field, and add to existing B_ext field:
// (must be added after relaxing/minimising)

B_ext.add(field1, sin(omega*t)*exp(-pow(t-t0, 2)/(4*b1)))
B_ext.add(field2, cos(omega*t)*exp(-pow(t-t0, 2)/(4*b1)))
```

We use just one excitation field to make a simple beam, but the wave is thus emitted in both the positive and negative x direction. However, the left-going part of the beam is removed by the absorbing boundaries, and the right part can enter the lens. The required code is provided below.

LISTING I.3: Mumax code snippet to make a beam

```
...
field1 := newVectorMask(Nx, Ny, Nz)
// make source 8 cells wide & constant amplitude in x
for xInd := trunc((Nx/2) - (source_positionx/Cx) - 4);
xInd < trunc((Nx/2) - (source_positionx/Cx) + 4); xInd++ {
  for yInd := 0; yInd < Ny; yInd++ {
    r := index2coord(xInd, yInd, 0)
    // make Gaussian in y only:
    gaussy := exp(- pow(r.Y()+source_positiony, 2) /(4*a1))
      for zInd := 0; zInd < Nz; zInd++ {
          field1.setVector(xInd,yInd,zInd,vector(stimAmp*gaussy, 0, 0))
      }
        }
}

// Apply time dependence to spatial field, and add to existing B_ext field:
// (must be added after relaxing/minimising)
// (1 - exp(-0.1*omega*t)) ramps up the oscillation gradually

B_ext.add(field1, (1 - exp(-0.1*omega*t))*sin(omega*t))
```

Finally, we show a simple point source also used in Chapter 5. In this case, we found that the Gaussian spot in x and y was most easily controlled when expressed in terms of the wavelength $\lambda_0 = 2\pi/k_0$, so we write the code for this below.

LISTING I.4: Mumax code snippet to make a Gaussian 'point' source

```
...
// field
```

```
field1 := newVectorMask(Nx, Ny, Nz)

for xInd := 0; xInd < Nx; xInd++ {
  for yInd := 0; yInd < Ny; yInd++ {
    r := index2coord(xInd, yInd, 0)
    x := r.X()
        y := r.Y()
        // Gaussian in x * Gaussian in y:
        Gxy := exp(-(1/2)*pow((x+source_positionx)/(0.1*wavelength), 2))
            *exp(-(1/2)*pow((y+source_positiony)/(0.1*wavelength), 2))
    for zInd := 0; zInd < Nz; zInd++ {
                    field1.setVector(xInd,yInd,zInd,
                    vector(stimAmp*Bxy, stimAmp*Bxy, 0))
      }
        }
}

// Apply time dependence to spatial field, and add to existing B_ext field:
// (must be added after relaxing/minimising)

B_ext.add(field1, sin(omega*t)*exp(-pow(t-t0, 2)/(4*b1)))
```

Appendix J

Validation of the Modelling

We now briefly confirm that the modelling method in Chapters 5 and 6 is indeed valid, particularly in the latter case where we consider a large range of spin wave wavelengths. First, we check that our choice of cell size is valid for the results in both Chapters. Then, for Chapter 6, we confirm that the steps in magnetisation are adequate to represent the majority of the steering lenses correctly, and show why equal steps in magnetisation are preferable to equal steps in index.

J.1 Numerical vs. Analytical Dispersion

The first test for the work in both Chapters is that the cell size is adequately representing the smallest wavelength in the film plane, and also that the use of 1 cell across the thickness is permissible. The most straightforward way to confirm this is to overlay the numerical and analytical dispersion relations in each case, and check that the two match in the $f - k$ region of interest. We show that this is satisfied for the two different thicknesses of YIG-like film in Fig. J.1 and J.2, relevant for the results in Chapter 5 and 6, respectively.

All of the images are constructed by exciting the YIG-like film with a sinc pulse in time and Gaussian spatial dependence across x (constant across y). The same parameters as in the main text are used (M, H, s) but with a smaller model size of $1024 \times 1024 \times 1$ cells in the $x - y - z$ planes, respectively. It is easier to process the Fourier transforms for a smaller model, the only disadvantage is that the model extent limits the smallest step size in k. However, the lower resolution is acceptable for our requirements. In both figures, the numerical and analytical dispersions overlay well around the range of frequencies (hence wave numbers) excited in the models (when $f \approx 1$ GHz), confirming that they should be representing the waves appropriately.

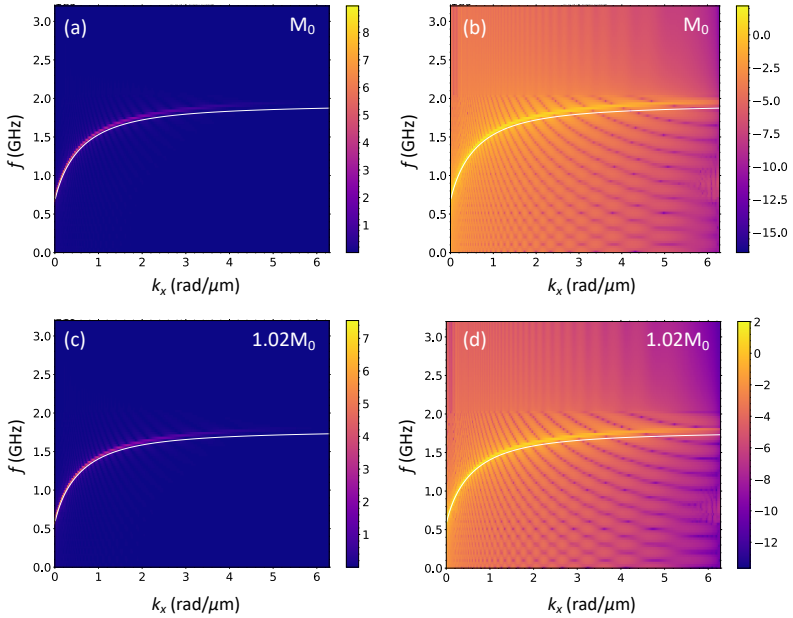

FIGURE J.1: Numerical dispersion (density plot) overlaid with the dipolar analytical dispersion (white solid line) for the YIG-like sample studied in Chapter 5, where $f_0 = 1$ GHz. M is set to (a, b) M_0 and (c, d) $1.02M_0$. The results are shown with an (a, c) linear colour scale or (b, d) logarithmic colour scale. Colour scale shows the Fourier amplitude of the numerical dispersion in arbitrary units.

J.2 Modelling a Steep Graded Index with Steps in the Magnetisation

One issue encountered when studying the steering lenses in Chapter 6 was that the beam or wave packet would encounter strong scattering/noise when interacting with the central region of the lens. This is mostly due to the cell size restricting how well we can represent the steep change in index[1]. As we will see, imposing constant steps in M is the preferable solution, since we are limited by a fixed number of regions. We show the results for the most extreme steering profile we have encountered; the Eaton lens.

The profile is designed to have 255 concentric circular regions between which the magnetisation changes in equal ('ideal') steps; the remaining regions are used for the absorbing boundary layers. The size of each circular region ensures that the stepped profile follows the desired magnetisation profile as closely as possible. For the majority of the Eaton lens this works correctly, as we show in Fig.

[1]It is also due to the small wavelengths induced by the new index being smaller than the cell size. This is more difficult to distinguish in the results, and likely forms numerical noise.

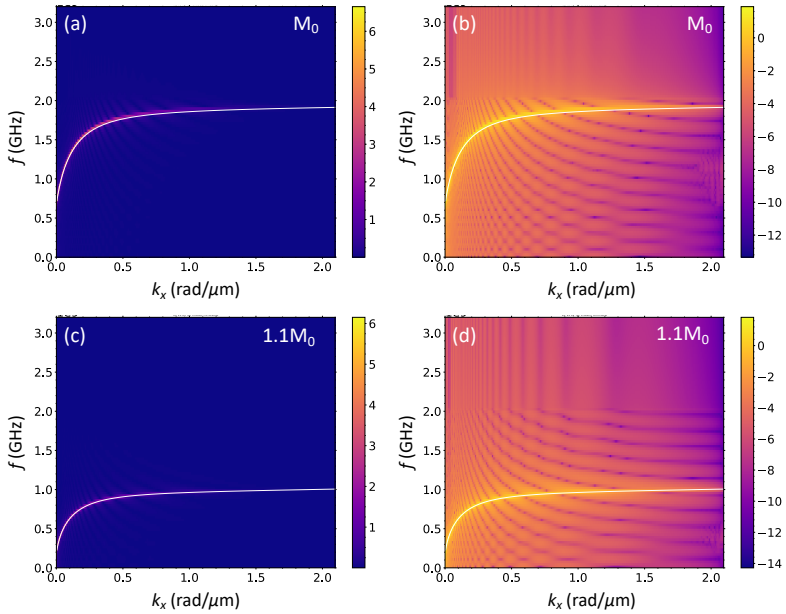

FIGURE J.2: Numerical dispersion (density plot) overlaid with the dipole-exchange analytical dispersion (white solid line) for the YIG-like sample studied in Chapter 6, where $f_0 = 1$ GHz. M is set to (a, b) M_0 and (c, d) $1.1M_0$. The results are shown with an (a, c) linear colour scale or (b, d) logarithmic colour scale. Colour scale shows the Fourier amplitude of the numerical dispersion in arbitrary units.

J.3 (a). We show the resulting index steps in panel (b). These images are created using 'ListStepPlot' in *Mathematica* software, fixing the step in M, and either rounding to the nearest cell along the x axis (to create the 'cell size limited steps', which is how we expect MuMax3 to be modelling the profile) or allowing fractional values of cell size, to create the 'ideal steps'. Both are compared to the 'ideal profile', a smooth function which would create the Eaton lens exactly, up to $M = 1.1M_0$. We can see from the insets of these figures that the magnetisation and index are clearly restricted by the cell size towards the centre, so the steps are larger than the 'ideal steps' profile, particularly in the central radius of 10 cells.

It is still preferable to impose constant steps in M instead of n, however. The stepped profile created using constant increments of n is shown in Fig. J.4. We can see that although the 'ideal steps' are resolving the central region much better than before, the 'cell size limited steps' are almost identical to those in Fig. J.3. Due to the limited number of regions, the steps towards the outer radius are also much larger for when we fix n than when we fix M, since n needs to change linearly by 53 in 255 steps (rather than nonlinearly when changing M in the same number of steps). Crucially, these constant steps in n are much larger than the

wavelength (corresponding to around 113 cells). As a result, we would observe strong scattering throughout the entire lens when it is created with constant n steps. It is preferable to have the steps in index occurring on a length scale smaller than the wavelength, which is achieved with constant steps in M.

To reiterate, this is purely a compromise due to the finite-difference modelling technique, and the limitations with the computational power. A smaller cell size, larger model size and more regions would enable a more accurate result, for either steps in n or M.

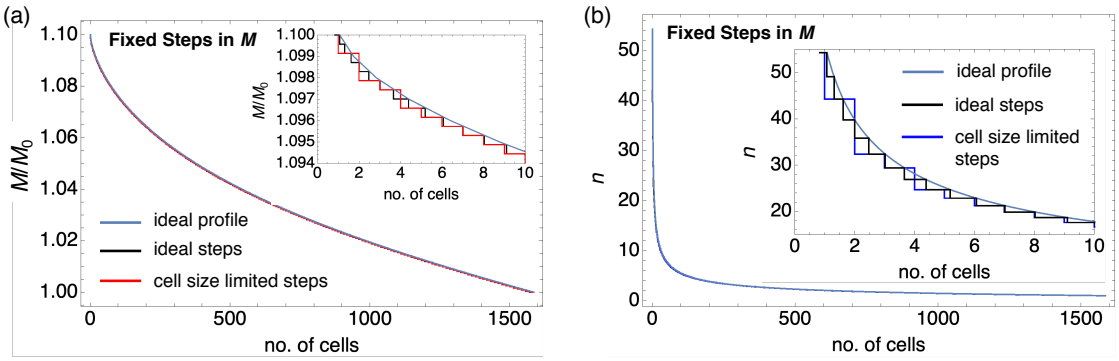

FIGURE J.3: Profile of (a) M and (b) n across the range of cells from $r = 0$ to $r = R$ when implemented by constant steps in M, to create the Eaton lens refractive index profile. The ideal profile (light blue line) is compared to the ideal stepped profile specified in MuMax3 (black line) in both panels. These are both compared to the likely profile that MuMax3 can implement, due to the cell size, written as 'cell size limited steps' in (a) M (red line) and (b) index (deep blue line). The profiles for the central 10 cells are shown in the inset. All graphs overlay eachother well in the main figure, but can be distinguished more clearly in the insets.

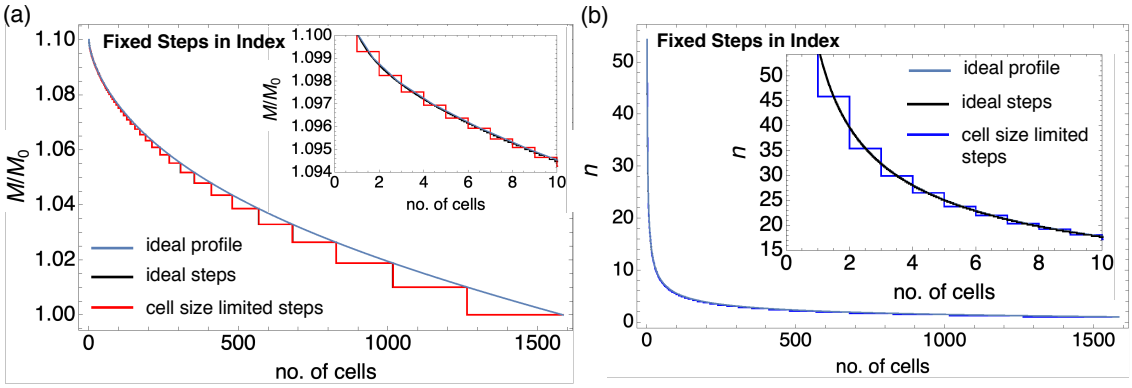

FIGURE J.4: Profile of (a) M and (b) n across the range of cells from $r = 0$ to $r = R$ when implemented by constant steps in n (this method is not used in the main text) to create the Eaton lens refractive index profile. The ideal profile (light blue line) is compared to the ideal stepped profile specified in MuMax3 (black line) in both panels. These are both compared to the likely profile that MuMax3 can implement, due to the cell size, written as 'cell size limited steps' in (a) M (red line) and (b) index (deep blue line). The black line is obscured by the light blue line in the main figure of (a) and (b), and the light blue line is obscured by the black line in the inset in (b), since the ideal steps are very small towards the centre (they overlay eachother in each case).

References

[1] V. V. Kruglyak, S. O. Demokritov, and D. Grundler, "Magnonics," J. Phys. D: Appl. Phys. **43**, 264001 (2010).

[2] A. A. Serga, A. V. Chumak, and B. Hillebrands, "YIG magnonics," J. Phys. D: Appl. Phys. **43**, 264002 (2010).

[3] B. Lenk, H. Ulrichs, F. Garbs, and M. Münzenberg, "The building blocks of magnonics," Phys. Rep. **507**, 107–136 (2011).

[4] A. V. Chumak, V. I. Vasyuchka, A. A. Serga, and B. Hillebrands, "Magnon spintronics," Nat. Phys. **11**, 453–461 (2015).

[5] D. D. Stancil and A. Prabhakar, *Spin Waves* (Springer US, Boston, MA, 2009).

[6] F. Bloch, "Zur Theorie des Ferromagnetismus," Z. Phys. **61**, 206–219 (1930).

[7] L. D. Landau and E. Lifshitz, "On the theory of the dispersion of magnetic permeability in ferromagnetic bodies," Phys. Z. Sowjetunion **8**, 101–114 (1935).

[8] Duncan T. Moore, "Gradient-index optics: A review," Appl. Opt. **19**, 1035–1038 (1980).

[9] U. Leonhardt and T. G. Philbin, *Geometry and Light: The Science of Invisibility* (Dover Publications, Inc, Mineola, New York, 2010).

[10] B. Liu, K. Song, and J. Xiao, "Two-Dimensional Optical Metasurfaces: From Plasmons to Dielectrics," Adv. Cond. Matter Phys. **2019**, 2329168 (2019).

[11] Y. Jin, B. Djafari-Rouhani, and D. Torrent, "Gradient index phononic crystals and metamaterials," Nanophotonics **8**, 685–701 (2019).

[12] C. S. Davies and V. V. Kruglyak, "Graded-index magnonics," Low Temp. Phys. **41**, 760–766 (2015).

[13] C. Bayer, S. O. Demokritov, B. Hillebrands, and A. N. Slavin, "Spin-wave wells with multiple states created in small magnetic elements," Appl. Phys. Lett. **82**, 607–609 (2003).

[14] E. V. Tartakovskaya, M. Pardavi-Horvath, and R. D. McMichael, "Spin wave localization in tangentially magnetized films," Phys. Rev. B **93**, 214436 (2016).

[15] C. S. Davies, A. Francis, A. V. Sadovnikov, S. V. Chertopalov, M. T. Bryan, S. V. Grishin, D. A. Allwood, Y. P. Sharaevskii, S. A. Nikitov, and V. V. Kruglyak, "Towards graded-index magnonics: Steering spin waves in magnonic networks," Phys. Rev. B **92**, 020408 (2015).

[16] P. Gruszecki and M. Krawczyk, "Spin-wave beam propagation in ferromagnetic thin films with graded refractive index: Mirage effect and prospective applications," Phys. Rev. B **97**, 094424 (2018).

[17] M. Vogel, R. Aßmann, P. Pirro, A. V. Chumak, B. Hillebrands, and G. von Freymann, "Control of Spin-Wave Propagation using Magnetisation Gradients," Sci. Rep. **8**, 11099 (2018).

[18] C. S. Davies, A. V. Sadovnikov, S. V. Grishin, Yu. P. Sharaevskii, S. A. Nikitov, and V. V. Kruglyak, "Generation of propagating spin waves from regions of increased dynamic demagnetising field near magnetic antidots," Appl. Phys. Lett. **107**, 162401 (2015).

[19] C. S. Davies and V. V. Kruglyak, "Generation of Propagating Spin Waves From Edges of Magnetic Nanostructures Pumped by Uniform Microwave Magnetic Field," IEEE Trans. Magn. **52**, 1–4 (2016).

[20] O. Dzyapko, I. V. Borisenko, V. E. Demidov, W. Pernice, and S. O. Demokritov, "Reconfigurable heat-induced spin wave lenses," Appl. Phys. Lett. **109**, 232407 (2016).

[21] A. G. Gurevich and G. A. Melkov, *Magnetization, Oscillations and Waves* (CRC Press Inc, New York, 1996).

[22] B. D. Cullity and C. D. Graham, *Introduction to Magnetic Materials*, 2nd ed. (IEEE/Wiley, Hoboken, N.J, 2009).

[23] M. L. Plumer, J. Van Ek, and D. Weller, *The Physics of Ultra-High-Density Magnetic Recording* (Springer, Berlin; New York, 2001).

[24] I. Žutić, J. Fabian, and S. Das Sarma, "Spintronics: Fundamentals and applications," Rev. Mod. Phys. **76**, 323–410 (2004).

[25] A. Kirilyuk, A. V. Kimel, and T. Rasing, "Ultrafast optical manipulation of magnetic order," Rev. Mod. Phys. **82**, 2731–2784 (2010).

[26] O. Chubykalo-Fesenko and P. Nieves, "Landau-Lifshitz-Bloch Approach for Magnetization Dynamics Close to Phase Transition," in *Handbook of Materials Modeling*, edited by W. Andreoni and S. Yip (Springer International Publishing, Cham, 2018) pp. 1–28.

[27] T. L. Gilbert, "A phenomenological theory of damping in ferromagnetic materials," IEEE Trans. Magn. **40**, 3443–3449 (2004).

[28] Stefan Maendl, Ioannis Stasinopoulos, and Dirk Grundler, "Spin waves with large decay length and few 100 nm wavelengths in thin yttrium iron garnet grown at the wafer scale," Appl. Phys. Lett. **111**, 012403 (2017).

[29] Takashi Manago, Kazuto Yamanoi, Shinya Kasai, and Seiji Mitani, "Damping factor estimation using spin wave attenuation in permalloy film," J. Appl. Phys. **117**, 17D121 (2015).

[30] B. A. Kalinikos, "Excitation of propagating spin waves in ferromagnetic films," IEE Proc. H - Microw. Opt. Antennas **127**, 4– (1980).

[31] G. Venkat, D. Kumar, M. Franchin, O. Dmytriiev, M. Mruczkiewicz, H. Fangohr, A. Barman, M. Krawczyk, and A. Prabhakar, "Proposal for a Standard Micromagnetic Problem: Spin Wave Dispersion in a Magnonic Waveguide," IEEE Trans. Magn. **49**, 524–529 (2013).

[32] G. S. Abo, Y. K. Hong, J. Park, J. Lee, W. Lee, and B. C. Choi, "Definition of Magnetic Exchange Length," IEEE Trans. Magn. **49**, 4937–4939 (2013).

[33] B. A. Kalinikos and A. N. Slavin, "Theory of dipole-exchange spin wave spectrum for ferromagnetic films with mixed exchange boundary conditions," J. Phys. C: Solid State Phys. **19**, 7013 (1986).

[34] C. Liu, J. Chen, T. Liu, F. Heimbach, H. Yu, Y. Xiao, J. Hu, M. Liu, H. Chang, T. Stueckler, S. Tu, Y. Zhang, Y. Zhang, P. Gao, Z. Liao, D. Yu, K. Xia, N. Lei, W. Zhao, and M. Wu, "Long-distance propagation of short-wavelength spin waves," Nat. Commun. **9**, 1–8 (2018).

[35] E. W. Merchand, *Gradient Index Optics* (Academic Press, London, 1978).

[36] U. Leonhardt and T. G. Philbin, "Chapter 2 Transformation Optics and the Geometry of Light," in *Progress in Optics*, Vol. 53, edited by E Wolf (Elsevier, 2009) pp. 69–152.

[37] U. Leonhardt, "Optical Conformal Mapping," Science **312**, 1777–1780 (2006).

[38] J. B. Pendry, "Controlling Electromagnetic Fields," Science **312**, 1780–1782 (2006).

[39] M. Elyasi, C. S. Bhatia, C.-W. Qiu, and H. Yang, "Cloaking the magnons," Phys. Rev. B **93**, 104418 (2016).

[40] M. Kadic, G. W. Milton, M. van Hecke, and M. Wegener, "3D metamaterials," Nat. Rev. Phys. **1**, 198–210 (2019).

[41] D. R. Smith, J. J. Mock, A. F. Starr, and D. Schurig, "Gradient index metamaterials," Phys. Rev. E **71**, 036609 (2005).

[42] V.V. Kruglyak, M. Dvornik, R.V. Mikhaylovskiy, O. Dmytriiev, G. Gubbiotti, S. Tacchi, M. Madami, G. Carlotti, F. Montoncello, L. Giovannini, R. Zivieri, J.W. Klos, M.L. Sokolovskyy, S. Mamica, M. Krawczyk, M. Okuda, J.C. Eloi, S. Ward, W. Schwarzacher, T. Schwarze, F. Brandl, D. Grundler, D.V. Berkov, E. Semenova, and N. Gor, "Magnonic Metamaterials," in *Metamaterial*, edited by Xun-Ya Jiang (InTech, 2012).

[43] M. Born and E. Wolf, *Principles of Optics*, 4th ed. (Pergamon Press Ltd., Oxford, 1970).

[44] S. A. Reshetnyak, "The approximation of geometrical optics for bulk spin waves in spatially inhomogeneous ferromagnetic insulators with an exchange defect," Low Temp. Phys. **30**, 295–298 (2004).

[45] A. Vansteenkiste, J. Leliaert, M. Dvornik, M. Helsen, F. Garcia-Sanchez, and B. Van Waeyenberge, "The design and verification of MuMax3," AIP Adv. **4**, 107133 (2014).

[46] K. S. Kunz and R. J. Luebbers, *The Finite Difference Time Domain Method for Electromagnetics* (CRC Press, 1993).

[47] S. Wang, D. Wei, and K. Gao, "Limits of Discretization in Computational Micromagnetics," IEEE Trans. Magn. **47**, 3813–3816 (2011).

[48] C. Andreas, S. Gliga, and R. Hertel, "Numerical micromagnetism of strong inhomogeneities," J. Magn. Magn. Mater. **362**, 7–13 (2014).

[49] H. Nyquist, "Certain Topics in Telegraph Transmission Theory," Trans. Am. Inst. Electr. Eng. **47**, 617–644 (1928).

[50] C. E. Shannon, "Communication in the Presence of Noise," Proc. IRE **37**, 10–21 (1949).

[51] D. B. Rozhdestvenskii, "Sampling and the discretization theorem," Autom. Remote Control **67**, 1991–2001 (2006).

[52] V. E. Demidov, S. Urazhdin, and S. O. Demokritov, "Direct observation and mapping of spin waves emitted by spin-torque nano-oscillators," Nat. Mater. **9**, 984–988 (2010).

[53] P. S. Keatley, V. V. Kruglyak, A. Neudert, M. Delchini, R. J. Hicken, J. R. Childress, and J. A. Katine, "Time- and vector-resolved magneto-optical Kerr effect measurements of large angle precessional reorientation in a 2x2μm^2 ferromagnet," J. Appl. Phys. **105**, 07D308 (2009).

[54] M. R. Freeman, W. K. Hiebert, and A. Stankiewicz, "Time-resolved scanning Kerr microscopy of ferromagnetic structures (invited)," J. Appl. Phys. **83**, 6217–6222 (1998).

[55] T. Sebastian, K. Schultheiss, B. Obry, B. Hillebrands, and H. Schultheiss, "Micro-focused Brillouin light scattering: Imaging spin waves at the nanoscale," Front. Phys **3**, 35 (2015).

[56] J. Jersch, V. E. Demidov, H. Fuchs, K. Rott, P. Krzysteczko, J. Münchenberger, G. Reiss, and S. O. Demokritov, "Mapping of localized spin-wave excitations by near-field Brillouin light scattering," Appl. Phys. Lett. **97**, 152502 (2010).

[57] S. Bonetti, R. Kukreja, Z. Chen, F. Macià, J. M. Hernàndez, A. Eklund, D. Backes, J. Frisch, J. Katine, G. Malm, S. Urazhdin, A. D. Kent, J. Stöhr, H. Ohldag, and H. A. Dürr, "Direct observation and imaging of a spin-wave soliton with p-like symmetry," Nat. Commun. **6**, 8889 (2015).

[58] F. Groß, N. Träger, J. Förster, M. Weigand, G. Schütz, and J. Gräfe, "Nanoscale detection of spin wave deflection angles in permalloy," Appl. Phys. Lett. **114**, 012406 (2019).

[59] Á. Papp, W. Porod, Á. I. Csurgay, and G. Csaba, "Nanoscale spectrum analyzer based on spin-wave interference," Sci. Rep. **7**, 9245 (2017).

[60] E. Schlömann, "Generation of Spin Waves in Nonuniform Magnetic Fields. I. Conversion of Electromagnetic Power into Spin-Wave Power and Vice Versa," J. Appl. Phys. **35**, 159–166 (1964).

[61] A. N. Kuchko, M. L. Sokolovskii, and V. V. Kruglyak, "Spectrum of spin waves in a magnonic crystal with a structure defect," Phys. Met. Metallogr. **101**, 513–518 (2006).

[62] V.S. Tkachenko, V.V. Kruglyak, and A.N. Kuchko, "Spin wave reflection from semi-infinite magnonic crystals with diffuse interfaces," Metamaterials **3**, 28–32 (2009).

[63] V. S. Tkachenko, V. V. Kruglyak, and A. N. Kuchko, "Spectrum and reflection of spin waves in magnonic crystals with different interface profiles," Phys. Rev. B **81**, 024425 (2010).

[64] Y. Au, T. Davison, E. Ahmad, P. S. Keatley, R. J. Hicken, and V. V. Kruglyak, "Excitation of propagating spin waves with global uniform microwave fields," Appl. Phys. Lett. **98**, 122506 (2011).

[65] A. García-Arribas, E. Fernández, A. V. Svalov, G. V. Kurlyandskaya, A. Barrainkua, D. Navas, and J. M. Barandiaran, "Tailoring the magnetic anisotropy of thin film permalloy microstrips by combined shape and induced anisotropies," Eur. Phys. J. B **86** (2013), 10.1140/epjb/e2013-30933-6.

[66] M. Krawczyk and D. Grundler, "Review and prospects of magnonic crystals and devices with reprogrammable band structure," J. Phys.: Condens. Matter **26**, 123202 (2014).

[67] Yu. I Gorobets, A. N. Kuchko, and S. V. Vasil'ev, "Excitation of modulated spin waves by a model one-dimensional anisotropy defect," Phys. Met. Metallogr. **85**, 272–275 (1998).

[68] D. K. Koltsov and M. E. Welland, "Control of micromagnetics in Permalloy nanomagnets by means of indentation," Journal of Applied Physics **94**, 3457 (2003).

[69] K. An, X. Ma, C.-F. Pai, J. Yang, K. S. Olsson, J. L. Erskine, D. C. Ralph, R. A. Buhrman, and X. Li, "Current control of magnetic anisotropy via stress in a ferromagnetic metal waveguide," Phys. Rev. B **93**, 140404 (2016).

[70] A. K. Shukla, M. Goto, X. Xu, K. Nawaoka, J. Suwardy, T. Ohkubo, K. Hono, S. Miwa, and Y. Suzuki, "Voltage-Controlled Magnetic Anisotropy in Fe_{1-x} Co_x/Pd/MgO system," Sci. Rep. **8**, 1–6 (2018).

[71] K. Xu, D. K. Schreiber, Y. Li, B. R. Johnson, and J. McCloy, "Effect of defects, magnetocrystalline anisotropy, and shape anisotropy on magnetic structure of iron thin films by magnetic force microscopy," AIP Adv. **7**, 056806 (2017).

[72] M. Kateb, H. Hajihoseini, J. T. Gudmundsson, and S. Ingvarsson, "Comparison of magnetic and structural properties of permalloy $Ni_{80}Fe_{20}$ grown by dc and high power impulse magnetron sputtering," J. Phys. D: Appl. Phys. **51**, 285005 (2018).

[73] Hans J. Weber and George B. Arfken, *Essential Mathematical Methods for Physicists, ISE* (Academic Press, 2004).

[74] Z.-H. Wei, M.-F. Lai, C. Chang, N. A. Usov, J. C. Wu, and J.-Y. Lai, "Magnetization reversals in elliptical permalloy particles," IEEE Trans. Magn. **40**, 2107–2109 (2004).

[75] L. F. Yin, D. H. Wei, N. Lei, L. H. Zhou, C. S. Tian, G. S. Dong, X. F. Jin, L. P. Guo, Q. J. Jia, and R. Q. Wu, "Magnetocrystalline Anisotropy in Permalloy Revisited," Phys. Rev. Lett. **97**, 067203 (2006).

[76] K. Y. Guslienko, J. Y. Lee, and S. K. Kim, "Dynamics of Domain Walls in Soft Magnetic Nanostripes: Topological Soliton Approach," IEEE Trans. Magn. **44**, 3079–3082 (2008).

[77] Y. Yoshimura, K.-J. Kim, T. Taniguchi, T. Tono, K. Ueda, R. Hiramatsu, T. Moriyama, K. Yamada, Y. Nakatani, and T. Ono, "Soliton-like magnetic domain wall motion induced by the interfacial Dzyaloshinskii-Moriya interaction," Nat. Phys. **12**, 157–161 (2016).

[78] F. Garcia-Sanchez, P. Borys, R. Soucaille, J.-P. Adam, R. L. Stamps, and J.-V. Kim, "Narrow Magnonic Waveguides Based on Domain Walls," Phys. Rev. Lett. **114**, 247206 (2015).

[79] X. S. Wang and X. R. Wang, "Domain Walls as Spin Wave Waveguides," arXiv:1512.05965v2 [cond-mat.mes-hall] (2015).

[80] K. Wagner, A. Kákay, K. Schultheiss, A. Henschke, T. Sebastian, and H. Schultheiss, "Magnetic domain walls as reconfigurable spin-wave nanochannels," Nat. Nanotechnol. **11**, 432–436 (2016).

[81] A. A. Thiele, "Excitation spectrum of magnetic domain walls," Phys. Rev. B **7**, 391 (1973).

[82] S. J. Hermsdoerfer, H. Schultheiss, C. Rausch, S. Schäfer, B. Leven, S.-K. Kim, and B. Hillebrands, "A spin-wave frequency doubler by domain wall oscillation," Appl. Phys. Lett. **94**, 223510 (2009).

[83] P. E. Roy, T. Trypiniotis, and C. H. W. Barnes, "Micromagnetic simulations of spin-wave normal modes and the resonant field-driven magnetization dynamics of a 360 ° domain wall in a soft magnetic stripe," Phys. Rev. B **82**, 134411 (2010).

[84] B. Mozooni and J. McCord, "Direct observation of closure domain wall mediated spin waves," Appl. Phys. Lett. **107**, 042402 (2015).

[85] V. Sluka, T. Schneider, R. A. Gallardo, A. Kákay, M. Weigand, T. Warnatz, R. Mattheis, A. Roldán-Molina, P. Landeros, V. Tiberkevich, A. Slavin, G. Schütz, A. Erbe, A. Deac, J. Lindner, J. Raabe, J. Fassbender, and S. Wintz, "Emission and propagation of 1D and 2D spin waves with nanoscale wavelengths in anisotropic spin textures," Nat. Nanotechnol. **14**, 328–333 (2019).

[86] B. Van de Wiele, S. J. Hämäläinen, P. Baláž, F. Montoncello, and S. van Dijken, "Tunable short-wavelength spin wave excitation from pinned magnetic domain walls," Sci. Rep. **6**, 21330 (2016).

[87] Y. Le Maho, J.-V. Kim, and G. Tatara, "Spin-wave contributions to current-induced domain wall dynamics," Phys. Rev. B **79**, 174404 (2009).

[88] S. Flügge, *Practical Quantum Mechanics* (Springer, Berlin, Heidelberg, 1971).

[89] H. Yildirim and M. Tomak, "Intensity-dependent refractive index of a Pöschl-Teller quantum well," J. Appl. Phys. **99**, 093103 (2006).

[90] L. V. Thekkekara, Venu Gopal Achanta, and S. Dutta Gupta, "Optical reflectionless potentials for broadband, omnidirectional antireflection," Opt. Express **22**, 17382–17386 (2014).

[91] J. Lekner, "Reflectionless eigenstates of the sech^2 potential," Am. J. Phys. **75**, 1151 (2007).

[92] S. V. Vasiliev, V. V. Kruglyak, M. L. Sokolovskii, and A. N. Kuchko, "Spin wave interferometer employing a local nonuniformity of the effective magnetic field," J. Appl. Phys. **101**, 113919 (2007).

[93] L. D. Landau and E. M. Lifshitz, *Electrodynamics of Continuous Media* (Pergamon Press Ltd., Oxford, 1960).

[94] S. Middelhoek, "Domain Walls in Thin Ni–Fe Films," J. Appl. Phys. **34**, 1054–1059 (1963).

[95] J. Rubinstein, "Sine-Gordon Equation," J. Math. Phys. **11**, 258–266 (1970).

[96] R. Wieser, E. Y. Vedmedenko, and R. Wiesendanger, "Quantized spin waves in ferromagnetic and antiferromagnetic structures with domain walls," Phys. Rev. B **79**, 144412 (2009).

[97] A. L. González, P. Landeros, and Á. S. Núñez, "Spin wave spectrum of magnetic nanotubes," J. Magn. Magn. Mater. **322**, 530–535 (2010).

[98] P. Borys, F. Garcia-Sanchez, J.-V. Kim, and R. L. Stamps, "Spin-Wave Eigenmodes of Dzyaloshinskii Domain Walls," Adv. Electron. Mater. **2**, 1500202 (2016).

[99] K. F. Riley, M. P. Hobson, and S. J. Bence, *Mathematical Methods for Physics and Engineering: A Comprehensive Guide* (Cambridge University Press, 2006).

[100] L. D. Landau and E. M. Lifshitz, *Quantum Mechanics: Non-Relativistic Theory* (New York, Paris: Pergamon Press, Oxford, 1965).

[101] E. Kreyszig, H. Kreyszig, and E. J. Norminton, *Advanced Engineering Mathematics*, 10th ed. (John Wiley, Hoboken, NJ, 2011).

[102] A. García-Arribas, E. Fernández, A. V. Svalov, G. V. Kurlyandskaya, A. Barrainkua, D. Navas, and J. M. Barandiaran, "Tailoring the magnetic anisotropy of thin film permalloy microstrips by combined shape and induced anisotropies," Eur. Phys. J. B **86**, 136 (2013).

[103] C. T. Boone and I. N. Krivorotov, "Magnetic Domain Wall Pumping by Spin Transfer Torque," Phys. Rev. Lett. **104**, 167205 (2010).

[104] S. P. Li, W. S. Lew, J. A. C. Bland, L. Lopez-Diaz, M. Natali, C. A. F. Vaz, and Y. Chen, "Microstructures: Spin-engineering magnetic media," Nature **415**, 600–601 (2002).

[105] R. K. Luneburg, *Mathematical Theory of Optics* (University of California Press, Berkeley & Los Angeles, 1964).

[106] G. Csaba, A. Papp, and W. Porod, "Spin-wave based realization of optical computing primitives," J. Appl. Phys. **115**, 17C741 (2014).

[107] J.-N. Toedt, M. Mundkowski, D. Heitmann, S. Mendach, and W. Hansen, "Design and construction of a spin-wave lens," Sci. Rep. **6**, 33169 (2016).

[108] A. V. Kozhevnikov, Yu. V. Khivintsev, G. M. Dudko, V. K. Sakharov, A. S. Dzhumaliev, S. L. Vysotskii, A. V. Stal'makhov, and Yu. A. Filimonov, "Filtration of Surface Magnetostatic Waves in Yttrium Iron Garnet Films of Variable Width Excited by Focusing Transducers," Tech. Phys. Lett. **44**, 705–708 (2018).

[109] S. Choi, S.-K. Kim, V. E. Demidov, and S. O. Demokritov, "Double-contact spin-torque nano-oscillator with optimized spin-wave coupling: Micromagnetic modeling," Appl. Phys. Lett. **90**, 083114 (2007).

[110] A. D. Falco, S. C. Kehr, and U. Leonhardt, "Luneburg lens in silicon photonics," Opt. Express **19**, 5156–5162 (2011).

[111] T. Zentgraf, Y. Liu, M. H. Mikkelsen, J. Valentine, and X. Zhang, "Plasmonic Luneburg and Eaton lenses," Nat. Nano. **6**, 151–155 (2011).

[112] J. A. Dockrey, M. J. Lockyear, S. J. Berry, S. A. R. Horsley, J. R. Sambles, and A. P. Hibbins, "Thin metamaterial Luneburg lens for surface waves," Phys. Rev. B **87**, 125137 (2013).

[113] S.-H. Kim, "Sound Focusing by Acoustic Luneburg Lens," ArXiv14095489 Cond-Mat (2014).

[114] D. B. Dove, "Demagnetizing Fields in Thin Magnetic Films," Bell Syst. Tech. J. **46**, 1527–1559 (1967).

[115] E. Schlömann and R. I. Joseph, "Surface-Roughness-Induced Demagnetizing Fields in Thin Films and Their Influence Upon the Approach to Saturation," J. Appl. Phys. **41**, 1336–1337 (1970).

[116] M. Langer, F. Röder, R. A. Gallardo, T. Schneider, S. Stienen, C. Gatel, R. Hübner, L. Bischoff, K. Lenz, J. Lindner, P. Landeros, and J. Fassbender, "Role of internal demagnetizing field for the dynamics of a surface-modulated magnonic crystal," Phys. Rev. B **95**, 184405 (2017).

[117] J. Fassbender and J. McCord, "Control of saturation magnetization, anisotropy, and damping due to Ni implantation in thin $Ni_{81}Fe_{19}$ layers," Appl. Phys. Lett. **88**, 252501 (2006).

[118] G. Venkat, H. Fangohr, and A. Prabhakar, "Absorbing boundary layers for spin wave micromagnetics," J. Magn. Magn. Mater. **450**, 34–39 (2018).

[119] M. M. Mattheakis, G. P. Tsironis, and V. I. Kovanis, "Luneburg lens waveguide networks," J. Opt. **14**, 114006 (2012).

[120] J. D. de Pineda, R. C. Mitchell-Thomas, A. P. Hibbins, and J. R. Sambles, "A broadband metasurface Luneburg lens for microwave surface waves," Appl. Phys. Lett. **111**, 211603 (2017).

[121] P. Rozenfeld, "The electromagnetic theory of three-dimensional inhomogeneous lenses," IEEE Trans. Antennas Propag. **24**, 365–370 (1976).

[122] F. Gaufillet and É Akmansoy, "Graded Photonic Crystals for Luneburg Lens," IEEE Photonics J. **8**, 2400211 (2016).

[123] M. Dvornik, A. N. Kuchko, and V. V. Kruglyak, "Micromagnetic method of s-parameter characterization of magnonic devices," J. App. Phys. **109**, 07D350 (2011).

[124] K. Vogt, H. Schultheiss, S. Jain, J. E. Pearson, A. Hoffmann, S. D. Bader, and B. Hillebrands, "Spin waves turning a corner," Appl. Phys. Lett. **101**, 042410 (2012).

[125] X. Xing, Y. Yu, S. Li, and X. Huang, "How do spin waves pass through a bend?" Sci. Rep. **3**, 2958 (2013).

[126] X. Xing, W. Yin, and Z. Wang, "Excitation of antisymmetric modes and modulated propagation of spin waves in bent magnonic waveguides," J. Phys. D: Appl. Phys. **48**, 215004 (2015).

[127] J. Lan, W. Yu, R. Wu, and J. Xiao, "Spin-Wave Diode," Phys. Rev. X **5**, 041049 (2015).

[128] A. V. Sadovnikov, C. S. Davies, V. V. Kruglyak, D. V. Romanenko, S. V. Grishin, E. N. Beginin, Y. P. Sharaevskii, and S. A. Nikitov, "Spin wave propagation in a uniformly biased curved magnonic waveguide," Phys. Rev. B **96**, 060401 (2017).

[129] C. S. Davies, A. Francis, A. V. Sadovnikov, S. V. Chertopalov, M. T. Bryan, S. V. Grishin, D. A. Allwood, Y. P. Sharaevskii, S. A. Nikitov, and V. V. Kruglyak, "Towards graded-index magnonics: Steering spin waves in magnonic networks," Phys. Rev. B **92**, 020408 (2015).

[130] J. Eaton, "On spherically symmetric lenses," Trans. IRE Prof. Group Antennas Propag. **PGAP-4**, 66–71 (1952).

[131] S. Cornbleet and P. J. Rinous, "Generalised formulas for equivalent geodesic and nonuniform refractive lenses," IEE Proc. H - Microw. Opt. Antennas **128**, 95–101 (1981).

[132] J. C. Miñano, "Perfect imaging in a homogeneous three-dimensional region," Opt. Express **14**, 9627–9635 (2006).

[133] M. Schmiele, V. S. Varma, C. Rockstuhl, and F. Lederer, "Designing optical elements from isotropic materials by using transformation optics," Phys. Rev. A **81**, 033837 (2010).

[134] T. M. Chang, G. Dupont, S. Enoch, and S. Guenneau, "Enhanced control of light and sound trajectories with three-dimensional gradient index lenses," New J. Phys. **14**, 035011 (2012).

[135] M. Šarbort and T. Tyc, "Spherical media and geodesic lenses in geometrical optics," J. Opt. **14**, 075705 (2012).

[136] T. Tyc and U. Leonhardt, "Transmutation of singularities in optical instruments," New J. Phys. **10**, 115038 (2008).

[137] I. R. Hooper and T. G. Philbin, "Transmutation of singularities and zeros in graded index optical instruments: A methodology for designing practical devices," Opt. Express **21**, 32313–32326 (2013).

[138] S. A. R. Horsley, I. R. Hooper, R. C. Mitchell–Thomas, and O. Quevedo–Teruel, "Removing singular refractive indices with sculpted surfaces," Sci. Rep. **4**, 4876 (2014).

[139] P. Gruszecki, J. Romero-Vivas, Yu. S. Dadoenkova, N. N. Dadoenkova, I. L. Lyubchanskii, and M. Krawczyk, "Goos-Hänchen effect and bending of spin wave beams in thin magnetic films," Appl. Phys. Lett. **105**, 242406 (2014).

[140] Y. G. Ma, C. K. Ong, T. Tyc, and U. Leonhardt, "An omnidirectional retroreflector based on the transmutation of dielectric singularities," Nat. Mater. **8**, 639–642 (2009).

[141] R. E Camley, "Magnetization dynamics in thin films and multilayers," J. Magn. Magn. Mater. **200**, 583–597 (1999).

[142] B. Vasić, G. Isić, R. Gajić, and K. Hingerl, "Controlling electromagnetic fields with graded photonic crystals in metamaterial regime," Opt. Express, OE **18**, 20321–20333 (2010).

[143] T. G. Philbin, "Making geometrical optics exact," J. Mod. Opt. **61**, 552–557 (2014).

[144] M. Vogel, A. V. Chumak, E. H. Waller, T. Langner, V. I. Vasyuchka, B. Hillebrands, and G. von Freymann, "Optically reconfigurable magnetic materials," Nat. Phys. **11**, 487–491 (2015).

[145] B. A. Kalinikos, M. P. Kostylev, N. V. Kozhus, and A. N. Slavin, "The dipole-exchange spin wave spectrum for anisotropic ferromagnetic films with mixed exchange boundary conditions," J. Phys.: Condens. Matter **2**, 9861–9877 (1990).

[146] M. Krawczyk, M. L. Sokolovskyy, J. W. Klos, and S. Mamica, "On the Formulation of the Exchange Field in the Landau-Lifshitz Equation for Spin-Wave Calculation in Magnonic Crystals," Adv. Cond. Matter Phys. **2012**, 764783 (2012).

[147] R. W. Damon and J. R. Eshbach, "Magnetostatic modes of a ferromagnet slab," J. Phys. Chem. Solids **19**, 308–320 (1961).

[148] R. W. Damon and H. Van De Vaart, "Propagation of Magnetostatic Spin Waves at Microwave Frequencies in a Normally-Magnetized Disk," J. Appl.Phys. **36**, 3453–3459 (1965).

[149] L. R. Walker, "Magnetostatic Modes in Ferromagnetic Resonance," Phys. Rev. **105**, 390–399 (1957).

[150] D. J. Griffiths, *Introduction to Electrodynamics* (Prentice-Hall, New Jersey, 1999).

[151] H. Bateman, *Higher Transcendental Functions*, edited by Arthur Erdélyi, Vol. I (McGraw-Hill Book Company, New York, 1953).